



**HAL**  
open science

# The superconducting properties research of iron based-122 by transport and scanning micro-squid measurements

Zhao-Sheng Wang

► **To cite this version:**

Zhao-Sheng Wang. The superconducting properties research of iron based-122 by transport and scanning micro-squid measurements. Other [cond-mat.other]. Université de Grenoble; University of Chinese academy of sciences, 2012. English. NNT : 2012GRENY029 . tel-01128251

**HAL Id: tel-01128251**

**<https://theses.hal.science/tel-01128251>**

Submitted on 9 Mar 2015

**HAL** is a multi-disciplinary open access archive for the deposit and dissemination of scientific research documents, whether they are published or not. The documents may come from teaching and research institutions in France or abroad, or from public or private research centers.

L'archive ouverte pluridisciplinaire **HAL**, est destinée au dépôt et à la diffusion de documents scientifiques de niveau recherche, publiés ou non, émanant des établissements d'enseignement et de recherche français ou étrangers, des laboratoires publics ou privés.

## THÈSE

Pour obtenir le grade de

### DOCTEUR DE L'UNIVERSITÉ DE GRENOBLE

Spécialité : **Physique**

Arrêté ministériel : 7 août 2006

Présentée par

**Zhao-Sheng WANG**

Thèse dirigée par **Klaus HASSELBACH**  
et codirigée par **Hai-Hu WEN, Cong REN**

préparée au sein du **Institut Néel**, dans l'**École Doctorale Physique**, et the **Institute of Physics, Chinese Academy of Sciences**

## Recherche sur les propriétés supraconductrices des supraconducteurs à base de Fer 122 par mesure de transport et microscopie à squid

Thèse soutenue publiquement le **26/05/2012**,  
devant le jury composé de :

**M. John R. KIRTLEY**

Rapporteur

**M. Qingming ZHANG**

Rapporteur

**M. Kees VAN DER BEEK**

Président

**M. Klaus HASSELBACH**

Directeur

**M. Hai-Hu WEN**

Directeur

**M. Cong REN**

Directeur







UNIVERSITÉ DE GRENOBLE

## THÈSE

Pour obtenir le grade de

**DOCTEUR DE L'UNIVERSITÉ DE GRENOBLE**

Spécialité : Physique

Arrêté ministériel : 7 août 2006

Présentée et soutenue publiquement par

Zhao-Sheng WANG

le 26 mai 2011

---

SUPERCONDUCTING PROPERTIES OF IRON-BASED BA-122 BY TRANSPORT  
MEASUREMENTS AND SCANNING NANO-SQUID MICROSCOPY

---

Thèse dirigée par Klaus HASSELBACH et codirigée par Hai-Hu WEN, Cong REN

## JURY

John R.	KIRTLEY	Professeur, Stanford University	Rapporteur
Klaus	HASSELBACH	Directeur de Recherche, Institut Néel	Directeur
Qingming	ZHANG	Professeur, Renmin University of China	Rapporteur
Hai-Hu	WEN	Professeur, Institute of Physics, CAS	Directeur
Cong	REN	Professeur, Institute of Physics, CAS	Directeur
Kees	VAN DER BEEK	Directeur de Recherche CNRS	Président

Thèse préparée au sein de l'institut Néel, CNRS/Université Joseph Fourier, Grenoble, et  
de l'Institute of Physics, Chinese Academy of Sciences, Beijing



# Abstract

More than twenty years after the discovery of high temperature superconductors, the underlying physical mechanism is still not well understood. In 2008, the discovery of a new family of high temperature superconductors, the iron-based superconductors, provided us a new chance to understand the high temperature superconductivity. Synthesizing high quality sample, detecting the basic superconducting properties, the gap structure and order parameter symmetry are essential steps in revealing the mechanism and application of new superconductors. This dissertation describes the growth of  $\text{Ba}_{1-x}\text{K}_x\text{Fe}_2\text{As}_2$  single crystals and the study of superconducting properties, gap structure and order parameter on Ba-122 iron-based superconductors with resistivity, Hall probe, point contact Andreev reflection spectroscopy and scanning nano-squid microscopy measurements.

Some historical events concerning superconductivity are recalled, and some key properties and theories of superconductivity are presented in Chapter 1. Then we will briefly introduce the discovery and current research situation of the iron-based superconductors.

In Chapter 2, the growth procedure of  $\text{Ba}_{1-x}\text{K}_x\text{Fe}_2\text{As}_2$  single crystals with self-flux method, and the characterization of the crystals with diffraction and energy dispersive analysis of x-ray, AC susceptibility and resistivity measurements are described. Then we report some results from temperature dependent resistivity measurements on  $\text{Ba}_{1-x}\text{K}_x\text{Fe}_2\text{As}_2$  ( $0.23 \leq x \leq 0.4$ ) single crystals in magnetic fields up to 9 T and angle dependent resistivity measurements on  $\text{Ba}_{0.6}\text{K}_{0.4}\text{Fe}_2\text{As}_2$  single crystals.

In Chapter 3, we introduce some details about a Hall probe measurement system we built. Then we present local and global magnetization measurements on high pressure  $\text{SmFeAsO}_{0.9}\text{F}_{0.1}$  polycrystals and  $\text{Ba}_{0.6}\text{K}_{0.4}\text{Fe}_2\text{As}_2$  single crystals with Hall probe and VSM. The results suggest that there is no node in the superconducting energy gap in  $\text{SmFeAsO}_{0.9}\text{F}_{0.1}$ , but indicate a multi-gap nature in  $\text{Ba}_{0.6}\text{K}_{0.4}\text{Fe}_2\text{As}_2$  single crystals.

In Chapter 4, we give a brief introduction about point contact Andreev reflection spectroscopy, then we report the measurements on  $\text{Ba}_{0.6}\text{K}_{0.4}\text{Fe}_2\text{As}_2$  single crystal and a series of electron-doped  $\text{BaFe}_{2-x}\text{Ni}_x\text{As}_2$  single crystals over a wide doping range. An extended s-wave can reproduce well the experimental data of  $\text{Ba}_{0.6}\text{K}_{0.4}\text{Fe}_2\text{As}_2$ . For  $\text{BaFe}_{2-x}\text{Ni}_x\text{As}_2$ , the analytical fitting illustrates an evolution of the gap structure from a nodeless in the underdoped side to a nodal feature in the overdoped region.

In Chapter 5, the development of a scanning nano-SQUID force microscope and measurements performed on a 80 nm Rhenium film are presented. The microscope can take topographic and magnetic images simultaneously. The maximal scanning range is  $70 \mu\text{m} \times 85 \mu\text{m}$  and the magnetic resolution is about  $1.5 \times 10^{-4} \Phi_0 / \sqrt{\text{Hz}}$ . Measurements on Rhenium film shows a very weak pinning force of vortices. Furthermore, the penetration depth  $\lambda$  of this sample was determined as a function of temperature, consistent with a BCS behavior.

In Chapter 6, we present some results from lower critical field, tunnel diode oscillator, heat capacity and scanning nano-squid microscopy measurements on systematic doped  $\text{Ba}(\text{Fe}_{1-x}\text{Ni}_x)_2\text{As}_2$  single crystals. Combining the results from all the measurements, the clean two-gap model is excluded for this system, and  $\lambda(0)$  can be scaled with  $T_c$  by a power law on both sides of the superconducting dome, indicating pair breaking is important in  $\text{Ba}(\text{Fe}_{1-x}\text{Ni}_x)_2\text{As}_2$  system. Flux penetration measurements were performed to explain the difference of the results between the lower critical field measurements and scanning nano-squid microscopy measurements.

---

Finally, in Chapter 7, a detailed summary is presented.

## **Keywords**

---

iron-based superconductor, Ba-122, superconducting anisotropy, Hall probe, Point-contact Andreev reflection spectroscopy, scanning nano-squid microscopy, penetration depth measurement

# Resumé français

Plus de vingt ans après la découverte de la supraconductivité à haute température critique, le mécanisme physique sous-jacent n'est pas encore bien cerné. En 2008, la découverte d'une nouvelle famille de supraconducteurs à haute température critique, les supraconducteurs à base de fer, a donné l'espoir de trouver une compréhension plus profonde des mécanismes de ce type de supraconductivité. Synthétiser des échantillons de grande qualité, la caractérisation des propriétés supraconductrices, l'étude des symétries du gap et du paramètre d'ordre sont des étapes essentielles pour révéler le mécanisme. La connaissance précise du mécanisme permettra de profiter pleinement des propriétés remarquables de ces matériaux dans leurs applications industrielles si prometteuses. Le présent thèse décrit d'abord la croissance de monocristaux de  $Ba_{1-x}K_xFe_2As_2$  et l'étude de leurs propriétés supraconductrices, menant vers la proposition d'une structure de gap du supraconducteur et d'un paramètre d'ordre pour les supraconducteurs à base de fer. Ensuite, à partir de mesures de résistivité, de sondes à effet Hall, de spectroscopie d'Andreev en mode point-contact et de l'imagerie magnétique par la microscopie à nano-SQUID.

Dans le chapitre 1, les événements historiques les plus marquants de la supraconductivité sont rappelés, les propriétés essentielles des supraconducteurs et le développement des théories de la supraconductivité sont esquissés avant de présenter brièvement la découverte des supraconducteurs à base de fer et de donner un aperçu des questions actuelles de recherche dans ce domaine.

Dans le chapitre 2, la procédure de croissance de monocristaux de  $Ba_{1-x}K_xFe_2As_2$  par la méthode de "self-flux", leur caractérisation par diffraction et par l'analyse de dispersion d'énergie des rayons X et la sensibilité des mesures de résistivité et de susceptibilité AC sont décrites. Puis nous présentons quelques résultats des mesures de la résistivité dépendante de la température de monocristaux du composé  $Ba_{1-x}K_xFe_2As_2$  ( $0,23 \leq x \leq 0,4$ ) sous champs magnétiques allant jusqu'à 9 T et dépendante de l'angle.

Dans le chapitre 3, nous exposons quelques points essentiels du système de mesure à base de sonde de Hall que nous avons construit. Ensuite, nous présentons des mesures d'aimantation locale et globale sur des polycristaux de  $SmFeAsO_{0,9}F_{0,1}$  synthétisés à haute pression, et de monocristaux de  $Ba_{0,6}K_{0,4}Fe_2As_2$  effectuées par sonde de Hall et VSM. Les résultats suggèrent qu'il n'y a pas de nœud dans le gap d'énergie du supraconducteur  $SmFeAsO$  dopé au fluor, mais indiquent la présence d'un multi-gap dans le cas de  $Ba_{0,6}K_{0,4}Fe_2As_2$ .

Dans le chapitre 4, nous donnons une brève introduction à la spectroscopie d'Andreev en mode point-contact, puis nous appliquons cette technique à des monocristaux de  $Ba_{0,6}K_{0,4}Fe_2As_2$  et à une série de monocristaux de  $BaFe_{2-x}Ni_xAs_2$  couvrant une large gamme de dopage. Une forme de gap de symétrie "s-étendue" peut reproduire les données expérimentales de  $Ba_{0,6}K_{0,4}Fe_2As_2$ . Pour  $BaFe_{2-x}Ni_xAs_2$ , l'ajustement analytique des courbes révèle une évolution systématique de la structure du gap à partir d'une symétrie sans nœud dans la région sous-dopée du diagramme de phase vers une symétrie du gap avec des nœuds dans la région surdopée.

Dans le chapitre 5, le développement d'un microscope de force à nano-SQUID et les mesures effectuées sur un film Rhénium d'épaisseur de 80 nm sont présentés. Le microscope peut acquérir des images topographiques et magnétiques simultanément. La plage de balayage maximale est de  $0,8 K$  et sa résolution magnétique est d'environ  $1,5 \times 10^{-4} \Phi_0 / \sqrt{Hz}$ . L'imagerie magnétique des films épitaxiés de Rhénium montre une force d'ancrage des vortex très faible. En

---

outre, la valeur absolue de la profondeur de pénétration  $\lambda$  de cet échantillon a été déterminée et son évolution avec la température est compatible avec un comportement BCS.

Dans le chapitre 6, nous présentons quelques résultats des mesures de  $\lambda$  par imagerie par microscopie de force nano-squid sur des monocristaux de  $\text{Ba}(\text{Fe}_{1-x}\text{Ni}_x)_2\text{As}_2$ , couvrant tout le diagramme de phase. Sur les mêmes cristaux ont été effectuées des mesures du premier champ critique, de la variation de fréquence d'un oscillateur diode tunnel et de la capacité calorifique. En combinant les résultats de toutes les mesures, un modèle à deux gaps dans la limite propre est exclu, et  $\lambda(0)$  suit une loi de puissance unique en fonction de  $T_c$  sur les deux côtés du diagramme supraconducteur, indiquant que la brisure de paires de Cooper est importante dans ce système. Par l'imagerie magnétique des mesures de pénétration du flux ont été effectuées permettant d'expliquer la différence des résultats entre les mesures du premier champ critique et les résultats obtenus par l'imagerie par microscopie de force nano-SQUID.

Enfin, au chapitre 7, un résumé détaillé et critique est présenté.

# Acknowledgements

The work I report in this thesis would never have been possible without the support of a great number of people who have unselfishly given their help and supported me intellectually as well as personally throughout the last six years. Chief among them are my three Ph.D. advisors: Dr. Cong Ren, Dr. Hai-Hu Wen and Dr. Klaus Hasselbach.

I would like to thank Dr. Cong Ren, the first teacher to initiate me into scientific research. He has spent a lot of time and effort to guide me, teach me, encourage me, discuss and do experiments with me. I would like to thank Dr. Hai-Hu Wen for his guide, inspiration, discussion, and especially giving me the opportunity to study at Institut Néel. His combination of expertise and enthusiasm makes him a great role model as a scientist. I would like to thank Dr. Klaus Hasselbach for his guidance, help, discussion, trust and encouragement throughout the process in doing my research and writing this thesis. He has also helped me a lot in my life in Grenoble. He is not only a good advisor but also a nice friend. I'm grateful to have been so lucky to meet so nice advisors.

I would also like to thank Dr. Lei Shan for the guidance and valuable discussions on various physics problems. Thank to my friends and coworkers who made it such a great place to work at the Institute of Physics and Institut Néel: Huan Yang, Chunhong Li, Jing Yan, Yan Huang, Min Zhu, Huiqian Luo, Lei Fang, Ying Jia, Gang Mu, Yonglei Wang, Xiyu Zhu, Peng Cheng, Bing Shen, Bin Zeng, Fei Han, Jing Gong, Zhenyu Wang, Jun Zhu, Xinyuan Hou, Danny Hykel, Meryll Colombet, Germain Souche, Oana Bunau, David Rio, Maela Bazin, Maxime Leroux, Tao Wu, Jun Wang, Qingyang Wang, Peng Liu, Zheng Han, Yusuke Shibata, Dibyendu Hazra and Martin Dvoracek. Special thanks to Danny Hykel, who is a great person to work with, and has not hesitated to get his hands dirty in helping out wherever necessary. He helped me a lot both in lab and outside. He introduced a lot of friends to me, and with his help, I got used to the life in Grenoble very quickly.

Thank Wen-Xin Wang, Zhi-An Ren, Huiqian Luo and Xingye Lu for providing the 2DEG wafer, F-SmFeAsO and  $\text{BaFe}_{2-x}\text{Ni}_x\text{As}_2$  samples. Thank all collaborators and their discussion: John R. Kirtley, Pierre Rodière, Thierry Klein, Christophe Marcenat, Michel Saint-Paul and Laureline Porcar. Thank Gregory Garde and Anne Gerardin for the manufacture of the pieces of the microscope. Thank Thierry Crozes and Dominique Mailly for the fabrication of SQUID. Thank Julien Minet, Jean-Luc Mocellin, Olivier Exshaw, Pierre Carecchio and Guillaume Bres for the help on electronics. Thank Thierry Fournier for the help on scanning electron microscope. Thank Hong Chen, Lihong Yang, Weiwen Huang and Yingzi Zhang for their help on X-ray and magnetization measurements.

I gratefully acknowledge the French Embassy in Beijing and the CROUS, who provided me the scholarship for the study in Grenoble and helped for the application of visa and my life in France. I also appreciate the work of the many fine administrative staff who made my life so much easier: Jun Liu, Si Xu, Jin Chen, Elisabeth Rochat, Christine Martinelli and Patricia Poirier.

Thank you to all of my friends from my high school, Wuhan University and I met at the Institute of Physics, who have shared these years, and whose contributions I cannot possibly begin to list.

Thank my reading and oral defense committee members: Prof. John R. Kirtley, Prof. Kees van der Beek, Prof. Shiping Feng, Prof. Guang-Ming Zhang, Prof. Yayu Wang, Prof. Qingming Zhang, Prof. Zhong-Yi Lu, Prof. Pengcheng Dai and Prof. Xianggang Qiu, for their time, interest, helpful comments and insightful questions.

---

Finally, I want to thank my family for all their love and encouragement. For my parents who raised me and supported me in all my pursuits. For the concern and care all the time of my sisters and brothers in law. And most of all for my beloved wife Ying Ye whose faithful support in last 6 years is so appreciated. Without their love, I would not have been able to complete this work.

# Contents

<b>Abstract</b>	<b>i</b>
<b>Resumé français</b>	<b>iii</b>
<b>Acknowledgements</b>	<b>v</b>
<b>1 Introduction</b>	<b>1</b>
1.1 Overview of superconductivity . . . . .	1
1.1.1 Zero electrical resistivity and Meissner effect . . . . .	1
1.1.2 Two types of superconductors . . . . .	3
1.1.3 BCS Theory . . . . .	6
1.1.4 Superconducting gap and superfluid density . . . . .	7
1.1.5 Josephson effect . . . . .	9
1.2 Iron-based superconductors . . . . .	9
1.2.1 Structural properties . . . . .	10
1.2.2 Symmetry and mechanisms of pairing . . . . .	12
<b>2 Growth, characterization and <math>H_{c2}</math> anisotropy of <math>\text{Ba}_{1-x}\text{K}_x\text{Fe}_2\text{As}_2</math> single crystals</b>	<b>15</b>
2.1 Growth of $\text{Ba}_{1-x}\text{K}_x\text{Fe}_2\text{As}_2$ single crystals . . . . .	15
2.2 Characterization of $\text{Ba}_{1-x}\text{K}_x\text{Fe}_2\text{As}_2$ single crystals . . . . .	16
2.3 $H_{c2}$ anisotropy of $\text{Ba}_{1-x}\text{K}_x\text{Fe}_2\text{As}_2$ single crystals . . . . .	20
2.4 Summary . . . . .	24
<b>3 Hall probe measurements</b>	<b>25</b>
3.1 Hall probe . . . . .	25
3.1.1 The Hall effect . . . . .	25
3.1.2 Hall probe fabrication . . . . .	26
3.1.3 Resolution and sensitivity . . . . .	28
3.2 Measurements on $\text{SmFeAsO}_{0.9}\text{F}_{0.1}$ polycrystal . . . . .	29
3.2.1 Sample synthesis . . . . .	30
3.2.2 $H_{c1}$ measurement . . . . .	31
3.3 Measurements on $\text{Ba}_{0.6}\text{K}_{0.4}\text{Fe}_2\text{As}_2$ single crystal . . . . .	35
3.4 Summary . . . . .	40
<b>4 Point-Contact Andreev Reflection measurements</b>	<b>41</b>
4.1 Point-contact Andreev reflection spectroscopy . . . . .	41
4.1.1 Andreev reflection . . . . .	41
4.1.2 Fabrication of point contacts . . . . .	45
4.2 Measurements on $\text{Ba}_{0.6}\text{K}_{0.4}\text{Fe}_2\text{As}_2$ single crystal . . . . .	46
4.3 Measurements on $\text{BaFe}_{2-x}\text{Ni}_x\text{As}_2$ single crystals . . . . .	49
4.3.1 Optimally-doped $\text{BaFe}_{1.9}\text{Ni}_{0.1}\text{As}_2$ . . . . .	50
4.3.2 Underdoped $\text{BaFe}_{2-x}\text{Ni}_x\text{As}_2$ . . . . .	53
4.3.3 Overdoped $\text{BaFe}_{2-x}\text{Ni}_x\text{As}_2$ . . . . .	55
4.4 Summary . . . . .	57

<b>5</b>	<b>Scanning nano-SQUID microscopy</b>	<b>58</b>
5.1	Introduction . . . . .	58
5.2	SQUID . . . . .	60
5.2.1	The main principle . . . . .	60
5.2.2	Fabrication . . . . .	61
5.2.3	Measurement of the critical current . . . . .	62
5.3	AFM . . . . .	65
5.3.1	Tuning Fork . . . . .	65
5.3.2	Regulation . . . . .	67
5.4	Motion system . . . . .	68
5.4.1	Scanner . . . . .	68
5.4.2	Coarse motion system . . . . .	69
5.4.3	Position read-out . . . . .	70
5.5	Others . . . . .	72
5.5.1	Cryostat . . . . .	72
5.5.2	Thermometry . . . . .	73
5.5.3	Magnetic field . . . . .	73
5.5.4	Electronics and Software . . . . .	74
5.6	Calibration . . . . .	75
5.7	SQUID/sample distance . . . . .	77
5.8	Possible improvements . . . . .	79
5.9	Measurements on Rhenium film . . . . .	80
5.9.1	Rhenium film . . . . .	80
5.9.2	Penetration depth measurements . . . . .	80
5.9.3	Vortex pinning . . . . .	82
5.10	Summary . . . . .	83
<b>6</b>	<b>Measurements on <math>\text{Ba}(\text{Fe}_{1-x}\text{Ni}_x)_2\text{As}_2</math> single crystals</b>	<b>84</b>
6.1	Introduction . . . . .	84
6.2	Transport measurements . . . . .	85
6.2.1	Lower critical field measurements . . . . .	85
6.2.2	Tunnel diode oscillator measurements . . . . .	87
6.2.3	Heat capacity measurements . . . . .	87
6.3	Scanning nano-squid microscopy measurements . . . . .	88
6.3.1	Penetration depth measurements . . . . .	88
6.3.2	Flux penetration measurements . . . . .	92
6.3.3	Anti-vortices, weak pinning and partial vortices . . . . .	94
6.3.4	$\lambda(T)$ measurements . . . . .	97
6.4	Summary . . . . .	97
<b>7</b>	<b>Summary</b>	<b>99</b>
	<b>Bibliography</b>	<b>102</b>

# 1

## Introduction

One century has passed since the discovery of superconductivity. During this period, many new superconductors were found and considerable progress in theory was made. Until now, superconductivity is one of the most actively studied field in the condensed matter physics and attracts immense experimental and theoretical efforts. As a novel macroscopic quantum phenomenon, superconductivity contains deep physics which remains to be unraveled. In this chapter, I will recall some historical events concerning superconductivity, briefly discuss some key properties of superconductivity and review shortly some theories of superconductivity before introducing the iron-based high-temperature superconductors.

### 1.1 Overview of superconductivity

---

Superconductivity was discovered in mercury by Heike Kamerlingh Onnes in 1911. Now hundreds of superconducting materials are known, including more than half of the known elements (shown in figure 1.1), a lot of intermetallic compounds, organic, spinel and perovskite compounds. Owing to the continuous efforts of physicists and material scientists, we have made significant progress in understanding the properties and physical principle of superconductors. Below I will describe some important achievements of both experiment and theory in superconductivity research accomplished in the last 100 years.

#### 1.1.1 Zero electrical resistivity and Meissner effect

Zero electrical resistivity and the Meissner effect are the two hallmarks of superconductivity. In 1908, H. Kamerlingh Onnes became the first person who succeeded in liquefying helium. Three years later, when he investigated the low temperature electrical resistance of mercury, he found that the resistivity of mercury abruptly dropped to zero as temperature was lowered below 4.21 K [2], shown in figure 1.2. He named this phenomenon superconductivity. The superconductor has finite resistivity above the transition temperature  $T_c$ , it is in the normal state, and the resistivity quickly decreases to zero below  $T_c$ , it is in the superconducting state. The superconducting transition is a second order phase transition.

The second defining characteristic of a superconductor is much less obvious than its zero electrical resistance. It was over 20 years after the discovery of superconductivity that W. Meissner and R.

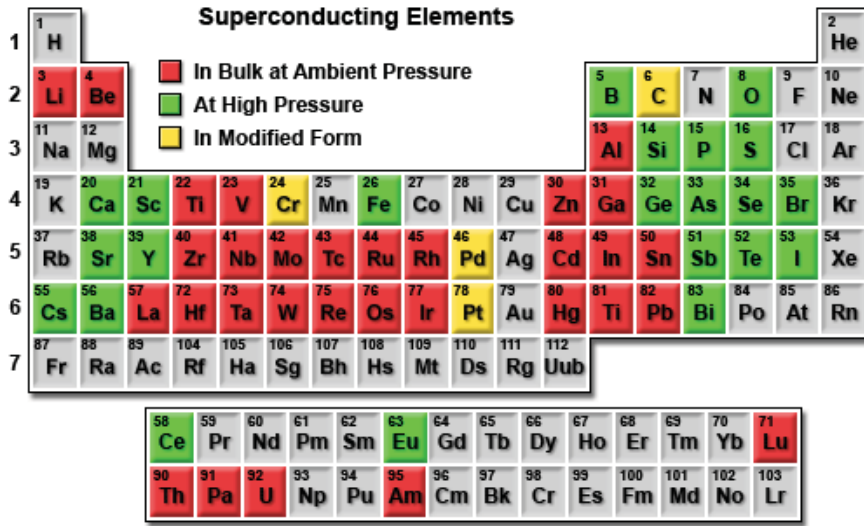


Figure 1.1: More than half of the known elements are superconductors. Image taken from [1].

Ochsenfeld discovered that when a superconductor is cooled below the transition temperature under an applied magnetic field, the applied field is excluded from the bulk of the superconductor, so that  $B = 0$  throughout its interior[3], excluded by superconducting screening currents at the surface. This property of the superconducting state is known as the Meissner effect.

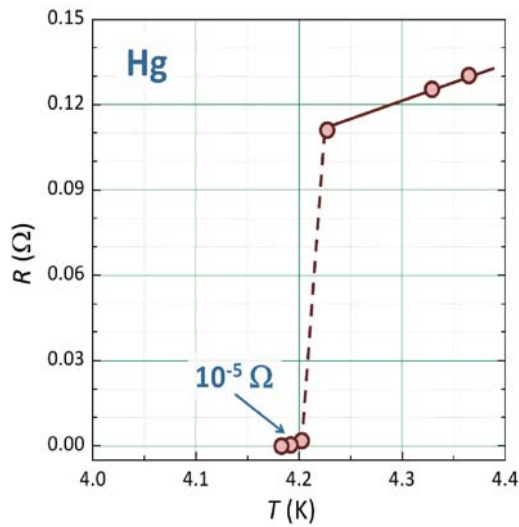


Figure 1.2: Vanishing of electrical resistivity below a critical temperature  $T_c$ , discovered in mercury by Kamerlingh Onnes in 1911[2]. The image is taken from [4].

It is important to recognize that the exclusion of the magnetic field from inside a superconductor cannot be predicted by applying Maxwell's equations to a **perfect conductor** which has zero electrical resistance below a certain  $T_c$ . As shown in figure 1.3, when a weak magnetic field is applied to a perfect conductor above its "critical" temperature  $T_c$ , since the resistivity is not zero in the normal state, the magnetic induction  $\mathbf{B}$  inside the perfect conductor is not zero. Then the perfect conductor is cooled down below  $T_c$ . According to the Maxwell's equations

$$\nabla \times \mathbf{E} = -\frac{\partial \mathbf{B}}{\partial t} \tag{1.1}$$

the zero resistivity below  $T_c$  leads to a constant  $\mathbf{B}$ . So  $\mathbf{B}$  will not change and it is not zero. However,

for the superconductor,  $\mathbf{B}$  is always zero. Therefore, the Meissner effect distinguishes a superconductor from a perfect conductor.

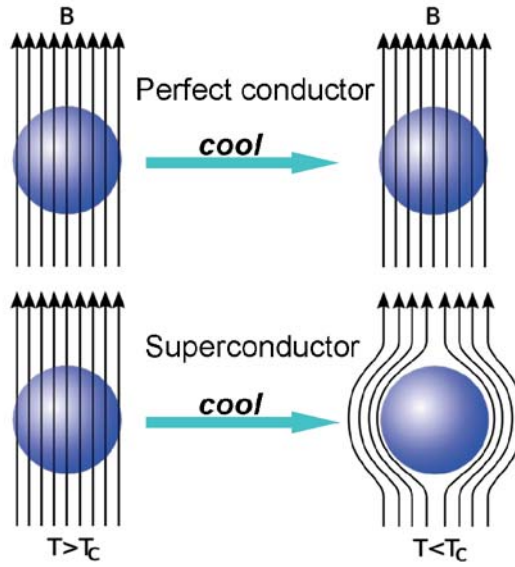


Figure 1.3: A comparison of the response of a perfect conductor and a superconductor to an applied magnetic field. When they are cooled below their critical temperatures, the magnetic field within the perfect conductor doesn't change, but the magnetic field within the superconductor is expelled (Meissner effect).

Shortly after the discovery of the Meissner effect, the brothers Fritz and Heinz London put forward a simple but useful description of the electrodynamics of superconductivity in 1935[5]. They used a two-fluid model to describe superconductivity: the total charge carrier density  $n$  can be written as the sum of the density of normal carriers  $n_n$  and the density of superconducting carriers  $n_s$ ,  $n = n_n$  in normal state and  $n = n_s$  at  $T = 0$ . By assuming the superconducting current is always dependent on the local magnetic field, combining with the Maxwell's equations, they got the **London equations**:

$$\frac{\partial \mathbf{j}_s}{\partial t} = \frac{n_s e^2}{m} \mathbf{E} \quad (1.2)$$

$$\nabla \times \mathbf{j}_s = -\frac{n_s e^2}{m} \mathbf{B} \quad (1.3)$$

Equation 1.2 accounts for the zero resistivity and equation 1.3 accounts for the Meissner effect. It is important to note that these equations are not an explanation of superconductivity. They were introduced as a restriction on Maxwell's equations so that the behavior of superconductors deduced from the equations was consistent with experimental observations, and in particular with the Meissner effect. In the case of a superconductor in the  $x > 0$  half space with an applied field  $\mathbf{B} = B_0 \mathbf{z}$ , the solution of equation 1.3 is

$$B_z(x) = B_0 e^{-x/\lambda_L} \quad (1.4)$$

This means the Meissner effect does not cause the field to be completely ejected but instead the field penetrates the superconductor over a very small distance  $\lambda_L$ , called the **London penetration depth**, and is decaying exponentially to zero within the bulk of the material.

### 1.1.2 Two types of superconductors

The superconducting state can be destroyed by an external magnetic field, the field  $H_c$  is called thermodynamic critical field. According to the different behavior under magnetic field at the transition

from the superconducting to the normal state, superconductors are divided to two types: type-I and type-II superconductors.

For a type-I superconductor, as shown in figure 1.4(a), if the magnetic field is below  $H_c$ , the material is in the superconducting state; but as soon as the magnetic field is above  $H_c$ , it transits in the normal state. The phase transition is abrupt. But for a type-II superconductor, there are two critical fields: the **lower critical field**  $H_{c1}$  and the **upper critical field**  $H_{c2}$ . Below  $H_{c1}$ , the superconductor is in a pure superconducting state, the same as a type-I superconductor in magnetic field below  $H_c$ , which is called the **Meissner state**. But between  $H_{c1}$  and  $H_{c2}$ , magnetic flux from external fields is no longer completely expelled, and the superconductor is in a **mixed state**. Above  $H_{c2}$ , the superconductivity is completely destroyed, and the material exists in a normal state, as shown in 1.4(b).

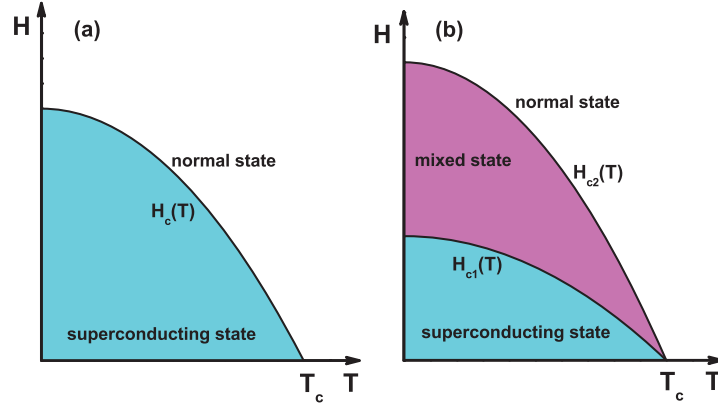


Figure 1.4: Phase diagrams for type-I (a) and type-II (b) superconductors.

Ginzburg-Landau theory(G-L theory) is a very successful mathematical theory used to model superconductivity. By introducing the interface energy, it can explain the two types of superconductor very well. G-L theory is based on Landau's previously-established theory of second-order phase transitions. Landau and Ginzburg argued that all superconducting electrons behaved coherently and superconducting electrons could be described by a complex order parameter  $\psi$ . Then the free energy  $F$  of a superconductor near the superconducting transition has the form

$$F = F_n + \alpha|\psi|^2 + \frac{\beta}{2}|\psi|^4 + \frac{1}{2m}|(-i\hbar\nabla - 2e\mathbf{A})\psi|^2 + \frac{|\mathbf{B}|^2}{2\mu_0} \quad (1.5)$$

where  $F_n$  is the free energy in the normal phase,  $\alpha$  and  $\beta$  are phenomenological parameters,  $m$  is an effective mass,  $e$  is the charge of an electron,  $\mathbf{A}$  is the magnetic vector potential, and  $\mathbf{B} = \nabla \times \mathbf{A}$  is the magnetic field. By minimizing the free energy with respect to fluctuations in the order parameter and the vector potential, two coupled **Ginzburg-Landau equations** can be obtained

$$\alpha\psi + \beta|\psi|^2\psi + \frac{1}{2m}(-i\hbar\nabla - 2e\mathbf{A})^2\psi = 0 \quad (1.6)$$

$$\mathbf{J}_s = -\frac{ie\hbar}{m}(\psi^*\nabla\psi - \psi\nabla\psi^*) - \frac{4e^2}{m}|\psi|^2\mathbf{A} \quad (1.7)$$

where  $\mathbf{J}_s$  denotes the superconducting electrical current density[6]. The first equation determines the order parameter  $\psi$  based on the applied magnetic field, and the second equation provides the superconducting current.

The Ginzburg-Landau equations produce many interesting and valid results. The prediction of the existence of two characteristic lengths in a superconductor is one of these. The first is a **coherence length**  $\xi$ , given by

$$\xi = \sqrt{\frac{\hbar^2}{2m|\alpha|}} \quad (1.8)$$

which describes the shortest length over which the order parameter  $\psi$  can vary significantly. The second is the **penetration depth**  $\lambda$ , given by

$$\lambda = \sqrt{\frac{m}{4\mu_0 e^2 |\psi_0|^2}} \quad (1.9)$$

where  $\psi_0$  is the equilibrium value of the order parameter in the absence of an electromagnetic field. The penetration depth describes the depth to which an external magnetic field can penetrate the superconductor.

The ratio  $\kappa = \lambda/\xi$  is known as the **Ginzburg-Landau parameter**. Assuming there is a mixture of superconducting and normal domains in the external field, the sign of the interface energy  $\delta_{ns}$  is determined by  $\kappa$ . When  $\kappa < \frac{1}{\sqrt{2}}$ ,  $\delta_{ns} > 0$ , the formation of the interface is not energy favorable, the superconducting phase and the normal state will only exist at  $H < H_c$  or  $H > H_c$  respectively. This type of superconductor is the type-I superconductor. When  $\kappa > \frac{1}{\sqrt{2}}$ ,  $\delta_{ns} < 0$ , the formation of the interface becomes energetically favorable under certain circumstances. This type of superconductor is the type-II superconductors.

The most important finding from Ginzburg-Landau theory is **flux quantization** made by Alexei Abrikosov in 1957[7]. Flux quantization occurs in type-II superconductors subjected to a magnetic field. From the lower critical field  $H_{c1}$  up to the upper critical field  $H_{c2}$ , flux penetrates in discrete units while the bulk of the material remains superconducting.

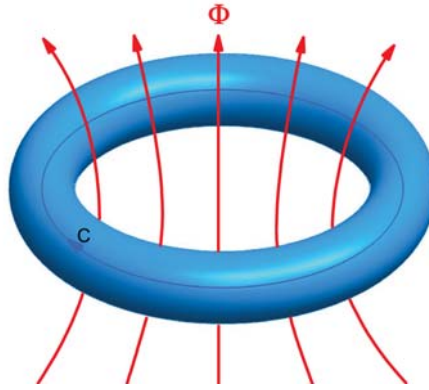


Figure 1.5: The magnetic flux in a superconducting ring.

Let us think about a superconducting ring in magnetic field like figure 1.5. From equation 1.7, we can get

$$\nabla\psi = \frac{2e}{\hbar}\mathbf{A} + \frac{m}{\hbar e|\psi|^2}\mathbf{J}_s \quad (1.10)$$

Integrating the equation along the closed loop C, we obtain

$$\oint_C \nabla\psi \cdot d\mathbf{l} = \frac{2e}{\hbar} \oint_C \mathbf{A} \cdot d\mathbf{l} + \oint_C \frac{m}{\hbar e|\psi|^2} \mathbf{J}_s \cdot d\mathbf{l} \quad (1.11)$$

As  $\psi$  has to be a single-valued function, the integral on the left hand side should be an integral multiple of  $2\pi$ . And using the Stokes theorem we have

$$\oint_C \mathbf{A} \cdot d\mathbf{l} = \iint_s \nabla \times \mathbf{A} \cdot d\mathbf{s} = \iint_s \mathbf{B} \cdot d\mathbf{s} = \Phi_C \quad (1.12)$$

In a superconductor  $\mathbf{J}_s = 0$ , so we get

$$\Phi_C = 2n\pi \frac{\hbar}{2e} = n \frac{h}{2e} = n\Phi_0 \quad (1.13)$$

where  $\Phi_0$  is the **flux quantum** and

$$\Phi_0 = \frac{h}{2e} \approx 2.07 \times 10^{-15} \text{Wb} \quad (1.14)$$

So when a type-II superconductor is put in a magnetic field, when  $H < H_{c1}$ , the average field  $B$  inside the specimen is zero which shows the pure Meissner effect. When  $H_{c1} < H < H_{c2}$ , the magnetic field penetrates inside the specimen, the superconductor is divided into normal and superconducting domains which are parallel to the external field. The normal domains are **vortices**, each with a radius of the order  $\xi$  and magnetic flux of  $\Phi_0$ . The density of the vortices increases with increasing external field until  $H_{c2}$ , at which the distance between two vortices is about  $\xi$  and the specimen transits from the superconducting to the normal state.

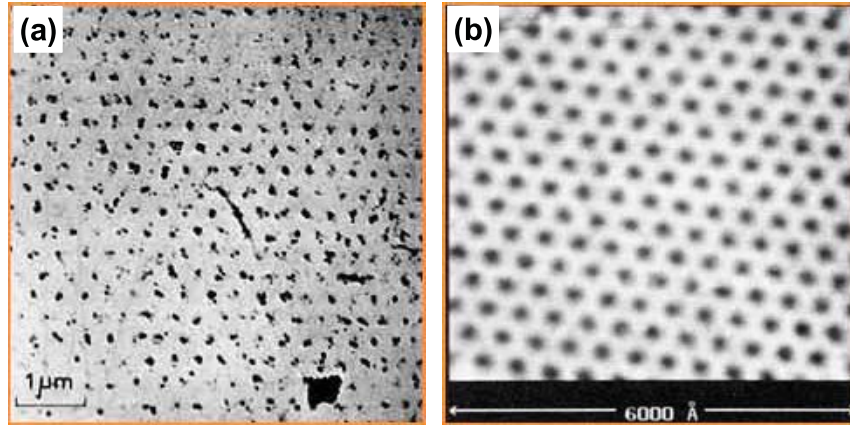


Figure 1.6: (a) First image of vortex lattice by Bitter decoration on the surface of a lead-indium alloy at 1.1 K[8]. (b) Vortex lattice in NbSe<sub>2</sub> at 1 T by STM[9]

Because the interaction between the vortices, they are most commonly arranged in a hexagonal lattice, which is called the **vortex lattices**. The vortex lattice was first observed by U. Essmann and H. Tr uble by means of Bitter decoration in 1967[8], as shown in figure 1.6(a). Nowadays, there are a lot of ways to see the vortex lattice. In figure 1.6(b) is a vortex lattice in NbSe<sub>2</sub> observed by STM[9].

### 1.1.3 BCS Theory

The first microscopic theory of superconductivity was proposed by John Bardeen, Leon Cooper, and Robert Schrieffer in 1957[10, 11], now known as the **BCS theory**. A key conceptual element in this theory is the pairing of electrons close to the Fermi level into **Cooper pairs** through interaction with the crystal lattice. Roughly speaking the picture is the following as shown in figure 1.7:

An electron moving through a conductor will attract nearby positive charges in the lattice. This deformation of the lattice causes another electron, with opposite momentum and spin, to move into the region of higher positive charge density. This looks like one electron attracts another electron through the lattice vibration, which can overcome the Coulomb repulsion, then two electrons become correlated. Individual pairs are not stuck together forever. They are constantly breaking and reforming. Individual electrons cannot be identified, so rather than consider them to be dynamically changing pairs, they may be considered as permanently paired.

Pairs of electrons can behave very differently from single electrons which are fermions and must obey the Pauli exclusion principle. The pairs of electrons act more like bosons which can condense into the same energy level. There are a lot of such electron pairs in a superconductor, so that they overlap very strongly, forming a highly collective "condensate". The condensate is energetically separated from the first excited state by the gap energy.

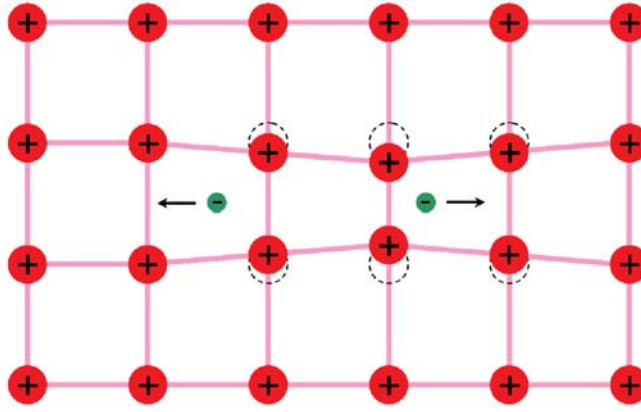


Figure 1.7: The formation of a cooper pair: A passing electron attracts the positive charged ions of the lattice, causing a slight ripple in its wake. Another electron passing in the opposite direction is attracted to that displacement.

The BCS theory shows a isotope effect, which is the observation that for a given superconducting material, the critical temperature is inversely proportional to the mass of the isotope used in the material, the isotope effect has been observed in a large number of superconductors. Two of the most important predictions of BCS theory concern the superconducting transition temperature  $T_c$  and the gap: In the weak coupling limit, the BCS theory predicts

$$k_B T_c = 1.14 \hbar \omega_D e^{-1/N(0)V} \quad (1.15)$$

$$\Delta(0) \approx 2 \hbar \omega_D e^{-1/N(0)V} \quad (1.16)$$

where  $k_B$  is the Boltzmann constant,  $\omega_D$  is the Debye frequency,  $N(0)$  is the electronic density of states at the Fermi energy and  $V$  is the interaction potential. Then we can get the famous equation

$$2\Delta(0) = 3.53 k_B T_c \quad (1.17)$$

The BCS theory is a successful theory, but there are still some experimental results which cannot be explained by it, such as  $2\Delta(0)/k_B T_c$  of Pb (4.1) and Hg (4.6) are not 3.53[12]. This is because in BCS theory, to simplify the calculation, a lot of assumptions were made, such as a constant electron-phonon interaction, spherical Fermi sphere assumption, etc. In 1960, G. M. Eliashberg considered a more realistic situation and considered the electron-phonon spectral function, band structure, etc[13]. Eliashberg theory can be regarded as an extension of BCS theory. The original BCS theory only discusses the situation in which the superconductor is fully gapped, also called *s*-wave. Eliashberg theory extends BCS theory to the *d*-wave case. In 1968, McMillan predicted that there was a highest possible  $T_c$  of about 30 K from the BCS theory[14], which is called the **McMillan limit**. Now materials that display superconductivity as described by BCS theory or its extensions are called **conventional superconductors**, and **unconventional superconductors** for others.

#### 1.1.4 Superconducting gap and superfluid density

For spin singlet pairing states, a  $\mathbf{k}$ -dependent superconducting gap function takes the form

$$\Delta(T, \mathbf{k}) = \Delta_0(T) g(\mathbf{k}) \quad (1.18)$$

where  $g(\mathbf{k})$  is a dimensionless function describing the angular variation of the gap on the Fermi surface.  $\Delta_0(T)$  carries the temperature dependence[15]. As  $\Delta_0(T)$  involves a Fermi surface average

of  $g(\mathbf{k})$ , it depends on the pairing symmetry in general. One of the most widely used expressions for  $\Delta_0(T)$  is

$$\Delta_0(T) = \Delta_0(0) \tanh \left( \frac{\pi T_c}{\Delta_0(0)} \sqrt{a \left( \frac{T_c}{T} - 1 \right)} \right) \quad (1.19)$$

where  $\Delta_0(0)$  is the gap magnitude at zero temperature and  $a$  is a parameter dependent upon the particular pairing state[16]. For (1) isotropic  $s$ -wave gap,  $g(\mathbf{k}) = 1$ ,  $a = 1$ ,  $\Delta_0(0) = 1.76k_B T_c$ ; (2)  $d$ -wave gap,  $g(\mathbf{k}) = \cos(2\varphi)$ ,  $\Delta_0(0) = 2.14k_B T_c$ ,  $a = 4/3$ . Then the normalized superfluid density is given by[17, 18]

$$\tilde{\rho}(T) = 1 + \frac{1}{\pi} \int_0^{2\pi} \int_{\Delta(T,\varphi)}^{\infty} \frac{\partial f(E)}{\partial E} \frac{E}{\sqrt{E^2 - \Delta(T,\varphi)^2}} dE d\varphi \quad (1.20)$$

$f = [1 + \exp(E/K_B T)]^{-1}$  is the Fermi function,  $\varphi$  is the angle along the Fermi surface.

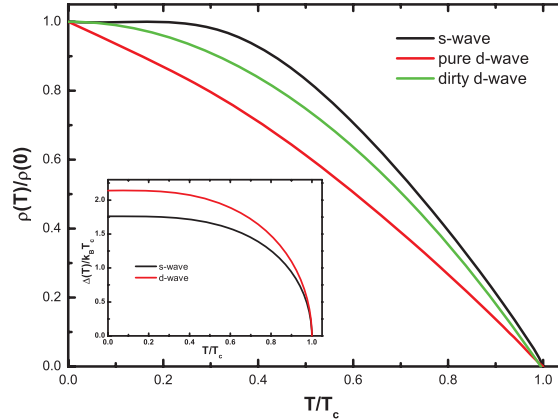


Figure 1.8: Temperature dependence of the superfluid density for  $s$ -wave, pure  $d$ -wave and dirty wave. Inset: Temperature dependence of the superconducting gap for  $s$ -wave and  $d$ -wave.

As the inset of figure 1.8 illustrates, the gap function is almost constant at temperature below  $0.25T_c$  even if nodes are present. Therefore, it is only in this limit where the temperature dependence of the superfluid density or penetration depth allows one to draw general conclusions about the pairing state. At higher temperatures, the temperature dependence of the gap itself cannot be ignored and strong coupling corrections can change this dependence substantially[15]. In the low temperature limit, for  $g = 1$  ( $s$ -wave) we obtain the standard BCS result,

$$\tilde{\rho}(T) \simeq 1 - \sqrt{\frac{2\pi\Delta_0}{T}} \exp \left( -\frac{\Delta_0}{T} \right) \quad (1.21)$$

and for the pure  $d$ -wave gap with  $\Delta = \Delta_0(0) \cos(2\varphi)$ , at low temperatures the superfluid density varying as

$$\tilde{\rho}(T) \simeq 1 - \frac{2 \ln 2}{\Delta_0(0)} T \quad (1.22)$$

However, in real materials, the low temperature dependence of  $\rho$  will be suppressed by impurity scattering and the linear term will be replaced by a  $T^2$  term in the limit  $T \ll \Gamma_0$

$$\tilde{\rho}(T) \simeq \tilde{\rho}(0) \left( 1 - \frac{k_B^2 T^2}{6\pi\Gamma_0\Delta_0(0)} \right) \quad (1.23)$$

where  $\Gamma_0$  is the scattering rate[18]. The temperature dependence of the superfluid density for all the three cases is shown in figure 1.8.

### 1.1.5 Josephson effect

The Josephson effect is the phenomenon of electric current passing between two weakly coupled superconductors, separated by a very thin insulating barrier. This arrangement (two superconductors linked by a non-conducting barrier) is known as a **Josephson junction**; the current that crosses the barrier is the **Josephson current**. The terms are named after British physicist Brian David Josephson, who predicted the existence of the effect in 1962[19].

If  $\varphi = \varphi_1 - \varphi_2$  denotes the phase difference of the GL order parameter (i.e., of the Cooper pairs) of the two superconductors across the junction, then

$$I = I_c \sin \varphi \quad (1.24)$$

$$\frac{d}{dt} \varphi = \frac{2eV}{\hbar} \quad (1.25)$$

Thus, even when no voltage  $V$  is applied across the junction, the electric current can pass the barrier, and its magnitude depends on the phase difference between the two superconductors. This is called the **DC Josephson effect**. If there is a finite DC voltage  $V$  applied across the junction, the current will oscillate at a frequency  $2eV/\hbar$ :

$$I(t) = I_c \sin(2eVt/\hbar) \quad (1.26)$$

This is called the **AC Josephson effect**.

## 1.2 Iron-based superconductors

After the discovery of superconductivity in mercury at 4 K by Kamerlingh Onnes in 1911, the search for new superconducting materials led to a slow increase of the highest known transition temperature  $T_c$  over the decades, reaching a plateau at 23 K with the discovery of the superconductivity of  $\text{Nb}_3\text{Ge}$  by Gavalier[20], and the field was considered by many to be at a dead end.

Until 1986, physicists had believed that BCS theory forbade superconductivity at temperatures above about 30 K. In that year, IBM researchers Karl Müller and Johannes Bednorz searched for superconductivity in a new class of oxide materials and discovered superconductivity in  $\text{LaBaCuO}$  which had a transition temperature of 35 K[21]. For the discovery of this new type of superconductivity they were awarded the Nobel Prize in Physics in 1987. The following year, the liquid nitrogen temperature barrier (77 K) was broken with the discovery of  $\text{YBa}_2\text{Cu}_3\text{O}_{7-x}$ [22], being superconducting at 93 K. Soon a whole host of related materials were found, and the  $T_c$  was risen to 138 K at ambient pressure[23] and 164 K under high pressure[24], as shown in figure 1.9. Since a copper-oxide ( $\text{CuO}_2$ ) plane is the common element in all these new high temperature superconductors these materials are referred to as the "cuprates".

The discovery of superconductivity in the cuprates was surprising and exciting, not simply because of the large increase in  $T_c$ , but also because no previous oxide superconductors had ever been found. Furthermore, in their stoichiometric form (with no additional oxygen or other dopant atoms added), these materials are antiferromagnetic Mott insulators. It is commonly accepted that magnetism cannot coexist with superconductivity. For example, Abrikosov and Gor'kov showed that magnetic impurities disrupt superconductivity and depress  $T_c$ [26].

The obvious differences between these new high-temperature superconductors and the conventional superconductors created a great deal of excitement. Rapidly, all the old experiments which had led to the unifying theory of conventional superconductors were repeated, but the results were often confusing and/or contradictory. Until now, there is still no real consensus as to the mechanism causing the high  $T_c$  in these materials.

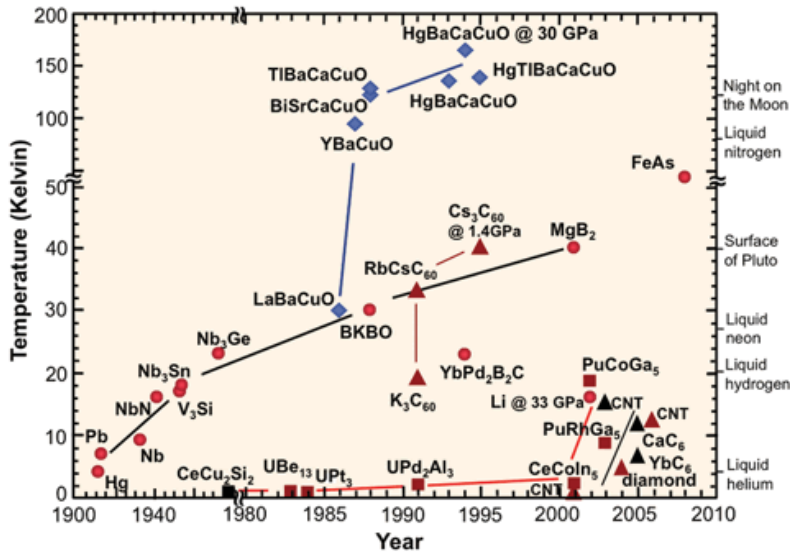


Figure 1.9: Evolution of critical temperatures of superconducting materials with time. Image is taken from [25].

Until 2008, the term "high-temperature superconductor" was used interchangeably with cuprate superconductor. This situation was changed when iron-based superconductors (FeSC) were discovered by Hideo Hosono. This new type of superconductors is based instead on conducting layers of iron and a pnictide, such as arsenic, phosphorus, or chalcogens. This is currently the family with the second highest critical temperature, behind the cuprates. Interest in their superconducting properties began in 2006 with the discovery of superconductivity in LaFePO at 4 K [27] and gained much greater attention in 2008 after the analogous material LaFeAs(O,F) [28] was found to superconduct at up to 43 K under pressure [29] or replace La with Sm [30]. Now the highest record of  $T_c$  in this family is about 55 K found in SmFeAsO<sub>0.9</sub>F<sub>0.1</sub> [31] and Ca<sub>0.4</sub>Nd<sub>0.6</sub>FeAsF [32].

### 1.2.1 Structural properties

To date, superconductivity has been found in compounds like LnFeAsO (Ln=La,Ce,Nd,Pr,Sm...) and AFeAsF (A = Ba, Sr...), AFe<sub>2</sub>As<sub>2</sub> (A=Ba,Sr...), and KFe<sub>2</sub>Se<sub>2</sub>, AFeAs (A=Li,...), FeSe(Te) and Sr<sub>4</sub>V<sub>2</sub>O<sub>6</sub>Fe<sub>2</sub>As<sub>2</sub>, which are often referred to as '1111', '122', '111', '11' and '42622'. These structures are shown in figure 1.10. All structures of iron-based superconductors share a common layered structure based upon a planar layer of iron atoms joined by tetrahedrally coordinated pnictogen (P, As) or chalcogen (S, Se, Te) anions arranged in a stacked sequence separated by alkali, alkaline earth or rare earth and oxygen/fluorine "blocking layers." Now it is widely thought that the interaction that leads to the high-temperature superconductivity originates within these common iron layers, similar in nature to the common copper-oxide building block found in the cuprate high-temperature superconductors [33].

Except 122 belongs to the tetragonal I4/mmm space group, the other four belong to the tetragonal P4/nmm space group. 1111, 122 and 111 compounds are formed by the layers of (FeAs)<sup>-</sup> with covalent bonding, interlaced by the layers of (LnO)<sup>+</sup> or A<sup>2+</sup><sub>0.5</sub> or A<sup>+</sup>, while interlayer bonding is ionic. Ions of Fe<sup>2+</sup> are surrounded by four ions of As, which form tetrahedra. 11 is especially simple. It only consists of layers of FeSe<sub>4</sub> edge-sharing tetrahedra. While 42622 is more complicated, it composes both antiferroite pnictide layers and perovskite oxide layers.

As temperature lowers, most of the undoped iron-based compounds show a tetragonal-orthorhombic structural phase transition accompanied simultaneously or followed by an antiferromagnetic (AFM) transition (probably of SDW type), similar to the cuprate superconductors [34]. However, they are

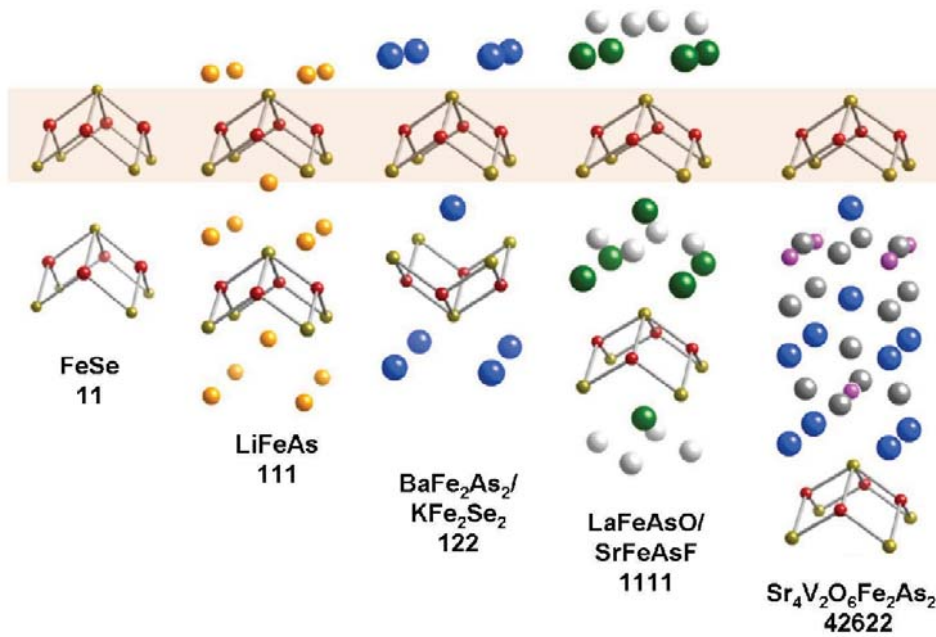


Figure 1.10: Five crystal structures of the iron-based superconductors. All these structures share a common layered structure based upon a planar layer of iron atoms (red) joined by tetrahedrally coordinated pnictogen (P, As) or chalcogen (S, Se, Te) anions (gold) [33].

poor metals rather than Mott insulators and have five bands at the Fermi surface rather than one. As in the cuprates, chemical substitution also plays a key role in inducing the superconducting phase in iron-based superconductors.

The generic phase diagram of the FeSC systems can be produced by manipulating the structural or chemical properties, using either applied external pressure or chemical doping/substitution to drive an antiferromagnetic, non-superconducting parent compound to a superconducting, non-AFM state. A compilation of experimental phase diagrams is presented in figure 1.11 for both F-doped 1111 and Co doping Ba-122 materials. In F-doped 1111 systems such as  $\text{LaFeAsO}_{1-x}\text{F}_x$  [35], where AFM and SC phases are completely separated as a function of doping and do not overlap. However, the coexistence of AFM and SC phases such as reported for  $\text{SmFeAsO}_{1-x}\text{F}_x$  [36] is believed to be a common trait of the generic FeSC phase diagram. The phase diagrams of  $\text{Ba}(\text{Fe}_{1-x}\text{Co}_x)_2\text{As}_2$  [37] is composed of an AFM state that is suppressed with substitution and a SC phase that is more or less centered near the critical concentration where AFM order is destroyed.

Actually, in  $\text{BaFe}_2\text{As}_2$ , the systematic substitution of either the alkaline earth (Ba), transition metal (Fe) or pnictogen (As) atom with a different element almost universally produces a similar phase diagram as  $\text{Ba}(\text{Fe}_{1-x}\text{Co}_x)_2\text{As}_2$ . The quantitative similarity between phase diagrams produced by substitutions involving both obvious (i.e.,  $\text{K}^{1+}$  for  $\text{Ba}^{2+}$ ) [38] and subtle (i.e.,  $\text{Co-}3d^7$  for  $\text{Fe-}3d^6$ ) [37] charge doping, as well as nominally isovalent ( $\text{P-}3p^3$  for  $\text{As-}4p^3$ ) [39] substitutions, is attractive due to the implied versatility of chemical tuning parameters available to experimentalists for studying these systems. Furthermore, it promotes the idea that simple charge doping is not the sole factor in determining the phase boundaries of these systems, as understood to be the case in the cuprates, and that structural tuning may play a role. Now strong evidence has already emerged in 1111 that the  $T_c$  value varies with the As-Fe-As bond angles and shows that the optimal  $T_c$  value is obtained with undistorted  $\text{FeAs}_4$  tetrahedra [40].

Much work has gone into clarifying the magnetic and electronic structures of these materials, since an interplay of magnetic and electronic interactions likely playing an important role in determining the shape of the phase diagram of all FeSC systems. In general, these materials can be well described as consisting of two-dimensional (2D) metallic sheets derived from Fe  $d$ -states hybridized with As

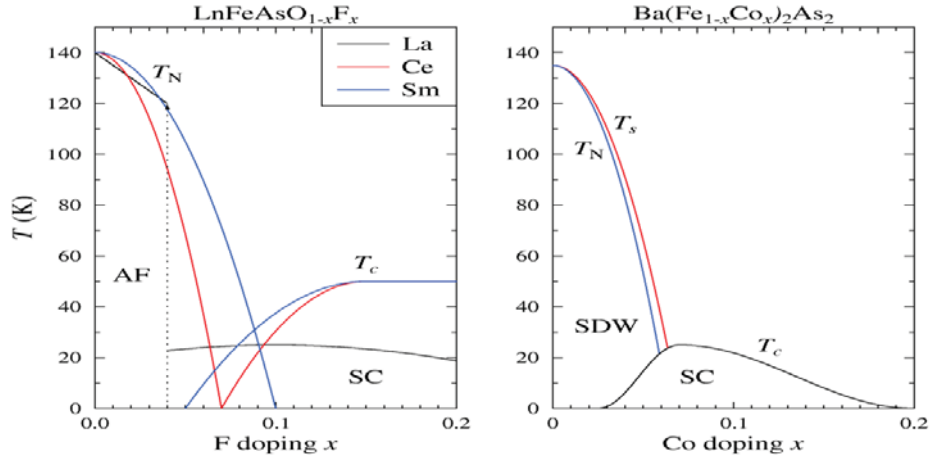


Figure 1.11: Simplified doping dependent phase diagrams of iron-based superconductors for both Ln-1111 and Co doping Ba-122 materials. The phases shown are the antiferromagnetic/spin density wave (AF/SDW) phase close to zero doping and the superconducting phase around optimal doping. The Ln-1111 phase diagrams for La[35] and Sm[36] were determined using muon spin spectroscopy, the phase diagram for Ce[34] was determined using neutron diffraction. The Co doping Ba-122 phase diagram is based on [37]. Image is taken from [25].

$p$ -orbital derived bands, sitting in a quasi-ionic framework composed of rare earth, oxygen, alkali or alkaline earth "blocking layers", as shown in figure 1.10. This arrangement leads to a metallic material with nominal Fe valence of  $2+$ , low carrier concentration and high electronic density of states dominated by Fe  $d$ -states[41]. Based on this FeAs-layered framework, the electronic band structure calculated using the local density approximation[42], shows that the electronic properties are dominated by five Fe  $d$ -states at the Fermi energy, with a Fermi surface consisting of at least four quasi-2D electron and hole cylinders. These consist of two electron pockets centered at  $(0, \pi)$  and  $(\pi, 0)$  and two hole pockets centered at the Brillouin zone center. As there are two nonequivalent As positions which are staggered above and below the Fe lattice, it results in folding of the Brillouin zone to include two Fe atoms per unit cell and to put the electron pockets at  $(\pi, \pi)$ . A fifth hole band is also proposed to sit at  $(0, \pi)$  in the folded Brillouin zone, but its presence may be very sensitive to structural details [43].

All of the FeSC systems share a similar pattern of long range magnetic order. As shown in the square lattice displayed in figure 1.12, the iron sublattice undergoes magnetic ordering with an arrangement consisting of ferromagnetically arranged spins along one chain of nearest neighbors and antiferromagnetically arranged along the other direction within the iron lattice plane. In figure 1.12, this is displayed on a tetragonal lattice, but actually it only occurs after these systems undergo an orthorhombic deformation as explained before. In the orthorhombic state, the distance between iron atoms with ferromagnetically aligned nearest neighbor spins which is highlighted in figure 1.12, shortens by approximately 1% as compared to the perpendicular direction[33].

## 1.2.2 Symmetry and mechanisms of pairing

As for the high-temperature cuprates, the fundamental mechanism which causes the high temperature superconductivity in the FeSCs is a primordially important question. To date, the experimental evidence favors an unconventional pairing mechanism closely tied to magnetism in both cases. Although at present the exact nature of the pairing is not known in either system, experimentalists have performed many experiments aimed to determine the pairing symmetry. For the cuprates, the experimental evidence favors a singlet  $d$ -wave symmetry which involves a change in

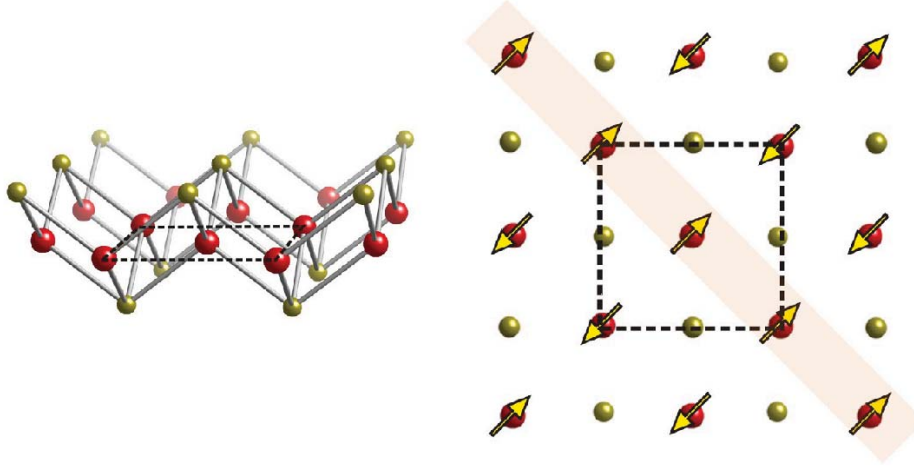


Figure 1.12: Depiction of the active planar iron layer common to all superconducting compounds in figure 1.10, with iron ions in red and pnictogen/chalcogen anions in gold. The dashed line indicates the size of the unit cell of the FeAs-type slab that includes two iron atoms due to two nonequivalent As positions[33].

sign of the superconducting order parameter (OP) phase at nodal points situated at the Fermi energy ( $E_F$ )[44, 45, 46] and directed along  $(\pi, \pi)$  in the simple 2D band structure of cuprates. For the FeSCs, the initial measurements probing the OP symmetry gave a fully gapped OP consistent with a fully symmetric  $s$ -wave symmetry[47, 48]. However, before experiments, the OP symmetry of FeSCs was in fact predicted theoretically by calculation to have  $s$ -wave symmetry, but with a sign change that occurs between different bands in the complex multi-band electronic structure, which is the so-called " $s_{\pm}$ " symmetry[49].

Probing the symmetry of the SC phase can provide important information about the energy and momentum dependence of Cooper pairing, and therefore these kind of experiments are pivotal to helping elucidate the pairing mechanism in this new class of high- $T_c$  superconductors. To date, many experiments have been performed on different systems or different chemical compositions of the same crystalline system. Unfortunately, due to the vastness of the iron-pnictide family and the nature of chemical substitution, it is difficult to compare all these results. However, some general conclusions still can be drawn from several experiments which show good consistency.

For instance, a lot of NMR experiments show that the SC state spin symmetry is likely singlet [50, 51, 52] in several different structures, which imply an even OP symmetry (i.e.  $s$ -wave,  $d$ -wave, etc). In polycrystalline 1111 no half-integer flux was found by a scanning SQUID experiment[53]. However, half-integer flux quantum jumps were observed in a loop formed by Nb and polycrystalline  $\text{NdFeAsO}_{0.88}\text{F}_{0.12}$ [54]. These jumps were interpreted as arising from  $\pi$  phase shifts at a few polycrystal boundaries as current is passed through the sample, which could only occur if the symmetry is a sign-changing  $s_{\pm}$ . A robust  $c$ -axis Josephson effect was found between Pb and K-doped  $\text{Ba}_{1-x}\text{K}_x\text{Fe}_2\text{As}_2$ [55], which rules out a predominant  $d$ -wave symmetry in these materials at the measured K concentrations. In  $\text{Fe}(\text{Se}, \text{Te})$ , Hanaguri et al. found that the sign of the gap is reversed between the electron and hole pockets[56]. This, along with an absence of low-energy quasiparticle excitations in the tunneling gap (as would be seen from the nodes in a  $d$ -wave SC), strongly suggests an  $s_{\pm}$  symmetry. Together, all of these results favor the  $s_{\pm}$  symmetry in the FeSCs, but definitive phase experiments on more materials are needed to conclusively settle the case.

Figure 1.13 presents three possible scenarios for the superconducting order parameter symmetry in the iron-based superconductors. Since the simplest  $s$ -wave gap symmetry with constant phase has been widely ruled out by experimental evidence, more complicated scenarios are required to explain all observed properties. In particular, a lot of evidences support a picture where the sign

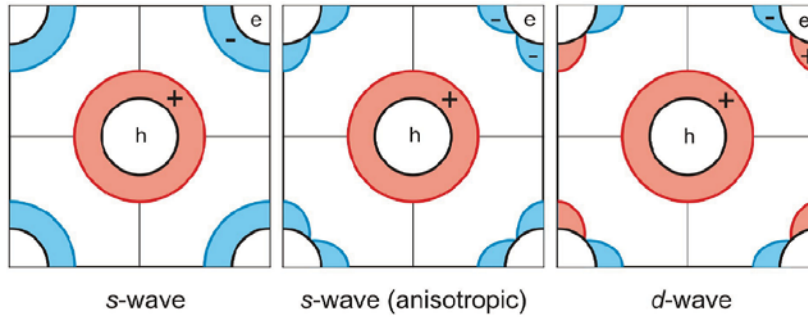


Figure 1.13: Schematic picture of the two-dimensional ( $k_x - k_y$ ) projection of the Brillouin zone of superconducting FeAs-based materials. The multiple bands are reduced to single hole (h) and electron (e) pockets. The shaded regions on hole (red) and electron (blue) pockets are the proposed multi-band pairing gap symmetries, shown for  $s\pm$  symmetry with isotropic gaps (left) and anisotropic gaps with accidental nodes on the electron pocket (middle), and for a  $d$ -wave symmetry (right)[33].

of the energy gap must change somewhere in the Brillouin zone. Since there are multiple Fermi surfaces in the iron-based superconductors, this can be realized by positioning a node either away from the Fermi energy (so-called  $s\pm$ ) or directly at the Fermi energy (i.e.,  $d$ -wave). Moreover, even in the  $s$ -wave case, a modulation of the gap amplitude can occur: some so-called "accidental" nodes may be present on some Fermi surfaces, allowing plentiful low-energy excitations even at temperatures much below the energy of the gap, and this can explain the node observed in LaFePO,  $\text{BaFe}_2(\text{As}_{1-x}\text{P}_x)$  and  $\text{KFe}_2\text{As}_2$ .

From a general standpoint, the interplay of superconductivity and magnetism strongly suggests that magnetic fluctuations are involved either indirectly or directly in the Cooper pairing in the FeSCs. With the close relation between superconductivity and spin fluctuations from the suppression of SDW order, it is fair to say that quantum criticality may play an important role. Therefore, due to difficulties in probing the underlying ground state near the quantum critical point, studies of the coexistence region of SC and AFM are among the most important ongoing efforts[33].

Because almost immediately the crystals of millimeter sizes were obtained since its discovery, the Ba-based 122 system is the most widely studied of the five families of iron-based superconductor to date, and widely thought to capture the main traits of all FeSCs. The most of work of this thesis is also done on this system. This thesis will be organized as following: In Chapter 2, details about the growth, characterization and the anisotropy of the upper critical field measurement of  $\text{Ba}_{1-x}\text{K}_x\text{Fe}_2\text{As}_2$  single crystals will be given. In Chapter 3, the  $H_{c1}$  measurement on  $\text{SmFeAsO}_{0.9}\text{F}_{0.1}$  polycrystal and  $\text{Ba}_{0.6}\text{K}_{0.4}\text{Fe}_2\text{As}_2$  single crystal by hall probe will be presented. Chapter 4 is about some point contact measurements on  $\text{Ba}_{0.6}\text{K}_{0.4}\text{Fe}_2\text{As}_2$  and  $\text{BaFe}_{2-x}\text{Ni}_x\text{As}_2$  single crystals. In Chapter 5, I will introduce something about scanning nano-squid microscopy, and present the work on Rhenium film with it. Chapter 6 is about the scanning nano-squid microscopy measurements on  $\text{BaFe}_{2-x}\text{Ni}_x\text{As}_2$  single crystals. Chapter 7 is a summary of the work in this thesis and some of the conclusions drawn from it.

# 2

## Growth, characterization and $H_{c2}$ anisotropy of $\text{Ba}_{1-x}\text{K}_x\text{Fe}_2\text{As}_2$ single crystals

Since the discovery of high temperature superconductivity in the iron-based superconductor, great interest has been stimulated in the community of condensed-matter physics and material sciences. Because high quality single crystals are essential for advanced scientific research, the material scientists tried to grow single crystals of iron-based superconductors. However, it is found that to grow sizable single crystals of the Fe-1111 system [ $\text{LnFeAsO}$  ( $\text{Ln}=\text{La}, \text{Ce}, \text{Nd}, \text{Pr}, \text{Sm} \dots$ ) and  $\text{AFeAsF}$  ( $\text{A} = \text{Ba}, \text{Sr} \dots$ )] is quite hard. Fortunately, big single crystals of Fe-122 system [ $\text{AFe}_2\text{As}_2$  ( $\text{A}=\text{Ba}, \text{Sr} \dots$ ) and  $\text{KFe}_2\text{Se}_2$ ] can be grown using an additional metal as flux or by the self flux method. With this success, more accurate measurements have become possible on this iron-based superconducting system. The upper critical field and its anisotropy are fundamental parameters of each superconductor, and they are crucial for both understanding the superconducting mechanism and the potential applications. In this chapter, details about the growth, characterization and the anisotropy of the superconducting properties revealed by the upper critical field measurements of  $\text{Ba}_{1-x}\text{K}_x\text{Fe}_2\text{As}_2$  single crystals are presented.

### 2.1 Growth of $\text{Ba}_{1-x}\text{K}_x\text{Fe}_2\text{As}_2$ single crystals

---

The high temperature solution growth method is widely used and recognized as a powerful technique for obtaining single crystals of complex materials. It is a viable technique for both congruently and incongruently melting materials and can be used to control high vapor pressures of constituent elements. The solvent used in high-temperature solution growth is also called "flux". Flux can be classified into two types: one is self flux, the excess of one or more constituent elements of the desired compound is used as the solvent; the other one is non-self-flux which introduces elements other than the ones in the desired compound to act as a solvent. It is often preferable to use a self flux since it does not introduce any other elements into the melt, and thus no other element can enter into the desired single crystal, and the number of possible undesired phases can also be reduced[57].

The 122 compound has a tetragonal  $\text{ThCr}_2\text{Si}_2$ -type structure with infinite FeAs layers[58]. By replacing the alkaline earth elements (Ba, Sr and Ca) with alkali elements (Na, K, and Cs), superconductivity was induced[59, 60, 61, 62].  $T_c$  varies from 2.7 K in  $\text{CsFe}_2\text{As}_2$  to 38 K in  $\text{A}_{1-x}\text{K}_x\text{Fe}_2\text{As}_2$  ( $\text{A} = \text{Ba}, \text{Sr}$ )[59, 63]. Meanwhile, superconductivity could also be induced in the parent phase

by high pressure [64, 65] or by replacing some of the Fe by Co Ni, and Pt[66, 67, 68, 69], or by replacing some of the As by P[39, 70, 71]. More excitingly, large single crystals could be obtained by the Sn flux method in this family[72, 73, 74]. However, single crystals with high homogeneity and low contamination are still hard to obtain by this method [75]. To avoid these problems, the FeAs self-flux method may be more appropriate.

The FeAs precursor was synthesized by the reaction of Fe powder (Alfa Aesar, 99.99% in purity) and As chips (99.999%) at 500°C for 10 h and then 700°C for 20 h in a sealed silica tube. The starting materials of FeAs, and high purity Ba(Alfa Aesar, 99.2% in purity) were mixed in the ratio 4:(1-x), then a soft bulk of the proper amount of K was added to cover the powder. The whole procedure was performed in a glove box with a protective argon atmosphere in which the concentrations of both O<sub>2</sub> and H<sub>2</sub>O were less than 1 ppm. The mixture was placed in an aluminum oxide crucible and sealed under vacuum in a silica tube.

Because the silica tube would break due to the gas pressure of potassium at a temperature around 1000°C, the superconducting samples could only be obtained by using a limited amount of potassium and a thick enough silica tube. For example, if the total mass of starting material was supposed to be 2.0 g with the ratio of Ba:K:Fe:As = 0.6:0.4:4.0:4.0, the mass for each materials was  $m(Ba) = 0.265$  g,  $m(K) = 0.050$  g and  $m(FeAs) = 1.684$  g, respectively. Considering the loss of K during the growth (about 0.12 g in most cases), the total amount of K should be 0.170 g. It should be noted that the safe amount of K is less than 0.25 g under our conditions to prevent explosion of the silica tube. The actual contents of K in the as-grown crystals were determined by quantitative analysis in later measurements. Since the amount of K is limited, it is very difficult to grow the overdoped sample. A better way is to seal the crucible in a metal tube such as Tantalum or stainless steel, then seal the metal tube in a silica tube.

The sealed silica tube was placed in a muffle furnace and heated up to 750°C, and kept at the temperature for 10 hours. After the reaction completed, the furnace was heated up to 1000-1150°C to melt the FeAs flux completely. Then it was cooled down to a temperature below 800°C at a very slow speed (less than 10°C/hour). The melting temperature and cooling down speed depended on the ratio of Ba:K in the starting material. Finally, the muffle furnace was switched off. After it cooled down to room temperature, the tube was fetched and broken. The crystals were obtained by cleaving the as-grown bulk. Then they were selected and shaped under a microscope. By varying the content of potassium in the starting material, we obtained non-superconducting and superconducting crystals with the composition  $Ba_{1-x}K_xFe_2As_2$ . Figure 2.1 shows the schematics of the growth and a photograph of some crystals cleaved from the as-grown bulk. They all have very shiny plate-like cleaved surfaces. The sizes of the largest one are about 2.5 mm × 4.0 mm × 0.2 mm, and the others have sizes up to 2 mm.

## 2.2 Characterization of $Ba_{1-x}K_xFe_2As_2$ single crystals

---

In the flux method, the final concentration of each element in the crystal always deviates from those in the starting material. The composition of our single crystals was determined by an energy dispersive x-ray (EDX) analysis. From each batch, 3-5 pieces of as-grown single crystals were selected carefully. Then they were cleaved under a microscope and the EDX measurements were taken immediately, before the surface deteriorated in air. A typical EDX spectrum is shown in figure 2.2. The inset is the scanning electron microscopy(SEM) photograph of this crystal, which shows a very flat surface morphology and a layered structure. We successfully obtained five concentrations of superconducting samples with K doping level  $x = 0.40, 0.28, 0.25, 0.23$  and  $0.17$ . The  $T_c$ s are 36.3 K, 31.8 K, 27.5 K, 23.4 K and 12.6 K, respectively. The non-superconducting crystals also contain a bit of K, which is less than 10%.

The crystal structures of the samples were examined by x-ray diffraction measurements with the

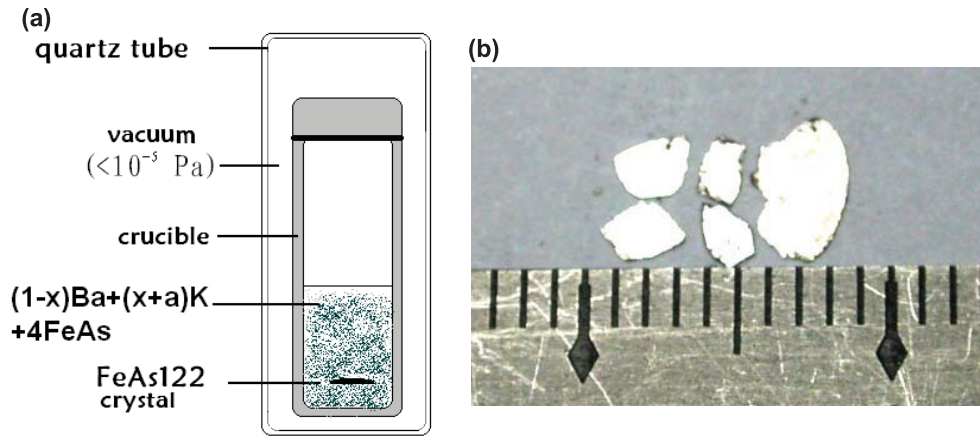


Figure 2.1: (a) The schematics of self-flux method to grow  $\text{Ba}_{1-x}\text{K}_x\text{Fe}_2\text{As}_2$  single crystals. (b) Photograph of some crystals cleaved from the as-grown bulk. The crystals have rather shiny surfaces with sizes up to 4 mm.

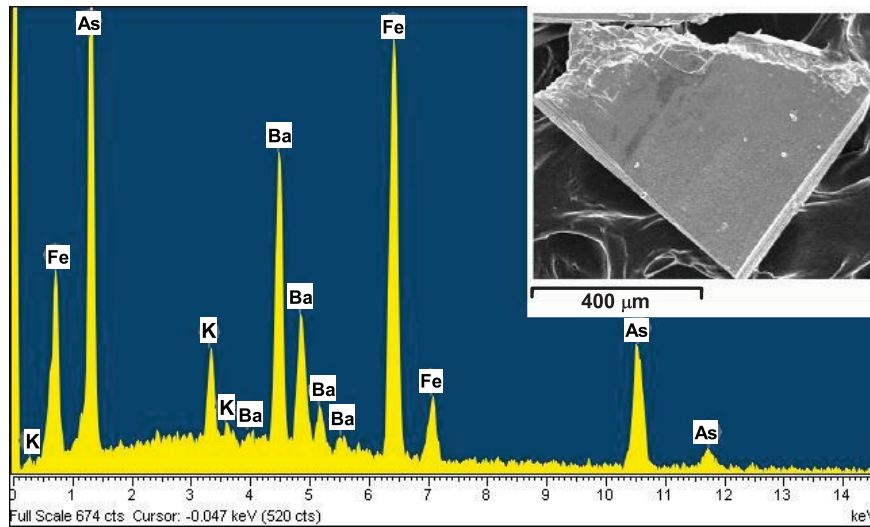


Figure 2.2: A typical EDX spectrum for one  $\text{Ba}_{1-x}\text{K}_x\text{Fe}_2\text{As}_2$  single crystal. The inset is the SEM photograph of this crystal, which shows a very flat surface morphology and a layered structure.

incident x-ray oriented along the  $c$ -axis.  $K\alpha$  radiation from a Cu target was used. Typical diffraction patterns are shown in figure 2.3. Only sharp peaks along  $(00l)$  could be observed, and the full width at half maximum (FWHM) of each peak is around  $0.10^\circ$ , indicating high  $c$ -axis orientation and high crystalline quality of our samples. The raw XRD data were analyzed by PowderX software, with the zero shift,  $K\alpha_2$  elimination and other factors taken into account[76]. The  $c$ -axis parameters were calculated. They are very close to results known from the polycrystalline compound. In figure 2.3, a systematic shift for each peak appears, which indicates that the lattice undergoes a small variation after doping K into the parent phase.

AC susceptibility measurements were used to characterize the superconducting  $\text{Ba}_{1-x}\text{K}_x\text{Fe}_2\text{As}_2$  single crystals. They were performed on an Oxford cryogenic system (Maglab-EXA-12). An alternating magnetic field ( $H = 1$  Oe) was applied perpendicular to the  $ab$ -plane at a frequency  $f = 333$  Hz when the AC susceptibility measurement was undertaken. Figure 2.4 shows three typical groups of the susceptibility curves. The  $T_c$  value was determined as the onset point of  $\chi'$ , and the transition width was defined as  $\Delta T_c = T(10\% \chi'_{2K}) - T(90\% \chi'_{2K})$ . In the low-temperature region the diamagnetic signal is flat and the superconducting transition around  $T_c$  is very sharp. The demagnetization

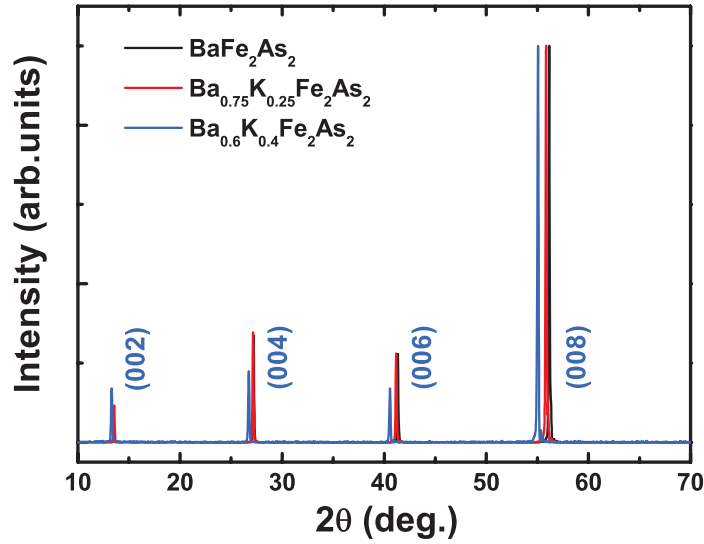


Figure 2.3: Typical XRD patterns for cleaved  $Ba_{1-x}K_xFe_2As_2$  crystals. The FWHM of each peak is around  $0.10^\circ$ . A clear shift of the diffraction peak position was observed after doping.

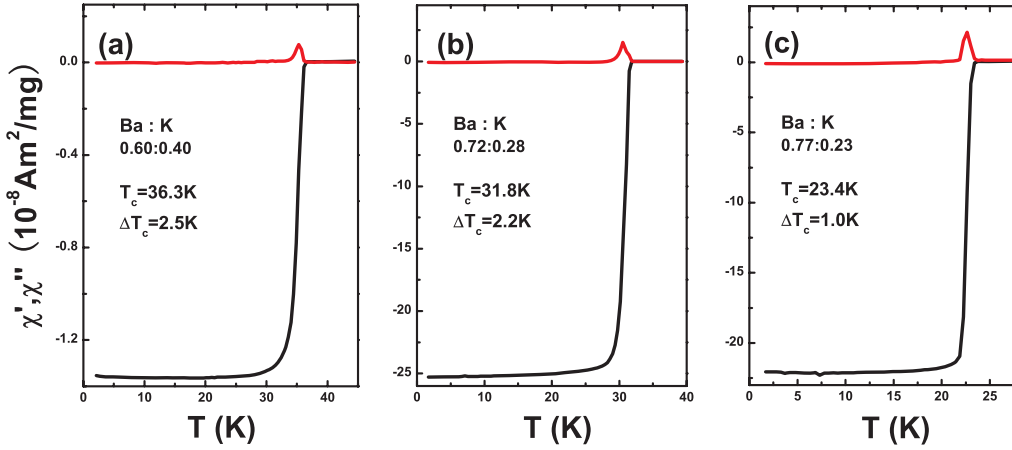


Figure 2.4: Temperature dependence of AC susceptibility for superconducting  $Ba_{1-x}K_xFe_2As_2$  single crystals. The  $T_c$  value was derived from the point where the real part of the susceptibility becomes flat, and the transition width was defined as  $\Delta T_c = T(10\% \chi'_{2K}) - T(90\% \chi'_{2K})$ .

factor is not taken into account in these measurements. The  $T_c$  value increases gradually as more and more K is doped into the samples. The superconducting transition is almost the same for single crystals cleaved from the same batch, which indicates that our samples are very homogeneous.

The resistivity measurements were carried out on a Quantum Design physical property measurement system (PPMS) using a standard four-probe method with a low contact resistance ( $<1\Omega$ ). Figure 2.5 shows the temperature dependence of the resistivity under zero field. The applied current is 5 mA, and it flows in the ab-plane during the measurements. For  $BaFe_2As_2$ , a strong anomaly shows up at  $T_s \simeq 138 K$  (figure 2.5(a)). The resistivity has a nearly  $T$ -linear dependence above this temperature, and sharply drops down below this temperature. This resistivity anomaly could be attributed to the SDW instability and the structural transition, which was also observed in other systems [61, 77, 78]. Increasing the hole doping further will suppress the SDW transition, and superconductivity eventually emerges[79]. Therefore, the superconducting  $Ba_{1-x}K_xFe_2As_2$  samples were obtained by adding more K into the starting material. For  $Ba_{0.83}K_{0.17}Fe_2As_2$ , both the SDW/structural transition and superconducting transition can be seen from the temperature dependent resistivity curve. After more

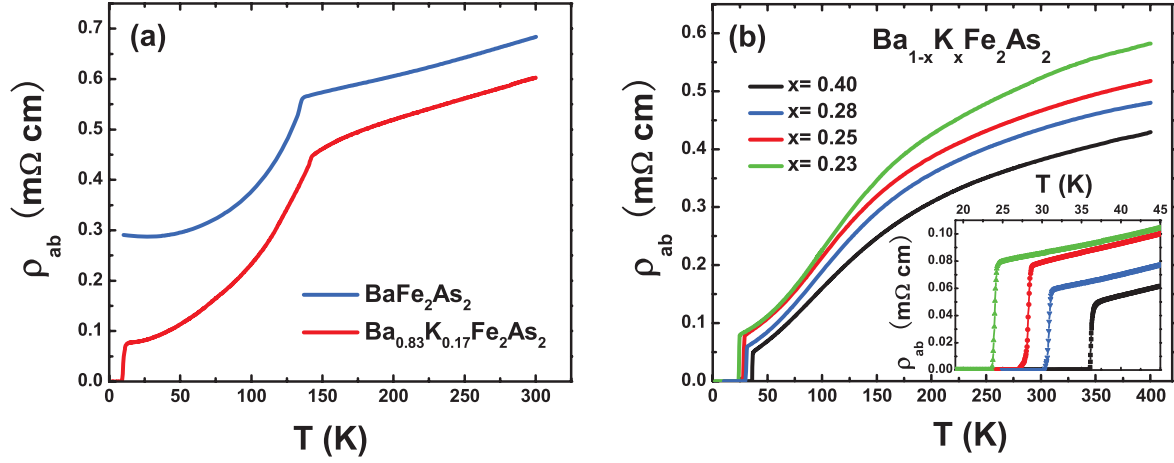


Figure 2.5: (a) Temperature dependence of the resistivity for  $\text{BaFe}_2\text{As}_2$  and  $\text{Ba}_{0.83}\text{K}_{0.17}\text{Fe}_2\text{As}_2$  crystals. The SDW anomaly appears clearly as a cusp in the resistivity data. (b) Temperature dependence of the resistivity for other four superconducting single crystals. The inset is an enlarged graph around the superconducting transition.

K doped in the sample, the SDW/structure transition becomes indiscernible. Figure 2.5(b) shows the temperature dependence of the resistivity for the other four concentrations of the superconducting single crystals. The SDW anomaly is smeared in the normal state, and a superconducting transition emerges at low temperature. The  $T_c$  (onset) values for different levels of doping are about 36.6, 31.4, 28.7, and 24.5 K. The resistivity data also indicate a sharp transition in our samples, with  $\Delta T_c = 0.44, 0.49, 0.71,$  and  $0.40$  K (90%-10% of normal state resistivity). Furthermore, if we extrapolate the data just above the superconducting transition by a straight line, it could be roughly estimated that the residual resistivity is almost close to zero for the sample with  $T_c = 36$  K. This indicates that our samples are rather clean.

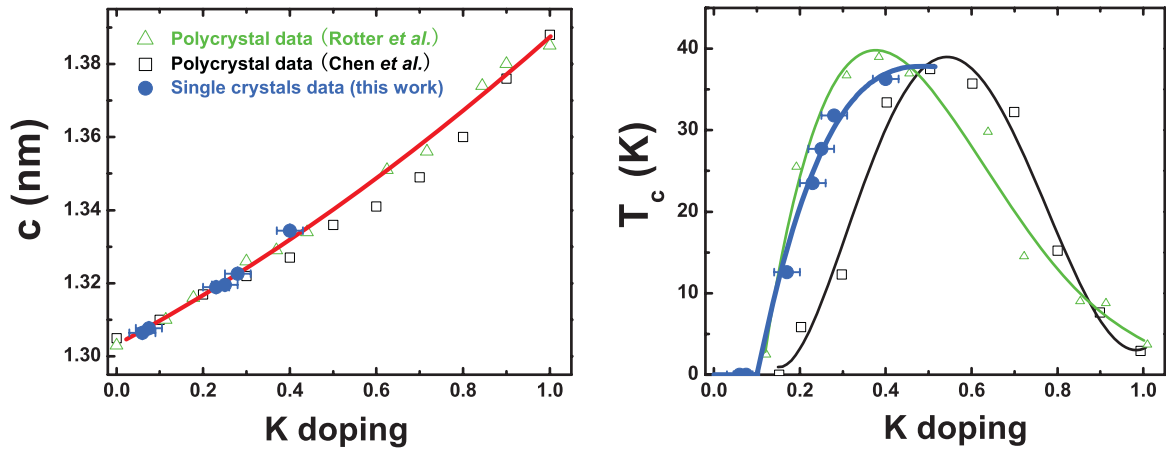


Figure 2.6: Doping dependence of the  $c$ -axis and  $T_c$  for our single crystals (blue points). The open black squares and green triangles are polycrystalline data from ref.[79] and ref.[38], respectively.

There are also some studies on  $\text{Ba}_{1-x}\text{K}_x\text{Fe}_2\text{As}_2$  polycrystalline samples with a series of doping levels which were reported when we were doing this work[79, 38]. Thus we made a comparison of the doping dependence of the  $c$ -axis length and  $T_c$  value between the polycrystalline samples and our single crystals. The result is shown in figure 2.6. Our data are consistent with the data in ref. [38],

while a small deviation is found for the data in ref.[79]. However, the general behavior is almost the same between the polycrystalline samples and single crystals: The  $c$ -axis length expands almost linearly on increasing the K content, while the  $T_c$  value increases quickly as a little amount of K is doped into the parent compound, then it grows slowly between  $x = 0.3$  and  $0.4$ .

### 2.3 $H_{c2}$ anisotropy of $\text{Ba}_{1-x}\text{K}_x\text{Fe}_2\text{As}_2$ single crystals

As one of the basic parameters, the superconducting anisotropy  $\Gamma = H_{c2}^{ab}/H_{c2}^c$  is crucial for both understanding the superconducting mechanism and the potential applications, where  $H_{c2}^{ab}$  and  $H_{c2}^c$  are the upper critical fields when the magnetic field is applied within the  $ab$ -plane or along the  $c$ -axis, respectively. With a layered structure in the FeAs-based superconductors, such as cuprates, strong anisotropy of superconductivity might be expected[41]. An estimation of  $\Gamma \geq 30$  was made based on the  $c$ -axis infrared plasma frequency[80] of  $(\text{Nd}, \text{Sm})\text{FeAsO}_{0.82}\text{F}_{0.18}$  polycrystals. However, an anisotropy of about 4-6 for the upper critical field was found in  $\text{NdFeAsO}_{0.82}\text{F}_{0.18}$  single crystals[81] based on transport measurements. Therefore, it is very necessary to determine the upper critical fields and the superconductivity anisotropy of the  $\text{Ba}_{1-x}\text{K}_x\text{Fe}_2\text{As}_2$  system, especially for different doping levels.

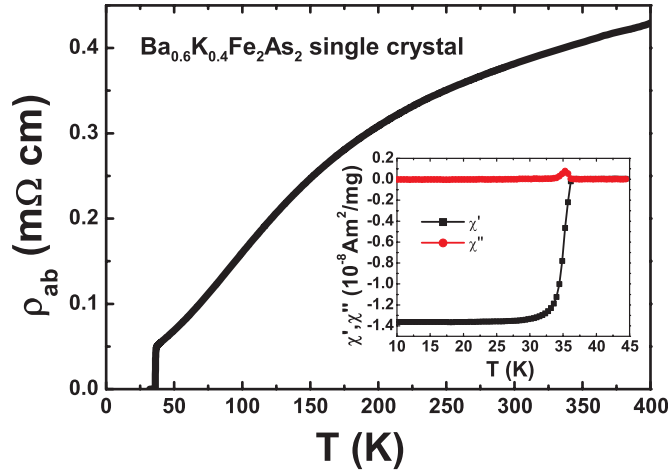


Figure 2.7: Temperature dependence of the in-plane electrical resistivity for a  $\text{Ba}_{0.6}\text{K}_{0.4}\text{Fe}_2\text{As}_2$  single crystal in zero field up to 400 K. One can see that the  $\rho_{ab}(T)$  curve exhibits a continuous curvature up to 400 K. The inset shows the temperature dependent AC susceptibility for the  $\text{Ba}_{0.6}\text{K}_{0.4}\text{Fe}_2\text{As}_2$  single crystal. Sharp superconducting transitions are obvious both in the resistive and the AC susceptibility data.

The resistivity measurements were carried out on a physical property measurement system (PPMS) (Quantum Design) with magnetic fields up to 9 T. The electrical resistivity of  $\text{Ba}_{1-x}\text{K}_x\text{Fe}_2\text{As}_2$  ( $x = 0.23, 0.25, 0.28,$  and  $0.4$ ) single crystals and the angle dependent resistivity of  $\text{Ba}_{0.6}\text{K}_{0.4}\text{Fe}_2\text{As}_2$  single crystal were measured by the standard four-probe method. Figure 2.7 presents the in-plane resistivity  $\rho_{ab}$  of the  $\text{Ba}_{0.6}\text{K}_{0.4}\text{Fe}_2\text{As}_2$  single crystal in zero field up to 400 K. One can see that the  $\rho(T)$  data exhibit a continuous curvature up to 400 K. In the angle-resolved resistivity measurement, by means of a rotator inset of the PPMS, the angle  $\theta$  was varied from  $0^\circ$  to  $180^\circ$ , where  $\theta = 0^\circ$  corresponded to the configuration of  $H \parallel c$ -axis and  $\theta = 90^\circ$  to  $H \parallel ab$ -plane, respectively. The current was applied in the  $ab$ -plane and perpendicular to the magnetic field in all cases (as shown in the inset of figure 2.8(b)). The sample with  $x = 0.4$  exhibited a sharp resistive superconducting transition at  $T_c \simeq 36.5$  K (90% of the normal state resistivity) with  $\Delta T_c < 0.5$  K. The residual resistivity is about  $\rho(38\text{K}) = 0.05\text{m}\Omega\text{cm}$  and residual resistivity ratio is found to be  $\text{RRR} = \rho(300\text{K})/\rho(38\text{K}) = 7.4$ .

Many experiments had revealed high upper critical fields in the  $\text{LnFeAsO}_{1-x}\text{F}_x$  (The estimated  $H_{c2}^{ab}$

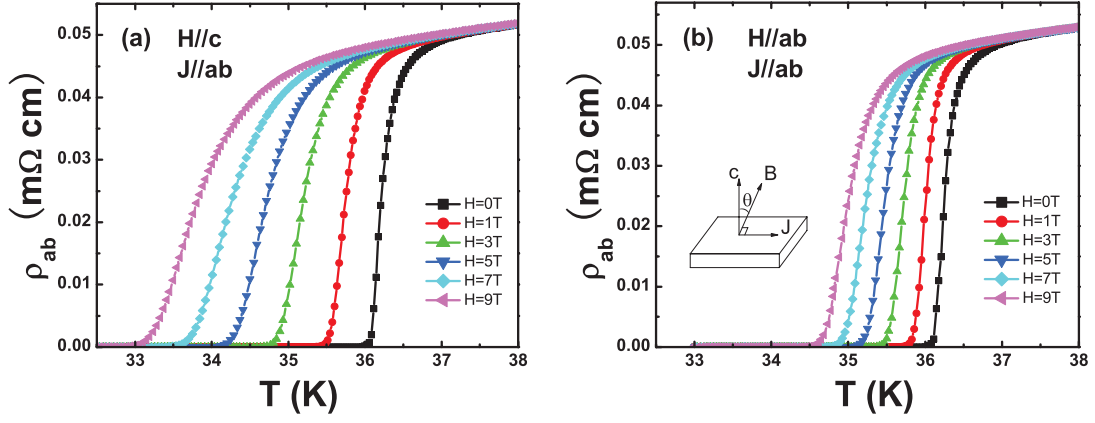


Figure 2.8: Temperature dependence of the in-plane electrical resistivity for the  $Ba_{0.6}K_{0.4}Fe_2As_2$  single crystal at fields  $\mu_0H = 0, 1, 3, 5, 7, 9$  T with (a)  $H \parallel c$  and (b)  $H \parallel ab$ , respectively. The inset of (b) illustrates the definition of angle  $\theta$ .

is beyond 50 T for  $Ln = La$ , and beyond 100 T for  $Ln = Sm, Pr, \text{ and } Nd$ ) system[81, 82, 83]. In the  $Ba_{1-x}K_xFe_2As_2$  system, the value of the upper critical field seems also very high[84, 85]. Figure 2.8 (a) and (b) show the temperature dependent resistivity  $\rho(T)$  curves of the  $Ba_{0.6}K_{0.4}Fe_2As_2$  single crystal at magnetic fields up to 9 T along the  $c$ -axis and  $ab$  planes, respectively. It is found that the superconducting transitions are broadened slightly, which indicates that the upper critical field should be very high. One can also see that the resistive transition curves shift parallel down to lower temperatures upon using a magnetic field, this may suggest a field induced pair breaking effect in the present system. This is again very different from the case in the cuprate superconductors where the  $\rho(T)$  broadens by exhibiting a fan structure with the onset transition part barely changed by the magnetic field due to the vortex phase transition. From the transition curves in figure 2.8(a) and (b), we have already an idea that the anisotropy ratio is quite small. In figure 2.9(a) we present the  $H_{c2}$ - $T$  curves for the  $Ba_{0.6}K_{0.4}Fe_2As_2$  single crystal for both  $H \parallel c$  and  $H \parallel ab$ , respectively. The  $H_{c2}(T)$  is determined at the point where  $\rho = 90\% \rho_n$ . The curves of  $H_{c2}(T)$  are very steep with average slopes  $-dH_{c2}^{ab}/dT_c|_{T_c} = 9.35$  T/K for  $H \parallel ab$  and  $-dH_{c2}^c/dT_c|_{T_c} = 5.49$  T/K for  $H \parallel c$ . According to the Werthamer-Helfand-Hohenberg (WHH) formula[86]  $H_{c2} = -0.69(dH_{c2}/dT)|_{T_c} T_c$  and taking  $T_c = 36.5$  K, the values of upper critical fields are  $H_{c2}^{ab}(0) = 235$  T and  $H_{c2}^c(0) = 138$  T. These high values of upper critical fields may subject to a modification when the direct measurements are done in the high field experiments, since a lot of experiments have shown a strong coupling effect in this material[47, 87], which is not considered in the WHH theory. However, we believe that the FeAs-based superconductors are really robust against the magnetic field. From this orbital limit, it is possible to deduce the superconducting coherence length  $\xi_{ab} \simeq 2$  nm.

For example, taking the zero temperature values we obtained using the WHH formula, we have  $\mu_0 H_{c2}^{ab}(0)/k_B T_c = 235/36.5$  T/K = 6.43 T/K. This ratio is much beyond the Pauli limit  $\mu_0 H_{c2}(0)/k_B T_c = 1.84$  T/K for a singlet pairing when the spin-orbital coupling is weak[88]. This may manifest an unconventional mechanism of superconductivity in this material. The values of  $H_{c2}(0)$  for other three samples with different doping levels of potassium and thus the anisotropy ratios were also determined in the same way. The results are shown in figure 2.9 (b). It is found that the  $H_{c2}(0)$  decreases quickly with the decrease of  $T_c$ . We note that a recent article reports that the WHH approximation may not be simply applicable in this family. For  $LaO_{0.9}F_{0.1}FeAs_{1-\delta}$ , WHH theory predicts a much higher value of  $B_{c2}$  than experiments under pulsed high magnetic field report[89]. Because of disorder effects, the Pauli spin paramagnetism limitation should be included in the WHH model by a Maki parameter  $\alpha$ . With this correction, the calculation reproduce the experiment results well. Even  $H_{c2}(0)$  may be also affected by the multiband property, however, our results clearly indicate that the upper critical fields in the present system are really very high without any doubt. The large value of

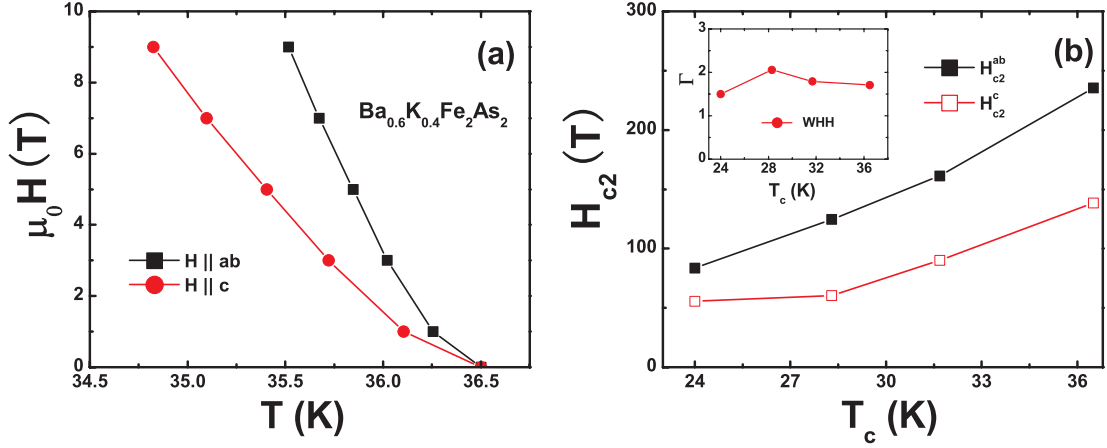


Figure 2.9: (a) The upper critical field of  $Ba_{0.6}K_{0.4}Fe_2As_2$  single crystal for  $H \parallel c$  and  $H \parallel ab$  respectively. (b) The upper critical field versus  $T_c$  of  $Ba_{1-x}K_xFe_2As_2$  crystals ( $x = 0.23, 0.25, 0.28,$  and  $0.4$ ) single crystals with  $T_c = 24, 28.3, 31.7, 36.5$  K. The inset of (b) presents the anisotropy ratio of  $H_{c2}(0)$  along  $c$ -axis and  $ab$ -planes for the four samples. The lines are guides to eyes.

the ratio  $\mu_0 H_{c2}^{ab}(0)/k_B T_c$  was also found in our previous measurements on  $NdFeAsO_{0.82}F_{0.18}$  single crystals[81].

In an anisotropic type-II superconductor, the magnetic field destroys superconductivity at the upper critical fields  $H_{c2}^{ab}$  and  $H_{c2}^c$  for applied fields  $H \parallel ab$  and  $H \parallel c$ , respectively. The effective upper critical field varies between the two orientations depending on the superconducting anisotropy ratio  $\Gamma = H_{c2}^{ab}/H_{c2}^c$ . In the inset of figure 2.9 (b), we show the doping dependence of the anisotropy ratio  $H_{c2}^{ab}(0)/H_{c2}^c(0)$  for the samples with different doping levels. One can see that the anisotropy for different samples all locate around 2. This result is surprising to us since the band structure calculations by Singh[90] clearly show that the Fermi surface sheets and dimensionality strongly depend on the doping level. For the  $Ba_{0.6}K_{0.4}Fe_2As_2$  single crystal it is found that  $\Gamma \approx 1.70 \sim 1.86$  at zero temperature, and  $\Gamma$  are below 2.1 for all other samples. This value is quite close to that derived on similar samples also from the shift of the resistive transitions under magnetic fields[72]. The values of anisotropy are rather small in comparison with all cuprate superconductors, and slightly lower than that of F-doped  $NdFeAsO$  with  $\Gamma = 4 - 6$ [81, 91].

The anisotropy ratio determined above may subject to a modification because of the uncertainties in determining the upper critical field value by taking different criterions of resistivity and in using different formulas. One major concern was that the zero temperature value  $H_{c2}(0)$  was determined by using the experimental data near  $T_c$ . This concern can be removed by the measurements of angular dependent resistivity. According to the anisotropic Ginzburg-Landau theory, the resistivity in the mixed state depends on the effective field  $H/H_{c2}^{GL}(\theta)$ . In this case the resistivity measured at different magnetic fields but at a fixed temperature should be scalable with the variable  $H/H_{c2}^{GL}(\theta)$ . The effective upper critical field  $H_{c2}^{GL}(\theta)$  at an angle  $\theta$  is given by

$$H_{c2}^{GL}(\theta) = H_{c2}^c / \sqrt{\cos^2(\theta) + \Gamma^{-2} \sin^2(\theta)}. \quad (2.1)$$

Thus using the scaling variable  $\tilde{H} = H \sqrt{\cos^2(\theta) + \Gamma^{-2} \sin^2(\theta)}$ , the resistivity should collapse onto one curve in different magnetic fields at a certain temperature[92] when an appropriate  $\Gamma$  value is chosen. Figure 2.10 presents four sets of data of angular dependence of resistivity at 34.5, 35, 35.5, and 36 K for the  $Ba_{0.6}K_{0.4}Fe_2As_2$  single crystal. At each temperature, a cup-shaped feature centered around  $\theta = 90^\circ$  is observed. As shown in figure 2.11, the curves measured at different magnetic fields but at a fixed temperature are scaled nicely by adjusting  $\Gamma$ . The values of  $\Gamma$  were

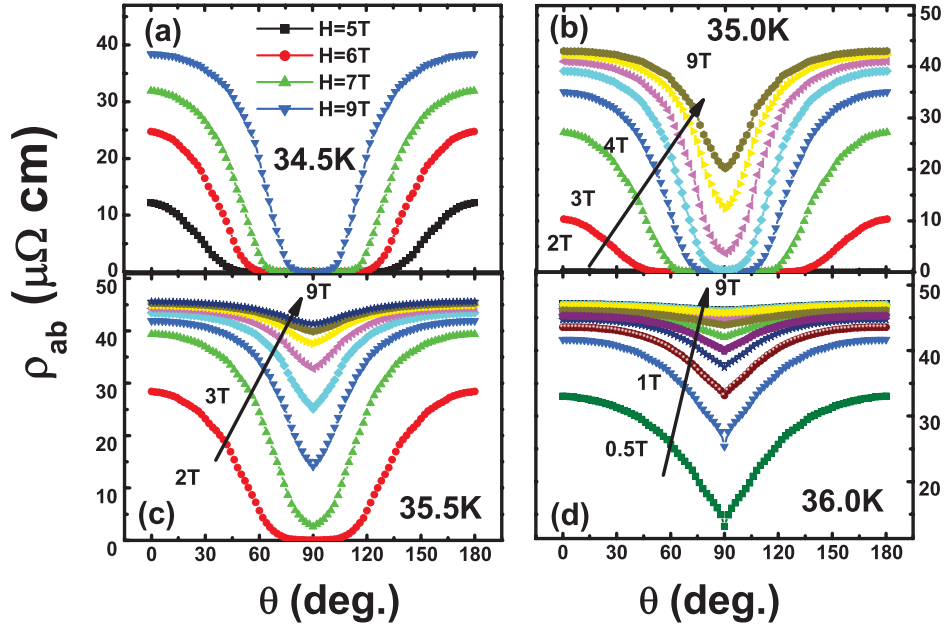


Figure 2.10: Angular dependence of resistivity at (a) 34.5 K in  $\mu_0H = 5, 6, 7, 9$  T, (b) 35 K in  $\mu_0H = 2, 3, 4, 5, 6, 7, 8, 9$  T, (c) 35.5 K in  $\mu_0H = 2, 3, 4, 5, 6, 7, 8, 9$  T, (d) 36 K in  $\mu_0H = 0.5, 1, 1.5, 2, 2.5, 3, 4, 5, 6, 7, 8, 9$  T for the  $Ba_{0.6}K_{0.4}Fe_2As_2$  single crystal.

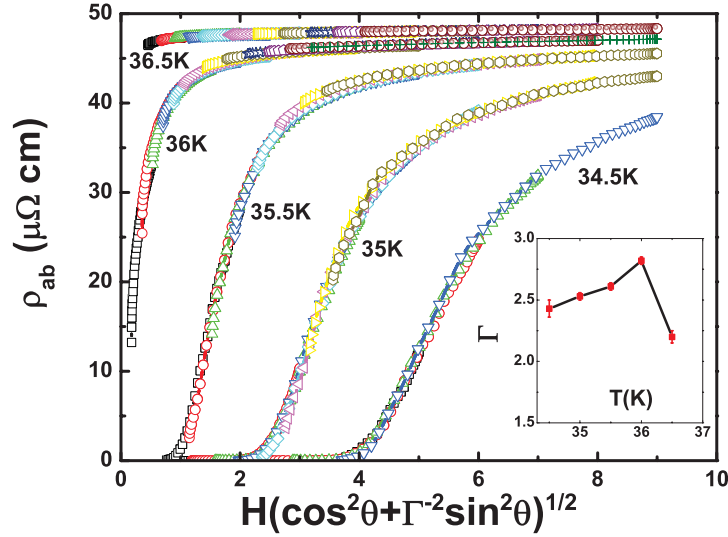


Figure 2.11: Scaling of the resistivity versus  $\tilde{H} = H\sqrt{\cos^2(\theta) + \Gamma^{-2}\sin^2(\theta)}$  at 34.5, 35, 35.5, 36, 36.5 K in different magnetic fields. Each curve is scaled nicely by adjusting  $\Gamma$ . The inset presents the temperature dependent  $\Gamma(T)$  for the  $Ba_{0.6}K_{0.4}Fe_2As_2$  single crystal. The line is guided to eyes.

thus obtained for temperatures 34.5, 35, 35.5, 36, and 36.5 K. Because only one fitting parameter  $\Gamma$  is employed in the scaling for each temperature, the value of  $\Gamma$  is more reliable compared with the one determined from the ratio of  $H_{c2}^{ab}$  and  $H_{c2}^c$  as used above. But both methods yield similar values of  $\Gamma$ , which implies the validity of the values determined in this work. It is found that, the anisotropy increases from 2.43 for 34.5 K to 2.82 for 36 K, and then decreases slightly for 36.5 K, as plotted in the inset of figure 2.11. Actually the anisotropy was also measured to much higher fields and lower temperatures [84, 85] in the same system and was found to decrease with temperature and finally reached a value of about 1-1.5 in the low T limit. This kind of temperature dependence

of  $\Gamma(T)$  is not expected for a single band anisotropic superconductor and needs a further check by other measurements. It may be attributed to the the effect of two-gap scenario[93, 94, 47, 87]: one big gap dominates the transport properties at high temperature, but at low temperature, another more isotropic small gap dominates the transport properties, and interband scattering at low temperature also decreases anisotropy. In addition, it should be noted that the good scaling behavior suggests a field-independent anisotropy in the temperature and field range we investigated. The small anisotropy can be qualitatively understood based on the recent band structure calculations[90] in which it is shown that the Fermi surface sheets are not 2D cylinder like but rather exhibit a complicated 3D feature with a quite strong dispersion along  $c$ -axis. Our results here, very high upper critical fields and very low anisotropy, should be stimulating in fulfilling a quantitative calculation on the electronic structure of the doped samples, and ultimately providing an understanding to the underlying mechanism of superconductivity.

## 2.4 Summary

---

In summary, we have successfully grown single crystals of  $Ba_{1-x}K_xFe_2As_2$  with high quality by using FeAs as the self-flux. By varying the K content during the growth, we obtained non-superconducting  $BaFe_2As_2$  single crystals and superconducting  $Ba_{1-x}K_xFe_2As_2$  single crystals with  $x = 0.17, 0.23, 0.25, 0.28$  and  $0.40$ . The samples have sizes up to 4 mm with flat and shiny cleaved surfaces. The x-ray diffraction patterns with only  $(00\ell)$  peaks suggest that they have high crystalline quality. The superconductivity was also characterized by AC susceptibility and resistivity measurements, which exhibit very sharp superconducting transitions. The temperature dependence of the resistivity for the non-superconducting crystals shows that the SDW instability and structure transition occur at about 138 K for the Ba-based compounds. The doping dependence of the  $c$ -axis parameter and  $T_c$  are consistent with previous data from polycrystalline samples[79, 38], which indicates the effects of different levels of potassium doping.

Then we investigated the temperature dependent resistivity for  $Ba_{1-x}K_xFe_2As_2$  ( $0.23 \leq x \leq 0.4$ ) single crystals in magnetic fields up to 9 T. It is found that the system poses a very high upper critical field and a very low superconducting anisotropy ratio which is around 2 for all the samples. In an alternative way, we also determined the anisotropy ratio by investigating the angle dependent resistivity in the  $Ba_{0.6}K_{0.4}Fe_2As_2$  single crystals. Both methods yield the similar values of the anisotropy ratio  $\Gamma$ . Our results strongly suggest that the anisotropic Ginzburg-Landau theory can be used very well to describe the data in the mixed state.

# 3

## Hall probe measurements on $\text{SmFeAsO}_{0.9}\text{F}_{0.1}$ polycrystal and $\text{Ba}_{0.6}\text{K}_{0.4}\text{Fe}_2\text{As}_2$ single crystal

Hall probes are magnetic field sensors based on the Hall effect. When a current runs through a conductor in a magnetic field, a voltage is induced perpendicular to the current direction. This voltage is proportional to the applied field, so it is very easy to use Hall probes as direct and quantitative magnetic field sensors. Since the size of Hall probe can be very small, it is often used to do local magnetization measurements on superconductors. As a fundamental parameter, the temperature dependence of the lower critical field  $H_{c1}(T)$ , or equivalently, superfluid density  $\rho(T)$  provide important information regarding the symmetry of the superconducting state, since the appearance of nodes in the gap of the electronic density of states strongly modifies the temperature dependence of the superfluid density and thereby the penetration depth. In this chapter, I will introduce the local magnetization measurements we did on  $\text{SmFeAsO}_{0.9}\text{F}_{0.1}$  polycrystal and  $\text{Ba}_{0.6}\text{K}_{0.4}\text{Fe}_2\text{As}_2$  single crystal with Hall probe.

### 3.1 Hall probe

---

#### 3.1.1 The Hall effect

Hall probes are based on the simple principle of the Hall effect, discovered by Edwin Hall in 1879[95]. When a current carrying conductor is placed in a perpendicular magnetic field, a voltage is induced perpendicular to the current direction due to the Lorentz force on the charge carriers. This voltage is proportional to the current and field, and inversely proportional to the carrier density of the conductor. The Hall effect is often used to determine the density and the sign of the charge carries in a material, however it can also be used to measure a magnetic field if the carrier density  $n$  is known. The basic geometry of a Hall probe, the Hall cross, is shown in figure 3.1.

A charged carrier is subjected to a Lorentz force

$$\mathbf{F} = q(\mathbf{E} + \mathbf{v} \times \mathbf{B}) \quad (3.1)$$

where  $\mathbf{E}$  is the electric field and  $\mathbf{B}$  is the magnetic field in which the charged carrier is moving. Since the charged carriers are confined to the conductor, they maintain their trajectory and the force of the

magnetic field on the charge causes a charge imbalance between the sides of the conductor which exactly counteracts the force caused by the magnetic field:

$$q\mathbf{E} = -q\mathbf{v} \times \mathbf{B} \quad (3.2)$$

$\mathbf{E}$  is perpendicular to the current direction and can also be written as  $V_H/w$ , where  $V_H$  is the generated Hall voltage and  $w$  is the width of the conductor. Because the current can be written as

$$\mathbf{I} = -n_V q v t w \quad (3.3)$$

where  $n_V$  is the volume density of charges,  $t$  is the conductor thickness and  $w$  is the conductor width. Thus equation 3.2 turns into

$$IB_z = n_V q t V_H \quad (3.4)$$

where  $B_z$  is the component of the magnetic field perpendicular to the conductor. Expressing the Hall voltage as a function of the magnetic field this is

$$V_H = \frac{IB_z}{n_V q t} \quad (3.5)$$

This equation shows that in order to achieve a high Hall response, it is important to reduce carrier density and thickness. Hall probes are often fabricated from some heterostructure such as GaAs/AlGaAs, which have a conduction layer of electrons confined to one of the GaAs/AlGaAs interfaces, known as a "two-dimensional electron gas"(2DEG). At low temperature the electronic wavefunction is confined to a single mode in the vertical direction. In this kind of structure the volume density of electron is not a relevant parameter, instead the sheet density( $n_{2D}$ ) is the correct measure, so the formula for the Hall effect turns into:

$$V_H = \frac{IB_z}{n_{2D}e} = R_H IB_z \quad (3.6)$$

where  $R_H = 1/n_{2D}e$  is defined as the Hall coefficient.

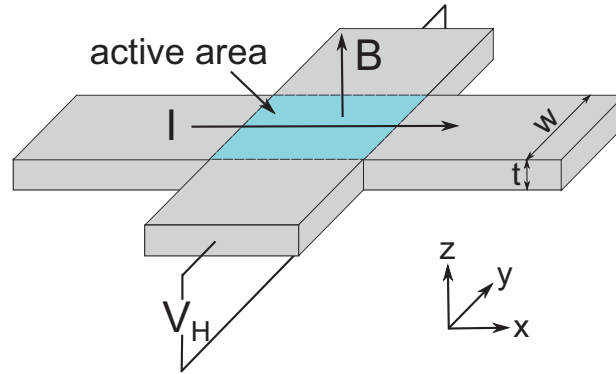


Figure 3.1: The Hall cross. The Hall voltage  $V_H$  is proportional to the current  $I$  in the  $x$  direction and the  $z$  component of the magnetic field  $B$  within the active area.

### 3.1.2 Hall probe fabrication

Our Hall probes are fabricated on GaAs/AlGaAs heterostructures. This material is employed as the carrier density ( $n_{2D}$ ) of the 2DEG at low temperatures can be set very low during the heterostructure growth process by tuning the number of dopants, while the mobility  $\mu$  can be very high, which can decrease the resistance of the leads, and for a large temperature region,  $n_{2D}$  and  $\mu$  are constant.

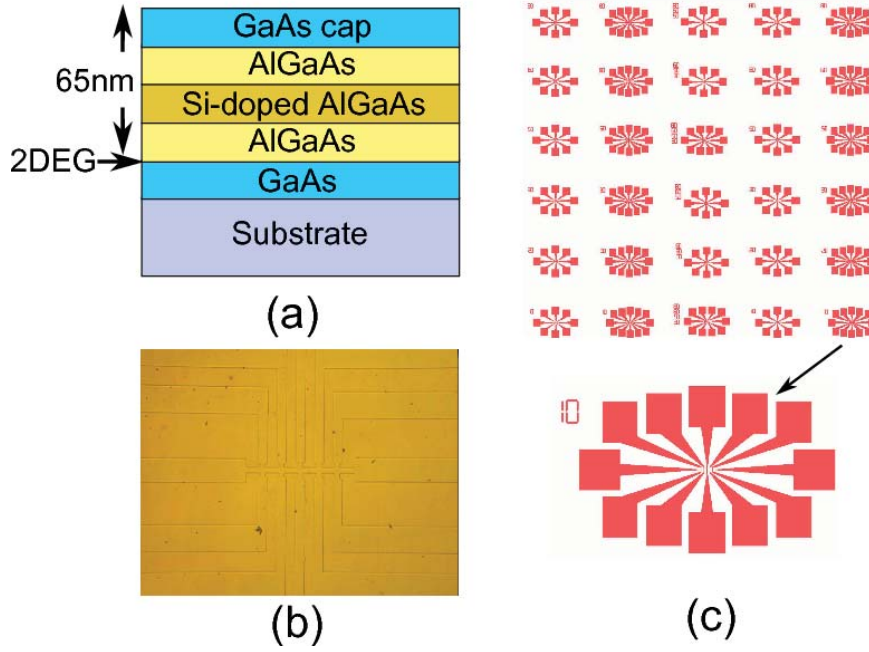


Figure 3.2: (a) 2DEG structure we used to fabricate our Hall probes. (b) Photograph of a Hall probe array I made. The size of the active area is  $10 \mu\text{m} \times 10 \mu\text{m}$ , and the distance between adjacent Hall bars is  $50 \mu\text{m}$ . (c) The mask I designed for the fabrication. The bottom part is a zoom of one pattern in the top part.

The wafers we used are grown using molecular beam epitaxy by Prof. Wen-Xin Wang and Hong Chen in the Laboratory of Microfabrication, Institute of Physics, Chinese Academy of Sciences. This 2DEG lies 65 nm underneath the surface. The wafer structure is shown in figure 3.2(a). The 2D carrier density  $n_{2D}$  is about  $2.6 \times 10^{11} \text{cm}^{-2}$  and the mobility  $\mu$  is about  $7 \times 10^4 \text{cm}^2/\text{Vs}$  at 77 K.

To fabricate the Hall probe we used ultraviolet lithography. Figure 3.2(c) is the mask I designed. There are thirty patterns with different sizes of the active area, numbers of the array and distances between each adjacent Hall bar. The 2DEG wafer is cut by a diamond knife, then the fabrication process is illustrated in figure 3.3:

1. Clean the wafer by acetone under ultrasonic, then flush by ethanol and deionized water.
2. Put a drop of fresh resist BP215 on the wafer and spin at 5000 RPM for 50 sec. Then bake at  $80^\circ\text{C}$  for 15 min.
3. Expose to ultraviolet under mask for 30 sec.
4. Develop in the 0.8% NaOH solution for 30 sec. Then bake at  $80^\circ\text{C}$  for 15 min.
5. Etch in the  $\text{H}_2\text{SO}_4 : \text{H}_2\text{O}_2 : \text{H}_2\text{O} = 1 : 8 : 824$  solution for 65 sec.
6. Wash by deionized water and acetone, then flush by deionized water.

We usually fabricate four different sizes of Hall probes, the active areas are  $20 \mu\text{m} \times 20 \mu\text{m}$ ,  $10 \mu\text{m} \times 10 \mu\text{m}$ ,  $5 \mu\text{m} \times 5 \mu\text{m}$  and  $2 \mu\text{m} \times 2 \mu\text{m}$ . In figure 3.2(b) is a photograph of one  $10 \mu\text{m} \times 10 \mu\text{m}$  Hall probe array I made. The distance between each adjacent Hall bar is  $50 \mu\text{m}$ .

The next step is to put ohmic contacts on the probes which allow electrical connections to be made to the 2DEG, 65 nm underneath the surface. In order to make good ohmic contacts, we built an annealing furnace, as shown in figure 3.4. The material I used to make the contact is In-Sn alloy. After soldering a droplet of In-Sn alloy on each contact pad, I put the wafer in the furnace. A mixture of  $\text{N}_2 : \text{H}_2 = 4 : 1$  gas was used to protect the alloy against oxidation. Usually after 15 minutes

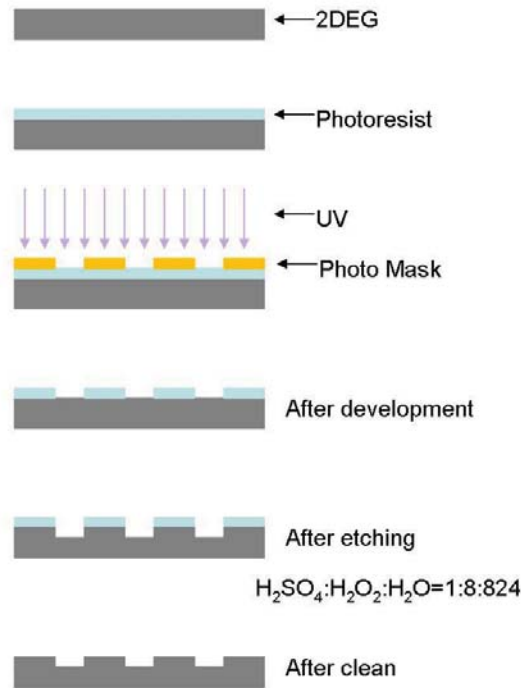


Figure 3.3: Schematics of the fabrication process. For details refer to text.

at 400°C, good ohmic contacts were obtained. It is believed that during the annealing process, Ga atoms diffuse out of the wafer and Sn atoms spike down into the wafer creating electrical connection to the 2DEG. After the anneal, thin gold wires were soldered on each contact pad with the In-Sn alloy.

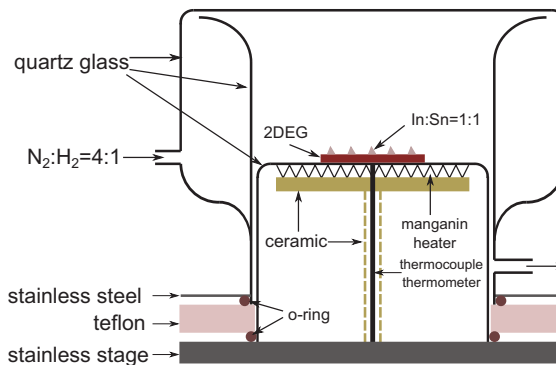


Figure 3.4: Schematic of the annealing furnace. The main parts of the furnace are made of quartz glass which are sealed by two o-rings of teflon. A mixture gas of  $N_2 : H_2 = 4 : 1$  was used to protect the alloy against oxidation. A thermocouple thermometer and a manganin heater are used for temperature control.

### 3.1.3 Resolution and sensitivity

After the fabrication, we tested the Hall probes at low temperature. The low temperature and magnetic environment was provided by an Oxford cryogenic system Maglab-EXA-12. I built an insert for this system and wrote the measurement programs using labview. The response of the Hall probe to the applied field shows a useful linear behavior. The Hall coefficient  $R_H$  varies from

0.14  $\Omega/\text{G}$  to 0.25  $\Omega/\text{G}$ . A typical curve is shown in figure 3.5. The active area of the Hall probe is  $10\ \mu\text{m} \times 10\ \mu\text{m}$ . The measurement was performed at  $T = 10\ \text{K}$  and  $I_{bias} = 1\ \mu\text{A}$  using lock-in detection with  $\tau = 0.1\ \text{s}$  and  $f = 133.33\ \text{Hz}$ . The applied magnetic field swept at  $60\ \text{G}/\text{min}$ . The slope gives the Hall coefficient  $R_H = 0.225\ \Omega/\text{G}$ . After subtracting a straight line from the curve, one can quantify the Hall resistance noise to about  $0.075\ \Omega$ , giving  $B_{noise} \approx 0.11\ \text{G}/\sqrt{\text{Hz}}$ . Below  $77\ \text{K}$ , there was a small shift between the response curves due to a small change of the contact resistance of the electrodes, but the Hall coefficient almost didn't change. For the  $H_{c1}$  measurement, the most important thing is the linear behavior of the magnetic field response of the Hall probe, thus the small shift can be ignored.

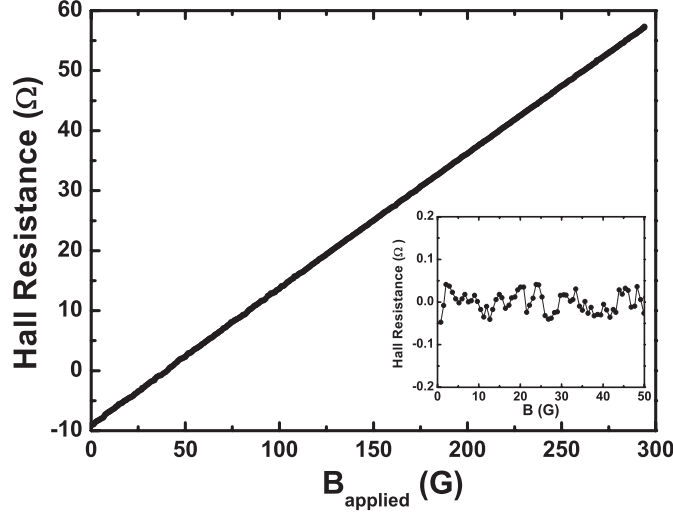


Figure 3.5: Response of a  $10\ \mu\text{m} \times 10\ \mu\text{m}$  probe to the applied field. The slope gives the Hall coefficient  $R_H = 0.225\ \Omega/\text{G}$ . The measurement was performed at  $T = 10\ \text{K}$  and  $I_{bias} = 1\ \mu\text{A}$  using lock-in detection with  $f = 133.33\ \text{Hz}$  and  $\tau = 0.1\ \text{s}$ . Inset: The curve subtracted by its linear fitting, giving  $B_{noise} \approx 0.11\ \text{G}/\sqrt{\text{Hz}}$ .

Then we did some measurements on Bi-2212 single crystals to test our system. Figure 3.6 shows one typical magnetization curve we obtained with the Hall probe. The initial part is a straight line which is due to the Meissner effect, but the slope of the line is not -1. This is because the sample is not big enough, and not close enough to the surface to shield all the magnetic field from the Hall bar. There are two peaks on the lower part of the curve, the low magnetic field one is the flux penetration peak and the other one is the so called "second magnetization peak" [96], which is attributed to the dislocation of a 3D vortex line to 2D pancake vortices that can better accommodate to pinning sites and thus lead to higher magnetization and higher critical current density. Since the flux penetration peak is very sharp, it is easy to define the penetration magnetic field. However, the sample is very thin, resulting in a big demagnetization factor, so the penetration field is much smaller than the lower critical field.

## 3.2 Measurements on $\text{SmFeAsO}_{0.9}\text{F}_{0.1}$ polycrystal

One of the most important issues to understand the underlying superconducting mechanism in FeAs-based superconductors is the pairing interaction. One important precondition for pinpointing the pairing interaction is the knowledge of the symmetry of the superconducting order parameter and the nature of the low energy excitations. Just several months after the discovery of the FeAs-based superconductors, some experiments such as specific heat [97],  $\mu\text{SR}$  [98, 99] and NMR [100] favor a  $d$ -wave state in the superconducting gap. The presence of nodes in the gap has also been inferred from the observation of angle dependent zero-bias conductance peak in point-contact

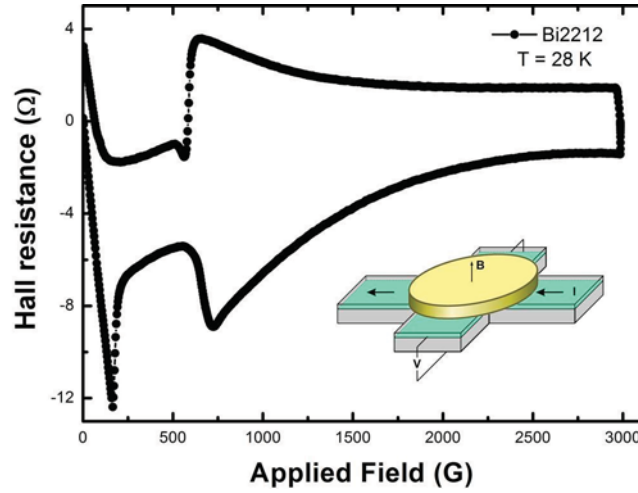


Figure 3.6: Typical magnetization curve of Bi-2212 measured with Hall probe. The sketch is how the measurement was done.

tunneling spectra [101, 102]. On the other hand, another point-contact tunneling measurement indicates a conventional  $s$ -wave state in  $\text{SmFeAsO}_{0.85}\text{F}_{0.15}$  with relatively low  $T_c$  [48]. In-plane magnetic penetration depth measurement suggests the possibilities of the existence of either two or an anisotropic superconducting gap(s) in gap function [103]. Because sizable single crystals of 1111 FeAs-based superconductors of high quality were not accessible, most of the current experiments were performed on polycrystalline samples, and the experimental results within the context of the symmetry of the pair state was not yet well determined.

As the temperature dependence of the lower critical field  $H_{c1}(T)$  can provide important information regarding the symmetry of the superconducting state, we performed detailed magnetization measurements on a  $\text{SmFeAsO}_{0.9}\text{F}_{0.1}$  (F-SmFeAsO) polycrystalline sample. The global and local magnetization measurements combined permit a more precise determination of the temperature dependence of the lower critical fields  $H_{c1}$ . We found that the obtained  $H_{c1}$  data show a very weak temperature dependence below 10 K. The  $H_{c1}(T)/H_{c1}(0)$  are inconsistent with a simple isotropic  $s$ -wave type as well as a  $d$ -wave type of order parameter, but can be well described by two  $s$ -wave gaps or an anisotropic  $s$ -wave gap picture. This implies that there are no nodes in the superconducting energy gap in F-SmFeAsO.

### 3.2.1 Sample synthesis

Because of the lack of sizable single crystals of the 1111 system at the time, we had to do the measurements on polycrystalline samples. The polycrystalline F-SmFeAsO samples used in this experiment were synthesized in Z. X. Zhao's group at Beijing National Laboratory for Condensed Matter Physics, by using a high temperature ( $> 1100^\circ\text{C}$ ) high pressure technique. SmAs powder (pre-sintered) and As, Fe,  $\text{Fe}_2\text{O}_3$ ,  $\text{FeF}_2$  powders (the purities of all starting chemicals are better than 99.99%) were mixed together according to the nominal stoichiometric ratio of  $\text{SmFeAsO}_{1-x}\text{F}_x$ , then ground thoroughly and pressed into small pellets. The pellets were sealed in boron nitride crucibles and sintered in a high pressure synthesis apparatus under the pressure of 6 GPa and temperature of  $1250^\circ\text{C}$  for 2 hours[31]. Because of the inevitable loss of fluorine either by high pressure synthesis or ambient pressure synthesis, the real F-doped level is much smaller than the nominal one, and therefore the impurity phases always exist due to the unbalance of the stoichiometry for the nominal phase.

The structure of the samples was characterized by powder X-ray diffraction (XRD) analysis. The XRD patterns indicate that all samples have a main phase of SmFeAsO structure with some impurity

phases, and the impurity phases have been determined to be the known oxides, arsenides, and fluorides that were formed by starting chemicals. Then the sample was examined by AC and DC susceptibility measurements. As shown in the left of figure 3.7, the DC susceptibility (measured under a magnetic field of 1 Oe) and AC susceptibility data (measured using an AC amplitude of 0.1 Oe) exhibit a sharp magnetic transition. A rough estimate on the diamagnetic signal indicates that the superconducting volume is close to 100%. The width defined between the 10% and 90% cuts of the transition is below 2 K, with the middle of the superconducting transition at 51.5 K, indicating the good quality of the superconducting phase.

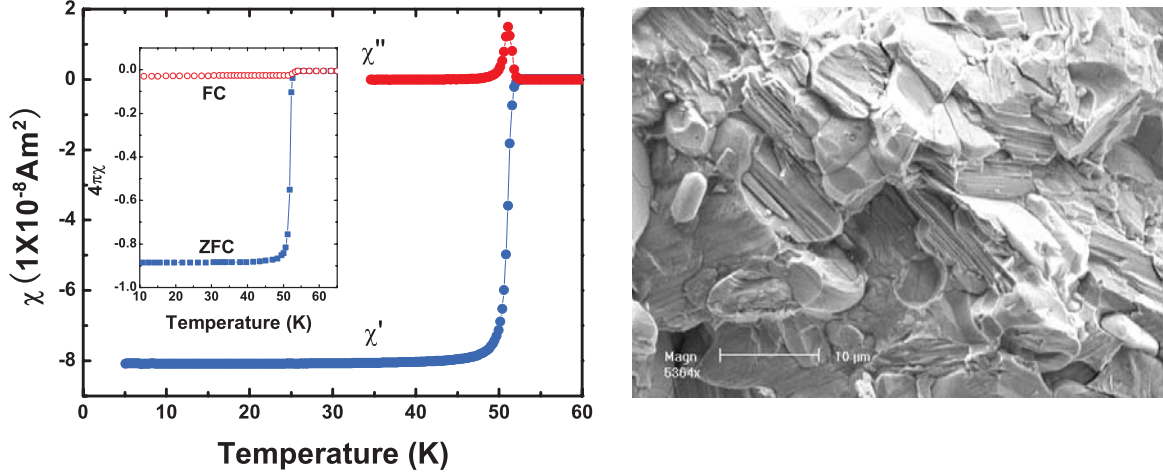


Figure 3.7: Left: Temperature dependence of AC susceptibility of one  $\text{SmFeAsO}_{0.9}\text{F}_{0.1}$  sample. Inset: DC susceptibility of the sample sample. Right: A scanning electron microscope picture of the  $\text{SmFeAsO}_{0.9}\text{F}_{0.1}$  sample, which is grown by high pressure technique. The grains with plate-like shape are highly compacted together.

The right of figure 3.7 shows a scanning electron microscopy (SEM) picture of the  $\text{SmFeAsO}_{0.9}\text{F}_{0.1}$  sample surface. Many microcrystals accumulate tightly, without obvious gaps between them. For a single microcrystal, the layered structure can be seen clearly, indicating its definite orientation, while the crystalline orientation is random from one crystal to another. Compared with samples synthesized by the common vacuum quartz tube method, the samples studied here are much more compact and rigid, and thus are more suitable for the  $H_{c1}$  measurements.

### 3.2.2 $H_{c1}$ measurement

In this experiment we used two samples, cut from the same batch. Both of them were very compact with a metallic shiny surface and were polished using fine sandpaper into rectangular shape with dimensions of  $2.60 \times 1.08 \times 1.50 \text{ mm}^3$  for sample No.1 and  $0.22 \times 0.18 \times 0.11 \text{ mm}^3$  for sample No.2, respectively. The ac susceptibility measurement of No.1 showed a very similar transition as the big batch [the inset of figure 3.8 (a)], indicating a good homogeneity of the sample.

Global dc magnetization measurement on No.1 was carried out by a Vibrating Sample Magnetometer (VSM) (Quantum Design) at the vibrating frequency of 40 Hz with a resolution better than  $10^{-6}$  emu. The magnetic field was applied parallel to the shortest lateral side of the sample to eliminate the difference of penetration of the magnetic field from the top and bottom surfaces. Local magnetization measurement was performed on sample No.2 using a Hall sensor with an active area of  $10 \times 10 \mu\text{m}^2$ . The Hall sensor was characterized without the sample attached at different  $T$  and at high  $T$  ( $< 60 \text{ K}$ ) with sample attached on. In both cases the Hall coefficient  $R_H$  was identical and measured to be  $0.22 \Omega/\text{Oe}$ , independent on  $T$  below 80 K.

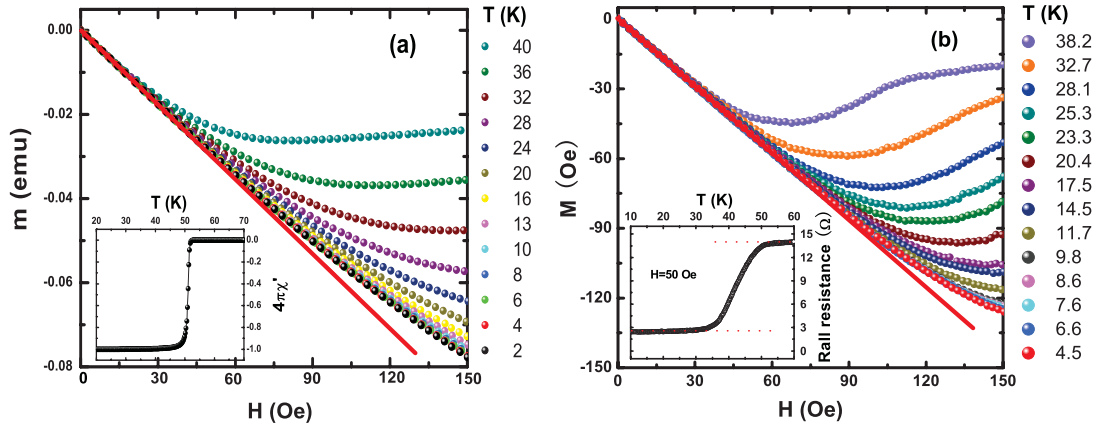


Figure 3.8: Magnetization hysteresis loops of  $\text{SmFeAsO}_{0.9}\text{F}_{0.1}$  at various temperatures measured (a) by VSM (sample No.1 with  $1.50 \times 1.08 \times 2.60 \text{ mm}^3$  sample size). Inset: The real part of ac susceptibility  $\chi'(T)$ , showing the superconducting transition region; (b) by Hall sensor (No.2 with  $0.22 \times 0.18 \times 0.11 \text{ mm}^3$ ). Inset: The magnetization in the unit of Hall resistance as a function of temperature for No.2 measured in ZFC mode with applied field. The two dotted lines show the superconducting transition step. The two solid red lines in (a) and (b) are the ‘Meissner line’ showing the linearity of these curves at low fields.

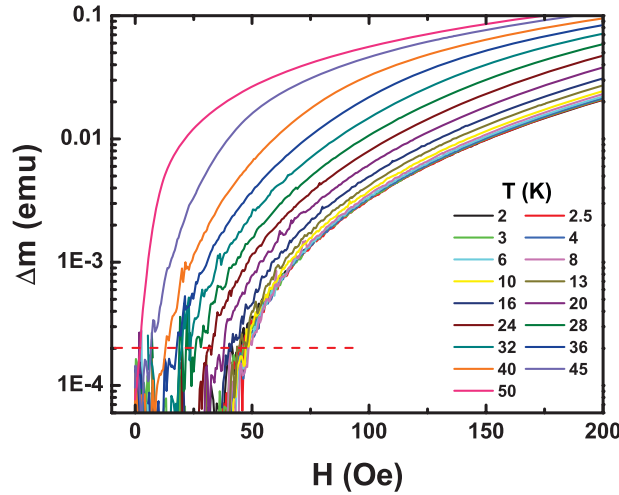


Figure 3.9: The initial  $M(H)$  data of sample No. 1 subtracted by the Meissner line (as described in text). The dashed red line sets up a criterion of  $2 \times 10^{-4} \text{ emu}$ .

An accurate determination of  $H_{c1}$  by magnetization measurements may suffer from vortex effects. In our experiment, all  $M(H)$  curves were taken in a zero-field-cool (ZFC) mode with initial temperature up to 55-60 K. For the local measurement, the field trapping in each  $M(H)$  measurement at fixed  $T$  was monitored by comparing the Hall resistance with that of initial measurement at the first cool down. By this way, we found the field trapping in our measurement was less than 0.4 Oe, of which the effect on magnetization is negligible in our experiment.

Additionally, the presence of the Bean-Livingston surface barrier [104] that, for perfect surfaces, prevents vortex entry until the fields is far above  $H_{c1}$ . However, making surface rough on the scale of  $\lambda$  reduces the surface barrier very effectively[105]. Since the samples we used are polycrystal, the surface is intrinsically rough. To minimize the complex effects of the character of the field penetration in layered structure, we used a low field sweep rate of 30 Oe/min to measure isothermal

magnetization  $M(H)$  curves by both decreasing ( $M_{dec}$ ) and decreasing ( $M_{inc}$ ) the fields.

Taking the circumstances described above into account, we extensively measured  $M(H)$  loops at various  $T$ , especially at  $T < 25$  K ( $0.5T_c$ ) for both samples. In figure 3.8 we display the typical  $M(H)$  curves at selected temperatures. It can be seen that, in figure 3.8(a) and (b) respectively, all curves clearly show a common linear dependence of the magnetization at low fields. For a strict treatment, we fit more than 50 data points lower than 30 Oe by a linear law at  $T < 5$  K for both samples No.1 and 2, respectively. These fitted straight lines describe the common Meissner shielding effects (“Meissner line”) at low fields, as evidenced quantitatively in local measurement. As shown in figure 3.8 (b), the slope of the fitted common line is  $-0.98$ , very close to  $-1$  ( $4\pi M = -H$ ). An alternative way to elucidate the full Meissner effect is the  $M(T)$  curve at a fixed  $H$ . What displayed in the inset of figure 3.8(b) are the raw data of the induction  $B = H + 4\pi M$  as a function of  $T$  in the transition region at  $H = 50$  Oe. The magnitude of the change in  $B$  through superconducting transition is 49.5 Oe, very close to the applied bias field.

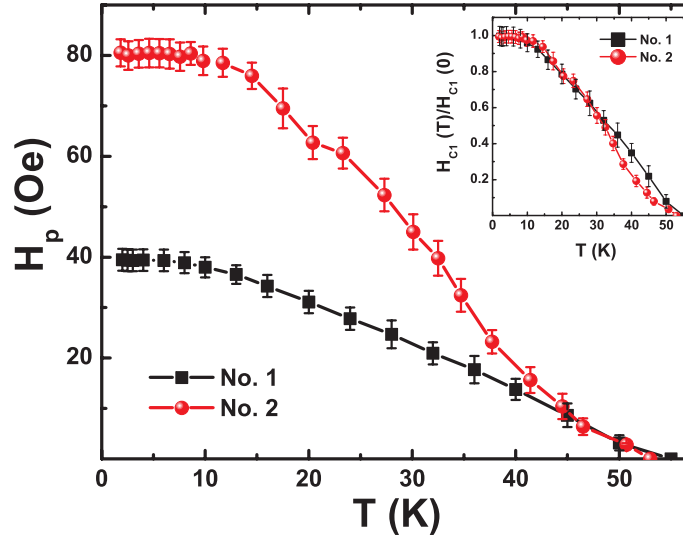


Figure 3.10: The  $T$  dependence of the  $H_p$  determined from the points deviation from the Meissner line of the initial  $M(H)$  curves for sample No.1 and 2. Inset: The normalized superfluid density  $\tilde{\rho}_s = H_{c1}(T)/H_{c1}(0)$  as a function of  $T$ . The results for both samples are very similar.

We determine the value of penetration field  $H_p$  by examining the point of departure from the Meissner line on the initial slope of the magnetization curve. Shown in figure 3.9 are the initial  $M(H)$  data of sample No. 1 subtracted by the “Meissner line”. By using a criterion of  $\Delta M = 2 \times 10^{-4}$  emu for No.1 and 0.3 G for No.2 (not shown here), which is the resolution limit of our technique, the extracted  $H_p$  as a function of  $T$  for these two samples are presented in figure 3.10, which show an overall similar behavior, except a large difference in absolute values due to the difference in demagnetization factors encountered in magnetization measurement. In the global magnetization measurement, the absolute value of  $H_{c1} = H_p/(1-N)$ , where  $N$  is the demagnetization factor and  $H_p$  the first penetration field. For a bar with a rectangle cross section, the  $H_{c1}$  and the first penetration field  $H_p$  have the relation [106]:  $H_{c1} = H_p / \tanh(\sqrt{0.36b/a})$ , where  $a$  and  $b$  are the width and the thickness of the sample, respectively. Using this formula, we estimate the demagnetization factor  $N = 0.54$  as we take  $a = 2.05$  mm and  $b = 1.08$  mm for sample No. 1. Then we get  $H_{c1}(0) = 87$  Oe, which is very close to the value of  $H_{c1}(0)$  of the sample No. 2 from the local magnetization measurements. In the inset of figure 3.10, the  $H_{c1}(T)$  of the two sample are both normalized. They have almost the same temperature dependent behavior, implying the reliability of the measurement. The  $H_p(T)$  data show a very weak temperature dependence at  $T < 10$  K, saturated at  $H_p = 40$  Oe for sample No.1 and 81 Oe for sample No.2 in low temperature limit. This weak temperature de-

pendence of  $H_{c1}$  is consistent with recent  $\mu$ SR results [98, 99]. In contrast to the  $\mu$ SR work, we found no sign of an upturn in  $H_{c1}(T)$  at lower temperature for both samples, implying a very weak paramagnetic ordering in these two samples [98, 99].

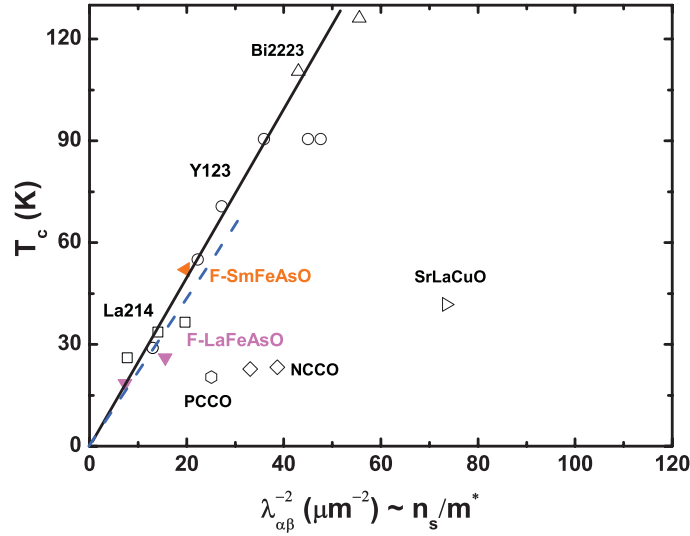


Figure 3.11: The correlation between  $T_c$  and the superfluid density  $n_s/m^*$ . The obtained  $\lambda_{ab}(0) = 225$  nm of F-SmFeAsO roughly follows the Uemura relation compared with F-LaFeAsO. The full triangles show the data for F-LaFeAsO [97, 98]. Points for the cuprates are taken from ref. [98].

We now analyze and discuss the data of  $H_{c1}(T)$  obtained for two samples to elucidate the pairing symmetry revealed in the gap function. We evaluate the penetration depth  $\lambda$  using the expression:  $H_{c1} = (\Phi_0/4\pi\lambda_{eff}^2)\ln\kappa$ , where  $\Phi_0 = hc/2e = 20.7$  Oe  $\mu\text{m}^2$  is the flux quantum, and  $\kappa$  is the Ginzburg-Landau parameter (here we assume that  $\kappa$  is temperature independent). Using the nominal  $H_{c1}(0) = 87$  Oe and  $\kappa = 100$  (The value of  $\kappa$  is estimated as follows: by  $\mu$ SR experiment,  $\lambda_{ab} = 190$  nm (Ref. [100]), and in an electrical transport measurement on a micro-size  $\text{SmFeAsO}_{0.9}\text{F}_{0.1}$  single crystal with  $T_c = 51$  K, the coherence length  $\xi_{ab} \sim 2$  nm, thus  $\kappa = \lambda_{ab}/\xi_{ab} \simeq 100$ ), we find  $\lambda_{eff}(0) = 295$  nm. It is noted that in  $\mu$ SR experiments, the effective magnetic penetration depth  $\lambda_{eff}$  in anisotropic superconductor is solely determined by the in-plane penetration depth as  $\lambda_{eff} = 1.31\lambda_{ab}$  [98, 107]. Assuming that we can apply this approximation (it is still hold in our magnetization measurement), the obtained  $\lambda_{eff}(0)$  leads to a  $\lambda_{ab}(0) = 225$  nm, which roughly follows the Uemura relation compared with F-LaFeAsO, as shown in figure 3.11. This value of  $\lambda_{ab}(0)$  is slightly larger than  $\lambda_{ab}(0) = 190$  nm by  $\mu$ SR for a similar F-SmFeAsO [108] and  $\lambda_{ab}(0) = 210$  nm from magnetization measurement by torque technique on a single crystal [109].

As the obtained data  $H_{c1}(T)/H_{c1}(0)$  of the two samples are so similar, we only analyzed the data of sample No.1. A very weak temperature dependence of  $H_{c1}$ , namely penetration depth  $\lambda$ , at low temperature is a character of  $s$ -wave isotropic weak-coupling BCS superconductors. Similarly a  $T^2$  dependence of  $H_{c1}$  with different physics also exists for some extent. We noted that the  $T^2$  quadratic power-law is a character of a dirty  $d$ -wave gap. However, our samples is in the clean limit. As a result, in figure 3.12 we fit the data by using four different models: (a)  $s$ -wave, (b)  $d$ -wave, (c) two  $s$ -wave, and (d) anisotropic  $s$ -wave. For a single gap superconductor,  $H_{c1}$  relates the normalized superfluid density as:  $\tilde{\rho}_s(T) = \lambda_{ab}^2(0)/\lambda_{ab}^2(T) = H_{c1}(T)/H_{c1}(0)$ , and  $\tilde{\rho}_s(T)$  is given by [17, 18]

$$\tilde{\rho}_s(T) = 1 + \frac{1}{\pi} \int_0^{2\pi} \int_{\Delta(T,\varphi)}^{\infty} \frac{\partial f(E)}{\partial E} \frac{E}{\sqrt{E^2 - \Delta(T,\varphi)^2}} dE d\varphi \quad (3.7)$$

$f = [1 + \exp(E/K_B T)]^{-1}$  is the Fermi function,  $\varphi$  is the angle along the Fermi surface, and one of

the most useful expressions for  $\Delta(T, \varphi)$  are[15]:

$$\Delta(T, \varphi) = \Delta_0(0) \tanh \left( \frac{\pi T_c}{\Delta_0(0)} \sqrt{a \left( \frac{T_c}{T} - 1 \right)} \right) g(\varphi) \quad (3.8)$$

where  $\Delta_0(0)$  is the maximum gap value at  $T = 0$ . For (1) *s*-wave gap,  $a = 1$ ,  $g(\varphi) = 1$ . (2) *d*-wave gap,  $a = 4/3$ ,  $g(\varphi) = \cos(2\varphi)$ . (3) anisotropic *s*-wave gap,  $a = 1$ ,  $g(\varphi) = (1 + \alpha \cos 4\varphi)/(1 + \alpha)$ . For a superconductor with two gaps, the normalized superfluid density may be written as:  $\tilde{\rho}_s = x\tilde{\rho}_s^1 + (1-x)\tilde{\rho}_s^2$ , where  $x$  is the fraction of superfluid density  $\tilde{\rho}_s^1$  associated with the small gap  $\Delta_0^1$  [87].

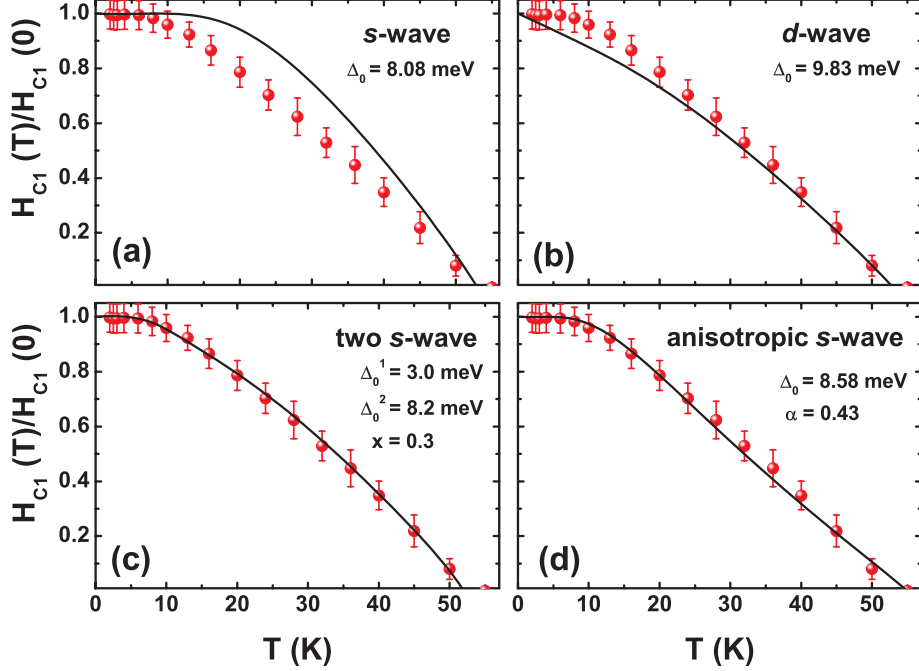


Figure 3.12: Temperature dependence of  $\tilde{\rho}_s = H_{c1}(T)/H_{c1}(0)$  of sample No.1. The fitting curves were obtained within the following models of the gap symmetries: (a) *s*-wave, (b) *d*-wave, (c) two *s*-wave, and (d) anisotropic *s*-wave.

The results of the analysis are shown in figure 3.12 by solid black lines. It is obvious that the *s*-wave model and the *d*-wave model can not describe the observed  $H_{c1}(T)/H_{c1}(0)$ . The fitting in wide temperature regime is in clear disagreement with the data [figure 3.12 (a) and (b)]. Thus the possibility of a single *s*-wave gap as well as *d*-wave seems unlikely in the present system. In contrast, both two *s*-wave and anisotropic *s*-wave models describe the data well [figures 3.12 (c) and (d)]. For the two *s*-wave case, the fit yields  $\Delta_0^1 = 3$  meV ( $0.67k_B T_c$ ),  $\Delta_0^2 = 8.2$  meV ( $1.82k_B T_c$ ), and  $x = 0.3$ . It is very close to the result reported by L. Malone in the single crystal samples [103]. For the anisotropic *s*-wave case, we get  $\Delta_0 = 8.58$  meV and  $\alpha = 0.43$ . The corresponding gap to  $T_c$  ratio is  $\Delta_0/k_B T_c = 1.8$ , which is very close to the weak coupling BCS value 1.76. The obtained variation with angle  $\Delta^{\max}/\Delta^{\min} \approx 2.5$  is slightly bigger than 1.2 in  $\text{NdFeAsO}_{0.9}\text{F}_{0.1}$ , which is reported in ref. [110].

### 3.3 Measurements on $\text{Ba}_{0.6}\text{K}_{0.4}\text{Fe}_2\text{As}_2$ single crystal

Unlike the 1111 system, it was found that sizable single crystals of 122 system can be grown by metal or self-flux method just after the discovery of this system. After we grew the  $\text{Ba}_{1-x}\text{K}_x\text{Fe}_2\text{As}_2$  single crystals, we performed the first detailed magnetic penetration depth measurements of superconducting  $\text{Ba}_{0.6}\text{K}_{0.4}\text{Fe}_2\text{As}_2$  single crystals by local magnetization measurements with Hall probe.

We found the presence of a possible full gap feature together with two gaps in  $\text{Ba}_{0.6}\text{K}_{0.4}\text{Fe}_2\text{As}_2$  superconductors.

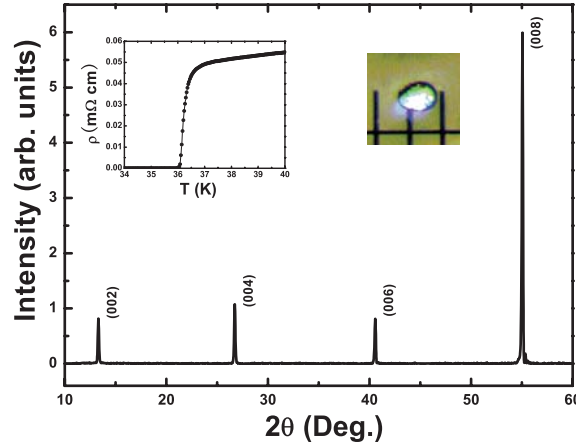


Figure 3.13: XRD pattern of the  $\text{Ba}_{0.6}\text{K}_{0.4}\text{Fe}_2\text{As}_2$  crystal. The right inset shows the sample (1#) under the optical microscope. The scale underneath with  $100\ \mu\text{m}/\text{grid}$  is used to display the size of the sample. The left inset shows the resistive transition on one crystal cut from the same piece.

The crystals of  $\text{Ba}_{0.6}\text{K}_{0.4}\text{Fe}_2\text{As}_2$  were grown by the FeAs flux method and characterized by resistivity measurements with  $T_c = 36.2\ \text{K}$  and a transition width of  $0.45\ \text{K}$  (10%-90% of normal state resistivity) [111], as displayed in left inset of figure 3.13. A single crystal (1#) was selected from the cleaved as-grown bulk under optical microscope. The sample has dimensions of  $110\ \mu\text{m}$  in diameter and  $40\ \mu\text{m}$  in thickness, as shown in the right inset of figure 3.13. The crystal structure was examined by X-ray diffraction, and only  $(00l)$  peaks were observed with the full-width-at-half-maximum around  $0.1^\circ$ , as shown in the main panel of figure 3.13, which indicates good crystallization of the samples.

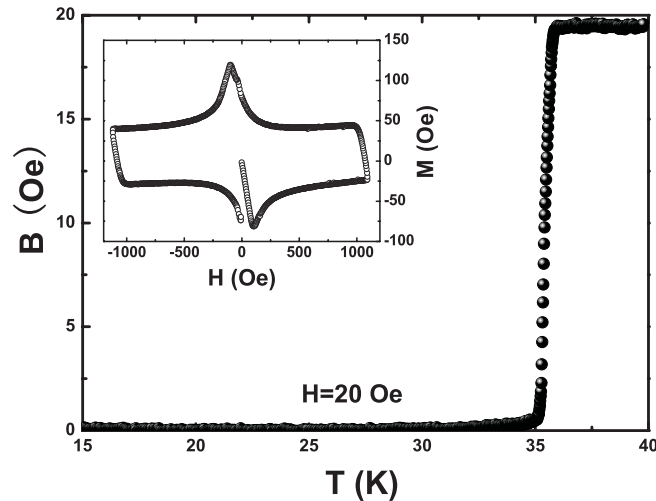


Figure 3.14: The induction  $B$  measured by a Hall probe as function of temperature measured after zero-field cooling. Inset: A typical magnetization hysteresis loop measured at  $32.1\ \text{K}$  by the Hall sensor.

The local magnetization measurement was performed on two crystals using a two dimensional electron gas based micro Hall sensor with an active area of  $10 \times 10\ \mu\text{m}^2$ . The Hall sensor was characterized without a sample attached at different temperatures. In our experiment, we used a low

field sweep rate of 30 Oe/min to measure the isothermal magnetization  $M(H)$  curves in both decreasing ( $M_{dec}$ ) and increasing ( $M_{inc}$ ) fields to minimize the complex effects of the character of the field penetration in a layered structure [105]. The pinning property has been checked by measuring the magnetization hysteresis loops. The result is shown in the inset of figure 3.14. The  $M(H)$  curve shows a symmetric feature at  $T=32.1$  K, indicative of the dominance of bulk pinning and the absence of the Bean-Levingson surface barrier for vortex entry. A second crystal (2#) with dimensions of  $210 \times 150 \times 50 \mu\text{m}^3$  was also measured by Hall sensor and vibrating sample magnetometry (VSM), and both measurements showed essentially identical behavior except for the difference in scale due to the demagnetization effect.

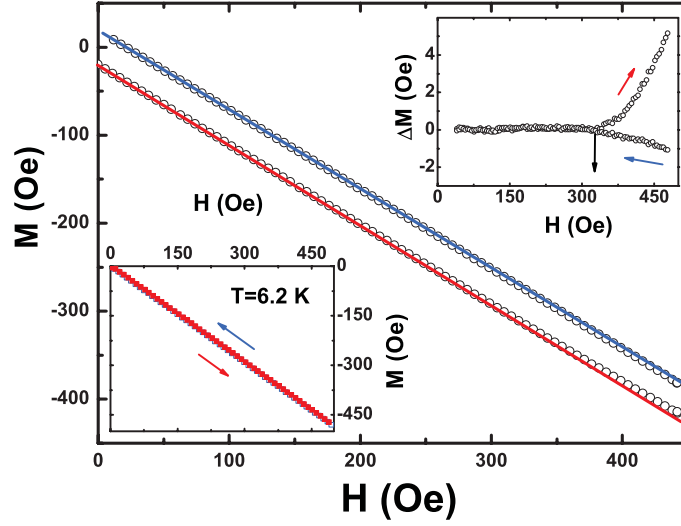


Figure 3.15: A typical magnetization hysteresis loop (symbols), the solid lines are the linear fitting curves using the low field data (Meissner line). The increasing and decreasing branches are shifted downward and upward, respectively, for clarity. The same case is shown in the bottom-left inset when the maximum field is less than  $H_{c1}$ . The upper-right inset shows the magnetization data after subtracting the Meissner line. The arrows indicate the direction of sweeping fields and the determination of  $H_{c1}$ .

The quality of the crystal and the accuracy of the local magnetization measurement were demonstrated in figure 3.14, in which the induction  $B = H + 4\pi M$  sensed by the Hall probe is plotted as a function of  $T$  under a bias field  $H = 20$  Oe. The superconducting transition can be detected at the induction jump at  $T_c = 35.8$  K with a width of  $\Delta T_c = 0.5$  K, which shows the high quality of the crystal. As shown in raw data of  $B(T)$ , at low temperatures,  $B$  is close to 0, implying a full Meissner shielding effect:  $4\pi M \simeq -H$ . Thus the achievement of full Meissner shielding effect in our measurement provides a reliable way to determine the value of  $H_{c1}$ .

Shown in figure 3.15 are the typical isothermal  $M(H)$  curves by taking  $M_{dec}$  and  $M_{inc}$  at  $T=17.1$  K, respectively. It can be seen that, at low  $H$ , the  $M_{dec}$  and  $M_{inc}$  are fully reversible, showing a common linear dependence of the magnetization on field as displayed in the bottom-left inset of figure 3.15. At high  $H$ , a deviation from the linear dependence occurs at  $H = H_{c1}$  for both  $M_{dec}$  and  $M_{inc}$  curves. To quantify these deviations, we fit more than 50 data points between 10 and 30 Oe by a linear relation to account for the common linear dependence of  $M(H)$ . These fitted linear lines describe the Meissner shielding effects (“Meissner line”) at low fields, as evidenced quantitatively in figure 3.15 in which the slope of the fitted lines are -0.98, very close to -1. Thus the deviation of  $M(H)$  from the linear Meissner shielding is an indication of the first penetration field  $H_{c1}$ . An alternative way to determine the value of  $H_{c1}$  from these reversible isothermal  $M(H)$  curves is to subtract the Meissner line from both  $M_{dec}(H)$  and  $M_{inc}(H)$  curves, as illustrated in the upper-right inset of figure 3.15. The threshold field of non-zero magnetization happens to be the divergence

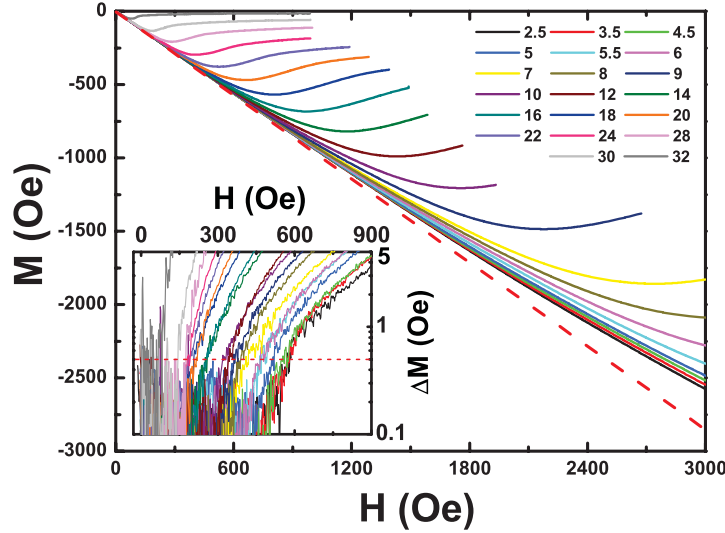


Figure 3.16: The initial part of the magnetization curves  $M(H)$  of 2# at various temperatures. The dashed line gives the Meissner linear approach. Inset: The same magnetization data in field subtracted by the Meissner line. The dashed line in the inset sets up a criterion of 0.5 Oe.

of the increasing and decreasing  $M(H)$  curves. It is noted that the values of  $H_{c1}$  with this criterion were determined in both increasing and decreasing field, so they are the true thermodynamic values and are not altered by the surface barrier [112].

For a strict treatment, we determined the value of  $H_{c1}$  by examining the point of departure from the Meissner line on the initial slope of the  $M(H)$  curve, which is the same as we did to the  $\text{SmFeAsO}_{0.9}\text{F}_{0.1}$  polycrystals. The inset of figure 3.16 shows how to determine  $H_{c1}$  by using a criterion of  $B = \Delta M = 0.5$  Oe at different temperatures. For a quantum of flux  $\phi_0 = 20.7$  Oe  $\mu\text{m}^2$ ,  $\Delta M = 0.5$  Oe is equivalent to about  $(2 \sim 3)\phi_0$  penetrating into the  $(10 \times 10)$   $\mu\text{m}^2$  sensing area, which is the limit of our Hall probe technique. The  $H_{c1}$  values determined in this way are about 4% larger than those estimated from the point where the reversible magnetization deviates from linearity, and we did not observe any significant difference in the  $T$ -dependence of  $H_{c1}$  deduced from either of the two criterion.

Shown in figure 3.17(a) and (b) are the obtained  $H_{c1}$  plotted as a function of  $T$  for 1# and 2#, respectively. At  $T < 4 \sim 5$  K,  $H_{c1}(T)$  is weakly  $T$ -dependent and seems to show a tendency towards saturation at lower  $T$  (in the limited temperature range). As illustrated in the insets of figure 3.17(a) and (b), the saturated  $H_{c1}$  reach 695 Oe for 1# and 590 Oe for 2#. This tendency of  $H_{c1}(T)$  reflects a possible fully gapped nature of superconducting state at low  $T$  for  $\text{Ba}_{0.6}\text{K}_{0.4}\text{Fe}_2\text{As}_2$  superconductors. With these data, we could not rule out the possibility of a small gap with nodes in the dirty limit with  $\rho_s(T)$  decaying with  $T^2$ , as in the cuprate superconductors, but that will lead to even larger  $\rho_s(0)$  and  $H_{c1}(0)$  as one would expect in the clean limit.

A pronounced *kink* can be easily observed in  $H_{c1}(T)$  curves at  $T \sim 15$  K for both samples. Obviously, the occurrence of the kink in  $H_{c1}(T)$  can not be explained by the model with an *s*-wave or *d*-wave *single gap*. On the other hand, this kinky structure in  $H_{c1}(T)$  resembles that of the related superfluid density of the two-band superconductor  $\text{MgB}_2$  [113], in which a positive curvature was observed and explained by the multi-band theory [114]. In addition, recent ARPES measurement resolved a two-gap nature in a similar  $\text{Ba}_{0.6}\text{K}_{0.4}\text{Fe}_2\text{As}_2$  crystal [47, 115]. Thus our observation of a kink in  $H_{c1}(T)$  strongly suggests the existence of multiple gaps in  $\text{Ba}_{0.6}\text{K}_{0.4}\text{Fe}_2\text{As}_2$  superconductors, which is consistent with that predicted in electronic band structure calculations [116].

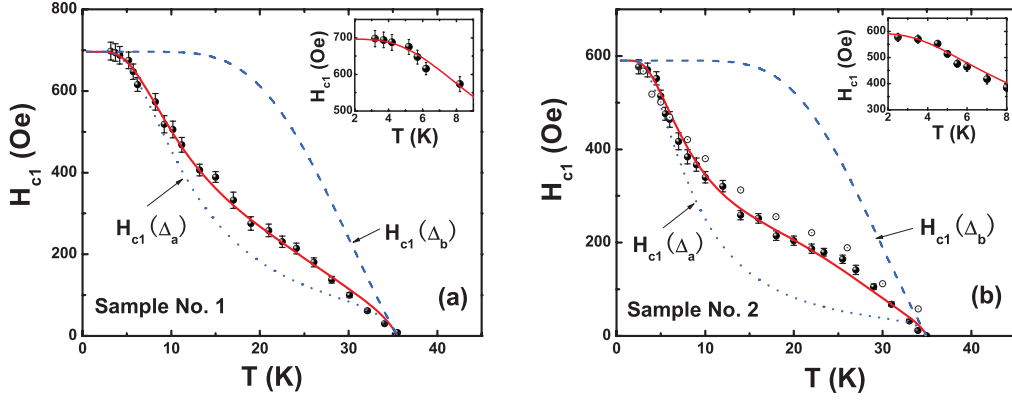


Figure 3.17: The extracted  $H_{c1}$  vs.  $T$  for sample 1# (a) and 2# (b) (full circles with error bars). The open dotted circles in (b) represent the  $H_{c1}$  determined from the VSM measurements taken into account of the demagnetization effect. The solid lines are the fitting curves using the two-gap model. The contributions of the small gap [ $H_{c1}(\Delta_a)$ ] and the large gap [ $H_{c1}(\Delta_b)$ ] in the model are also shown by the dotted and dashed lines, respectively. The two insets in (a) and (b) show the enlarged views of the data  $H_{c1}(T)$  in low temperature region together with the theoretical fitting curves (solid lines).

For our crystals, the coherence length  $\xi_{ab}(0)$  was estimated to be 2-2.5 nm from an extremely high upper critical field  $H_{c2}$  [ $\mu_0 H_{c2}^{||c}(0) = \phi_0/2\pi\xi_{ab}^2(0)$ ] [117, 84], and the mean free path (determined from the resistivity and the Hall effect data at 38 K) is  $\sim 15$  nm[111], our samples are therefore in the moderately clean, local limit. In this case the local London model is valid to describe the data. For a single gap superconductor,  $H_{c1}$  relates the normalized superfluid density as:  $\tilde{\rho}_s(T) \equiv \lambda_{ab}^2(0)/\lambda_{ab}^2(T) = H_{c1}(T)/H_{c1}(0)$ , and  $\tilde{\rho}_s(T)$  is given by [18, 118]

$$\tilde{\rho}_s(T) = 1 + 2 \int_{\Delta(T)}^{\infty} \frac{df(E)}{dE} \frac{E}{\sqrt{E^2 - \Delta(T)^2}} dE \quad (3.9)$$

with  $f$  the Fermi function. Here the total energy is  $E = \sqrt{\epsilon^2 + \Delta^2}$ , and  $\epsilon$  is the single-particle energy measured from the Fermi surface. We should note that above equation is based on the assumption of an isotropic Fermi velocity and gap, which may be validated by the very small anisotropy (about 2) determined from the transport measurements[117]. It is assumed that the gap  $\Delta$  on each Fermi surface follows the weak-coupling BCS temperature dependence. For a superconductor with two gaps, the normalized superfluid density may be written as:  $\tilde{\rho}_s = x\tilde{\rho}_s^a + (1-x)\tilde{\rho}_s^b$ , where  $x$  is the fraction of superfluid density  $\tilde{\rho}_s^a$  associated with the small gap  $\Delta_a$ . The results of the calculations and  $H_{c1}$  of 1# and 2# are shown by the red solid lines in figure 3.17(a) and (b), respectively. Fitting the data to above equations (with two  $s$ -wave gaps) yields:  $\Delta_a = 1.6 \pm 0.3$  meV,  $\Delta_b = 9.1 \pm 0.3$  meV and  $x=0.72$  for 1#, and  $\Delta_a = 2.2 \pm 0.2$  meV,  $\Delta_b = 8.8 \pm 0.3$  meV and  $x=0.70$  for 2#. We also tried to fit our data with a single  $s$ -wave gap which is anisotropic, having an in-plane angle dependence,  $\Delta(T, \varphi) = \Delta(T)(1 + \alpha \cos 4\varphi)/(1 + \alpha)$ , where  $\alpha$  is a fitting parameter which controls the anisotropy[15]. The overall fitting in wide temperature regime is in clear disagreement with our data. Thus the possibility of a single anisotropic gap seems unlikely when considering the almost symmetric circle-like Fermi surfaces in the present system. After several months, some similar results were reported on  $\text{Ba}_{1-x}\text{K}_x\text{Fe}_2\text{As}_2$  ( $T_c \simeq 32$  K) and  $\text{FeSe}_{1-x}$  under pressure by Muon-Spin Rotation and Angle-Resolved Photoemission[119, 120].

The gaps obtained from our  $H_{c1}(T)$  measurements are clearly smaller than those determined from the ARPES measurements[47, 115]. This discrepancy may be induced by the different ways and different criterions in determining the gaps, this should be checked by future experiments. It is interesting to note that the large gap accounts for only 30% of the total superfluid density. We must

stress that although a small gap with nodes (in the dirty limit) cannot be excluded from our low temperature data, this will not lead to a significant change to the general fitting results obtained here.

### 3.4 Summary

---

In summary, we fabricated Hall probes by photolithography and built a measurement system. We performed both global and local magnetization measurements on  $\text{SmFeAsO}_{0.9}\text{F}_{0.1}$  polycrystals. The temperature dependence of the lower critical field  $H_{c1}$  is reliably extracted. We obtained the lower critical field of  $H_{c1}(0) \sim 81$  Oe, and it roughly follows the Uemura relation compared with F-LaFeAsO. It is also found that the  $H_{c1}(T)/H_{c1}(0)$  are inconsistent with a simple isotropic  $s$ -wave type or a  $d$ -wave type of the order parameter. However, a good agreement was obtained between the experimental data and the theory within the framework of a two  $s$ -wave gap or an anisotropic  $s$ -wave gap picture, suggesting that the superconducting energy gap in F-SmFeAsO contains no nodes.

Then we also conducted local and global magnetization measurements on  $\text{Ba}_{0.6}\text{K}_{0.4}\text{Fe}_2\text{As}_2$  single crystals, and the lower critical field  $H_{c1}(T)$  is reliably extracted. It is found that  $H_{c1}$  exhibits a pronounced kink at  $T \sim 15$  K, which indicates a multi-gap nature. By using the two-gap weak coupling BCS model to fit the data, we obtained a small gap of  $\Delta_a(0) \simeq 2.0 \pm 0.3$  meV and a large gap of  $\Delta_b(0) \simeq 8.9 \pm 0.4$  meV.

# 4

## Point-Contact Andreev Reflection Study of $\text{Ba}_{0.6}\text{K}_{0.4}\text{Fe}_2\text{As}_2$ and $\text{BaFe}_{2-x}\text{Ni}_x\text{As}_2$ single crystals

Point-contact Andreev reflection (PCAR) spectroscopy has been adopted for probing the density of state (DOS) of superconductors with high energy resolution. In addition, the capability of this technique to study the anisotropy and the temperature dependence of the superconducting gap make it a unique tool in providing invaluable information for distinguishing various mechanisms of unconventional superconductivity. Several theoretical calculations have been reported on the PCAR conductance characteristics of a junction involving the  $s\pm$  symmetry in iron pnictide superconductors. We fabricated highly transparent  $c$ -axis direction contacts to perform the PCAR spectroscopy study on  $\text{Ba}_{0.6}\text{K}_{0.4}\text{Fe}_2\text{As}_2$  single crystals and a series of electron-doped  $\text{BaFe}_{2-x}\text{Ni}_x\text{As}_2$  single crystals over a wide doping range.

### 4.1 Point-contact Andreev reflection spectroscopy

---

#### 4.1.1 Andreev reflection

At the insulating interface between a superconductor(S) and a normal metal(N), an electron incident from the metal side with an energy higher than the energy gap in the superconductor(as the electron a shown in figure 4.1), will go into the superconductor through the barrier, and this is the tunnel effect. However, when the barrier is low enough, an electron incident from the metal side with an energy lower than the energy gap in the superconductor, will form a Cooper pair in the superconductor with the retro-reflection of a hole of opposite spin and momentum compared to the incident electron, as the electron b shown in figure 4.1. The electron-hole conversion is known as Andreev reflection. Through time-reversal symmetry, the process with an incident electron will also work with an incident hole (and retro-reflected electron)[121].

Even so Andreev reflection was discovered in 1964[122], it was only in 1982 that G. E. Blonder, M. Tinkham and T. M. Klapwijk gave a complete, even though simplified, theoretical discussion of the phenomenon, notably in including the effect of a finite transparency of the interface. This model is called the BTK model. The most noticeable simplification of the model is its reduction to 1D, i.e. all the involved momenta are normal to the interface and parallel to the  $x$  axis. The

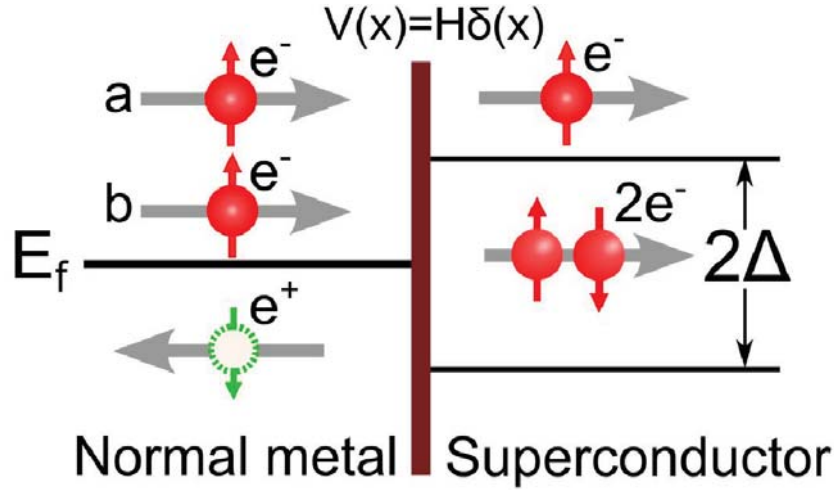


Figure 4.1: Electrical transport at an low barrier N/S interface. The energy of electron (red) a is bigger than the energy gap in the superconductor, it goes into the superconductor through the barrier by tunnel effect. The energy of electron b is smaller than the energy gap in the superconductor, it produces a Cooper pair in the superconductor and a retroreflected hole (green) in the normal metal by Andreev reflection. Vertical arrows indicate the spin band occupied by each particle.

barrier is represented by a repulsive potential  $H\delta(x)$  located at the interface, which enters in the calculations through the dimensionless parameter  $Z = k_F H / 2E_f = H / \hbar v_F$ . The smaller is  $Z$ , the more transparent is the barrier. The expression of the total current across the junction is given by

$$I_{NS} = 2N(0)e v_F \mathcal{A} \int_{-\infty}^{\infty} [f_0(E - eV) - f_0(E)] [1 + A(E) - B(E)] dE \quad (4.1)$$

where  $N(0)$  is the density of state of the electrons at the Fermi surface,  $v_F$  is the Fermi velocity,  $\mathcal{A}$  is the effective-neck cross-sectional area of the junction,  $f(E)$  is the Fermi distribution function,  $A(E)$  and  $B(E)$  are the coefficients giving the probability of Andreev and ordinary reflection[123]. The derivative of the current with respect to the bias,  $dI_{NS}/dV$ , provides the conductance of the junction

$$G_N = \int_{-\infty}^{\infty} \frac{df(E - V, T)}{dV} [1 + A(E) - B(E)] dE \quad (4.2)$$

When divided by the conductance of the same junction when the superconductor is in the normal state,  $dI_{NN}/dV$ , this gives the normalized conductance of the junction  $G$ , which is the usual normalization of the outcome of PCAR experiments[124].

The calculated normalized conductance  $G(V)/G_N$  is shown in figure 4.2 for various values of  $Z$  at  $T = 2$  K and  $\Delta = 2$  meV. The ideal Andreev reflection spectroscopy takes place in a perfectly transparent junction,  $Z = 0$ [figure 4.2(a)]. The conductance within the gap ( $|eV| < \Delta$ ) is doubled with respect to the normal-state one. When  $Z > 0$ [figure 4.2(b)(c)], two peaks appear at  $|eV| = \Delta$  and their amplitude increases on increasing  $Z$  while the zero-bias conductance (ZBC) is depressed. Finally, at  $Z \geq 10$ [figure 4.2(d)], the normalized conductance coincides with the BCS quasiparticle density of states. Indeed, it can be demonstrated that the results of the BTK model for  $Z \rightarrow \infty$  coincide with the standard results of the theory for NIS (I=insulator) tunnel junctions. Hence, the BTK model can reproduce, by simply changing a parameter, all the different experimental situations corresponding to different transparencies at the N/S interface, from zero to infinity.

Even if the BTK model gives a correct interpretation of some experiments in low-temperature superconductors, in most cases it predicts much sharper gap features than those actually observed in the

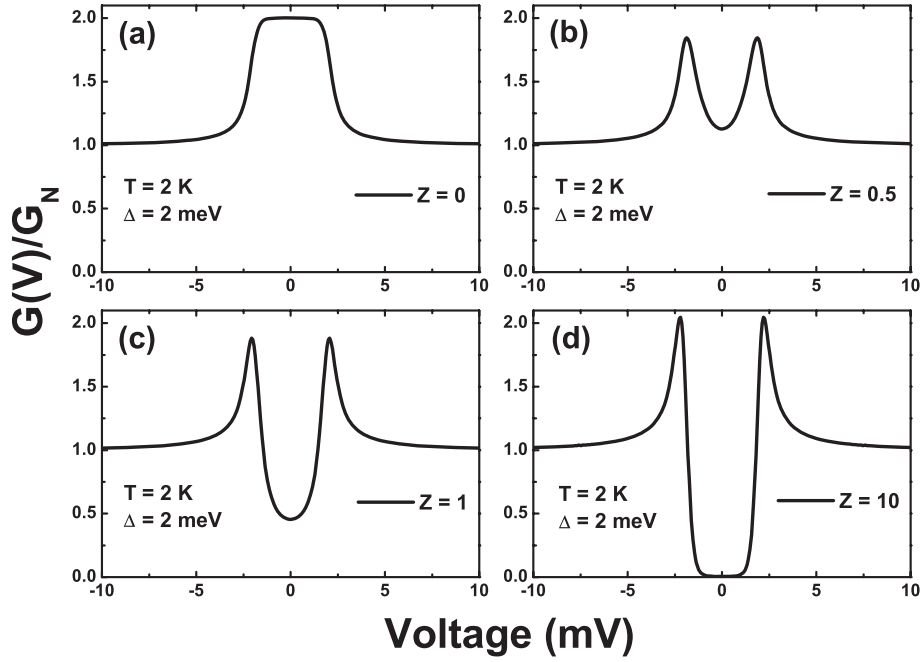


Figure 4.2: The point-contact spectroscopies calculated with the BTK model for different value of  $Z$  at  $T = 2$  K and  $\Delta = 2$  meV. In (a)-(d), the barrier  $Z$  is 0, 0.5, 1 and 10 respectively.

low temperature conductance curves. This means that the Andreev reflection structures in the experimental spectra are not only depressed in amplitude but also spread in energy[124]. This effect can be attributed to the reduction of the quasiparticle lifetime, resulting from the imaginary part of the quasiparticle self-energy[125]and the inelastic quasiparticle scattering processes occurring near the N/S interface (surface degeneration, contamination etc. either at the N or the S side)[126]. By properly solving the Bogoliubov-de Gennes equations in the presence of an inelastic scattering term, Plecen *et al.* have shown that it is possible to globally take these effects into account by including into the BTK model a single broadening parameter  $\Gamma$  in the form of an imaginary part of the energy, i.e.  $E \rightarrow E + i\Gamma$ [126].  $\Gamma$  can thus be considered as the lifetime parameter. In this extended BTK theory, the Bogoliubov coherence factors  $\mu_0$  and  $\nu_0$  can be obtained as

$$\mu_0^2 = 1 - \nu_0^2 = \frac{1}{2} \left[ 1 + \frac{\sqrt{(E + i\Gamma)^2 - \Delta^2}}{E + i\Gamma} \right] \quad (4.3)$$

Then  $A(E)$  and  $B(E)$  can be written as

$$A(E) = a^* \cdot a \quad (4.4)$$

$$B(E) = b^* \cdot b \quad (4.5)$$

where  $a = \mu_0 \nu_0 / \gamma$ ,  $b = -(\mu_0^2 - \nu_0^2)(Z^2 + iZ) / \gamma$ ,  $\gamma = \mu_0^2 + (\mu_0^2 - \nu_0^2)Z^2$ . By introducing expression 4.4 and 4.5 in expression 4.2, we can get the conductance of the junction with interface scattering, and this is the formula we use to fit the point-contact spectroscopy. Figure 4.3 are conductance curves calculated with the extended BTK model by using different  $\Gamma$ . As  $\Gamma$  becomes bigger and bigger, the feature of the curves is smeared. Thus in the point-contact measurement, to get a low value of  $\Gamma$ , a clean and stiff surface is very important. With the three fitting parameter: barrier factor  $Z$ , scattering factor  $\Gamma$  and superconducting gap  $\Delta$ , BTK theory can give a very precise value of the superconducting gap.

The assumption of an isotropic (*s*-wave) order parameter makes the BTK model particularly simple. Satoshi Kashiwaya *et al.* introduced the OP anisotropy into the expression of the superconducting transmission probability[127]. When the order parameter is a function of the angle  $\alpha$  with which

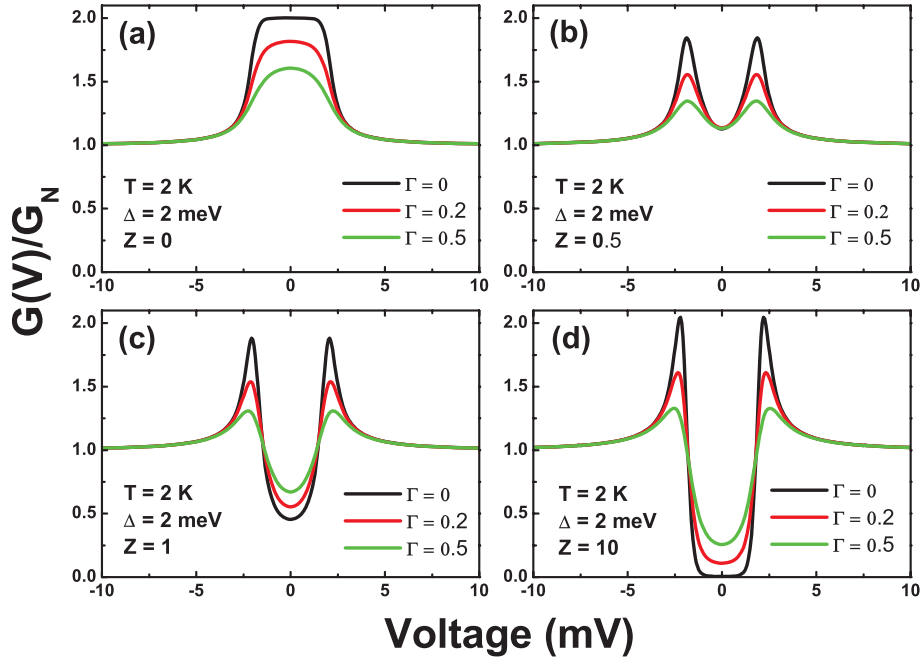


Figure 4.3: Conductance curves calculated with the extended BTK model by using  $\Gamma = 0, 0.2, 0.5$  and different value of  $Z$  at  $T = 2$  K and  $\Delta = 2$  meV. In (a)-(d), the barrier  $Z$  is 0, 0.5, 1 and 10 respectively.

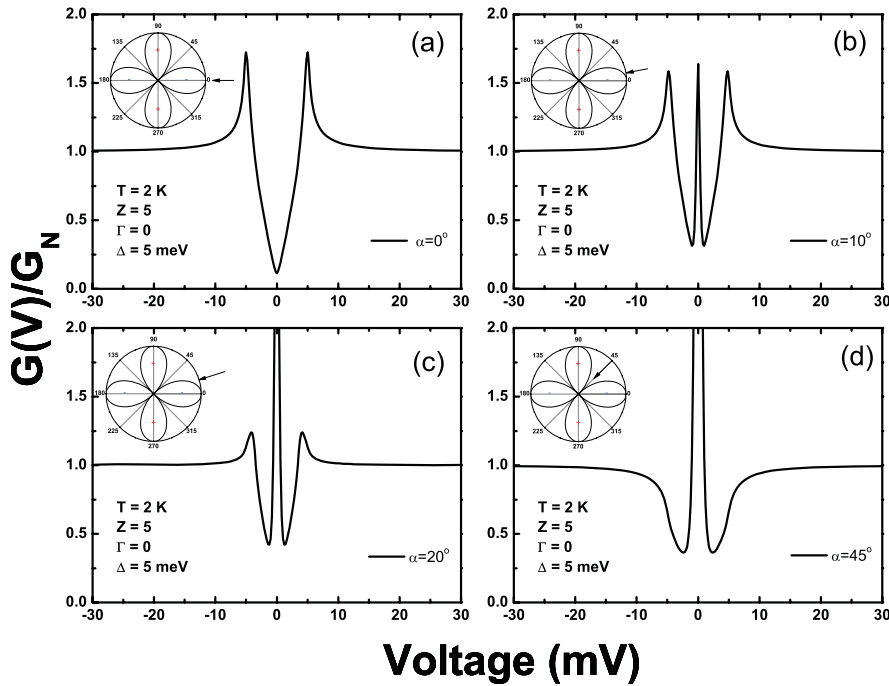


Figure 4.4: Conductance curves of a  $d$ -wave gap  $\Delta_d = \Delta \cos(2\theta)$  calculated with the extended BTK model by using different  $\alpha$  at  $T = 2$  K,  $Z = 5$ ,  $\Gamma = 0$  and  $\Delta = 5$  meV. In (a)-(d),  $\alpha = 0^\circ, 10^\circ, 20^\circ$  and  $45^\circ$  respectively.

electron-like quasiparticles are injected in the superconductor, the specific expression of  $\Delta(\alpha)$  depends on the kind of symmetry the OP shows in the  $k$  space. Figure 4.4 are conductance curves of a  $d$ -wave gap  $\Delta_d = \Delta \cos(2\theta)$  calculated with the extended BTK model by using different  $\alpha$ . Comparing with  $s$ -wave, the low bias conductance part of  $d$ -wave is much sharper. A more significant

feature of  $d$ -wave is that when the incident current deviated from the direction of the anti-nodes, as shown in figure 4.3(b) and (c), one can see a zero-bias conductance peak. When the incident current along the direction of the node, as shown in figure 4.3(d), the zero-bias conductance peak becomes most acute. Due to the sign change between the incident and reflected electron along the direction of node, an Andreev bound states will form in the interface, gathering a large number of quasi-particles near the Fermi level, and giving raise to the sharp zero-bias conductance peak[128]. So by fitting the conductance curves with BTK model, one also can get the symmetry of OP. Thus PCAR is a powerful tool to investigate the order parameter symmetry and the gap structure in superconductors.

#### 4.1.2 Fabrication of point contacts

A point contact is simply a contact between two metals, or a metal and a superconductor, but the radius of the contact should be smaller than the electron mean free path. Thus in most cases, the contact is nanometric. There are a number of ways to fabricate point contacts. The pioneering technique exploited by Yanson[129] was the realization of microshorts in the dielectric layer of a tunnel junction between two metals. Another widely used technique (especially in superconductors) is the break-junction technique, in which a single sample is broken into two pieces at low temperature, then brought back in contact. But it only allows the creation of homocontacts between two electrodes of the same material. Point contacts also have been made by lithographical creation of a small hole in a thin membrane then followed by a deposition of a metal film on it. Now the most used technique is to use a micromechanical apparatus to bring the two electrodes in contact, the sample to be studied is one of the electrodes, and the other is a electrochemically or mechanically sharpened metallic tip, which is gently pressed against the sample surface. This technique is called "needle-anvil"[124] and it is shown in figure 4.5(a). Typically, the tip has an ending diameter of some tens of micrometers and it is easily deformed during the contact[130]. Thus it is very likely to form parallel contacts between sample and tip[131]. In general this is not detrimental to spectroscopy, unless the sample is highly inhomogeneous on a length scale comparable with the tip end. The needle-anvil technique has several advantages: i) it is non-destructive and several measurements can be carried out in the same samples; ii) the resistance of the contact can be controlled to some extent by fine tuning of the pressure applied by the tip. Its main drawbacks are the poor thermal and mechanical stability of the junction and if the sample is very small (tens of micrometers, as it can happen with single crystals), the whole procedure becomes extremely difficult[124].

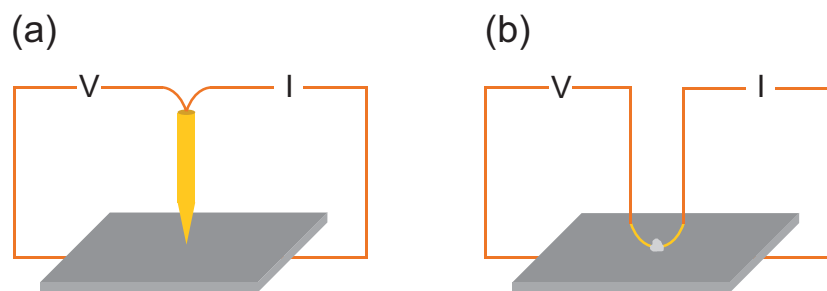


Figure 4.5: (a) Experimental arrangement for point-contact measurements with the typical needle-anvil technique. A metallic tip (Au, Pt-Ir, Pt, Ag) is gently pressed against the surface of the sample. (b) The soft point-contact technique where a tiny spot of Ag paste (or a tiny flake of In) replaces the tip.

For these reasons, a so-called "soft" point-contact technique is also often used, in which the contact is made between the clean sample surface and a small drop (about  $80 \mu\text{m}$  in diameter) of Ag paste or a small In flake[124]. The Ag or In counterelectrode is connected to current and voltage leads through a thin Au wire ( $10\text{-}25 \mu\text{m}$  in diameter) stretched over the sample, as depicted in

figure 4.5(b). Despite the large "footprint" of the counterelectrode (in particular in the case of Ag paste) if compared to the electronic mean free path, these contacts very often provide spectroscopic information. This clearly means that, on a microscopic scale, the real electrical contact occurs only here and there through parallel nanometric channels connecting the sample surface with the In flake or with individual grains in the Ag paste, whose size is  $2\text{-}10\mu\text{m}$ . With respect to the needle-anvil technique, the "soft" one does not involve any pressure applied to the sample and this can be sometimes very useful when the sample is sensitive to pressure. The resistance of the as-made contacts is usually already in the suitable range for Andreev reflection to occur. If needed, it can be tuned by applying short ( $\approx 50$  ms) voltage or current pulses until a spectroscopic contact is achieved. This effect (sometimes called "fritting") is well known in standard electrotechnics. The pulses have the effect of destroying some of the existing microjunctions and/or creating new ones by piercing a small oxide layer on the surface of either electrode. The contacts are mechanically and thermally very stable. Moreover, they can be made also on the thin side of small single crystals allowing directional point-contact spectroscopy even in samples too small for the needle-anvil technique. Often (but not always) the conductance curves of soft point contacts are more broadened than those obtained by the needle-anvil technique. This is probably related to inelastic scattering near the interface, possibly by an oxide layer on the surface of Ag grains or of the sample. As a matter of fact, the same holds for contacts made with the Au wire alone, or even with a tip, whenever the pressure applied by the tip on the sample is small[124].

After the discovery of the superconducting iron pnictides, some PCARS measurements have been carried out on this new family. However, the results along the  $c$ -axis direction of these measurements are not convincing. In most of them, the Andreev reflection signals are less than 20%, and some are even totally absent[132, 133]. This may be because the iron pnictide superconductors are very sensitive to pressure, so the "needle-anvil" technique is not suitable for the measurement on iron pnictide superconductors, and the "soft" point-contact technique would then be more appropriate.

## 4.2 Measurements on $\text{Ba}_{0.6}\text{K}_{0.4}\text{Fe}_2\text{As}_2$ single crystal

The single crystals of  $\text{Ba}_{0.6}\text{K}_{0.4}\text{Fe}_2\text{As}_2$  were grown by using FeAs as the self flux at ambient pressures. The detailed information about the synthesization is elaborated in section 2.1. The resistivity measurements were carried out on a Physical Property Measurement System (PPMS, Quantum Design). As shown in figure 4.6, the sample exhibited a sharp resistive superconducting transition at  $T_c \simeq 38.4$  K (50% of the normal state resistivity) with  $\Delta T_c < 1.5$  K. The residual resistivity is about  $\rho(38\text{K}) = 0.025\text{m}\Omega\text{cm}$  and the residual resistivity ratio is found to be  $RRR = \rho(300\text{K})/\rho(38\text{K}) = 12$ , demonstrating the good quality of the single crystal.

Typical four-terminal and lock-in techniques were used to measure the conductance-voltage ( $G - V$  with  $G = dI/dV$ ) characteristics on an Oxford cryogenic system Maglab-EXA-12. Instead of using a sharp metallic tip to press against the material under study, we used the "soft" point-contact technique[124], in which the contact is made between the fresh sample surface and a small drop of Ag paste(4929N DuPont) which is about  $80\mu\text{m}$ . The Ag counterelectrode is connected to the current and voltage leads through a thin Au wire ( $16\mu\text{m}$  in diameter) stretched over the sample. The contacts made in this way are very stable. After we cleaved the sample to get a fresh and shiny surface we made four or five contacts on each sample as soon as possible, since the  $\text{Ba}_{0.6}\text{K}_{0.4}\text{Fe}_2\text{As}_2$  material is reactive in air. We measured four pieces of  $\text{Ba}_{0.6}\text{K}_{0.4}\text{Fe}_2\text{As}_2$  single crystal from the same batch. The junction resistance varies from several Ohms to several tens of Ohms. Each measurement is comprised of two successive cycles, to check the absence of heating-hysteresis effects and the dip structures which are due to the Josephson effect[134].

Figure 4.7 shows typical  $G - V$  curves measured at various temperature on the  $\text{Ba}_{0.6}\text{K}_{0.4}\text{Fe}_2\text{As}_2$  single crystal with the point contact current preferably along the  $c$ -axis direction of the crystal. The

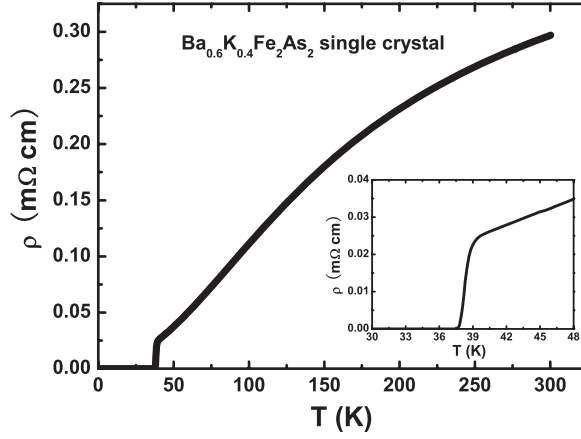


Figure 4.6: Temperature dependence of the in-plane electrical resistivity for the  $\text{Ba}_{0.6}\text{K}_{0.4}\text{Fe}_2\text{As}_2$  single crystal in zero field up to 300 K. The inset shows the expanded scale for temperatures near the superconducting transition.

prominent features are: the two peaks at temperature below 10 K, a strongly sloping background and a small conductance asymmetry, which are also observed by Lu *et al*[135]. Similar broad backgrounds and asymmetries are reported in the point-contact measurement on  $\text{SmFeAsO}_{0.8}\text{F}_{0.2}$ , where the sloping background is claimed to disappear around the Neel temperature (about 140 K) of the parent compound[136]. The temperature dependence shown in figure 4.7 verifies that the low-bias conductance enhancement is due to Andreev reflection. Although the junction resistance changes slightly with temperature, the Andreev reflection signal disappears only above the bulk  $T_c$ , giving confidence that we probe the bulk gap. The sloping background survives above  $T_c$ , so it doesn't originate from superconductivity, and must due to some other inelastic scattering mechanism, such as magnetic fluctuations etc[137, 138].

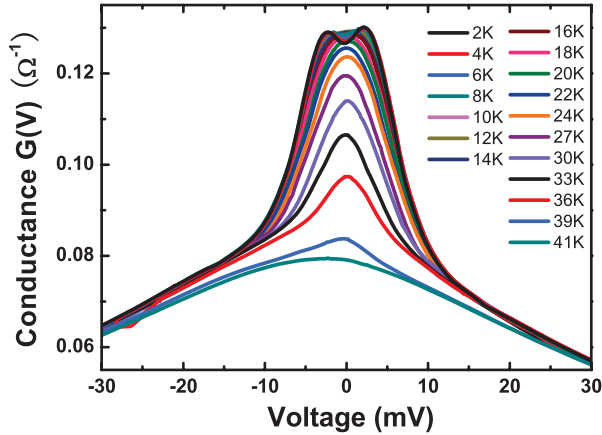


Figure 4.7: Temperature dependence of the conductance curves  $G(V)$  for the point-contact junction along the  $c$ -axis direction(the junction resistance slightly changes with temperature due to instability of the contact).

In order to compare the experimental curves to a suitable model, all the raw conductance curves at temperature below  $T_c$  were normalized by the normal-state curves at 41 K. Figure 4.8 shows the normalized conductance at 2 K, the Andreev reflection signal is about 65%, which is much higher than some PCARS results reported before[139, 133]. Another important feature of the spectra is that there is not any clear two-gap character in the results of our measurements. This observa-

tion is consistent with previous scanning tunneling microscope (STM) results [140, 141] and PCAR study [135, 132]. Within a double-gap picture, a possible explanation is that the values of the two gaps are too close to each other, and thus higher resolution methods are required to distinguish them. Or as Lu *et al* [135] proposed, according to the band structure calculations, the  $\alpha$ ,  $\gamma$  and  $\delta$  bands are highly two dimensional with cylindrical shapes, but the  $\beta$  band is strongly three dimensional due to the  $d_{3z^2-r^2}$  component [142]. Because the Fermi velocity on the  $\alpha$ ,  $\gamma$  and  $\delta$  bands is mostly in the  $ab$  plane and perpendicular to the  $c$ -axis, these bands contribute a relatively small spectral weight for current flowing along the  $c$ -axis. Maybe this is the reason why it is easy to observe two gaps in the  $ab$  plane but not along the  $c$ -axis [135, 139, 133, 143].

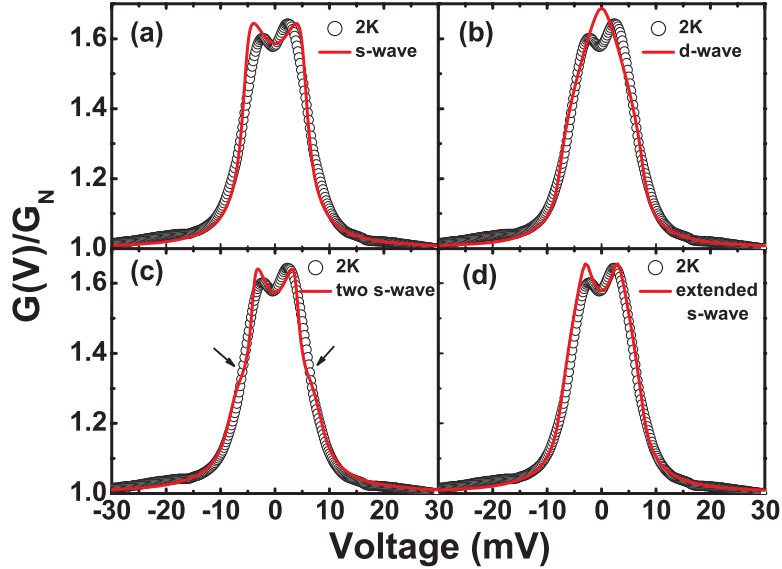


Figure 4.8: The open circles are the normalized conductance curve of 2 K. The solid lines are the fits to the extended BTK model with different gap functions. (a)  $s$ -wave, (b)  $d$ -wave, (c) two  $s$ -waves and (d) extended  $s$ -wave.

As shown in figure 4.8, we fitted the normalized conductance of 2 K to the extended BTK model with different gap functions: (a)  $s$ -wave ( $\Delta = \Delta_0$ ), (b)  $d$ -wave [ $\Delta = \Delta_0 \cos(2\theta)$ ], (c) two  $s$ -waves and (d) extended  $s$ -wave [ $\Delta = \Delta_0 + \Delta_1 \cos(2\theta)$ ]. Figure 4.8 (a) and (b) clearly show that a single  $s$ -wave or  $d$ -wave is unsuited to reproduce the experimental data. For the two gap  $s$ -wave model, the normalized conductance is the weighed sum of two BTK terms:  $G(V) = xG_1(V) + (1-x)G_2(V)$ , where  $x$  is the weight of gap 1's contribution. From figure 4.8 (c) one can see an obvious kink in the fitting curve at about  $\pm 5$  mV (indicated by arrows), but there is not this kind of feature in the experimental data curve. In the extended  $s$ -wave case, the fitting reproduces the experimental data well. Recently, Voronstov and Vekhter proposed an nearly isotropic gap  $\Delta_h(\phi) = \Delta_1$  on the hole Fermi surface and an anisotropic gap  $\Delta_e(\phi) = \Delta_2[(1-r) \mp r \sin(2\phi)]$  on the electron Fermi surface [144]. When  $r < 0.5$ , there is no node and when  $r > 0.5$ , there are nodes along  $\Gamma - M$  line. This can explain why there are nodes in some iron-pnictides and no nodes in other iron-pnictides. When the coupling of the two bands is very strong or only one band dominates the transport at the interface, the gap function is very similar to the one we used for the fitting. The fitting parameters are the two different energy gaps,  $Z$  as measure for the strength of the interface barrier and  $\Gamma$  for the spectral broadening in this formula. So the fitting processes become simpler. Comparing the four fitting results, one can see that the extended  $s$ -wave fitting is the best one. Therefore, we chose this model to fit all the normalized Andreev reflection data.

Figure 4.9 presents several representative spectra at different temperatures. All the spectra were normalized to the conductance measured at 41 K and fitted by the extend BTK model with an anisotropic gap  $\Delta = \Delta_0 + \Delta_1 \cos(2\theta)$ . In all the fits,  $Z$  remains a relatively small value about 0.23, indicating the high stability and transparency of the contact. The broadening term  $\Gamma$  is less than 0.6

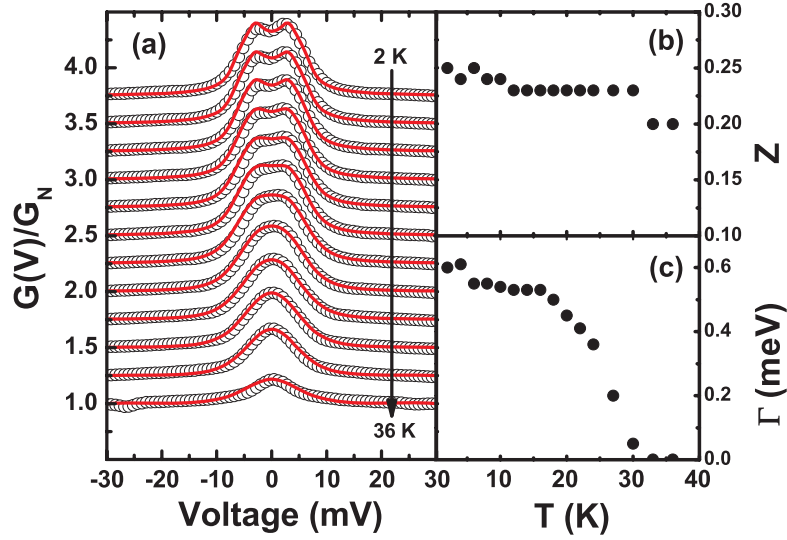


Figure 4.9: (a) Representative temperature dependence of the normalized spectra corresponding to figure 4.7. The solid lines are theoretical calculations according to the extended BTK model with an anisotropic gap  $\Delta = \Delta_0 + \Delta_1 \cos(2\theta)$ . All the curves except the bottom one are vertically offset for clarity. (b) and (c) show the temperature dependence of  $Z$  and  $\Gamma$  used in the fittings.

meV with a variation in the temperature range, which will not significantly decrease the accuracy of the established gap size. The gap values obtained in this way are:  $\Delta_0 = 5.1$  meV and  $\Delta_1 = 2.3$  meV. Then we can get the maximum of the gap is  $\Delta_{max} = 7.4$  meV and the minimum of the gap is  $\Delta_{min} = 2.8$  meV, with an anisotropic ratio  $\gamma = \Delta_{max}/\Delta_{min} = 2.7$ . The values of  $\Delta_{min}$  and  $\Delta_{max}$  are comparable to the results from STM experiments on the same samples[145].

### 4.3 Measurements on $\text{BaFe}_{2-x}\text{Ni}_x\text{As}_2$ single crystals

After we got a series of  $\text{BaFe}_{2-x}\text{Ni}_x\text{As}_2$  single crystals from Huiqian Luo, we also did point contact spectroscopy measurements on these samples. The single crystals of  $\text{BaFe}_{2-x}\text{Ni}_x\text{As}_2$  were grown from an FeAs/NiAs self-flux method, as described elsewhere[68]. The crystals were characterized using x-ray diffraction and energy dispersion (EDX). The doping levels in the crystals were determined by inductive coupled plasma emission spectrometer (ICP), which gave a Ni concentration roughly 0.8 times the nominal content  $x$ . We chose five compositions to do the measurements: underdoped, with  $x=0.075$  (UD13), 0.085 (UD17); overdoped, with  $x=0.12$  (OD18), 0.15 (OD14), and optimally doped with  $x = 0.1$  (OP20). The temperature dependence of resistivity for these five compositions under investigation is displayed in the inset of figure 4.10, by which the bulk transition temperature  $T_c$  is determined (95% of the normal state resistivity) for each composition:  $T_c = 13.2\text{K}$ , 16.9K, 20.1K, 19K, and 14.1K for UD13, UD17, OP20, OD18 and OD14, respectively. Consequently, the  $T_c$  value for each composition is shown on the phase diagram in the main panel of figure 4.10. For a comparison of the impurity level of these five samples, the residue resistance ratio [ $RRR = \rho(300\text{K})/\rho(0)$ ] are: 1.8 (UD13), 1.8 (UD17), 2.1 (OP20), 2.2 (OD18) and 2.4 (OD14). The typical level of impurity phases has been checked by specific heat measurement on the optimally doped crystal  $x = 0.1$ , in which a residual component  $\gamma_0$  at  $T \rightarrow 0$  revealed an impurity phases of  $\sim 5\%$  [146]. The way we made point contacts is the same as the  $\text{Ba}_{0.6}\text{K}_{0.4}\text{Fe}_2\text{As}_2$  samples.

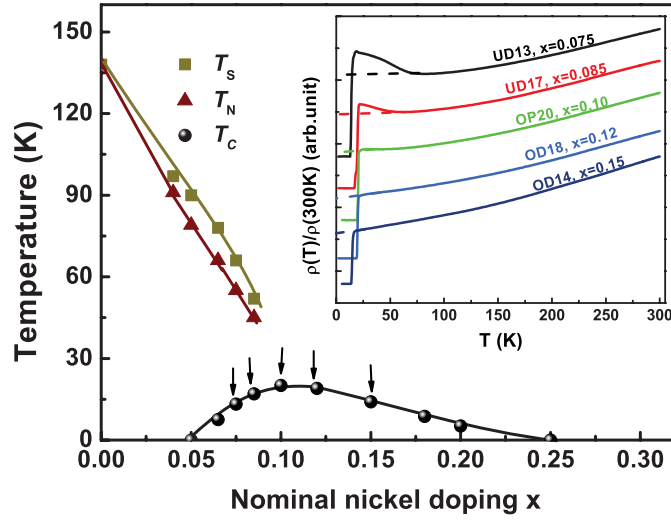


Figure 4.10: Phase diagram of  $\text{BaFe}_{2-x}\text{Ni}_x\text{As}_2$  as a function of Ni concentration  $x$ . The orthorhombic phase below  $T_s$  and the antiferromagnetic (AF) phase below  $T_N$  are also shown here. The arrows indicate the doping levels of the samples under investigation. Inset: Temperature dependence of the in-plane resistivity  $\rho$  for samples with the Ni nominal doping level  $x$  as labeled. Data are vertically shifted for clarity.

### 4.3.1 Optimally-doped $\text{BaFe}_{1.9}\text{Ni}_{0.1}\text{As}_2$

Figure 4.11(a) and (b) show the raw conductance curves  $G(V) = dI(V)/dV$  of two  $c$ -axis Ag/ $\text{BaFe}_{1.9}\text{Ni}_{0.1}\text{As}_2$  point contacts (OP20a and OP20b), respectively. The contacts made in the soft way remain stable in thermal cycling, and the contact resistance at high bias  $R_N$  varies very little ( $< 6\%$ ) over the whole  $T$  range up to  $T_c$ . The Andreev signal as the conductance enhancement decreases on increasing  $T$  and vanishes at  $T \geq T_c$ , leaving a slightly asymmetrical  $V$ -shaped normal state. Shown in the main panels of figure 4.11(a) and (b), the magnitude of the Andreev reflection reaches as high as 30%-40%, implying a relatively transparent boundary between the Ag nanoparticles and  $\text{BaFe}_{2-x}\text{Ni}_x\text{As}_2$  superconductors. The stabilities in  $R_N$  and the high level of Andreev signal indicate that the conduction channels through the contact is in ballistic regime, and therefore, energy-resolved spectroscopy is possible.

A feature shows up in these conductance curves: an additional peak at  $\sim 25$  mV, and the peak gradually disappears with  $T$  approaching  $T_c$ , as marked by the arrows in figure 4.11. It seems that this peak is much pronounced when the Andreev signal is relatively low, which is close to the case of tunneling side (see below). This conductance peak at the edge of the gap has been observed in Co-122 crystals [143], and is attributed to the signature of an electron-boson coupling associated with superconductivity. The observation of the electron-boson coupling mode in the conductance spectra implies the high quality of the point-contacts and thus their spectroscopic nature.

A close inspection to the main-gap conductance spectrum reveals a “kink” structure around 7 mV, as marked by the dashed line in figure 4.12(a) (OP20a) and (b) (OP20b). We ascribe the “kink” to the manifestation of the two-gap superconductivity of the iron pnictide superconductors. To explicitly describe the variety of spectral behavior observed and quantitatively resolve the gap amplitude, we invoke a generalized 3D BTK formula [123] developed by Tanaka and Kashiwaya [127, 147] with three parameters: a dimensionless parameter  $Z$  which represents the interface transparency; an imaginary quasiparticle energy modification  $\Gamma$  [125] which reflects the spectral broadening, and the superconducting gap  $\Delta$ . In this generalized 3D BTK model,

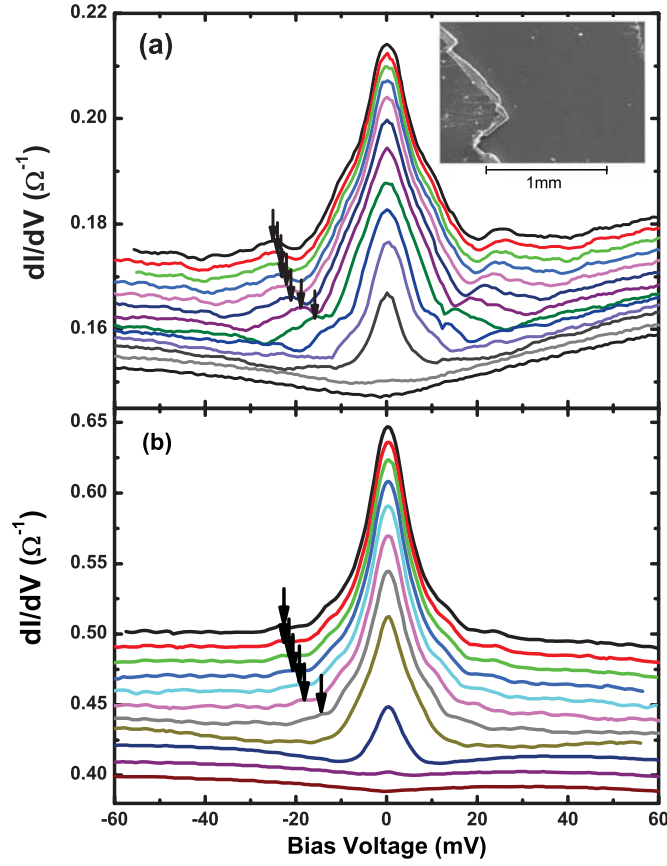


Figure 4.11: (a) The raw data of conductance spectra at various temperatures for  $c$ -axis Ag/BaFe<sub>1.9</sub>Ni<sub>0.1</sub>As<sub>2</sub> point-contact (OP20a). The temperatures at which the conductance curves are taken are from the top to the bottom: 2, 4, 6, 8, 10, 12, 14, 16, 17, 18, 19, 20 and 21 K. Data are vertically shifted downwards for clarity except for the top curves (2 K). The black arrows indicate the additional conductance peak at the edge of the gap. Inset: the typical cleaved crystal surface on which the point contact has been made. (b) The raw data of conductance curves  $G(V)$  as a function of temperature for another  $c$ -axis contact OP20b. The temperature is from 2 K to 22 K in a step of 2K. Data are vertically downward-shifted for clarity. The arrows mark the corresponding edge-gap conductance peaks in the raw  $G(V)$  curves.

$$\frac{dI}{dV} = \frac{\int_0^{2\pi} d\phi \int_0^{\pi/2} d\theta \int_{-\infty}^{\infty} dE \frac{df(E-eV)}{dV} \sigma_s(E, \phi) \sin(2\theta)}{\int_0^{2\pi} d\phi \int_0^{\pi/2} d\theta \sigma_N \sin(2\theta)} \quad (4.6)$$

where  $\sigma_s(E, \phi) = [1 + |\Lambda|^2 + Z^2(1 - |\Lambda|^4)] / |1 + Z^2(1 - |\Lambda|^2)|^2$ ,  $\Lambda = [(E - i\Gamma) - \sqrt{(E - i\Gamma)^2 - |\Delta|^2}] / |\Delta|$ ,  $\sigma_N = 1 / (1 + Z^2)$ , and  $Z = Z_{eff} / (\cos \theta)$ . To choose a gap function to calculate these two-gap conductance spectra, we assume, based on the  $\pm$  scenario, an isotropic gap  $\Delta_h$  and an anisotropic gap of the general form:

$$\Delta_M = \Delta_e [1 - r + r \cos(2\theta)] \quad (4.7)$$

with the gap anisotropy ratio  $r$  varying from  $r = 0$  (isotropic  $\pm$  state) to  $r = 1$  (completely  $d$ -wave) [148, 149, 150, 144, 151]. Therefore, by the standard two component conductance (current) model the conductance spectra is the total contributions of the hole-like ( $G_h$ ) and electron-like ( $G_e$ ) Fermi pockets:  $G = wG_h + (1 - w)G_e$ , where  $w$  is the spectral weight. For simplicity, we assume a balanced contribution of hole and electron Fermi surfaces to the spectral conductance by taking  $w = 0.5$ .

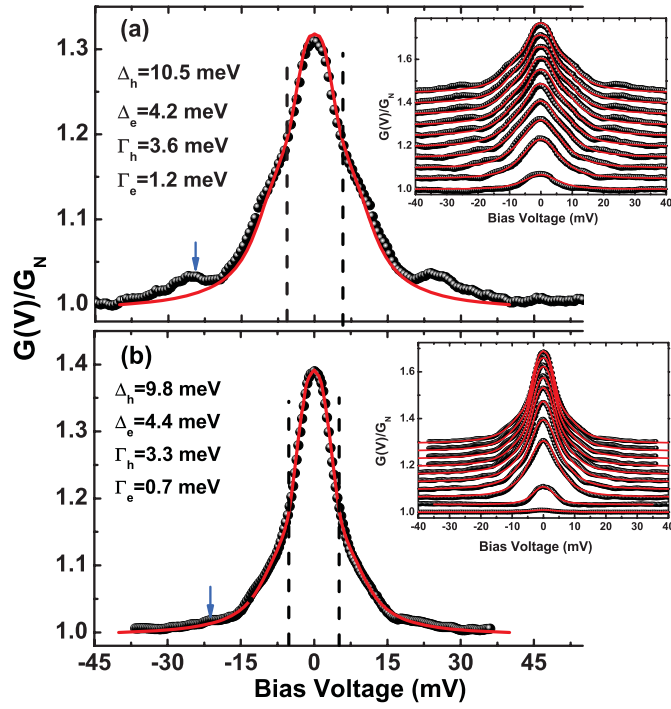


Figure 4.12: The normalized conductance spectrum  $G(V)/G_N$  at  $T = 2$  K with  $G_N$  the conductance spectrum of normal state background for (a)OP20a and (b)OP20b. The red lines are their two-gap BTK fits [equation 4.6] with the relevant fitting parameters, respectively. The blue arrows display the additional conductance peaks defined as underlying energy scales at the edge-gap, and the dashed lines mark the “kink” structures in the main-gap  $G(V)$  curves. Insets: the normalized conductance spectra of corresponding point contacts at various  $T$ s indicated as in figure 4.11. The red solid lines corresponds to their BTK fitting, respectively, see text.

Examples of normalized  $G(V)$  curves and their fits at  $T = 2$  K are shown in the main panels of figure 4.12(a) and (b) for junctions OP20a and OP20b, respectively. The two-gap BTK model (red lines) fit very well the main features of the experimental  $G(V)$  curves except the electron-boson coupling mode around 25 meV, yielding a set of fitting parameters associated with gap magnitude and anisotropy ratio:  $\Delta_h = 10.5$  meV,  $\Delta_e = 4.2$ , and  $r = 0.3$  for OP20a and  $\Delta_h = 9.5$  meV,  $\Delta_e = 4.5$  meV, and  $r = 0.3$  for OP20b, respectively. It is noted that the same gap magnitude is also extracted from a PCAR experiment on a  $c$ -axis Ag/BaFe<sub>1.8</sub>Co<sub>0.2</sub>As<sub>2</sub> with the comparable  $T_c = 24$  K [143].

With these fitting parameters, we check the validity of these fits by applying the fit with these fixed parameter values to the spectra at all temperatures. As shown in the inset of figure 4.12(a) and (b), the two-gap  $\pm$  model still fits reasonably well the  $T$ -dependence of these  $G(V)$  curves with fitted gap magnitude. In this overall- $T$  spectral fitting,  $r = 0.3$  and  $Z_h = 0.31$ ,  $Z_e = 0.2$  are kept constant while  $\Gamma_h$  and  $\Gamma_e$  slightly increase with  $T$ , as shown in figure 4.13 (a) (OP20a) and (b) (OP20b). The stability of the conductance spectrum in the increase of  $T$ , consequently the fitting parameters makes the  $T$ -dependent gaps  $\Delta_h(T)$  and  $\Delta_e(T)$  reliable. As shown in figure 4.13 (c) and (d), we plot the fitted gap  $\Delta_h$  and  $\Delta_e$  as a function of  $T$  for these two junctions, respectively. The obtained gaps can be approximated by an empirical BCS gap formula:  $\Delta(T) = \Delta_0 \tanh(\alpha \sqrt{T_c/T - 1})$  with  $\alpha = 1.95$  for  $\Delta_h$  and 1.86 for  $\Delta_e$  (cf.  $\alpha = 1.74$  for weak-coupling BCS gap).

We analyze now the physical meaning of the obtained gap values and gap function. It is shown from angle-resolved photoemission spectroscopy (ARPES) experiment on a Co-122 crystal that the large gap  $\Delta_h$  is located on the hole FS sheet, instead, the small gap  $\Delta_e$  is presented on one of the electron FS sheets [152]. The obtained anisotropy ratio  $r = 0.3$ , resolved in our  $c$ -axis PCAR spectroscopy of

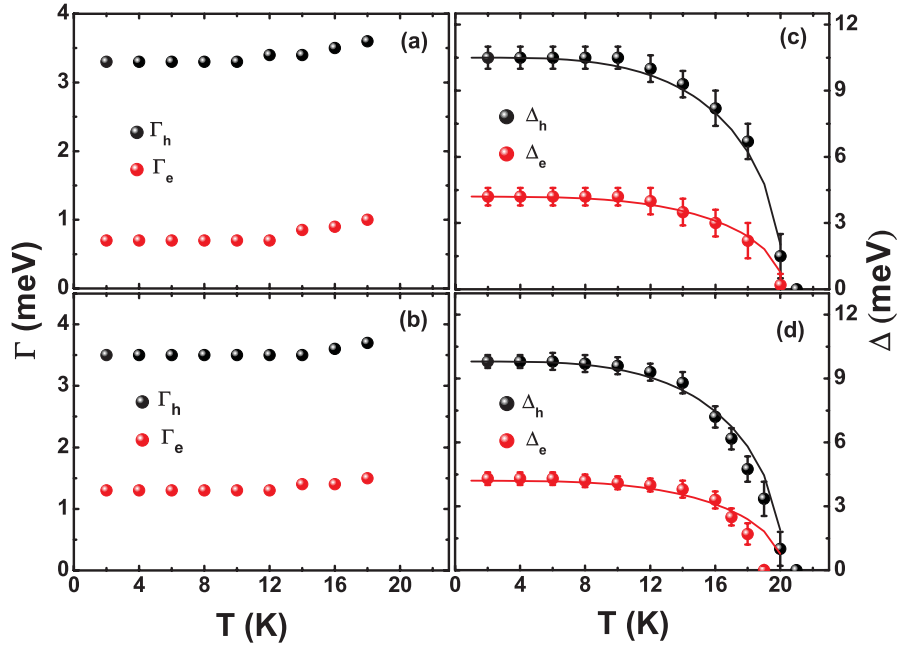


Figure 4.13: The superconducting gaps  $\Delta$  (a) and energy broadening factors  $\Gamma$  (b) obtained as the fitting parameters as a function of  $T$  for OP20a and for OP20b (c)(d), respectively. The solid lines in (c) and (d) are the fits to an empirical gap function, see text.

$\text{BaFe}_{1.9}\text{Ni}_{0.1}\text{As}_2$ , indicates a full gap state with gap minima located on the electron FS sheets along  $c$  axis. This nodeless state of optimally doped Ni-122 is in similarity with that of optimally-doped Co-122, in which a gap minima is already present at maximal  $T_c$  by the  $c$ -axis thermal conductivity measurements [153, 154]. The gap ratios  $2\Delta_h/k_B T_c \approx 11.6$  and  $2\Delta_e/k_B T_c \approx 5.0$ , both above the BCS weak-coupling ratio of 3.5. Besides, the  $\alpha$  value from the  $\Delta(T)$  function also points to a strong-coupling character for both  $\Delta_h$  (hole FS) and  $\Delta_e$  (outer electron FS). These gap ratios distinctly disagree with that of a two-band weak-coupling  $\gamma$  model in which a rule for the two superconducting gap limit is predicted [155] as  $\Delta_1 < \Delta_{BCS}$  and  $\Delta_2 > \Delta_{BCS}$ , as observed in the standard two-gap superconductor,  $\text{MgB}_2$  [156]. However, our results are consistent with a three-band  $s\pm$  Eliashberg model [157, 158], in which spin fluctuations mainly provide the interband coupling, and thus so in the electron-boson coupling matrix. Further, the existence of strong electron-boson coupling in this compound is manifested by the observation of the additional spectral peak  $E_p$  at about 25 meV. In figure 4.14 we plot  $E_p$  marked in figure 4.11 as a function of  $T$ . In our low-transparency ( $Z = 0.3$  for OP20a) point contact, a characteristic energy of  $\Omega_b = E_p - \Delta_{max} = 13$  meV and 11 meV (OP20b junction with  $Z = 0.2$ , displayed in the inset of figure 4.14). This energy scale is compatible with the spin-resonance energy observed by neutron scattering on the same crystals [159]. Thus our results that the two gaps are in the strong-coupling limit and the identification of the spin resonance energy strongly support the pairing interaction mediated by the antiferromagnetic spin fluctuations.

### 4.3.2 Underdoped $\text{BaFe}_{2-x}\text{Ni}_x\text{As}_2$

It is natural, to study the evolution of the superconducting gaps in crystals as function of doping. We have measured the point-contact  $G(V)$  curves in whole  $T$  range up to  $T_c$  for underdoped and overdoped crystals. Figure 4.15 shows the normalized conductance spectra  $G(V)$  of Ag/ $\text{BaFe}_{1.925}\text{Ni}_{0.075}\text{As}_2$  (UD13) point contact at various temperatures up to  $T_c$ , together in the inset with the typical  $G(V)$  curves of Ag/ $\text{BaFe}_{1.915}\text{Ni}_{0.085}\text{As}_2$  (UD17) point contact for demonstrating the spectroscopic nature for underdoped samples. As shown, some underlying conductance anomalies are observed as the conductance dips at the edge of the main-gap. These dip anomalies in  $G(V)$  is

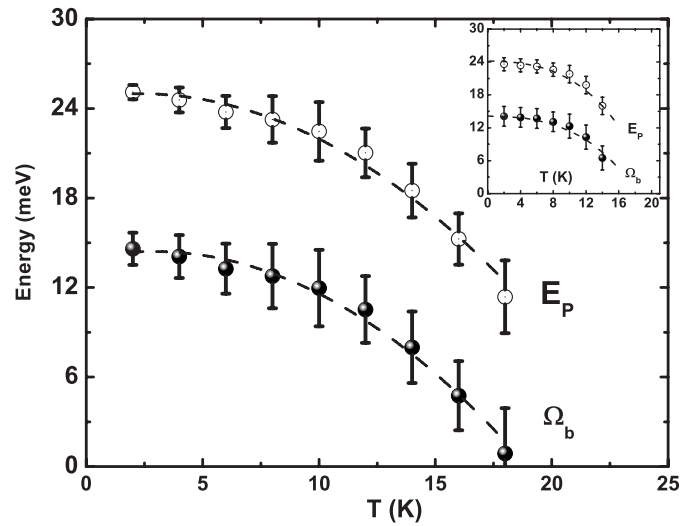


Figure 4.14: The temperature dependence of the energy scales of the peak  $E_p$  and the corresponding characteristic boson energy  $\Omega_b$  for OP20a. The dashed lines are the guides to the eye. Inset: The energy scales of the peak  $E_p$  and the corresponding characteristic boson energy  $\Omega_b$  for OP20b as a function of  $T$ . The dashed lines are the guides to the eye.

typical in S/N AR spectral curves, either in tip-sample or planar junction configurations for high- $T_c$  cuprates [160] and low- $T_c$  conventional superconductors [134]. On the other hand, except these dip anomalies, these  $G(V)$  curves exhibit a *dominant* single gap with a similar Andreev signal of 25%-30% at low temperatures for each contact. The single-gap feature of iron pnictide superconductors in point contact/STM experiments has been widely observed [55, 139, 140]. Within a double-gap picture, as mentioned by Zhang et al. for K-122 [55] and discussed above for optimally-doped Ni-122 superconductors, a possible explanation is that the two gaps are too close, and thus coupled to each other. Alternatively, for PCAR of a multiple band superconductor, if the corresponding spectral weight of a gap is intrinsically small as discussed by Golubov et al. [161], or/and if one type of carriers dominates the transport at the interface, it would be possible that some multi-gap feature is smeared out and only a single robust gap is present in AR/tunneling spectra within the resolution of the measurements.

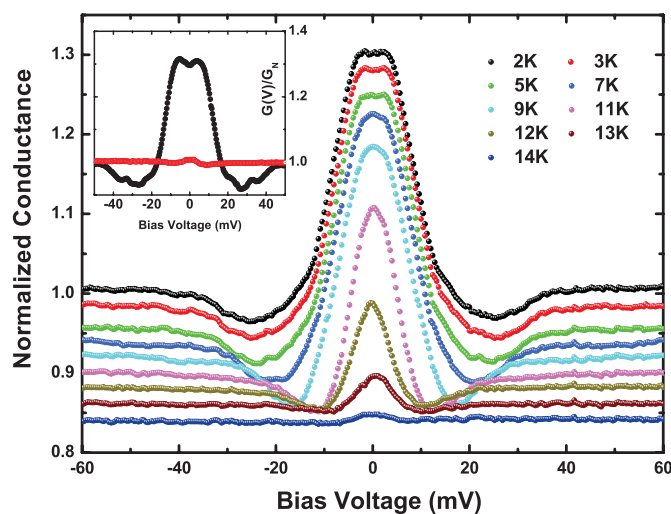


Figure 4.15: The normalized conductance spectra  $G(V)$  for UD13 at various temperatures. Insets: The normalized conductance curves of UD17 at  $T = 2$  and 17 K selected to show the spectroscopic nature of underdoped samples.

A feature of an in-gap conductance plateau and/or double peaks in these normalized  $G(V)$  curves is observed at low temperatures ( $< 5$  K). According to BTK formalism for stimulating the process of Andreev reflection in *high transparency limit*, a conductance plateau and/or a double peak around zero bias is a signature of a fully gapped state for superconducting electrode. To describe these featured  $G(V)$  curves by quantitative analysis, we use equation 4.6 in our calculation with a single  $s$ -wave gap which corresponds to the case of  $r = 0$  in equation 4.7. The best fit to the conductance spectrum at  $T = 2$  K is displayed in figure 4.16, yielding a gap value of 6.3 meV, S/N transparency  $Z = 0.5$  and energy broadening factor  $\Gamma = 3.0$  meV. As can be seen, the generalized BTK model with single isotropic gap fits the measured low bias conductance spectrum rather well, except the conductance anomaly at the edge of the gap. With these parameters ( $\Delta$ ,  $\Gamma$ ,  $Z$ ), the  $G(V)$  curves at various  $T$  presented in figure 4.15 also can be fitted, yielding  $\Delta$ ,  $\Gamma$ ,  $Z$  as functions of  $T$ . In these fitting, the transparency parameter  $Z$  is kept a constant of  $0.49 \pm 0.2$ , similar to the case of OP20 discussed above.  $\Gamma$  slightly increases from 3.0 meV to 3.4 meV with  $T$  increasing from 2 K to 14 K. The effective gap,  $\Delta$ , is obtained as a function of  $T$  and plotted in the inset of figure 4.16.

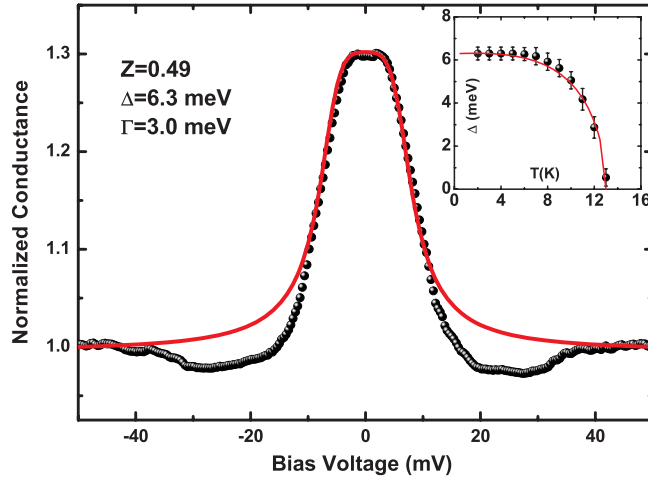


Figure 4.16: The normalized conductance curves at  $T = 2$  K and its fit using equation 4.6 with single  $s$ -wave gap for UD13. Insets: The corresponding gap as a function of  $T$  by fitting the temperature dependent conductance spectra shown in figure 4.15. The red solid line is the fit to the BCS gap function with  $\alpha = 1.82$ .

### 4.3.3 Overdoped $\text{BaFe}_{2-x}\text{Ni}_x\text{As}_2$

The conductance spectra  $G(V)$  of heavily overdoped contact  $\text{Ag}/\text{BaFe}_{1.85}\text{Ni}_{0.15}\text{As}_2$  (OD14) at various temperatures were measured and presented in figure 4.17. For a further demonstration, the conductance curves of another overdoped contact  $\text{Ag}/\text{BaFe}_{1.88}\text{Ni}_{0.12}\text{As}_2$  (OD17) are also displayed in the inset of figure 4.17 at  $T = 2$  K and 17 K. As compared with those of underdoped contacts, all these  $G(V)$  curves (including those of OD17) exhibit a consistent behavior: 1) an underlying feature of a distinguishing single gap is unambiguously identified with a similar Andreev signal as the conductance enhancements of 25%-35% at the low  $T$  limit of 2 K in our experiment; 2) at low temperatures ( $T < 5$  K) a low-bias conductance peak is present in the conductance spectrum, in contrast to the in-gap conductance plateau in the case of the underdoped contacts (figure 4.15).

Considering the overall spectral consistency in these contacts, the systematic evolution of the Andreev conductance spectra with doping concentration is nontrivial. In a generalized BTK theory developed by Tanaka et al. [127, 147], a low-bias conductance peak for *highly transparent junction at finite  $T$*  is a characteristic of an anisotropic gap state due to the presence of a finite DOS at low energy, like a  $d$ -wave gap in cuprates [160]. Quantitatively, we use equation 4.6 in simulating these peaked conductance spectra with a single  $d$ -wave gap which corresponds to the case of  $r = 1$  in

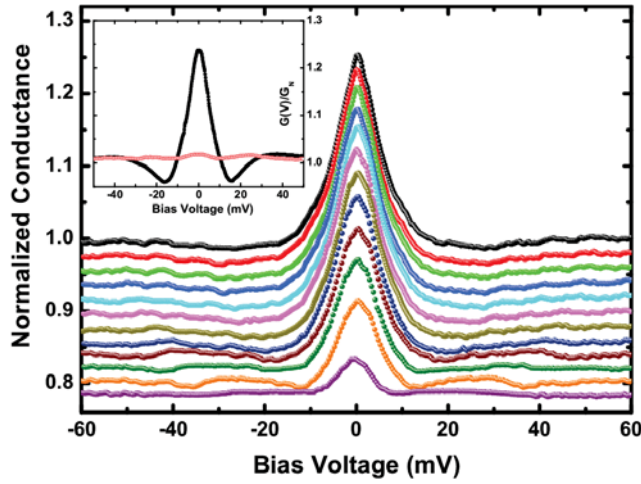


Figure 4.17: The normalized conductance spectra  $G(V)$  for OD14 at temperatures from 2 K to 13 K with a step of 1 K. Insets: The normalized conductance curves of OD18 at  $T = 2$  and 18 K selected to show the spectroscopic nature of overdoped samples.

equation 4.7. In figure 4.18 demonstrates the best fit to the conductance spectrum at  $T = 2$  K for heavily overdoped OD14, yielding an effective gap value of 5.1 meV, S/N transparency  $Z = 0.2$  and energy broadening factor  $\Gamma = 1.8$  meV.

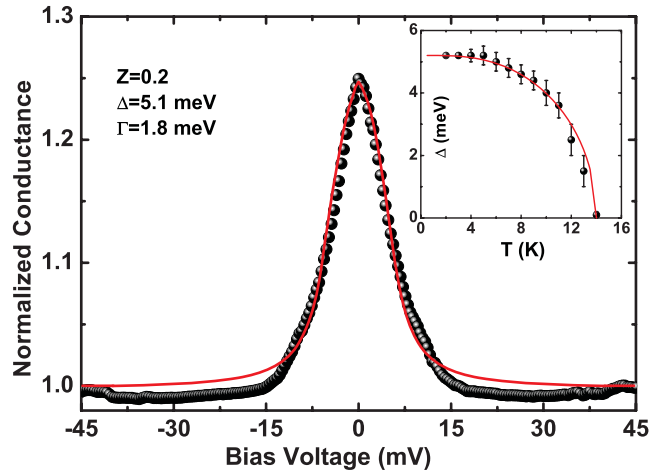


Figure 4.18: The normalized conductance curves at  $T = 2$  K and its fits using equation 4.6 with single  $d$ -wave gap for OD14. Insets: The corresponding gap as a function of  $T$  by fitting the temperature dependent conductance spectra shown in figure 4.17. The red solid line is the fit to the BCS-like gap function with  $\alpha = 1.78$

With Ni dopant increasing, the observation that the systematic evolution from the in-gap conductance plateau for the underdoped samples to the in-gap peak in  $G(V)$  curves for the overdoped samples indicates the existence of doping induced evolution of superconducting gaps with an isotropic feature ( $r = 0$ ) in the underdoped region to an anisotropic, even, nodal gap with  $r = 1$  in the heavily overdoped side. Naively, the evolution of the conductance spectra with the Ni dopant concentration may be attributed to extrinsic/intrinsic surface/boundary scattering, since Ni substitution in Ni-122 system acts not only as the source of electron dopant, but also as magnetic scatterer in superconducting FeAs-plane [162], exactly as the role of Co dopant in Co-122 system [163, 164, 165]. However, we argue that it is not the case for our  $c$ -axis Ag/BaFe<sub>2-x</sub>Ni<sub>x</sub>As<sub>2</sub> PCAR measurements. As a comparison for the level of impurity scattering, the RRR for our five samples are almost the same, shown in the inset of figure 4.10. It is hard to accept that the surface/boundary scattering with the same

level of bulk impurity can dramatically change the AR process, leading to a *systematic* evolution of AR spectroscopy with doping concentration.

Very recently several theoretical calculations have been put forward to seek the possibility of the evolution of symmetry and structure of the superconducting gap in Fe-based superconductors with doping and interactions [166]. As a matter of fact, ARPES experiments has shown that for electron-doped 122 superconductors, Ni(Co)-doping has induced electrons into this system, and thus resulted in a shrinkage of the hole pocket around  $\Gamma$  point and an enhancement of the electron pocket around  $M$  point [167]. This strongly modifies Fermi surface topology, and thus lead to a modulation of 3D superconducting gap function with chemical potential. This is highly consistent with the result of the low-temperature specific heat measurements in a series of Co-122 superconductors, in which a  $T^2$  term in the specific heat data is present in the overdoped sample, but absent both in the underdoped and optimal doped samples, and the field-induced electronic specific heat coefficient  $\gamma(H)$  increases more quickly with the field for the overdoped sample than the underdoped and optimal doped ones, indicating a strong doping dependent superconducting gap in the Co-122 system[168].

## 4.4 Summary

In summary, we studied the point-contact Andreev reflection spectroscopy of the  $\text{Ba}_{0.6}\text{K}_{0.4}\text{Fe}_2\text{As}_2$  single crystal with  $T_c=38.4$  K. The studies were performed with a soft contact method along the  $c$ -axis direction of the single crystals. By fitting the normalized conductance curves with different gap function according to the BTK model, we find an extended  $s$ -wave with a gap function  $\Delta = \Delta_0 + \Delta_1 \cos(2\theta)$  can reproduce the experimental data well. Then we obtained the maximum of the gap is  $\Delta_{max} = 7.4$  meV and the minimum of the gap is  $\Delta_{min} = 2.8$  meV, with an anisotropic ratio  $\gamma = \Delta_{max}/\Delta_{min} = 2.7$ . These results are comparable to the results from STM experiments on the same samples[145].

Then we also did point-contact Andreev reflection spectroscopy measurements on systematically doped  $\text{BaFe}_{2-x}\text{Ni}_x\text{As}_2$  single crystals, which illustrated an interesting evolution of the gap structure. The Andreev conductance spectra clearly show a full-gap state for underdoped crystals and a highly anisotropic, perhaps nodal-like gap state for overdoped crystals. Quantitative analysis of the spectral data of optimally-doped contacts using a generalized BTK formalism resolves two superconducting gaps in strong coupling limit. As a result from the analytical fitting, the small gap on the electron-like FS sheets shows a crossover from a nodeless in the underdoped side to a nodal feature in the overdoped region. This result provides evidence of the modulation of the gap amplitude on the FS with doping concentration, consistent with the calculation for the orbital dependent pair interaction mediated by the antiferromagnetic spin fluctuations.

# 5

## Scanning nano-SQUID microscopy

SQUID (for Superconducting Quantum Interference Device) is a very sensitive magnetometer, essentially made of a superconducting loop containing Josephson junctions. The SQUID is a detector of magnetic flux, based on the quantization of flux in a superconducting loop. It is sensitive enough to measure magnetic fields as low as  $5 \times 10^{-18}$  T. A Scanning SQUID microscope is a sensitive near-field imaging tool for the measurement of the distribution of weak magnetic fields at the surface. The microscope can map out buried current-carrying wires by measuring the magnetic fields produced by the currents, or can be used to image fields produced by magnetic materials. For superconductivity research, scanning SQUID microscope is used to image vortices in superconductors, from which one can get information about the penetration depth, pairing symmetry and flux dynamics of the superconductors. In this chapter, I will introduce how our scanning nano-SQUID microscope works, then I will present some results of scanning nano-SQUID microscopy measurements on Rhenium film.

### 5.1 Introduction

---

Studying the spatial variation of magnetic fields is a field with a relatively long history. Due to the special magnetic properties of superconductors, a lot of experimental techniques have been developed for the research on superconductivity, such as Bitter decoration, magneto-optical imaging, magnetic force microscopy, scanning Hall probe microscopy, scanning SQUID microscopy and so on. Figure 5.1 shows a comparison for the magnetic and spatial resolution of different techniques. All different techniques have specific strengths and weaknesses. In the following I will highlight some of the features of the different techniques.

**Bitter decoration:** The Bitter decoration technique involves depositing ferromagnetic or superconducting particles on the sample to form patterns along magnetic field lines. It is a mature technique for establishing the positions of vortices with relatively high spatial resolution (about 80nm) for static magnetic fields, but has poor sensitivity and yields very little quantitative information about vortex structures. Furthermore it is impossible to study dynamics as the sample surface must be cleaned after each decoration before another experiment can be performed.

---

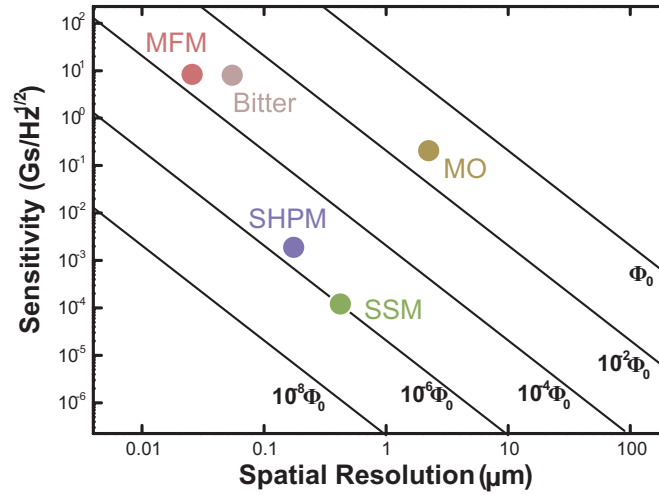


Figure 5.1: Comparison for the magnetic field sensitivity and spatial resolution of Bitter decoration, magneto-optics imaging(MO), magnetic force microscopy(MFM), scanning Hall probe microscopy(SHPM) and scanning SQUID microscopy(SSM). Data taken from [169].

**Magneto-optical imaging:** Magneto-optical imaging technique is based on the magneto-optical Faraday effect, which can be used to create magnetic contrast from a sample by covering the sample with a thin magneto-optical-active film. It is also a mature technology which has rather modest spatial resolution (about  $1\mu\text{m}$ ) and sensitivity, which are limited by the available magneto-optical materials and the need to bring them into intimate contact with the surface of the superconductor. The strength of this technique is in high-speed imaging. It is the only technique which can study vortex dynamics on sufficiently short time scales to resolve microscopic motion.

**Magnetic force microscopy:** In magnetic force microscopy, one measures the magnetic field from the magnetic force on a magnetic tip. However, the magnetic force sensed by the tip is proportional to the magnetic field gradient, not the field itself. It has not been widely used in the field of superconductivity despite its high spatial resolution (about  $50\text{nm}$ ) owing to its relatively poor sensitivity. The magnetic tip used can also be highly invasive and great experimental care must be taken during imaging.

**Scanning Hall probe microscopy:** In scanning Hall probe microscopy, a Hall probe is used as magnetic field sensor. Though the magnetic sensitivity of Hall probes is lower than the SQUID's, the size of Hall probes can be very small. Scanning Hall probe microscopy provides a unique compromise between spatial resolution (about  $200\text{nm}$ ) and sensitivity (about  $10^{-3}\text{G}/\sqrt{\text{Hz}}$ ), making it particularly well adapted for investigating vortices in superconductors.

**Scanning SQUID microscopy:** Scanning SQUID microscopy is the technique with the highest sensitivity (less than  $10^{-4}\text{G}/\sqrt{\text{Hz}}$ ), while the spatial resolution (about  $0.5\mu\text{m}$ ) is limited by current micro-fabrication capabilities. The environmental limitations for SQUIDs are they only work when they are superconducting. And they only work reliably in low magnetic field environments, because flux trapping and flux motion in the superconductor will change the SQUID properties. The scanning nano-SQUID microscope we use can work under  $100\text{G}$  and below  $300\text{mK}$ , because it is Aluminum SQUID with  $T_c \simeq 1.1\text{K}$ , and is of particular simple design taking advantage of thin width of its superconducting lines, limiting its susceptibility to flux pinning.

Figure 5.2 shows the scanning SQUID microscope we built. We use an atomic force microscope tuning fork technique to regulate the distance between the probe and sample surface. The SQUID

is made of aluminum deposited on a silicon chip and patterned by lift-off . The microscope has two motion systems: a fine motion system including a S-bender scanner and a Z piezo stack, and a coarse motion system including two attocube XY motors and a Z motor. With this two motion system, we can take image in a 4 mm × 4 mm region with a maximum scanning area of 70.0 μm × 85.0 μm. I will introduce details of the whole measurement system in the next several sections.

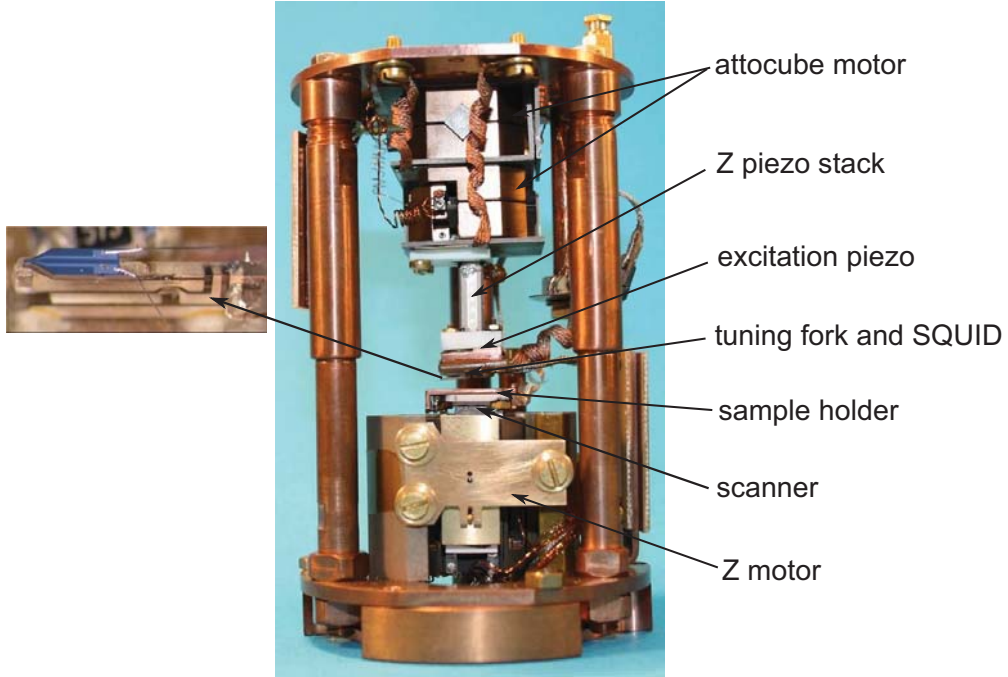


Figure 5.2: Photo of the scanning SQUID microscope we built. We use an atomic force microscope tuning fork technique to regulate the distance between the probe and sample surface. The SQUID chip is glued on the tuning fork, as shown on the left.

## 5.2 SQUID

### 5.2.1 The main principle

A dc SQUID consisting of a superconducting ring interrupted by two Josephson junctions is depicted in figure 5.3. According to the DC Josephson effect (equation 3.3),

$$I_{total} = I_1 + I_2 = I_{c1} \sin \varphi_1 + I_{c2} \sin \varphi_2 \quad (5.1)$$

with  $\varphi_1$  and  $\varphi_2$  are the phases drops across the junctions. For an inductive SQUID, the flux inside the SQUID loop is modified by its own current:

$$\Phi = \Phi_{ext} - L_1 I_1 + L_2 I_2 \quad (5.2)$$

Then using equation 1.12, we obtain

$$2n\pi = \varphi_2 - \varphi_1 + \frac{2\pi}{\Phi_0} (\Phi_{ext} - L_1 I_1 + L_2 I_2) \quad (5.3)$$

$n$  is an integer. Now we can consider the symmetric case:  $I_{c1} = I_{c2} = I_0$ ,  $L_1 = L_2 = L/2$ . Plugging this into equation 5.3 yields

$$2n\pi = \varphi_2 - \varphi_1 + f + \frac{g}{2} (\sin \varphi_2 - \sin \varphi_1) \quad (5.4)$$

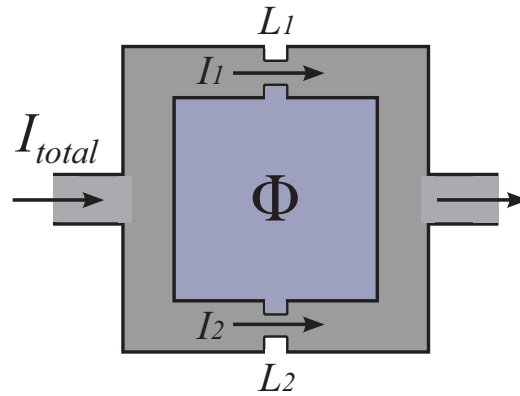


Figure 5.3: Diagram of a DC SQUID. The current  $I_{total}$  enters and splits, following to two paths, carrying currents  $I_1$  and  $I_2$ . The weak-links on each path are Josephson junctions, which separate the two superconducting regions.  $L_1$  and  $L_2$  are the inductances of the two arms of the SQUID.  $\Phi$  represents the magnetic flux threading the inside of the SQUID loop.

with  $f = 2\pi\Phi_{ext}/\Phi_0$  and  $g = 2\pi LI_0/\Phi_0$ . Plugging it into equation 5.1 and maximizing  $I$  yields the SQUID critical current  $I_c$ . The results are shown in figure 5.4. The parameter  $g$  determines the depth of the modulation of the SQUID critical current with flux: larger SQUID inductances lead to smaller modulations[170]. For the non-symmetric case, the solutions are more complicated[171], but it is qualitatively similar to those shown in figure 5.4.

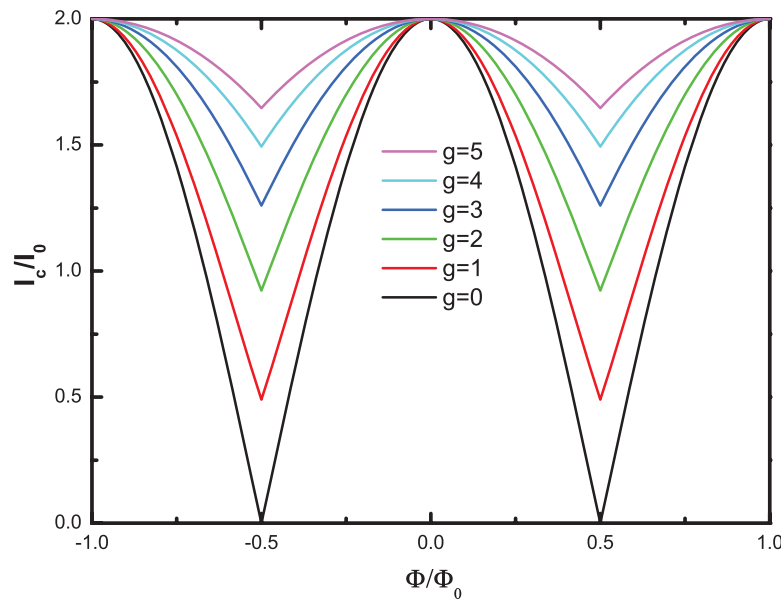


Figure 5.4: Results of the numerical calculations of the  $I_c$  over  $\Phi$  characteristics for symmetric SQUIDs, identical junctions  $I_{c1} = I_{c2} = I_0$  and  $g = 2\pi LI_{c0}/\Phi_0$ . Maximal modulation is achieved for  $g = 0$ , when neglecting the inductance of the SQUID.

### 5.2.2 Fabrication

The SQUIDs we used are fabricated by D. Mailly at LPN and T. Crozes at l'institut Néel with the lift-off method, which is illustrated in figure 5.5.

1. Spincoating with Poly methyl methacrylate(PMMA) on a silicon wafer.

2. Drawing the SQUID on the PMMA by an electron beam.
3. Removal of the exposed PMMA by development process. This results in a negative SQUID motif on the silicon.
4. Depositing a 30 to 40 nm thin aluminum film on the silicon by thermal evaporation.
5. Lifting off PMMA in acetone.

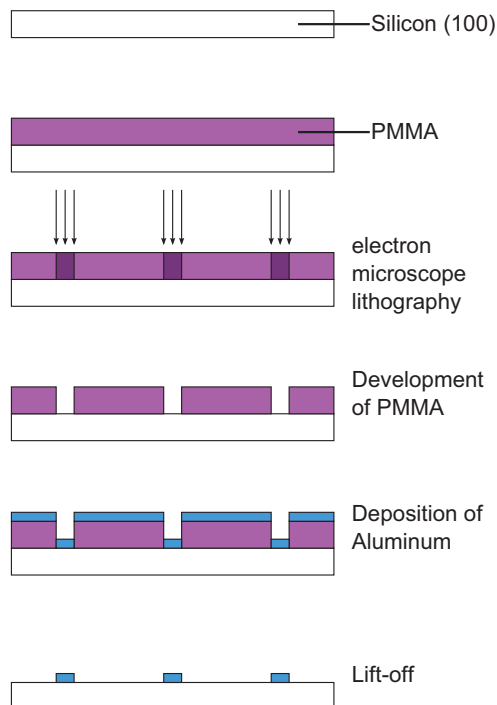


Figure 5.5: Schematics of the fabrication process. The image is taken from [4].

Usually hundreds of SQUIDs can be made on a wafer by this procedure. There are two different sizes of SQUID we used:  $1.1 \mu\text{m} \times 1.1 \mu\text{m}$  and  $0.6 \mu\text{m} \times 0.6 \mu\text{m}$ . In order to get a good resolution, we need the SQUID/sample distance to be as small as possible. Thus we hope the SQUID to be as close as possible to the border of the wafer. This is obtained by etching the wafer around the SQUID. What we used is a deep reactive ion etching, Bosch process. This technique provides good control of the SQUID position and can be used for complicated geometries. The distance between the SQUID and the tip can be smaller than  $5 \mu\text{m}$ , which allows the SQUID/sample distance smaller than  $0.5 \mu\text{m}$ .

Some electron microscope and optical photos of the SQUIDs are shown in figure 5.6. There are several different designs of the SQUIDs. The size of SQUIDs in 5 and 6 are  $1.1 \mu\text{m} \times 1.1 \mu\text{m}$ . One can see the distances between the SQUID and the tip are smaller than  $5 \mu\text{m}$ . When we align the SQUID chip to the sample surface with an angle smaller than  $5^\circ$ , the distances between the SQUID and the sample will be smaller than  $500 \text{ nm}$ .

### 5.2.3 Measurement of the critical current

What we use to measure the magnetic field is the modulation of the SQUID's critical current by an applied magnetic field, so it is important to measure the critical current of the SQUID precisely. However, nano-SQUIDs usually have a hysteretic  $V(I)$  characteristic, as shown in figure 5.7. Ramping the current up from zero, once the bias current exceeds the critical current  $I_c$ , the SQUID transits from the superconducting to the normal state. As the normal state resistance of the junction appears, a voltage step is generated and the dissipated energy heats the entire SQUID loop. When the current

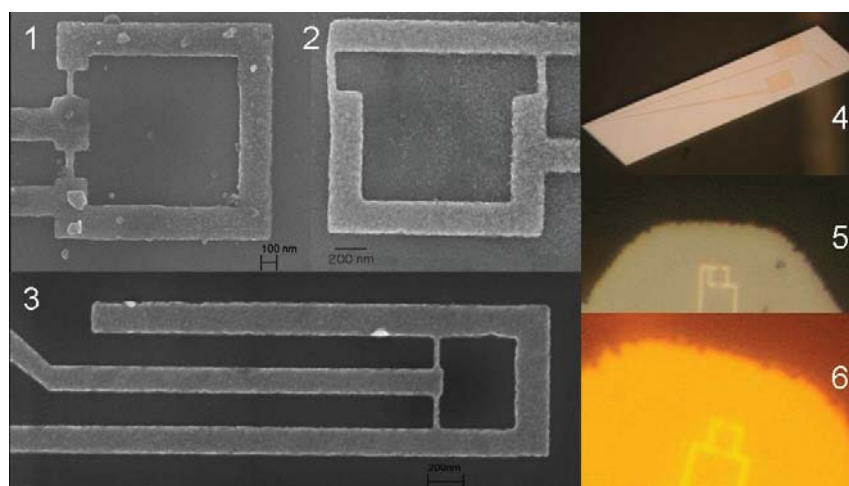


Figure 5.6: Some electron microscope images and optical photos of the SQUIDs. 1, 2, 5 and 6 are the  $1.1 \mu\text{m}$  SQUIDs, 3 is the  $0.6 \mu\text{m}$  SQUID. For 5 and 6, the distances between the SQUID and the tip are only about  $5 \mu\text{m}$ .

is lowered, the SQUID stays in the resistive state even for currents much smaller than  $I_c$ . Thus the thermal hysteresis excludes the usual current biasing schemes used as SQUID-readout[172].

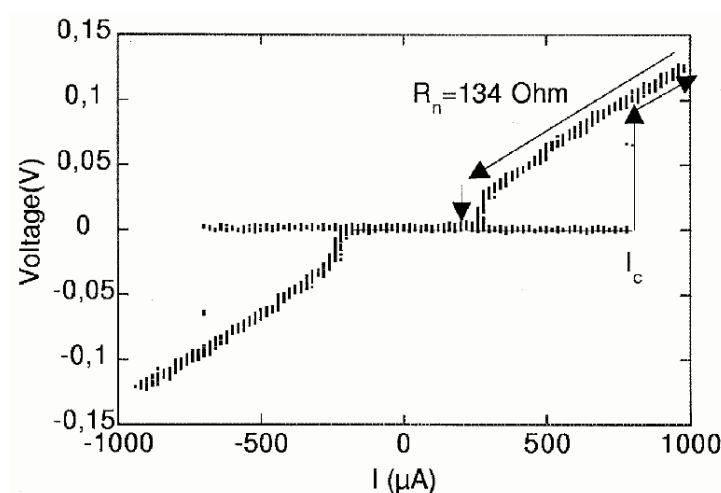


Figure 5.7: Because of the hysteretic  $V(I)$  characteristic, the critical current  $I_c$  of the SQUID is different from the current at which the superconductivity sets in again upon lowering the bias current. The image is taken from [172].

In order to overcome this problem, we use a dedicated detection technique. A computer-controlled circuit triggers simultaneously a current ramp and a 40 MHz quartz clock. As soon as the critical current is exceeded, a  $\partial V/\partial t$  pulse above a preset height will be detected at the SQUID, then the clock stops and the current is set to zero. The clock reading is transferred to the computer, and the cycle begins again. Thus the critical current is proportional to the duration of the current ramp, as shown in figure 5.8. The fastest repetition rate is 10 kHz, limited by the time needed to settle the current. For this technique, one single wire is sufficient to connect the SQUID, the  $\partial V/\partial t$  pulse is detected on the current biasing lead of the SQUID[172]. To improve the resolution, we can start the current ramp at a value close to  $I_c$  and choose an appropriate slope.

There are several advantages of this technique. We don't need a feedback, so the SQUID fabrication and the electric circuit are straightforward. The disadvantage is, that we don't have a feedback sys-

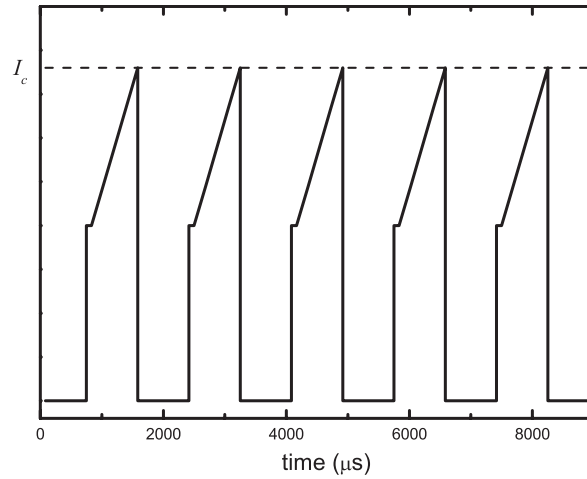


Figure 5.8: A current ramp is used to determine the critical current of the SQUID. The repetition rate is 600 Hz.

tem, thus we have to be careful to unambiguously translate the critical current values to a magnetic field scale.

Figure 5.9 shows two modulations curves of the SQUID critical current with applied magnetic field for two SQUIDS of different size. For the left one, the size of the SQUID is  $1.1 \mu\text{m} \times 1.1 \mu\text{m}$ , the period of the modulation is 16.8 G. For the right one, the size is  $0.6 \mu\text{m} \times 0.6 \mu\text{m}$ , and the period is about 54.3 G. This means when the SQUID becomes smaller, the range of the magnetic signal it can measure becomes bigger, but the resolution becomes lower. Both curves are asymmetric, because of the asymmetry in the design of the SQUIDS, and therefore we can do measurements at magnetic field around 0 G.

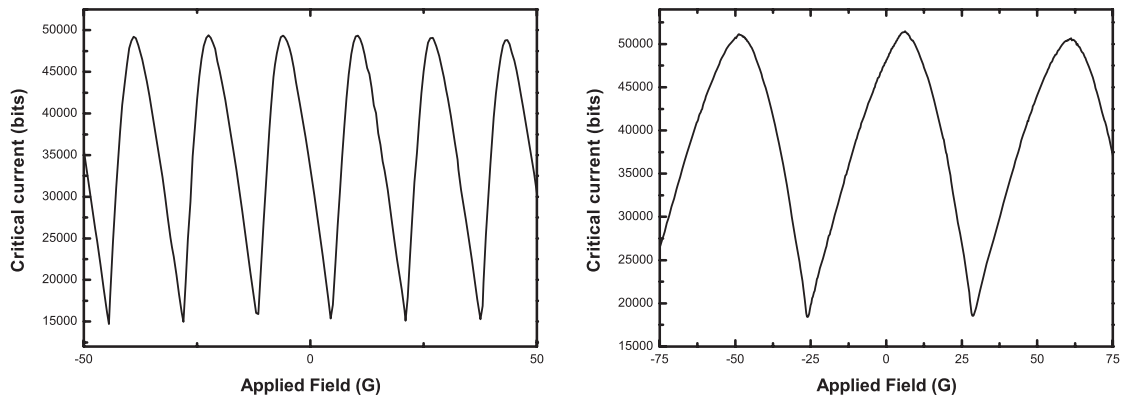


Figure 5.9: Typical modulations of the SQUID critical current with applied magnetic field. The ordinates shows the time it takes to reach the critical current for a given ramp. For the left, the size of the SQUID is  $1.1 \mu\text{m} \times 1.1 \mu\text{m}$ , the critical current is  $52 \sim 96 \mu\text{A}$  and the period is 16.8 G. For the right, the size of the SQUID is  $0.6 \mu\text{m} \times 0.6 \mu\text{m}$ , the critical current is  $42 \sim 76 \mu\text{A}$  and the period is 54.3 G.

The average slope of figure 5.9 left can be taken as  $\bar{s} \simeq 2 \times 34000 \text{ bits}/\Phi_0 = 68000 \text{ bits}/\Phi_0$ . The steepest slope corresponds to  $\bar{s}_{max} \simeq 169000 \text{ bit}/\Phi_0$ . Since the average standard deviation of 30 measurements is  $\delta \simeq 250 \text{ bits}$  and the sampling rate is 600 Hz, the noise of the SQUID is:  $n \simeq 250/68000/\sqrt{600}\Phi_0/\sqrt{\text{Hz}} = 1.5 \times 10^{-4}\Phi_0/\sqrt{\text{Hz}}$ . This flux noise level is much higher than in state-of-the-art SQUIDS. This is due to the difference in the measuring technique. The usual SQUIDS are current biased, and the apparent voltage is actually a periodic function of time with period  $2e\bar{V}(t)/h$ , e.g.,  $\bar{V}(t) = 10 \mu\text{V}$  results in 4.8 GHz. This high frequency averaging is absent in

the nano-SQUID technique as the first phase slip event triggers thermal dissipation, and the SQUID transits completely in the normal state[172].

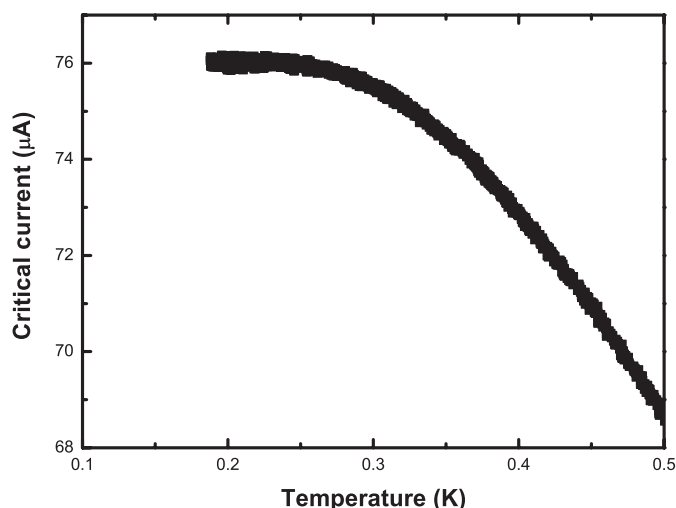


Figure 5.10: Temperature dependent of the critical current of the SQUID. Below 250 mK, the critical current doesn't change any more.

Figure 5.10 shows the temperature dependence of the critical current of one SQUID. As BCS theory describes, the critical current doesn't change any more when the temperature is lower than  $0.3T_c$ . For the SQUID we use, when temperature is lower than 250 mK, the critical current doesn't change any more. For our experiment, because both the SQUID and the sample are connected to the mixing chamber, when we heat the sample, the temperature of SQUID also changes. However, if we can keep the temperature of SQUID lower than 250 mK, it will not cause any impact on the measurement. Of course, this also constrains the temperature region we can do the measurement, else we have to measure the critical current modulation of the SQUID at the actual temperature it had during the imaging.

## 5.3 AFM

In order to image the magnetic field distribution on the sample surface, we need to put the SQUID probe to the sample surface as close as possible. What we use is an atomic force microscope technique using a tuning fork as proximity sensor. The quartz tuning fork is excited mechanically at its resonance frequency. When the tuning fork is resonating in a plane perpendicular to the sample, the interaction between tip and sample can be modeled as a viscous drag force using the differential equation of the harmonic oscillator. Due to the piezoelectricity of quartz, it is possible to deduce the oscillation amplitude and phase from the current in the quartz. As the sample is approached, damping sets in and the amplitude of oscillation is reduced, the phase begins to turn[172]. With a phase lock technique, we can keep the probe/sample distance constant, so we get at the same time the magnetic field distribution from the SQUID and topography of the sample surface by the force microscopy.

### 5.3.1 Tuning Fork

The tuning fork is one of the best mechanical oscillators. The important mode of tuning fork is the one where the two prongs oscillate in a mirrored fashion. This has the unique advantage that the center of mass stays at rest and all forces are compensated inside the material connecting the two prongs. Due to its high stability, precision, and low power consumption, furthermore, the

piezoelectric effect of quartz allows to excite and detect the oscillation of the tuning fork fully electrically, the quartz crystal tuning fork has become a valuable basic component for frequency measurements, and is used in a wide range of applications. For instance, since the late 1960s, mechanical pendulum or spring-based watches have largely been replaced by crystal watches, which are sufficiently stable for most daily uses [173]. After about twenty years, piezoelectric quartz tuning forks were introduced into scanning probe microscopy by Günther, Fischer and Dransfeld [174] for use in scanning near field acoustic microscopy and later by Karrai and Grober and others [175, 176, 177], as a distance control for a scanning near field optical microscope (SNOM).

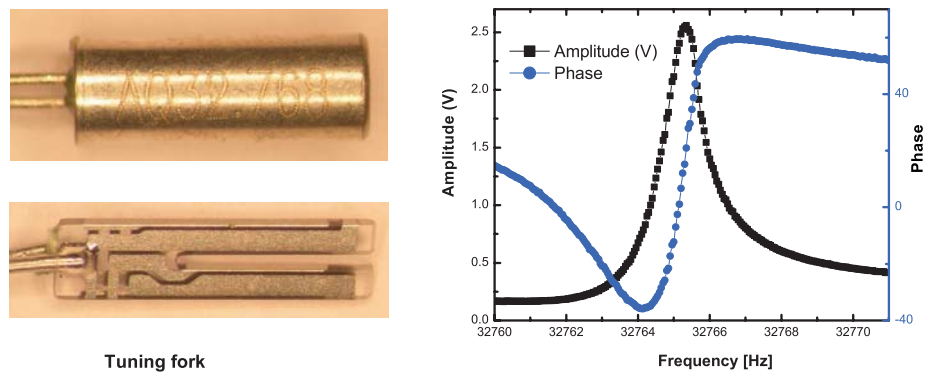


Figure 5.11: Piezoelectric quartz tuning forks are industrially produced in large numbers and serve as a frequency standard for example in wrist watches. They are packed in an evacuated steel casing and show quality factors of about 30000. The type shown in the left is the tuning fork we used, B rklin 78D202. Its resonance frequency is  $2^{15}\text{Hz} = 32768\text{ Hz}$ . The arms have a thickness of 0.6 mm, a width of 0.4 mm and a length of 3.98 mm. The right is the resonance curve we measured. The resonance peak shifted a bit and Q factor is about 20000.

As quartz is a piezo-electric material, when the tuning fork is bent, surface charges are generated. When the tuning fork oscillates the charge movement in the two prongs generates an ac-current. We can measure this ac-currents with a current-voltage amplifier. The resonance conditions will be strongly modified when one of the prongs is brought very near a surface. This change can be easily detected due to the sharpness of the resonance and used to measure the surface topography.

The tuning fork we use has a resonance frequency of  $2^{15} = 32768\text{ Hz}$  with a quality factor of about 30000 in an evacuated steel casing at room temperature (shown in figure 5.11). Once the casing and thus the vacuum are broken, the resonance frequency and the quality factor will drop due to the friction with the surrounding air. The tuning fork is very robust. We can easily glue its one prong on a PCB board, and glue the SQUID chip on the top of the free prong, as shown in figure 5.2. This naturally breaks the balance between the two prongs, increases the effective mass of the oscillator and decrease the eigen-frequency. Thus the resonance frequency and the quality factor drop a lot. However, the use of a low quality factor enabled us to decrease the response time and increase the stability of the tracking. The lower the quality factor, the higher the bandwidth. Consequently, it is more stable during the scanning [178]. A broad frequency spectrum allows a robust regulation. In high resolution force microscopy high quality factors translate to high gain in the regulation loop and lead to a very precise regulation.

Two typical resonance curves of the tuning fork with SQUID are shown in figure 5.12. They are measured at 300 K and 1 K respectively. Because the steel casing has been removed, and the tuning fork is glued on the PCB board and the SQUID is attached to the tuning fork, the resonance frequency and the quality factor drop significantly. At room temperature, the quality factor is only several hundreds. However, on decreasing the temperature, the quality factor becomes higher and higher. Below 4 K, usually it is about several thousands. The resonance frequency increases also with decreasing temperature, as the glue and the quartz itself become stiffer.

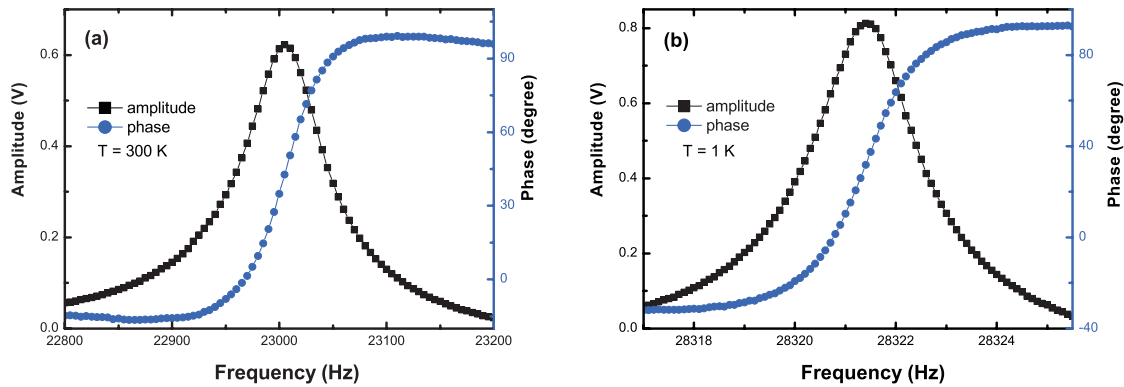


Figure 5.12: Typical resonance curves of the tuning fork with SQUID at 300 K and 1 K. At 300 K, the resonance frequency is reduced from 32768 Hz by the weight of the Si chip and the quality factor is only about 230. This is because the tuning fork is glued with the PCB board and the SQUID, leading to dissipation. On decreasing the temperature, the quality factor becomes higher and higher as the glue hardens. At 1 K, it is about 11000.

### 5.3.2 Regulation

When the distance between the tip and the sample becomes very small, the resonance amplitude and phase of tuning fork will change. We use a phase locked loop regulation to maintain the phase constant, then feed the obtained frequency into another electronic regulation, which controls the voltage of a Z piezo electrical stack (Piezo Ceramic, Model: P-885.90). By elongating or shortening the Z piezo, we can keep the phase and the frequency at the set points. Then we can deduce the sample topography from the variation of the Z piezo voltage. The length of the Z piezo is 3.6 cm and its piezo-electrical expansion coefficient is  $0.32 \mu\text{m}/\text{V}$  at room temperature and  $0.067 \mu\text{m}/\text{V}$  at 1 K. This yields a maximal elongation of  $35.2 \mu\text{m}$  at room temperature and  $7.33 \mu\text{m}$  at 1 K for 110 V.

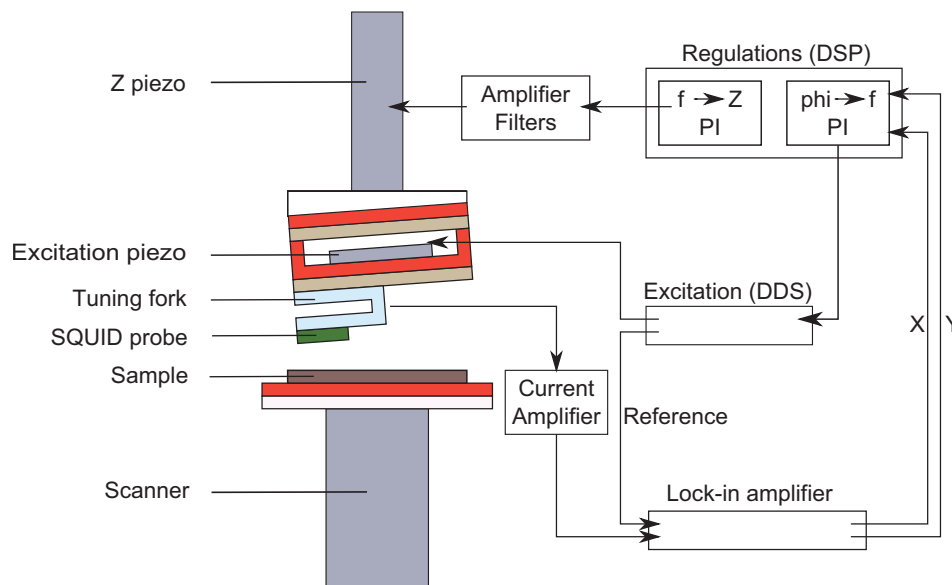


Figure 5.13: Schematic of the regulation loops. The tuning fork is excited by a piezo-electrical actuator which is controlled by the DDS card. The signal of the tuning fork is amplified and then measured by a lock-in, which outputs the in-phase (X) and out of phase (Y) components of the signal to the DSP card. In the DSP card two PI controllers are implemented regulating the phase of tuning fork and also the Z piezo stack.

Figure 5.13 is a schematic of the regulation loops. The tuning fork is excited by a piezo-electrical

actuator, which is controlled by the DDS card. The signal of the tuning fork is amplified by a custom built current-voltage amplifier with a very high gain ( $\sim 10^6\text{V/A}$ ), then measured by the lock-in. The time constant of the lock-in amplifier is set to 100/200  $\mu\text{s}$ . As the resonance frequency is about 25000 Hz to 29000 Hz, the signal is averaged over about 3-6 oscillations of the tuning fork. Before starting the regulation, we perform a frequency sweep to establish a frequency spectrum. Then we choose a frequency range containing a monotonic and distinct phase dependency, just like the center part of figure 5.12. We select a phase in the steepest region of the phase spectrum, and usually this region corresponds to the peak of the amplitude. When we begin the resonance frequency regulation, the lock-in will send the X and Y to the DSP card. Then the DSP card calculates the phase from the X and Y, and regulates the phase by changing the excitation frequency with proportional-integral controller(PI). This is done when the tip has no interaction with the sample surface, and what we get is the resonance frequency  $f_\infty$  (far away from sample). To regulate the distance between the tip and sample surface by the z-piezo stack, a set frequency  $f_{set}$  is required. Typically  $\Delta f = f_{set} - f_\infty$  is about 1 Hz to 3 Hz. After we send the set frequency to the DSP card, it will approach the frequency from the phase regulation to the set frequency by adjusting the voltage of the Z piezo with PI controller. When the tip is far away from the sample, the Z piezo will fully extend. When the tip is close to the sample, it will begin to regulate the tip/sample distance by extending or retracting. As the capacity of the z-piezo stack is quite high (3.3 $\mu\text{F}$ ), the charges needed to change its voltage are as well rather high and the charging current can heat up the microscope. Consequently, a fast regulation is needed, exempt of large and fast amplitude swings. The ideal parameters depend on the scanned surface.

## 5.4 Motion system

---

Our setup has two motion systems: a fine one and a coarse one. The fine one includes the scanner and the Z piezo, and the coarse one includes the XY motors and Z motor. The fine motion system is used to take images, the XY motors are used to move the probe to the different position over the sample, and the Z motor is used to approach the sample to the probe.

### 5.4.1 Scanner

Usually there are two ways for a scanning system to work: moving the probe or moving the sample. In our design the sample is moved. We use a piezoelectric S-bender scanner based on the design of Siegel[179], who developed this system for scanning Hall probes. This kind of scanner provides a large scan range at low temperature, offers precise control over the positioning, and it is very simple and less prone to vibration, hysteresis and creep.

The S-bender (see figure 5.14(a)) consists of a piezoelectric bender with four electrodes: two on the upper half, two on the lower half. When opposite voltages are applied to the upper half and the lower half, the piezo bends in a 's' shape, and the top and bottom of the S-bender remain parallel. To construct a scanner, we attach a pair of parallel S-benders(Piezo Systems,T220-A4-203X) at one end to the scan base, and at the other end to the secondary scan stage (see figure 5.14(b)). These benders then move the secondary scan stage relative to the scan base in the X direction, and keep it parallel to the scan base. Then we attach a second pair of parallel S-benders to the secondary scan stage at one end, and at the other end (near the scan base) to the primary scan stage. These benders now move the primary scan stage relative to the secondary scan stage in the Y direction[180]. The scan stages are made of Macor. The thermal contraction of the Macor is almost the same as the piezo elements, thus the stresses on the structure are small.

The S-bender scanner design intrinsically compensates for thermal contraction of the piezos elements since the X and Y bimorph pairs are nominally identical. Contraction of the bender pair

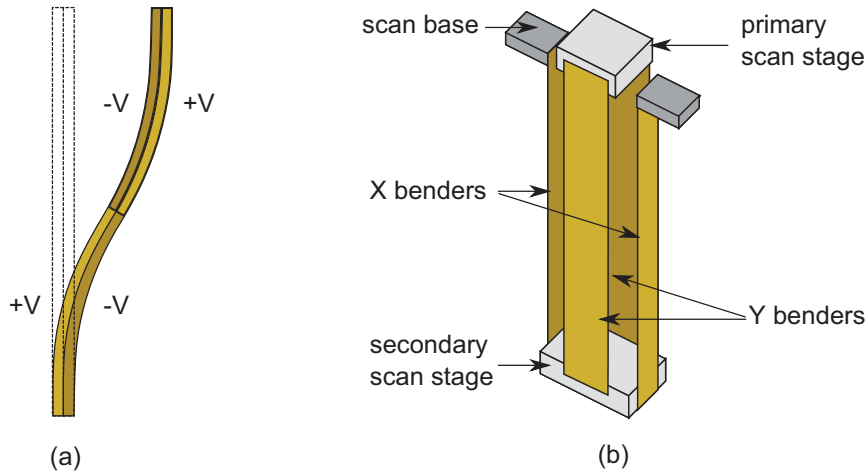


Figure 5.14: The S-bender scanner: (a) A piezoelectric S-bender. Applying opposite voltages on the upper half and the lower half causes the piezo to bend in an ‘S’ shape, and the top and bottom of the S-bender remains parallel. (b) Two pairs of parallel S-benders form a scanner which is compensated against thermal expansion and keeps the scan stage parallel to the scan base while scanning.

connecting the scan base and the secondary scan stage will decrease the distance between the sample and the probe, while contraction of the bender pair connecting the secondary and primary scan stages will increase that distance equally[181]. The primary scan stage is also kept parallel with the scan base at all times, preventing tilt of the sample relative to the sensor as a function of position.

The scan range depends on the length of the benders used, and the voltage applied. At low temperature, we apply a voltage  $\pm 200\text{ V}$  to the X and Y scanner, and can get a scan range of  $70\ \mu\text{m}$  by  $85\ \mu\text{m}$ . The height of the primary scan stage relative to the scan base change very slightly with position. This was calculated in reference [4]: the maximal drop is  $\sim 0.2\ \mu\text{m}$  for a deflection of  $\pm 42.5\ \mu\text{m}$ . This can be compensated for by the Z piezo which moves the sensor in the z direction.

#### 5.4.2 Coarse motion system

The XY plane motors are used to extend the useful range of our scanner, allowing us to move the probe relative to the sample so that we can image different areas of the sample. What we used is two attocube motors(AN-Pxyz101LT), which are controlled via the corresponding Controller (ANC150). At low temperature, the range of these motors can be up to  $5\text{ mm}$ . Usually the sample we measured is much smaller than this length, so we can take images on any position of the sample. We also can measure several samples within one cool down.

The Z motor is a home-made Pan style motor[182], as shown in figure 5.2. The design consists of 6 shear piezo actuators (EBL Products Inc.,PTZ-5A) on a titanium base. Titanium is used because its thermal contraction is almost the same as the piezo actuators. Each piezoelectric stack, sometimes referred to as legs, consists of 2 shear piezoelectric plates. The polarization of each piezo plate is glued with an antiparallel orientation relative to its adjacent neighbors. This allows for each leg to shear with a greater displacement than one single plate, which is critical for low temperature operation. Four legs are glued onto the titanium body and two legs are glued onto a brass plate, which is pressed against the slider by a tight spring plate. The geometry is such that all 6 legs press against the slider. Three sapphire pieces are glued on the faces of the slider where the piezo actuators touch. A sapphire or ruby ball is glued on the brass plate against the spring plate. A ball is used so that the force is equally distributed amongst all 6 legs. A brass stick is also glued on the brass plate to keep it vertical. The spring plate is typically made of Molybdenum, Stainless Steel,

or Beryllium Copper, and it can adjust how tight the piezo stacks press against the slider. When the piezos are not polarized, the assembly is held very rigidly giving the structure its outstanding mechanical rigidity[183].

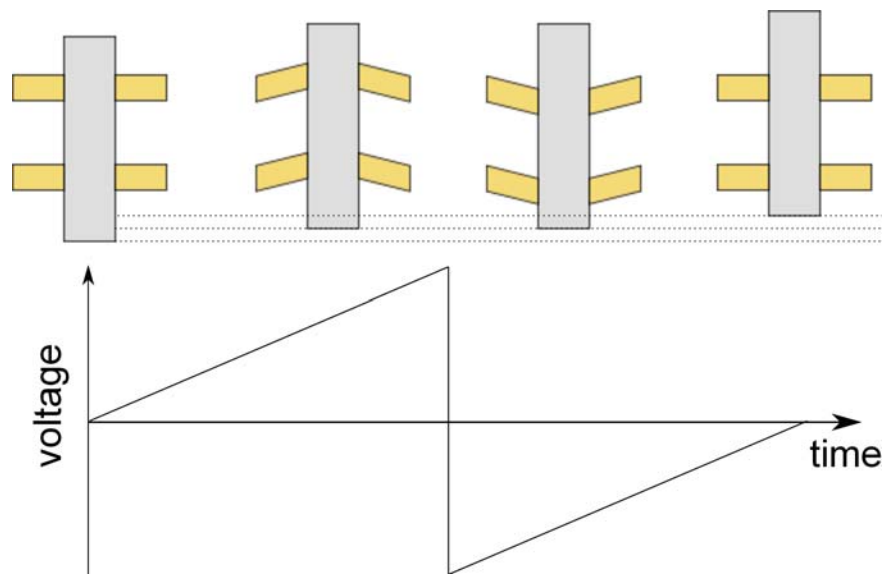


Figure 5.15: A schematic of the Z motor walking principle, but for 4 rather than 6 legs. On the bottom is the sawtooth voltage pulse applied to the piezo actuators. The response of the piezo to each part of the voltage pulse is given on the top. In each pulse, the slider moves two steps.

For the standard Pan walker, a steep rising voltage is applied to each individual stack sequentially and then the voltage applied to all legs is slowly relaxed to zero[183]. However, our Z motor uses a different walking way from the Pan walker. A voltage generator (Swissprobe Piezo-Motor Controller SP869) delivers a voltage ( $< \pm 400$  V sawtooth) to the 6 shear piezo actuators at the same time. As shown in figure 5.15, each pulse can be divided into four segments. At the beginning, the legs are relaxed. When the voltage ascends, the legs are sheared up slowly, and the slider is moved up by a fraction. Then the voltage changes to minus suddenly, so the legs are sheared down. Since the voltage is changed so quickly, the legs slip overcoming friction, and the slider doesn't move down because of inertia. As the voltage goes to zero, the legs relax slowly, and due to friction, the slider is moved up again. Thus in each pulse, the slider moves two steps. Motion in the opposite direction is achieved by following the same process but applying voltages with opposite polarity. However, because of gravity, moving up is much slower than moving down.

### 5.4.3 Position read-out

Both of the position read-outs of the attocube motors and the Z motor are done by capacitors. The capacitor consists of two interdigitated combs. One capacitor is fixed to the slider and the other one is attached to the immobile base. One comb of the immobile capacitor is excited with 10 V (Thandar TG503), the other comb is excited with the same signal but shifted by 180 degrees (figure 5.16).

The capacity between the mobile and immobile combs is of the order of a few pF. When the slider moves, its comb will alternate periodically to face the unshifted comb or the shifted comb. Thus the signal of the mobile comb will also change periodically. Measuring the signal with a lock-in amplifier (EG&G Instruments 7220), we can get a resolution which is higher than the step size of the motors at room temperatures. As the period of the double-comb is 2 mm, we can deduce the distance the motors moved. In order to get a big signal, the distance between the two combs  $d$  is smaller than 0.5 mm.

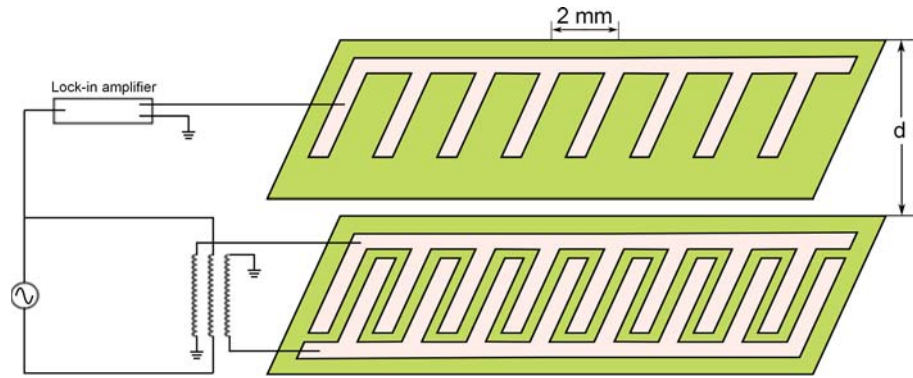


Figure 5.16: Schematic of the position read-out system. The two combs of the double-comb are excited with the same signal but inverse phase. When the up comb moves, it will alternate periodically facing either the unshifted comb or the shifted comb. The induced voltage is measured by a lock-in amplifier. The periodicity of the combs is 2 mm. In order to get a big signal, the distance between the two combs  $d$  is smaller than 0.5 mm.

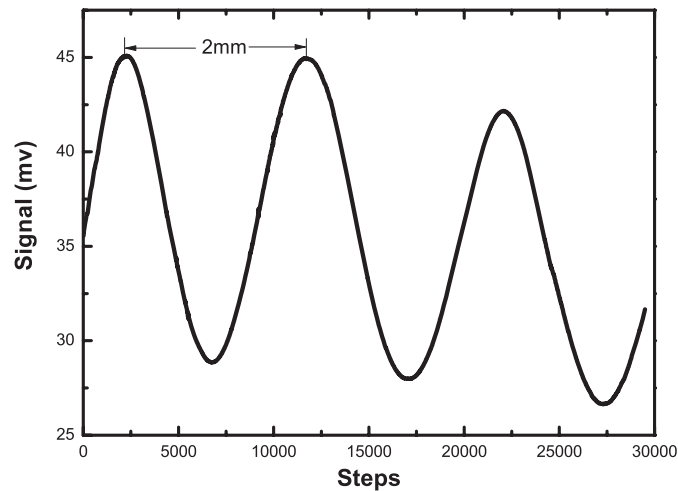


Figure 5.17: Position read-out for the Z motor. It is measured at 1 K, against gravity, and the voltage is  $\pm 200$  V. Because one period corresponds to 2 mm, the average step size is about 200 nm. The reason for the asymmetry of the curve is the two comb capacitors are not perfectly parallel to each other.

Figure 5.17 is the signal from the lock-in amplifier as a function of the number of walked steps of the Z motor. It is measured at 1 K, against gravity, and the voltage is  $\pm 200$  V. The average step size is about 200 nm. The curve is asymmetric, because the two comb capacitors are not perfectly parallel to each other. However, this brings a benefit: when the motor moves over one maximum or minimum, then we can know where it is. This is very useful when we approach the sample to the probe. The value of the curve changes much from room temperature to low temperature, but the shape and the positions of the maximum and minimum don't change. Therefore, we can find the sample at low temperature with the help of the room temperature curve.

## 5.5 Others

### 5.5.1 Cryostat

We use a home-made upside-down dilution refrigerator called "Sionludi", which was developed by A. Benoit, M. Caussignac and S. Pujol at the CRTBT (now Institut Néel). The lowest temperature is on the top stage, while the highest is at the bottom stage. Figure 5.18 shows a schematic of the whole setup. The cryostat is isolated from the building vibrations by an optical table with 4 spring isolators. The connection to the pumps of the dilution circuit is made of flexible pipes and tubes passing through heavy concrete blocks. The base temperature with the measurement wiring installed is about 120 mK.

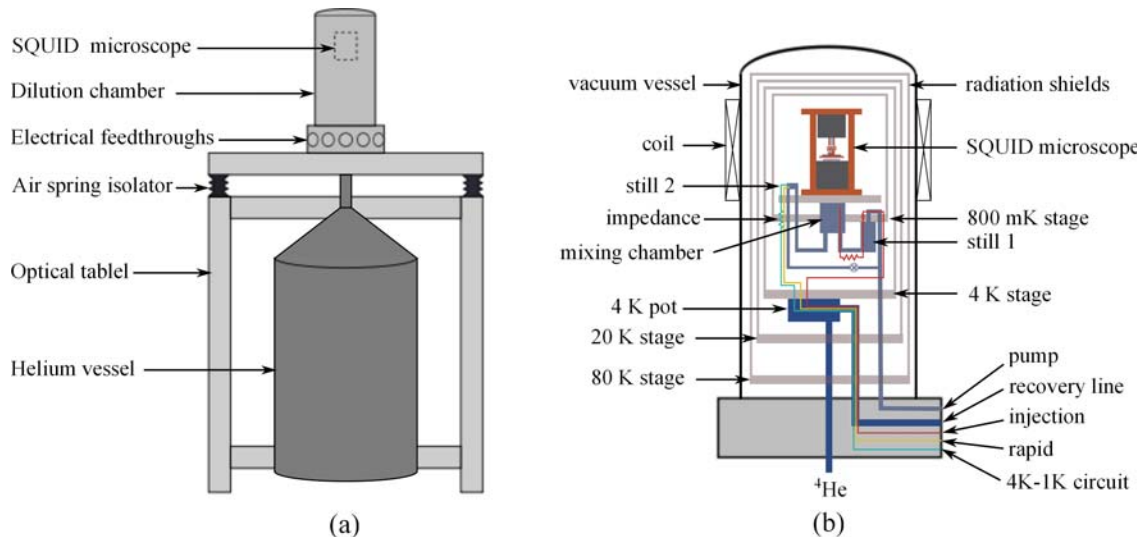


Figure 5.18: Schematics of the cryostat. (a) The cryostat is supported by an optical table with 4 spring isolators. The pressurized He vessel underneath provides the  $^4\text{He}$  flow. The SQUID microscope is located in the upper part of the dilution cryostat. (b) is an enlargement of the dilution chamber in (a).

The main advantages of our cryostat are its natural rigidity, the handy horizontal access and a very rapid cooling/heating cycling. The whole cryostat is enclosed in a single vacuum which is sealed by an o-ring at room temperature. There is no  $\text{N}_2$  liquid bath and therefore no vibrations due to  $\text{N}_2$  boiling. The 4 K stage is cooled by a  $^4\text{He}$  flow from a pressurized helium vessel. During cooling down to 4 K, a large flow of  $^3\text{He} - ^4\text{He}$  mixture thermalizes the dilution stage. Depending on the  $^4\text{He}$  flow, the cooling down to 4 K lasts about 8 ~ 10 hours. The  $^3\text{He} - ^4\text{He}$  mixture is injected in the cryostat at a pressure between 1 and 3 bar. After reaching 4 K, a fast cooling down to 1.5 K of the dilution stage is ensured by pumping, then the mixture begins to condense, and the dilution circuit is started[184]. In the dilution regime, the limit temperature is reached within 4 ~ 5 hours with the SQUID microscope installed. The cooling power is about  $10 \mu\text{W}$  at 200 mK.

The detailed cooling down process is like this:

1. Start the  $^4\text{He}$ -circuit to cool down the 4K pot. Typically we use a flow rate of 7.5 L/min, which is corresponds to 30% on the gauge.
2. At the same time, circulate the mixture in the injection, the rapid and the 4K-1K circuits under a pressure (between 1 and 3 bar) to obtain a flow rate of 2.5 L/min, which is corresponds to 10% on the gauge. The gas is cooled down by a counter flow heat exchanger. After about 8 ~ 10 hours, all components of the mixing stage are cooled down to 4 K.
3. Stop the rapid and the 4K-1K circuit and begin to pump (a roots pump and a rotary vane pump

in series are used). This will cool down the dilution stage to 1.5 K very quickly, because of the Joule-Thomson expansion of the mixture. Then the mixture begins to condense.

4. Open the valve of the tank of the mixture, all the mixture is injected in the cryostat at a pressure about 3.5 bar by the compressor. Under a high pressure and low temperature, the mixture condenses quickly.
5. When the pressure becomes lower than 3 bar, we begin to pump out the mixture in the tank and inject it to the cryostat. When the tank is empty, all the mixture has condensed. Then by tuning the valve shown in figure 5.18 (b) to get the same temperature of the still 1 and still 2, the temperature of the mixing chamber will go down to 120 mK.

We can use different thermal coupling schemes to establish different temperature zones on the microscope. When we connect the entire microscope to the mixing chamber, the temperature region useful for experiment is 160 mK to 1.8 K. When we connect the lower part of the microscope to still 1 with the sample connected to the mix chamber, the experiment temperature region is 680 mK to 2.5 K. When we also connect the sample to still 1, the experiment temperature region will be 900 mK to 9 K. Thus according the different temperature we want to measure, we can choose the most suitable way to do the thermal coupling.

### 5.5.2 Thermometry

The temperature measurement and control system we used is called TRMC2, which is specifically designed for measuring and control very low temperatures by means of different types of sensors by the electronic service of the lab. The measuring currents can be adjusted to extremely low values to create negligible sensor heating, even at the lowest temperatures. It offers from 1 to 8 channels, each enabled to be equipped with a measuring board adapted to the type of sensor used. Each one of these boards (measurement of very low temperature) is equipped with a four channels scanner that enables up to 32 resistive sensors to be measured per scan. Due to its high sensitivity and the possibility of adjusting the measurement and regulation parameters over a large range, its use extends from the lowest temperatures (a few mK) up to several hundred Kelvin.

For the different stages and locations of the cryostat we use different thermometers/resistors: The temperatures at the two stills are measured with two ruthenium resistors, the 4 K pot with platinum for temperature higher than 30 K and one carbon resistances(C100) for temperature lower than 30 K. The mixing chamber temperature is determined with four different thermometers: two different carbon resistances(C100 and AB10), one germanium and one ruthenium. The sample temperature is obtained by two different carbon resistors(C100 and AB10), which are glued on the sample holder. The temperature of the SQUID is measured by a carbon resistor(AB10) placed as close as possible to the SQUID. The critical current can also be used as temperature indication between scans at constant fields. Since the temperatures of the sample and the SQUID are the most important, we use two channels to measure them respectively, so we can get these temperatures all the time.

### 5.5.3 Magnetic field

We used one copper coil to produce a magnetic field along the  $z$ -direction. The coil is directly attached to the vacuum vessel[as shown in figure 5.18 (b)] and the magnetic field produced is 68 G/A. For the in-plane component of the magnetic field, we can add two Helmholtz-coils to generate a magnetic field of 16.8 G/A at the sample position.

The current sources to drive these coils is custom-built and can provide maximal 3 A, thus giving a magnetic field in  $z$ -direction of maximal 204 G. This is higher than the critical field of our aluminum SQUID ( $\sim 120$  G). Actually, most of our measurements are performed at a very low magnetic field

(several Gauss). Because when the magnetic field is higher, it will induce too many vortex, and screening currents around the vortex overlap.

#### 5.5.4 Electronics and Software

An overview of the electronics and software are shown in figure 5.19. PC1 controls the whole experiment except the temperature either directly or via the DSP card. PC2 is used to control the temperature via the TRMC2 and back up the data.

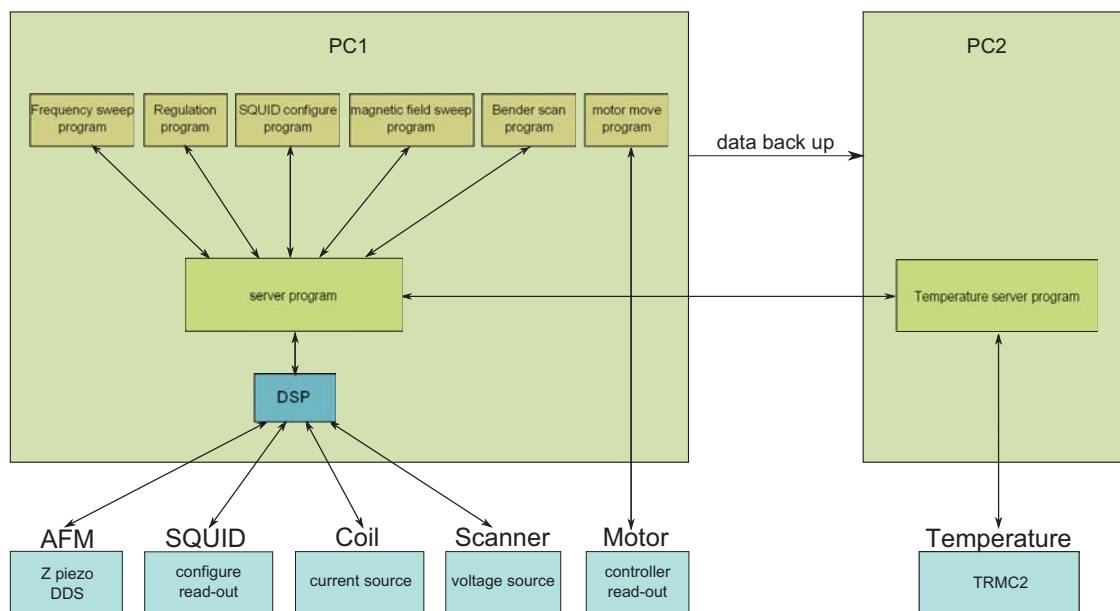


Figure 5.19: Schematics of the electronics and software. The whole experiment except the temperature is controlled by PC1 directly or via the DSP card. PC2 is used to control the temperature and back up the data.

The communication between the computers and the electronics are via ethernet, GPIB and one NI PCI card(6509). The DSP card (Sheldon Instruments, SI-C6713DSP-PCI) is put on the main board of PC1. The real time tasks (regulations) are delegated to the DSP. The current source connected to the coil and the voltage source connected to the scanner are controlled by the analog output signal of the DSP.

All the software is written in LabVIEW. In order to make different sub-systems have access to the same hardware resources, all the measure and control programs in PC1 except the motor move program connect to a TCP/IP server program which provides an interface to the DSP card to control the hardware. There are two programs for the AFM control: the frequency sweep program and the regulation program. The frequency sweep program uses an ethernet connection (UDP) to change the frequency, whereas the regulation program only passes the regulation parameters (proportional value  $P$ , integral value  $I$ ) and set points (set phase and frequency) to the DSP, then the DSP will change the DDS frequency and Z piezo voltage(see figure 5.13). The motor movement program is directly connected to the motor controllers and the lock-in amplifier for position read out interfaced by GPIB.

The two PCs are connected by local area network. In PC2, there is a temperature server program which is connected to the TRMC2. It is also connected to the sever program in PC1 by TCP/IP. Thus in PC1 we also can get the temperature information we want and control the temperature. PC2 is also used to back up all the data we get in PC1. All the measure programs in PC1 copy the data to PC2 automatically after the measurement is finished. Therefore, we can analyze the data as soon as

possible without influencing the measurement.

When we are doing the scanning measurement, the bender scan program is connected to the DSP via the TCP/IP server program to control the position of the scanner. At the same time, it reads out simultaneously the  $z$ -piezo stack voltage (for AFM imaging), the critical current of the SQUID (magnetic imaging), and the temperatures of the SQUID and the sample. Thus we can get the topograph and magnetic images at the same time, and we can also check if the temperature of the SQUID and sample is stable or not during the scan.

## 5.6 Calibration

For all the measurements I did, I began with calibration. There are two purposes to do the calibration every time: the first is to check the scanning scale, if it changed or not, and the second is to obtain the distance between the SQUID and the sample surface, in a way I will explain later.

The sample used to calibrate the microscope scanning scale is a thin niobium film (270nm) with 3 levels of self-similar checkerboard motifs as shown in figure 5.20(a): On the highest level it consists of  $5 \times 5$  squares with a side length of  $100 \mu\text{m}$ . One half of the squares are niobium squares. The niobium squares consist of a smaller  $10\mu\text{m} \times 10\mu\text{m}$  checkerboard [see figure 5.20(b)] with niobium islands of about  $1 \mu\text{m}$  side length [5.20(c) and (d)].

The whole checkerboard is surrounded by lines growing in thickness with distance to the main checkerboard. This feature was added to facilitate the search for the sample and is generally useful for orientation on a periodic motif. As one can see in figure 5.20(c), some features were also added in the empty squares in order to show the direction of the sample center and also for orientation purposes (see arrow).

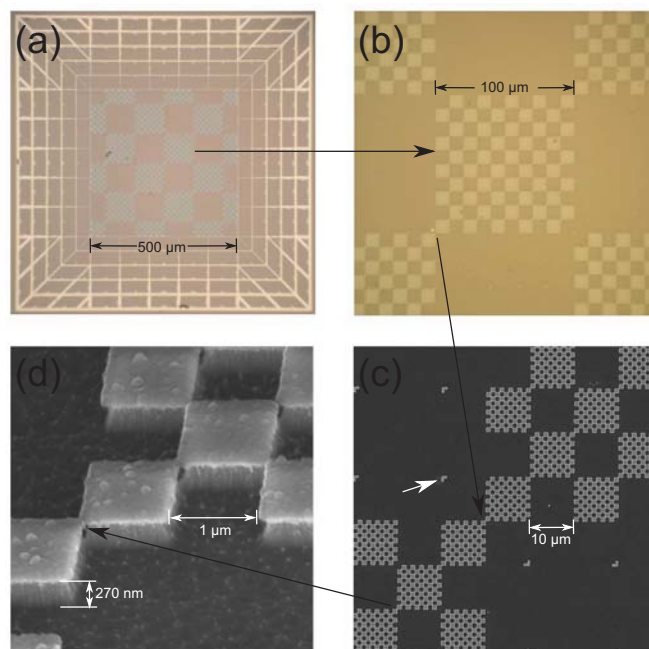


Figure 5.20: Nb self-similar checkerboard. (a) and (b) are optical photos. Around the chessboard there some lines which help to find the center. (b) zooms on one small square of (a). (c) and (d) are SEM photos, (c) zooms on one small square of (b). The arrow points to a motif in the empty square which serves for orientation purposes and indicates the direction of the sample center. (d) shows the smallest Nb element, which is 1 micron.

As already described our microscope does topographic and magnetic imaging simultaneously. In

figure 5.21, (a) is the magnetic image by measuring the critical current of the SQUID and (b) is the corresponding topographic image from the applied voltage on the Z piezo. The squares in both images correspond to  $10\mu\text{m} \times 10\mu\text{m}$ -squares in figure 5.20, while we can also see the  $1\mu\text{m}$  niobium islands. However, it is hard for us to get a good resolution in both the topographic and magnetic images, because our AFM tip is just the corner of the silicon chip, not a real sharp tip. And this is also the reason of the shadow in figure 5.21(b). If we want to get a good resolution of the topographic image, we need to align the probe to get a steep angle between the probe chip and the sample surface, but this will make the distance between the SQUID and the sample surface become too big, then the resolution of the magnetic image will become very low. Since we can see the smallest structure in figure 5.21, this means the tip is not so round and the distance between the SQUID and the sample surface is smaller than  $1\mu\text{m}$ . The black and white discs in the squares of the magnetic images are vortices.

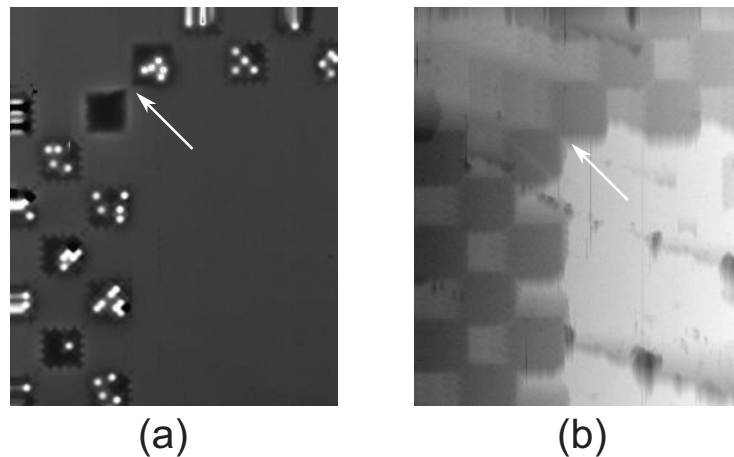


Figure 5.21: Calibration. (a) and (b) are respectively the magnetic and the topograph image of the same measurement on the Nb checkerboard. The squares in both images correspond to  $10\mu\text{m} \times 10\mu\text{m}$ -squares in figure 5.20, and we can also see the  $1\mu\text{m}$  niobium islands. The white and black discs in the squares in (a) are vortices. The arrows point to the corresponding spots between the magnetic and AFM images. The shadow in (b) is because the tip is not a real sharp tip. The shift of the two images is due to the SQUID not being at the AFM tip's position.

**scanner range:** From the topographic image or the magnetic image in figure 5.21, we can get the scanner range. What is shown in figure 5.22 (a) is a cross section taken from figure 5.21(a) along the vertical direction. Since the maximal voltage applied to the bimorph piezo elements constituting the scanner is  $\pm 200\text{ V}$ , we deduce the maximal image range along the vertical direction to be  $85.0\mu\text{m}(\pm 1.1\mu\text{m})$ . We also get the maximal image range along horizontal direction to be  $70.1\mu\text{m}(\pm 1.5\mu\text{m})$  with the same way.

**z-piezo range:** The data sheet of the z-piezo states that the maximal elongation is  $35.2\mu\text{m} \pm 3.5\mu\text{m}$  at  $110\text{ V}$  at room temperature. Typically the capacity and thus the piezo-electric properties decrease by a factor of 6 at low temperatures. Consequently, a voltage difference of  $3\text{ V}$  at low temperatures results in an elongation/shortening of about  $160\text{ nm}$ . However, we can get a more precise value from the topographic image we get. Figure 5.22 (b) shows a cross section taken from figure 5.21(b) along the vertical direction. As we know the height difference between the Nb pattern and the substrate is about  $270\text{ nm}$ , by comparing the different voltage value of the z-piezo when the tip is on the empty square and the Nb square, we get that a voltage difference of  $3\text{ V}$  at low temperatures results in an elongation/shortening of about  $200\text{ nm}$  of the Z piezo.

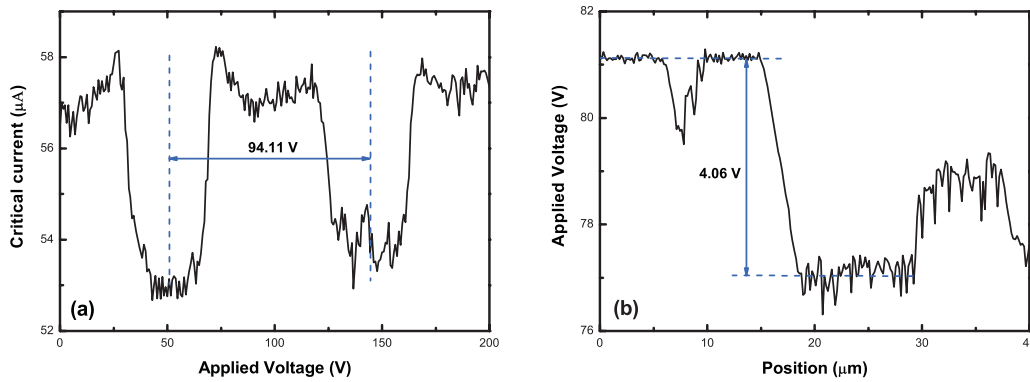


Figure 5.22: (a) and (b) are cross sections taken from figure 5.21(a) and (b) along the vertical direction. (a) The scanner moves  $20 \mu\text{m}$  for  $94.11 \text{ V}$ , yielding the maximal image range along the vertical direction to be  $85.0 \mu\text{m} (\pm 1.1 \mu\text{m})$ . (b) By comparing the thickness of the Nb pattern, we get a voltage difference of  $3 \text{ V}$  results in an elongation/shortening of about  $200 \text{ nm}$ .

## 5.7 SQUID/sample distance

Quite a number of models have been proposed to describe the current and magnetic field distribution induced by a vortex. In 1966, J. Pearl calculated the current distribution of an isotropic vortex deep inside the sample and at the sample surface[185]. In 1975, J. R. Clem calculated the form factor of vortices using GL theory for neutron scattering purposes[186]. Then V. G. Kogan and E. H. Brandt proposed more general approaches for calculating the magnetic field above a vortex for the anisotropic case and for an arbitrary sample thickness[187, 188], see figure 5.23.

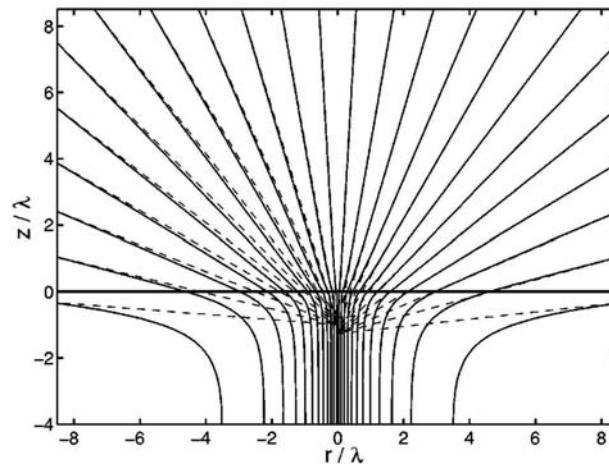


Figure 5.23: Magnetic field lines of a straight vortex in a superconducting half space. The dashed lines on the left side correspond to a magnetic monopole with the flux  $2\Phi_0$  (to compensate the flux in negative direction) at a depth  $z_0 = -\lambda$ , and the one on the right side correspond to the monopole at  $z_0 = -1.27\lambda$  which fits better to the near field, from [188].

To calculate the magnetic field above a vortex, the main idea is to calculate the magnetic field in the vacuum with the Maxwell equations, and the magnetic field in the interior of the sample with the London equations. By using the Fourier transform for both fields at the vacuum/sample interface and imposing continuity of the field and its normal derivative, for a vortex centered at  $x = y = 0$  with its axis oriented parallel to the  $z$  axis (normal to the plane) of the superconducting film of arbitrary thickness  $d$  with the center of the film at  $z = -d/2$ , one obtains [189]:

$$h_z(\mathbf{r}, z) = \frac{\Phi_0}{(2\pi\lambda_{ab})^2} \int d^2\mathbf{k} e^{i\mathbf{k}\cdot\mathbf{r}} \frac{e^{-kz}}{\alpha(\alpha + k \coth(ad/2))} \quad (5.5)$$

where  $\mathbf{r} = (x, y)$ ,  $\mathbf{k} = (k_x, k_y)$ ,  $k = \sqrt{k_x^2 + k_y^2}$  and  $\alpha = \sqrt{k^2 + \lambda_{ab}^{-2}}$ .  $\lambda_{ab}$  corresponds to the in-plane components of the penetration depth and  $z$  is the height above the sample plane. In the case  $(r^2 + z^2)^{1/2} \gg \lambda$ , to first order, one finds that the field profile resembles that of a monopole situated  $\lambda_{eff}$  below the surface[190]:

$$h_z(r) = \frac{\Phi_0}{2\pi} \frac{z + \lambda_{eff}}{[r^2 + (z + \lambda_{eff})^2]^{3/2}} \quad (5.6)$$

where  $\lambda_{eff} = \lambda \coth(d/2\lambda)$ .  $\lambda_{eff}$  differs appreciably from  $\lambda$  when the film is so thin that the vortex core is not well formed.

Since all the models fit the field distribution of vortex with a magnetic monopole, in order to determine  $\lambda$ , one has to estimate the SQUID/sample distance  $z$  very precisely. As V. G. Kogan pointed out: the absolute value of  $\lambda$  cannot be extracted from the response field with a better accuracy than that for the source position[191]. Specially from equation 5.6, one can see  $\lambda$  and  $z$  are anti-correlated. Thus a big error bar in  $z$  will lead to a big error bar in  $\lambda$ .

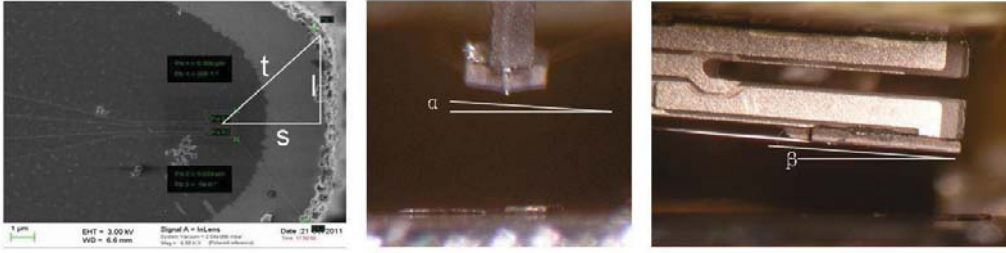


Figure 5.24: An electronic microscope photo of a SQUID chip tip and how we align the SQUID chip. From the distance of the SQUID and the tip, with the two angle between the SQUID chip and sample, we can calculate the SQUID/sample distance as  $z = l * \sin\alpha + s * \sin\beta$ . For the SQUID chip shown here, we get  $l = 4.1 \pm 0.2\mu m$ ,  $s = 4.4 \pm 0.2\mu m$ ,  $\alpha = 1.7^\circ \pm 0.2^\circ$ ,  $\beta = 3.7^\circ \pm 0.2^\circ$ , resulting in  $z = 0.41 \pm 0.04\mu m$ .

In order to get a precise SQUID/sample distance, we always measure the distance between the SQUID and the tip of the SQUID chip by electronic microscope before measurement. Then we align the SQUID very carefully to get small angles between the SQUID chip and the sample in both of two directions. For the SQUID chip shown in figure 5.24, we get  $l = 4.1 \pm 0.2\mu m$ ,  $s = 4.4 \pm 0.2\mu m$ ,  $\alpha = 1.7^\circ \pm 0.2^\circ$ ,  $\beta = 3.7^\circ \pm 0.2^\circ$ , resulting in  $z = 0.41 \pm 0.04\mu m$ . This is why we can still see the  $1\mu m$  niobium islands in figure 5.21(a), though the size of the SQUID is about  $1\mu m$ .

We also tried to calculate the SQUID/sample distance from the shift  $f$  between the topographic image and the magnetic image of the Nb self-similar checkerboard which we used to do the calibration. At the beginning, we thought we could get a more precise SQUID/sample distance with this way than with the way above, but it is not true. Because the tip we used to get the topographic image is not a real sharp tip, the resolution of the topographic image is not very high. Therefore, we can't determine precisely the shift between the topographic image and the magnetic image of the Nb checkerboard. Since  $t^2 - f^2 = z^2$  and  $z < 1\mu m$ , a small error bar of  $f$  will yield a big error bar of  $z$ , so until now it is impossible for us to get a precise  $z$  by this way.

## 5.8 Possible improvements

After many times measurements, we found some problems of the system and have had several ideas to improve the microscope.

**For regulation:** The first problem is that the resonance curve of tuning fork is asymmetric sometimes, as shown in figure 5.11. Usually this is not a big problem, but sometimes it will become difficult to regulate. We think this problem comes from the way we glue and excite the tuning fork. To solve this problem, we need more trials.

The second problem is that the resonance curve of tuning fork always changes after we moved the motors. This problem comes from the vibrations induced by the movement of the motors. What we can do is to replace the attocubes with scanning tube and use some springs to insulate the vibration from Z motor, or we can change our design to insulate the tuning fork from all the vibrations.

The third problem is that for a different tuning fork, the P and I values for regulation are different. Maybe it will be much better to use a self adjustable PI controller that can automatically find good P and I values for the regulation.

The fourth problem is that the resonance curve of tuning fork shifts when the applied voltage on the Z piezo changes. When this shift is bigger than 2 Hz, it will be impossible to regulate during scanning. We guess the problem is from an electrical field effect of the z-piezo. However, we need more tests to confirm or infirm this idea.

**For SQUID:** The SQUID we use is made of Al, so it can only work at very low temperature. And it also can only be used in a very small magnetic field region because of the periodic multi-valued critical current. There is an ongoing effort (SuperNanoCharac project of the NanoScience Fondation (Grenoble, France)) to develop shunted Nb SQUIDs which would allow for linear flux measurements. For a Nb SQUID, the working temperature can be much higher than for Al, and the sensitivity of a shunted SQUID would also be superior to the current SQUID as the SQUID noise is proportional to the factor  $\sqrt{f_{Josephson}/f_{sampling}}$ . Since this factor becomes 1 in the case of a shunted SQUID we could gain - in the ideal case - four order of magnitudes of sensitivity.

Because the tip of the SQUID chip is not a real sharp tip, the resolution of the topographic images is not very high, and it is also difficult to get a very precise SQUID/sample distance. To make a well defined tip maybe is an important improvement. The idea is to make a SQUID chip like figure 5.25. This may be possible with a well controlled chemical etching process.

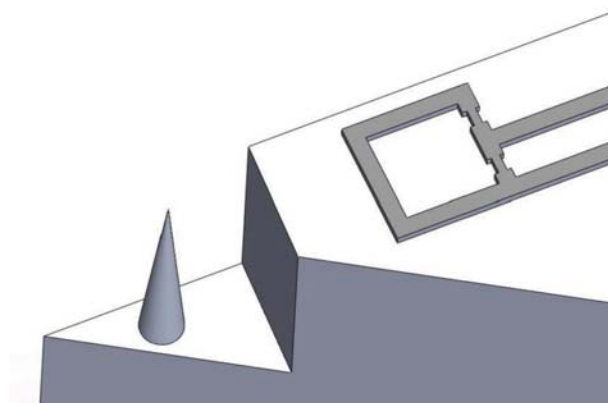


Figure 5.25: New design of the SQUID tip.

## 5.9 Measurements on Rhenium film

### 5.9.1 Rhenium film

The first vortex measurement I did is on Rhenium film. Rhenium is a conventional superconductor with almost the same lattice parameter as  $\alpha\text{-Al}_2\text{O}_3$ , and it does not oxidize, so it can be grown epitaxially on sapphire and used to fabricate very high quality Josephson junctions. The dielectric loss from two-level states in the tunnel junction barriers can lead to decoherence in the junction. Thus the research on Rhenium is important for giving us ways for a better understanding on the origin of the two level states in Josephson junctions and the way to reduce this effect. This research is done in the context of the ongoing project SuperNanoCharac supported by the NanoScience Foundation (Grenoble, France).

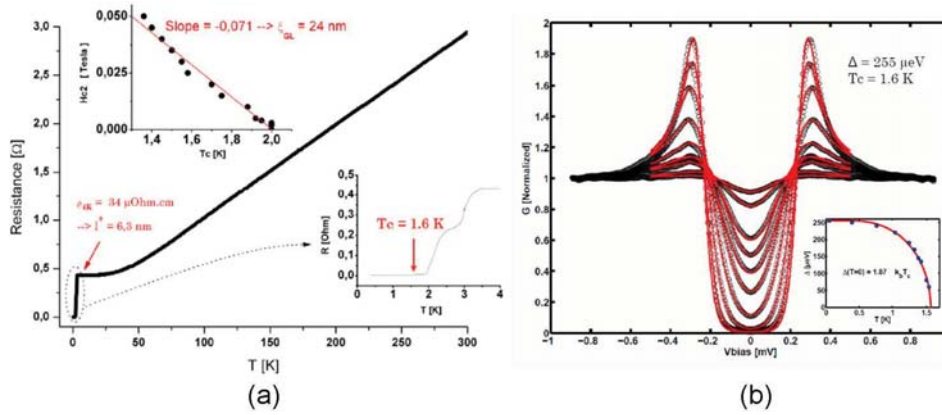


Figure 5.26: (a) The resistance measurement on the Rhenium film shows the superconducting critical temperature is about 1.6 K and the coherence length of  $\xi = 24$  nm. (b) The LT-STM measurement shows the temperature evolution of the superconducting gap follows BCS very well.

The Rhenium film was fabricated using Molecular Beam epitaxy on sapphire (0001) under UHV conditions by B. Gilles and M. Verdier at the SIMAP INPG laboratory. The thickness is 80 nm, and the superconducting critical temperature is about 1.6 K, as shown in figure 5.26 (a). The surface rugosity of the rhenium film was already characterized using scanning tunneling microscopy by Thomas Dubouchet in the group of Claude Chapelier at the CEA Grenoble. The measurements also found a coherence length of  $\xi = 24$  nm and the temperature evolution of the superconducting gap follows BCS, as shown in figure 5.26 (b).

### 5.9.2 Penetration depth measurements

As mentioned in section 1.1.2: for a type II superconductor, if the applied magnetic field exceeds the lower critical field, the magnetic field penetrates inside the specimen as vortices, and each vortex with magnetic flux of  $\Phi_0$ ; but for a type I superconductor, the magnetic field can't go inside the specimen when it is below  $H_c$ . However, the type I superconductor film shows a transition from a type I to a type II behavior when the film thickness decreases below a critical thickness  $d_c$  [192] given by

$$d_c \approx \frac{\xi - \lambda}{(1 - 2\kappa^2)^2} \quad (5.7)$$

with  $\lambda$  the penetration depth,  $\xi$  the coherence length and  $\kappa$  the Ginzburg-Landau parameter  $\lambda/\xi$ .

The lack of bulk measurements for  $\lambda$  makes it impossible to calculate the critical thickness for

rhenium, but typically the values are of the order of  $1 \mu\text{m}$  [192]. The thickness of the Rhenium film we got is  $80 \text{ nm}$ , so it will show a type II behavior and we can measure the vortex to get the penetration depth  $\lambda$ .

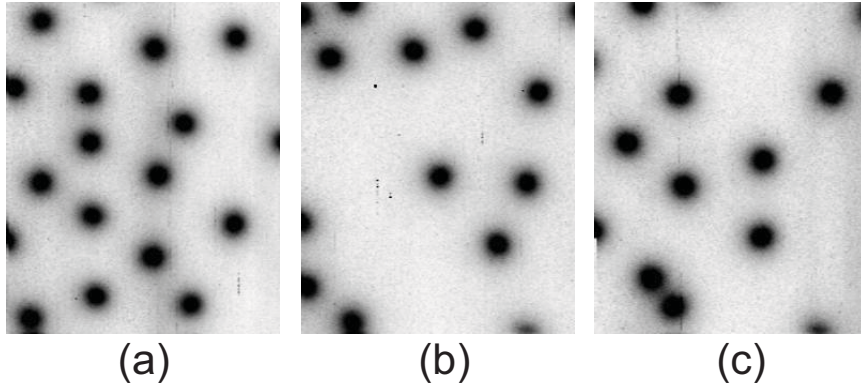


Figure 5.27: The vortices in Rhenium film at different temperature: (a) 325 mK, (b) 500 mK and (c) 1 K. The sizes of all images are  $17.5 \mu\text{m} \times 21.25 \mu\text{m}$  and the magnetic field is  $-2 \text{ G}$ .

Three vortices images are shown in figure 5.27. They were taken at the same position at different temperature. The position of vortices are different because the vortices move during subsequent scans and we will talk about this later. Because the applied magnetic field is very small, most of vortices are individual, and this allow us to fit the vortices easily.

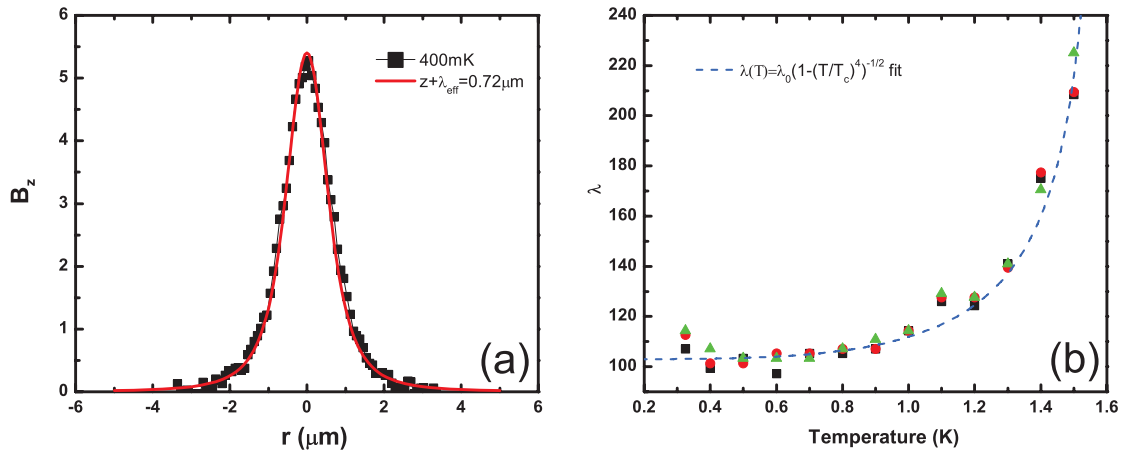


Figure 5.28: (a) Typical fitting of a vortex profile. The temperature is  $400 \text{ mK}$ . Since we knew the SQUID/sample distance  $z \simeq 0.45 \mu\text{m}$  at this measurement, we can get the value of  $\lambda_{eff} \simeq 270 \text{ nm}$ . (b) Temperature dependence of penetration depth of the Rhenium film. The blue curve is a BCS fit. With  $T_c = 1.6 \text{ K}$ , we get  $\lambda_{eff} = 278 \text{ nm}$  and  $\lambda_0 = 103 \text{ nm}$  for the Rhenium film.

We tried to fit the cross profile of vortices by equation 5.5 and 5.6 with the size of the SQUID, and we found very similar results. Since equation 5.6 is much simpler than equation 5.5, we used equation 5.6 to do all the fitting. One fitting for a vortex at  $400 \text{ mK}$  is shown in figure 5.28(a). As we knew the SQUID/sample distance  $z$  is about  $0.45 \mu\text{m}$  at this measurement, we can get the value of  $\lambda_{eff}$  from the fitting parameter  $z + \lambda_{eff}$ . From the fitting, we got the temperature dependence of penetration depth of the Rhenium film. By a BCS fitting, we got  $\lambda_{eff} = 278 \text{ nm}$  and  $\lambda_0 = 103 \text{ nm}$  for the Rhenium film. The results is shown in figure 5.28(b). It is consistent with the STM measurement.

Since Rhenium is a type I superconductor, the penetration depth  $\lambda$  should be smaller than the coherence length  $\xi$ . However, from the results we got,  $\lambda$  is bigger than  $\xi$ . This is because for a very

thin film, the mean free path  $l$  of the electrons are limited by the thickness. Even if the film is very clean, it is still in the dirty limit. Therefore,  $\xi = (\xi_c l)^{0.5} < \xi_c$  and  $\lambda = \lambda_c (\xi_c / l)^{0.5} > \lambda_c$ , where  $\xi_c$  and  $\lambda_c$  are the coherence length and penetration depth in the clean limit.

### 5.9.3 Vortex pinning

At the begin of the experiment, we found the vortices moved after temperature changed. As shown in figure 5.29 (a) and (b), when we cooled down the sample from 1 K to 340 mK, the vortices moved to some other regions of the sample. That means the pinning force of the vortex in the Rhenium film is quite weak, and in some part, the pinning force is bigger than at other parts. We explain this by the presence of growth islands in the film, and the connecting island borders pin the vortices much stronger than the inner of the islands.

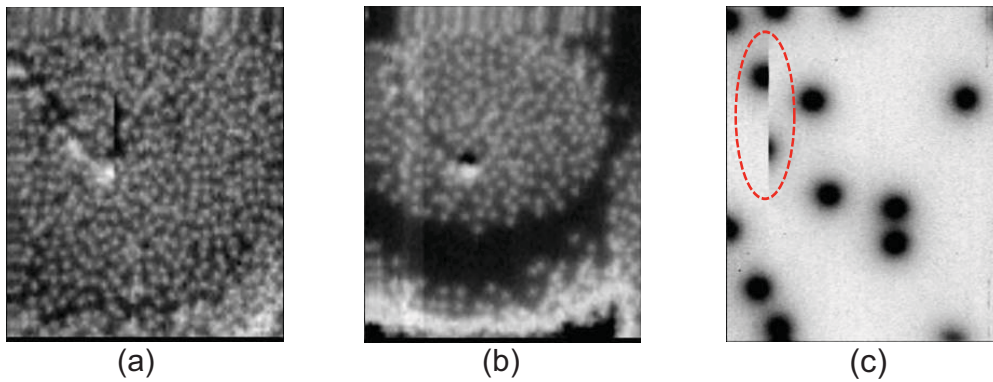


Figure 5.29: (a) is taken at 1 K. After cooled down to 360 mK, one can see the vortices moved in (b). The sizes of (a) and (b) are both  $70 \mu\text{m} \times 85 \mu\text{m}$ , the magnetic field is 1 G. (c) During the scan, one vortex moved. The image is taken at 900 mK and -2 G. The size is  $17.5 \mu\text{m} \times 21.25 \mu\text{m}$ .

The more interesting thing is that we found some vortices moved during the scan, as shown in figure 5.29 (c). There are two possible reasons for this movement: one is that the vortex moved by itself, because it is in an unstable state; the other one is that the SQUID moved the vortex by the force between each other. In order to find the reason we scanned the some region with different SQUID/sample distance. If the movement of vortex is due to the SQUID, when the SQUID/sample distance become big enough, the vortices should not move any more.

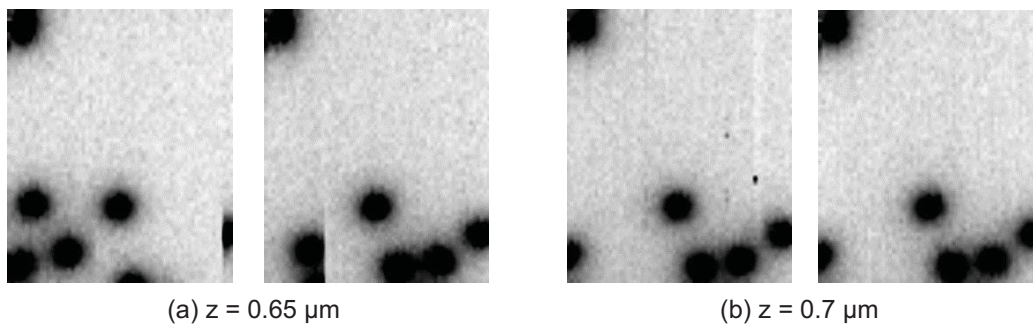


Figure 5.30: (a) When the SQUID/sample distance  $z = 0.65 \mu\text{m}$ , the positions of vortices are different in two successive scan. Some vortices also moved during the scan. (b) When  $z = 0.7 \mu\text{m}$ , the positions of vortices didn't change any more. All the images were taken at  $T = 290 \text{ mK}$  and  $H = 0 \text{ G}$ . The size of the images is  $17.5 \mu\text{m} \times 21.25 \mu\text{m}$ .

As shown in figure 5.30: when the SQUID/sample distance  $z = 0.65 \mu\text{m}$ , the vortices moved after the scan, and some vortices also moved during the scan; when  $z = 0.7 \mu\text{m}$ , the vortices didn't move

any more. Thus the vortices moved because of the force between the SQUID loop and the vortices. D. Hykel calculated the pinning force of the vortices, and the value he got is about  $7.5 \times 10^{-16}$  N. Normalized with the vortex length which is the film thickness, this value leads to  $0.01$  pN/ $\mu\text{m}$ , which is three orders of magnitude weaker than other materials used for superconducting devices[4].

Though what we measured is the minimal pinning force, the average pinning force should be much bigger, we still can claim that the pinning force of the Rhenium film is very weak. We think the reason for this low pinning is due to the film is epitaxial film, so it is very clean as single crystal. Therefore, our measurements showed the high quality of the Rhenium film, and allowed the first estimation of the penetration depth of Rhenium.

## 5.10 Summary

---

We built a nano-SQUID force microscope, which regulates the distance between the tip and sample surface with an atomic force microscope tuning fork technique. We used a current ramp to measure the critical current of the SQUID. Our microscope does topographic and magnetic imaging simultaneously.

After calibration with a thin niobium film with 3 levels of self-similar checkerboard motifs, we deduced the maximal image range to be  $70.1 \mu\text{m}(\pm 1.5 \mu\text{m}) \times 85.0 \mu\text{m}(\pm 1.1 \mu\text{m})$ . And by comparing the different voltage applied on the z-piezo when the tip is on the empty square and the Nb square, we got a voltage difference of 3 V at low temperatures results in an elongation/shortening of about 200 nm for the Z piezo.

Then we did nano-SQUID force microscopy measurements on epitaxial Rhenium film. We found the pinning of vortices in the Rhenium film is very weak and some places of the film (maybe domain walls) pin vortices. By fitting the vortices, we got the penetration depth of the film is about 103 nm.

# 6

## Measurements on $\text{Ba}(\text{Fe}_{1-x}\text{Ni}_x)_2\text{As}_2$ single crystals

Until now, the experimental results on the iron-based superconductors are very incompatible. For different compounds, different groups gave different results. Even for the same compound, different techniques gave different results. Maybe these inconsistencies stem from different sample qualities, or by the fact that different techniques get different information of the samples as the information obtained is often model dependent, and as the complicated electronic structures of the iron-based superconductors is not yet fully understood, different models may give different results. In order to resolve this problem, the best way is to measure the same sample with different techniques. Since we have systematically doped  $\text{Ba}(\text{Fe}_{1-x}\text{Ni}_x)_2\text{As}_2$  single crystals, made by Hui-Qian Luo, we tried to study the superconducting properties on one and the same samples of this family by means of lower critical field, tunnel diode oscillator, heat capacity and scanning nano-squid microscopy measurements. In this chapter I will present the results we have obtained from different techniques, then I will compare these results.

### 6.1 Introduction

---

As mentioned in chapter 1 and 3, the symmetry of the superconducting order parameter and the nature of the low energy excitations can provide important information about the pairing mechanism in the iron-based superconductors. Now it is generally accepted that superconductivity in this family results from a superexchange repulsion mediated by magnetic excitations, which couple electron and hole pockets of the Fermi surface (FS) [49, 116, 193]. Such pairing interactions favor either isotropic  $s$ -wave order parameters with opposite signs on different sheets of the Fermi surface ( $s_{\pm}$  model) or anisotropic  $s$ -wave or even  $d$ -wave order parameters with nodes [43, 194, 195]. Consensus has been reached on several systems, e. g.  $\text{LaFePO}$  [196, 197],  $\text{KFe}_2\text{As}_2$  [198, 199],  $\text{BaFe}_2(\text{As}_{1-x}\text{P}_x)_2$  [200], and so on, that nodes exist on the gap structure. However, experimental confirmations of such a nodal-gap state remains highly controversial in other systems [47, 152, 55, 201, 153, 202, 203, 204, 168, 205, 206, 148, 149]. For example, measurements of the electronic specific heat of  $\text{Ba}(\text{Fe}_{1-x}\text{Co}_x)_2\text{As}_2$  have shown a field dependence consistent with both a fully gapped FS [201] and a nodal quasiparticles at the Fermi level [204, 168]. Such scattered experimental results and interpretations may come from the different qualities and doping levels of the samples studied.

---

Table 6.1:  $x$ ,  $d$ ,  $w$  and  $l$  are the composition, thickness, width and length of the  $\text{Ba}(\text{Fe}_{1-x}\text{Ni}_x)_2\text{As}_2$  samples, respectively.  $H_{c1}$  is the lower critical field,  $\lambda$  is the London penetration depth (the values between brackets are deduced from specific heat measurements),  $\beta = \partial\lambda/\partial T^2$  and  $\kappa = \lambda/\xi$  is the Ginzburg-Landau parameter. All values are given for  $T \rightarrow 0$ .  $T_c$  is the critical temperature. Measurements techniques : HP = Hall Probe,  $C_p$ =Heat capacity, TDO = Tunnel Diode Oscillator and SSM = Scanning nano-SQUID Microscopy.

$x(\%)$	$d(\mu\text{m})$	$w(\mu\text{m})$	$l(\mu\text{m})$	$\mu_0 H_{c1}(\text{G})$	$\lambda(\text{nm})$	$\beta(\text{nm}/\text{K}^2)$	$\kappa$	$T_c$	measured by
2.6	70	260	390	30	530	-	150	6.8	HP
2.6	140	340	450	25	620	-		6.0	HP
2.6	20	1040	1420	-	1400	24		5.3	TDO+SSM
2.9	50	160	250	70	350(570)	-	120	11.0	HP+ $C_p$
2.9	20	70	80	80	330	-		11.2	HP
2.9	5	450	570	-	490	2.9		11.1	TDO+SSM
2.9	10	700	950	-	-	2.0		11.2	TDO
3.4	90	280	320	100	290(410)	-	100	16.0	HP+ $C_p$
3.4	90	280	320	110	270	-		15.6	HP
3.4	50	580	630	-	-	1.2		14.6	TDO
3.4	5	330	640	-	-	1.4		15.0	TDO
3.4	10	470	820	-	-	1.6		15.8	TDO
4.2	70	300	340	240	180(270)	-	75	20.2	HP+ $C_p$
4.2	10	45	45	180	210	-		19.6	HP
4.2	10	300	590	-	310	0.6		18.8	TDO+SSM
6.5	90	280	340	80	310(400)	-	90	12.5	HP+ $C_p$
6.5	100	250	300	70	340	-		12.5	HP
6.5	20	850	900	-	610	3.2		10.8	TDO+SSM
6.5	20	310	630	-	-	5.3		9.9	TDO
7.4	80	280	340	45	420	-	80	8.6	HP
7.4	50	190	220	50	400	-		9.0	HP
7.4	40	540	900	-	850	17		6.5	TDO+SSM

In order to get some comparable results, we tried to do transport measurements(lower critical field, tunnel diode oscillator and heat capacity measurements) and scanning nano-squid microscopy measurements on systematically doped  $\text{Ba}(\text{Fe}_{1-x}\text{Ni}_x)_2\text{As}_2$  single crystals. Some of the results are shown in table 6.1. Because lower critical field measurements and tunnel diode oscillator measurements have different sample size constraints, the samples used in this two measurements are not the same one but from the same batch. However, the samples used in heat capacity measurements were also used to do the lower critical field measurements, and the samples used in scanning nano-squid microscopy measurements were also measured by the tunnel diode oscillator technique.

## 6.2 Transport measurements

### 6.2.1 Lower critical field measurements

The lower critical field measurements were done by T. Klein with GaAs-based quantum well Hall sensors. The external field was increased up to  $H_a$  and swept back to zero in order to measure the remanent field ( $B_{rem}$ ). In the Meissner state, no vortex penetrates the sample and  $B_{rem}$  remains

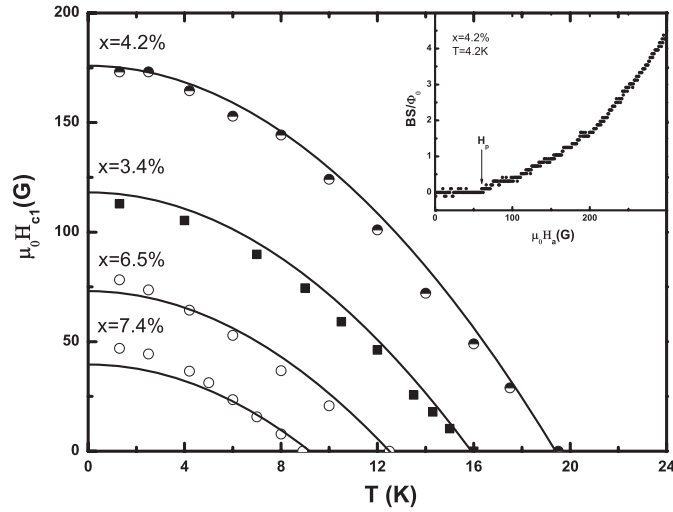


Figure 6.1: Temperature dependence of the lower critical field  $H_{c1}$  in  $\text{Ba}(\text{Fe}_{1-x}\text{Ni}_x)_2\text{As}_2$  single crystals (for the indicated doping concentrations  $x$ ). The solid lines are fits to the data using  $\rho_s \propto T_c^2 - T^2$ . Inset : remanent field (in flux units over the surface  $S$  of the probe) as a function of the applied field showing the presence of pinned vortices for  $H_a > H_p$ .

equal to zero up to the so-called first penetration field  $H_p$ . When  $H_a > H_p$ , a finite  $B_{rem}$  value will be obtained as vortices remain pinned in the sample (see inset of figure 6.1). In order to avoid spurious effects associated to strong pinning which prevents the vortex diffusing to the center of the sample,  $H_p$  has been measured on several locations with an array of miniature probes.

Due to the expulsion of the flux lines for  $H_a < H_p$  which increases the local field in the vicinity of the sample edges, and the presence of geometrical barriers (GB),  $H_p$  is smaller than the lower critical field  $H_{c1}$  with  $H_{c1} = \alpha H_p$ , where  $\alpha > 1$ . For elliptical samples without geometrical barriers, the standard "demagnetization" factor  $\alpha_{elliptical} = 1/(1-N) \propto w/d$  ( $w$  and  $d$  being the width and thickness of the sample, respectively). In the presence of geometrical barriers,  $\alpha_{GB} = 1/\tanh(\sqrt{\beta d/w})$  where  $\beta$  varies from 0.36 in strips to 0.67 in disks [106].

In order to minimize the deviation of  $\alpha$ , all samples were chosen to present very similar aspect ratios  $d/w$  (see table 6.1) leading to very similar corrections for the whole series whatever the origin of  $\alpha$ . The temperature dependence of  $H_{c1}$  for the indicated  $x$  values are displayed in figure 6.1.  $\lambda(0)$  was finally deduced from the lower critical field writing :  $\mu_0 H_{c1} = (\Phi_0/4\pi\lambda^2)(\ln(\kappa) + c(\kappa))$  where  $c(\kappa)$  is a  $\kappa$  dependent function tending towards  $\sim 0.5$  for large  $\kappa$  values. The corresponding  $\lambda(0)$  values have been reported on figure 6.8 as a function of  $T_c$ . As shown, similar values ( $\lambda(0) \sim 1/T_c^{0.85 \pm 0.2}$ ) have been obtained on both sides on the superconducting dome in striking contrast with the result obtained by Gordon et al. in  $\text{Ba}(\text{Fe}_{1-x}\text{Co}_x)_2\text{As}_2$  [207]. Our measurements do hence not support the scenario of a sharp increase of  $\lambda(0)$  due to the presence of a magnetic gap in underdoped samples but rather suggest that only a small fraction of the Fermi surface is affected by the antiferromagnetic coupling.

The most remarkable feature is the very large variation of the superfluid density which varies over one order of magnitude for  $T_c$  values ranging from  $\sim 6.8$  K to  $\sim 20.2$  K. Such a strong dependence is unexpected in conventional superconductors, but strongly suggest the presence of pair breaking effects. In order to obtain further indications on those effects we have performed Tunnel Diode Oscillator (TDO) measurements to obtain the temperature dependence of the superfluid density with high accuracy.

## 6.2.2 Tunnel diode oscillator measurements

The tunnel diode oscillator measurements were done by P. Rodière. The samples were glued at the end of a sapphire rod which was introduced in a coil of inductance  $L$ . The variation of the London magnetic penetration depth induces a change in  $L$  and hence a shift of the resonant frequency  $\delta f(T) = f(T) - f(T_{min})$  of a LC oscillating circuit (14MHz) driven by a Tunnel Diode. This shift, renormalized to the one corresponding to the extraction of the sample from the coil ( $\Delta f_0$ ) is then equal to the fraction ( $\delta V/V$ ) of the sample which is penetrated by the field. For  $H \parallel c$ ,  $\delta V$  is related to the in-plane penetration depth  $\lambda_{ab}$  through some calibration constant which can be altered by edge roughness effects[208]. We hence decided to apply the field in the  $ab$ -planes in which case  $\delta V/V \sim 2(\lambda_c/w + \lambda_{ab}/d)$  ( $\lambda_c$  being the penetration depth parallel to the  $c$ -axis) i.e.  $\delta V/V \sim 2/d \times [\lambda_{ab} + (d/w)\lambda_c]$  with  $\lambda_{ab} + (d/w)\lambda_c = \lambda_{mix} \simeq \lambda_{ab}$  for  $w \gg d$  (for weakly anisotropic systems, which is the case of iron-based superconductors). In contrast to  $H_{c1}$  measurements for which we used rather "thick" ( $d/w \simeq 1/4$ ) samples in order to reduce the uncertainty related to geometrical corrections, we have hence selected very thin samples ( $d/w \ll 1$ ) for the TDO measurements (see table 6.1).

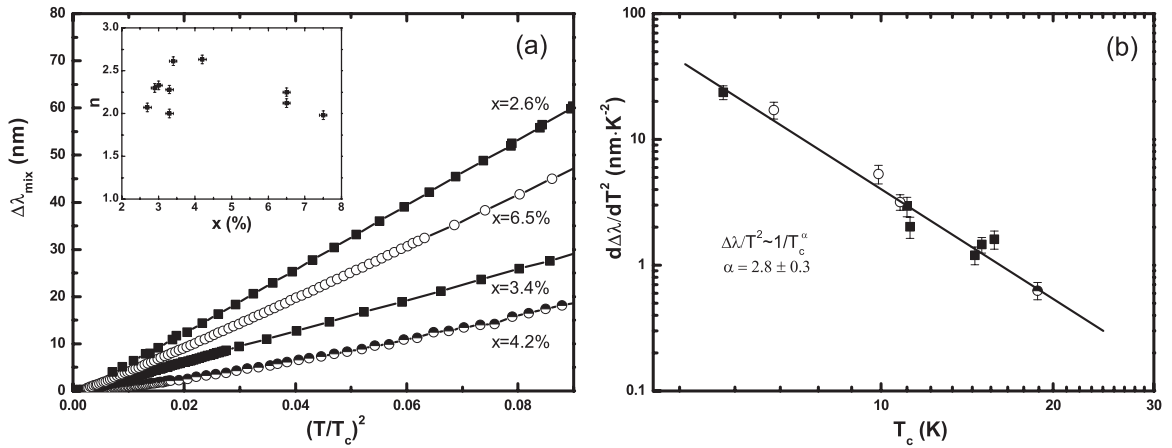


Figure 6.2: (a) Variation of London penetration depth  $\lambda_{mix} = \lambda_{ab} + (d/w)\lambda_c$  ( $\sim \lambda_{ab}$  for  $w \gg d$ ) as a function of  $(T/T_c)^2$  in  $\text{Ba}(\text{Fe}_{1-x}\text{Ni}_x)_2\text{As}_2$  single crystals for the indicated  $x$  values. Inset: best fit values for the exponent  $n$ , assuming that  $\Delta\lambda \propto T^n$ . (b) Slope of the  $\Delta\lambda$  vs  $T^2$  curve as a function of  $T_c$ .

The temperature dependence of the penetration depth is clearly non exponential in all measured samples but can be well described by a power law :  $\Delta\lambda_{mix}(T) = \lambda_{mix}(T) - \lambda_{mix}(0) = A * T^n$  with  $n \sim 2.3 \pm 0.3$  for  $T \leq T_c/3$  (see figure 6.2). A very similar behavior has been reported in a large number of pnictides in 11, 122 and 1111 systems [208, 209]. This dependence is a clear indication for the presence of pair breaking effects but it is also important to note that the slope of the  $\Delta\lambda$  vs  $T^2$  curve,  $\partial\Delta\lambda/\partial T^2|_{T \rightarrow 0}$  is proportional to  $1/T_c^{2.8}$ .

## 6.2.3 Heat capacity measurements

Heat capacity ( $C_p$ ) measurements have been performed at magnetic fields up to 28 T using an high sensitivity AC technique (typically 1 part in  $10^3$ ) by C. Marcenat. Heat was supplied to the sample by a light emitting diode via an optical fiber and the corresponding temperature oscillations were recorded with a thermocouple. Special care has been taken in the calibration procedure in order to obtain quantitative  $C_p$  values. For  $x = 3.4\%$ ,  $4.2\%$  and  $6.5\%$  well defined specific anomalies were obtained in zero field (see figure 6.3) and this anomaly progressively shifted with magnetic field.  $T_{c2}$  has hence been defined as the temperature corresponding to the mid point of the transition

for a given value of the external field. The transition became broader and weaker for  $x = 2.9\%$  (not shown) and finally too weak (and/or broad) to allow any accurate determination of  $H_{c2}$  from specific heat measurements for  $x = 2.6\%$  and  $x = 7.4\%$ .

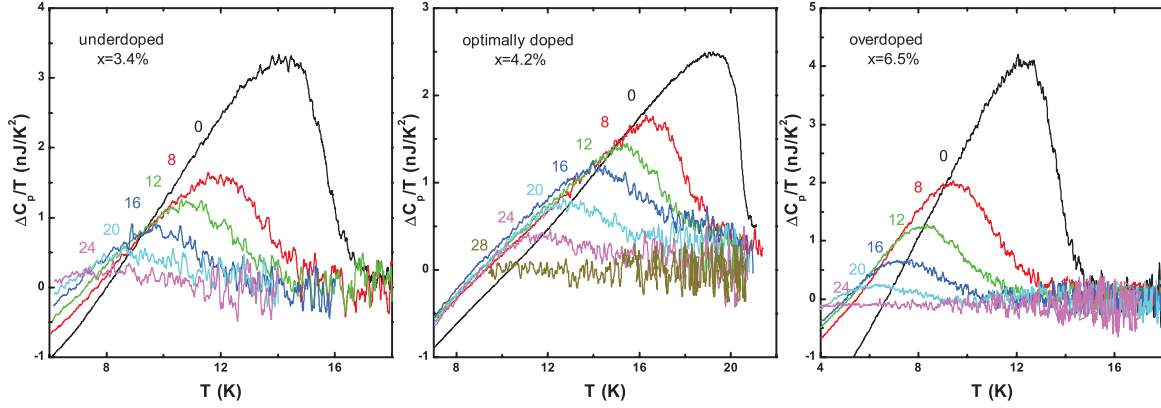


Figure 6.3: Temperature dependence of the field dependent part of the specific heat for the indicated field values in  $\text{Ba}(\text{Fe}_{1-x}\text{Ni}_x)_2\text{As}_2$ .

Note that the amplitude of the specific heat jump at  $T_c$  is equal to  $\Delta C_p = (\mu_0 T_c V) \cdot (dH_c/dT)_{|T \rightarrow T_c}^2 \sim (\mu_0 T_c V / 2\kappa^2) \cdot (dH_{c2}/dT)_{|T \rightarrow T_c}^2$ . Hence  $\lambda(0)$  can also be deduced from  $C_p$  measurements by deducing  $H_{c2}(T)$  from the shift of the specific heat anomaly under magnetic field and writing  $\lambda(0)^2 = \kappa^2 \Phi_0 / 2\pi H_{c2}(0)$  with  $\kappa^2 \sim (\mu_0 T_c V / 2\Delta C_p) \cdot (dH_{c2}/dT)_{|T \rightarrow T_c}^2$  and from WHH theory we know  $H_{c2}(0) \sim 0.69 T_c \cdot (dH_{c2}/dT)_{|T \rightarrow T_c}$  [86]. It is important to note that the corresponding  $\lambda(0)$  values do not depend on any demagnetization correction. As shown in table 6.1 and figure 6.8, they exceeds those deduced from  $H_{c1}$  by 30%.

### 6.3 Scanning nano-squid microscopy measurements

Since the variation of penetration depth can be obtained from tunnel diode oscillator measurements, and the value of penetration depth can be calculated from the lower critical field and heat capacity measurements, combining these techniques, one can get the temperature dependence of the superfluid density. However, the calculation of penetration depth from the lower critical field and heat capacity measurements may be subject to modification from the sample geometry, or unconventional behavior. Thus it is important to check the result with the one from some technique which can measure the penetration depth directly. Scanning nano-squid microscopy is one of this kind of techniques. Thus we also did scanning nano-squid microscopy measurements on  $\text{Ba}(\text{Fe}_{1-x}\text{Ni}_x)_2\text{As}_2$  single crystals, on which the tunnel diode oscillator measurements were performed.

#### 6.3.1 Penetration depth measurements

For each sample, we did the measurements at several different positions. Figure 6.4 shows two magnetic images we took at different positions of the  $\text{Ba}(\text{Fe}_{0.935}\text{Ni}_{0.065})_2\text{As}_2$  single crystal. These two images were taken at the same temperature and magnetic field after a field cooling process, but there are more vortices in (a) than in (b). This is because (a) is close to the edge of the sample and (b) is close to the center of the sample. The vortices accumulate at the edge of the sample due to pinning [104, 210].

Since taking a big image with high resolution will take too long time, we just chose some small regions where one or two isolated vortices are present to acquire high resolution images. From

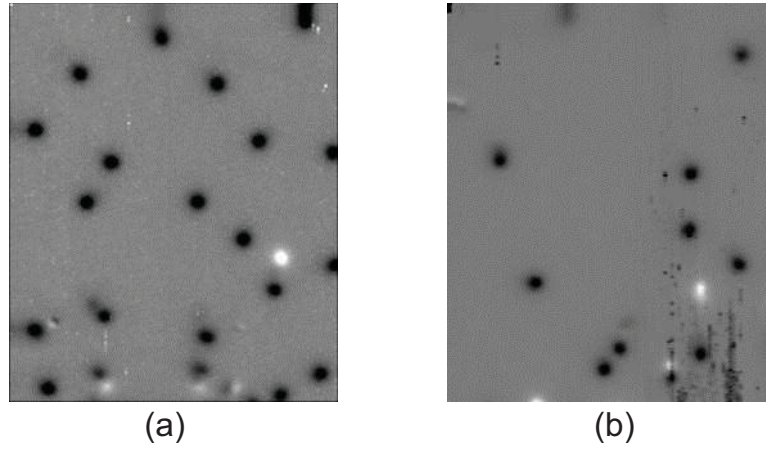


Figure 6.4: Two magnetic images we took at different position of  $\text{Ba}(\text{Fe}_{0.935}\text{Ni}_{0.065})_2\text{As}_2$  single crystal at  $T = 700$  mK and  $H = -0.75$  G. Both of the sizes of the two images are  $70 \mu\text{m} \times 85 \mu\text{m}$ . The reason for more vortices in (a) than (b) is that (a) is close to the edge of the sample and (b) is close to the center of the sample.

figure 6.4 one can see that some vortices are not round and some have a tail, a feature we will discuss later. Usually we made the high resolution images for the round vortices at 700 mK to 1.7 K, then we fitted the penetration depth of the samples at different temperatures from the vortices in the high resolution images.

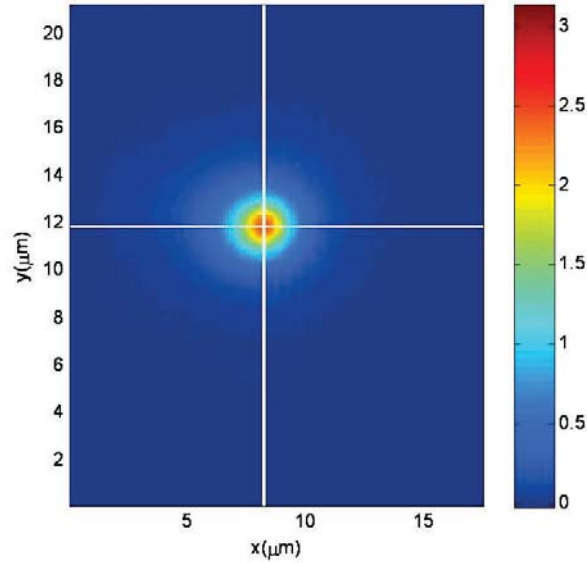


Figure 6.5: Fitting the penetration depth from the magnetic image. We convert the image from the critical current of SQUID to magnetic field, then use equation 6.1 to fit the vortex profile along a horizontal and vertical line. The color bar is calibrated in units of gauss.

Figure 6.5 shows how we fitted the penetration depth from the magnetic image. First we convert the image from the critical current of SQUID to magnetic field with the  $I_c - B$  curve we acquired before the scanning measurements, as shown in figure 5.9. Then we find by a fitting procedure the center of the vortex and take out the horizontal and vertical profiles to fit  $\lambda$ . When the thickness of the sample  $d \gg \lambda$ ,  $d$  can be considered as infinite, so equation 5.5 becomes[188]

$$h_z(r, z) = \frac{\Phi_0}{2\pi\lambda^2} \int_0^\infty dk \frac{kJ_0(kr)}{k^2 + \lambda^{-2}} \frac{\tau}{k + \tau} e^{-kz} \quad (6.1)$$

where  $\tau = \sqrt{k^2 + \lambda^{-2}}$  and  $J_0(x)$  is Bessel function. We fitted the profiles of several vortices in each sample at different temperatures. The results of  $\text{Ba}(\text{Fe}_{0.935}\text{Ni}_{0.065})_2\text{As}_2$  are shown in figure 6.6. From the fitting, we got  $\lambda \simeq 610 \pm 80$  nm. All the results of the penetration depths of the five different doping level samples we measured are shown in table 6.1 and figure 6.8.

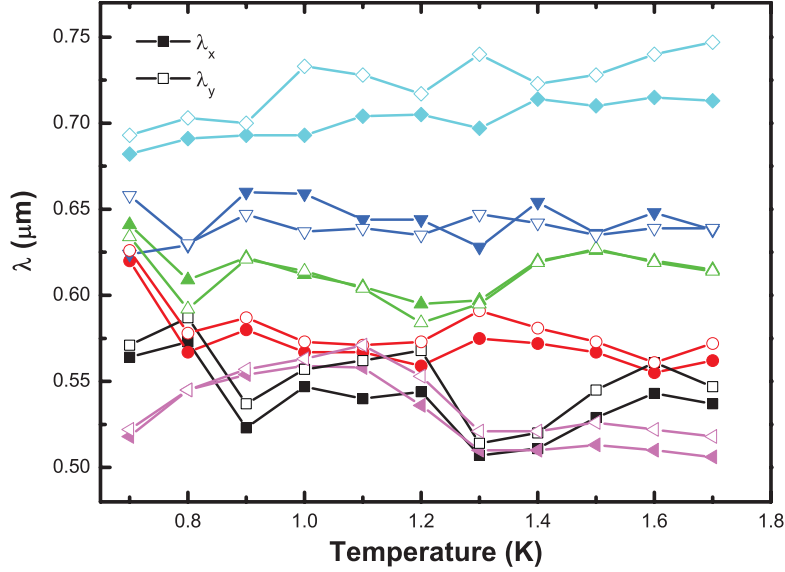


Figure 6.6: Fitting results of  $\text{Ba}(\text{Fe}_{0.935}\text{Ni}_{0.065})_2\text{As}_2$ . The solid symbols are from horizontal profile fitting and the open symbols are from vertical profile fitting. From the fitting, we got  $\lambda \simeq 610 \pm 80$  nm for this sample.

Since  $\tilde{\rho} = (1 + \Delta\lambda/\lambda)^{-2}$ , combining with the TDO results, we obtained the temperature dependent superfluid densities of the  $\text{Ba}(\text{Fe}_{1-x}\text{Ni}_x)_2\text{As}_2$  samples. We used the clean two-gap model to fit the temperature dependent superfluid densities as we did on  $\text{Ba}_{0.6}\text{K}_{0.4}\text{Fe}_2\text{As}_2$  single crystals. As mentioned in chapter 3, for a superconductor with two gaps, the normalized superfluid density may be written as:  $\tilde{\rho}_s = x\tilde{\rho}_s^1 + (1-x)\tilde{\rho}_s^2$ , where  $x$  is the fraction of superfluid density  $\tilde{\rho}_s^1$  associated with the gap  $\Delta_0^1$  [87]. The fitting results of  $\text{Ba}(\text{Fe}_{0.971}\text{Ni}_{0.029})_2\text{As}_2$  and  $\text{Ba}(\text{Fe}_{0.935}\text{Ni}_{0.065})_2\text{As}_2$  are shown in figure 6.7. For the two samples, both of the values of the two gaps are smaller than the BCS value, which is not compatible with the picture of two gap superconductors: Usually, for a two gap superconductor, one gap should be bigger than the BCS gap and the other smaller than the BCS gap, or it is hard to explain why the  $T_c$  of the superconductor is higher than the two gaps. For example: in  $\text{MgB}_2$ , one gap is  $\Delta = 0.69k_B T_c$ , smaller than the BCS value, and the other gap is  $\Delta = 1.86k_B T_c$ , which is bigger than the BCS value. The result we got in  $\text{Ba}_{0.6}\text{K}_{0.4}\text{Fe}_2\text{As}_2$  is also like that. Therefore, the clean two-gap model is not suitable for the  $\text{Ba}(\text{Fe}_{1-x}\text{Ni}_x)_2\text{As}_2$  system.

Figure 6.8 presents all penetration depth results for the three techniques: lower critical field, heat capacity and scanning nano-squid microscopy measurements. The results from the scanning nano-squid microscopy measurements are higher than the results from the lower critical field and heat capacity measurements. However, the behavior of all these results are consistent: on both sides of the superconducting dome,  $\lambda(0)$  can be scaled with  $T_c$  by a power law.

Since the penetration depth  $\lambda$  strongly varies with the critical temperature of the sample and can be scaled with  $T_c$  by a power law for both underdoped and overdoped samples, and the temperature dependence of  $\lambda$  is non exponential but varies as  $\Delta\lambda \propto T^{2.3 \pm 0.3}$  for  $T < T_c/3$ , all of these strongly suggest that pair breaking effects are important in the  $\text{Ba}(\text{Fe}_{1-x}\text{Ni}_x)_2\text{As}_2$  system. The superconducting condensate is hence progressively destroyed on both side of the superconducting dome, in agreement with the observation of a non residual Sommerfeld coefficient in specific heat data in Co-doped samples[201].

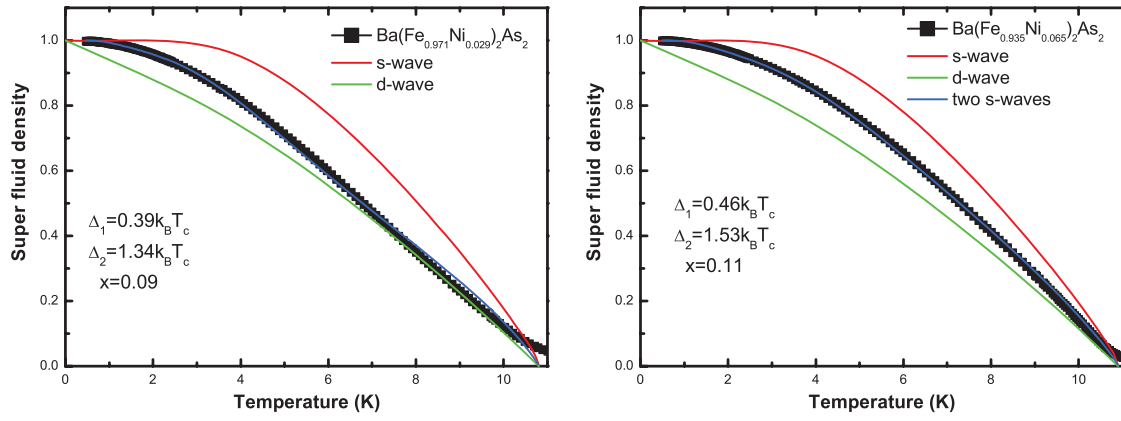


Figure 6.7: The two fitting results for the temperature dependent superfluid densities of  $\text{Ba}(\text{Fe}_{0.971}\text{Ni}_{0.029})_2\text{As}_2$  and  $\text{Ba}(\text{Fe}_{0.935}\text{Ni}_{0.065})_2\text{As}_2$  with clean two-gap model  $\tilde{\rho}_s = x\tilde{\rho}_s^1 + (1-x)\tilde{\rho}_s^2$ , where  $x$  is the fraction of superfluid density  $\tilde{\rho}_s^1$  associated with the gap  $\Delta_0^1$ . For the two samples, both of the values of the two gaps are smaller than the BCS value, which excludes a clean two-gap model for the  $\text{Ba}(\text{Fe}_{1-x}\text{Ni}_x)_2\text{As}_2$  system.

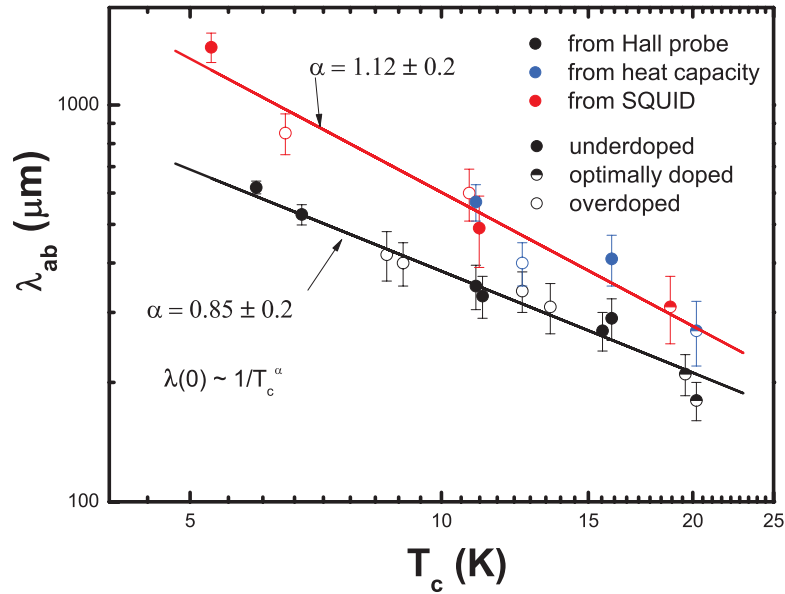


Figure 6.8: London penetration depth at  $T \rightarrow 0$  [ $\lambda(0)$ ] as a function of the critical temperature  $T_c$  in  $\text{Ba}(\text{Fe}_{1-x}\text{Ni}_x)_2\text{As}_2$  crystals deduced from  $H_{c1}$  measurements (black), heat capacity measurements (blue) and scanning nano-SQUID microscopy measurements (red). The thick line corresponds to  $1/T_c^\alpha$  with  $\alpha = 0.85 \pm 0.2$  for the black one and  $\alpha = 1.12 \pm 0.2$  for the red one.

According to the Quantum Critical Point (QCP) theory, for a superconductor,  $T_c$  vanishes as  $T_c \propto \delta^{z\nu}$  when approaching the QCP, where  $\delta$  is the deviation in doping from the QCP,  $z$  is the quantum dynamical exponent and  $\nu$  the correlation length exponent, respectively. At  $T = 0$ , the superfluid density vanishes as  $\rho_s(0) \propto \delta^{(z+D-2)\nu}$ , where  $D$  is the spatial dimensionality. By eliminating  $\delta$  between these two relations, one can obtain the scaling relationship:  $\rho_s(0) \propto T_c^{(z+D-2)/z}$  [211, 212, 213]. In  $D = 3$  dimensions,  $\rho_s(0) \propto T_c^{(z+1)/z}$ . Since  $\rho_s(0) \propto 1/\lambda_0^2$ , one can get  $\lambda_0 \propto 1/T_c^{(z+1)/2z}$ . For the case of presence of nodes in the superconducting gap,  $z = 1$ ,  $\lambda_0 \propto 1/T_c$ , and for the case of presence of pair breaking,  $z = 2$ ,  $\lambda_0 \propto 1/T_c^{0.75}$  [208, 214, 215]. On the other hand,  $1/\xi_0$  is also expected to scale as  $T_c^{(z+1)/2z}$ . In the dirty limit,  $\xi \sim (\xi_0 l)^{0.5}$ , where  $\xi_0$  and  $l$  are the coherence length without disorder and the mean free path, and  $\lambda \sim \lambda_0(\xi_0/l)^{0.5}$ , where  $\lambda_0$  is the

penetration depth without disorder. Combining all the relations above, one can obtain: for the case of the dirty limit and  $z = 2$ ,  $\lambda_0 \propto 1/T_c^{1.13}$ , which is consistent with the results we got from the scanning nano-SQUID microscopy measurements. Thus our results clearly indicates that pair breaking effects are important in the  $\text{Ba}(\text{Fe}_{1-x}\text{Ni}_x)_2\text{As}_2$  system. Those pair breaking effects are most probably a consequence of the  $s\pm$  pairing mechanism and could be at the origin of a quantum critical behavior[208].

### 6.3.2 Flux penetration measurements

In order to find out the reason for the difference between the results from the scanning nano-squid microscopy measurements and lower critical field measurements, we did the flux penetration measurements on the optimally doped sample  $\text{Ba}(\text{Fe}_{0.958}\text{Ni}_{0.042})_2\text{As}_2$ . What we did is almost the same as the low critical field measurements by Hall probes. We applied a magnetic field  $H_a$  and took an scanning nano-SQUID microscopy image, then we decreased the magnetic field to 0G and took an image again. When  $H_a < H_p$ , no vortex penetrated the sample. When  $H_a > H_p$ , we could see some vortices remained pinned in the sample in the 0G image. The difference between our measurements and the low critical field measurements by Hall probes is that we can directly measure the magnetic field at the edge of the sample to obtain  $H_{c1}$  without any calculation.

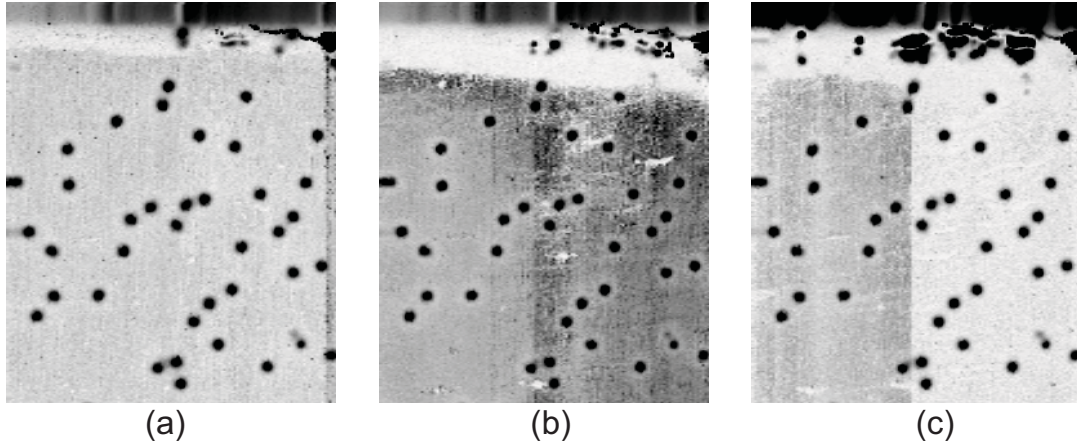


Figure 6.9: Flux penetration measurements on the edge of  $\text{Ba}(\text{Fe}_{0.958}\text{Ni}_{0.042})_2\text{As}_2$  sample. (a), (b) and (c) were taken after increasing the magnetic field to 15 G, 30 G and 45 G, then decreasing to 0 G, respectively. The flux began to penetrate the sample from 45 G. All the images were taken at  $T = 800$  mK and the sizes are  $70 \mu\text{m} \times 85 \mu\text{m}$ .

Figure 6.9 shows three images we took after increasing the magnetic field to 15 G, 30 G and 45 G respectively, then decreasing to 0 G. There are some magnetic traces on the upper right part of the images, the sizes of which are smaller than the vortices in the images. As the applied magnetic field became higher and higher, due to the magnetization effect, more and more black spots appeared in this part. From figure 6.9 (c) one can see some vortices remained pinned in the sample after the magnetic field decreased to 0G. Since we increased the magnetic field with a step 5 G, the flux began to penetrate the sample at  $H = 40 \sim 45$  G ( $H_p = 42.5 \pm 2.5$  G). Now we can do the same calculation as the lower critical field measurements. From the dimensions of the sample, the geometrical barriers  $\alpha_{GB} = 1/\tanh(\sqrt{\beta d/w}) = 1/\tanh(\sqrt{0.67 * 10/300}) = 6.74$ . Thus we can get  $H_{c1} = \alpha_{GB}H_p = 286 \pm 16$ Gs, which is even higher than the result from the lower critical field measurements. We think this is because the sample is too thin. The formula of the geometrical barriers is not suitable for this sample any more, and this is why for lower critical field measurements thick samples are preferred.

However, we can also get  $H_{c1}$  directly from the magnetic field profile of the image at magnetic field.

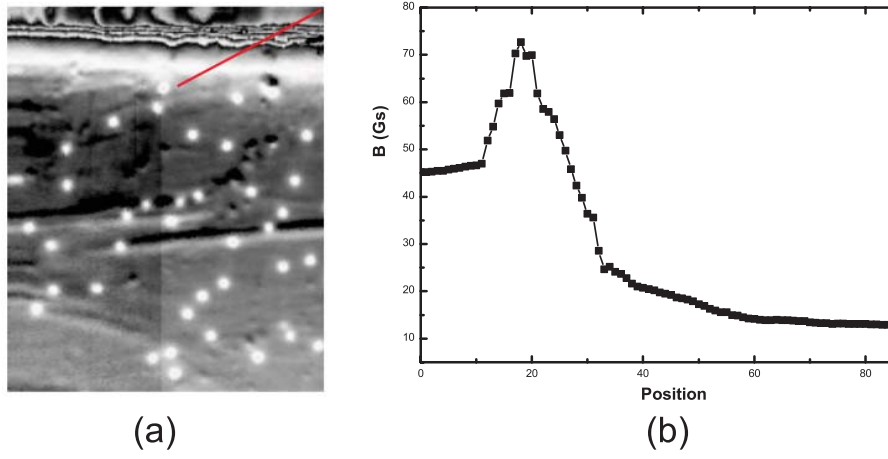


Figure 6.10: (a) Image taken at  $T = 800$  mK and  $H = 45$  G. The size is  $70 \mu\text{m} \times 85 \mu\text{m}$ . (b) The magnetic field profile along the red line in (a). The maximum is  $73 \pm 3$  G.

Figure 6.10 (a) is an image taken at  $T = 800$  mK and  $H = 45$  G. The black and white lines in the top part of the image is from the periodic modulation of the critical current of SQUID with magnetic field, shown in figure 5.9. Because of Meissner effect, the applied magnetic field was compressed on the edge of the sample. The range of the magnetic field spans several periods of the critical current of SQUID. The black and white lines correspond to the minimums and maximums of the critical current of SQUID in different periods. There are more black and white lines in the right side than the left side in the image, because the scanner didn't move any more in the region very close to the edge of the image. The right side of the sample was a bit farther away than the left side to the edge of the image, so we could see the whole distribution of the magnetic field near the edge of the sample in the right side of the image. Figure 6.10 (b) is the magnetic field profile along the red line in (a). The maximum is  $73 \pm 3$  G. Since the flux just began to penetrate the sample at  $H \sim 45$  G, so the lower critical field of the sample should be very close to the maximal magnetic field on the edge of the sample, i.e.  $H_{c1} = 73 \pm 3$  G. The  $\lambda(0)$  we got from the fitting of vortices for this sample is  $310 \pm 60$  nm, and  $\kappa \sim 75$  from other measurements on the sample from the same batch. Thus  $H_{c1} = (\Phi_0/4\pi\lambda^2)\ln(\kappa) = 74 \pm 20$  G, very consistent with the result above.

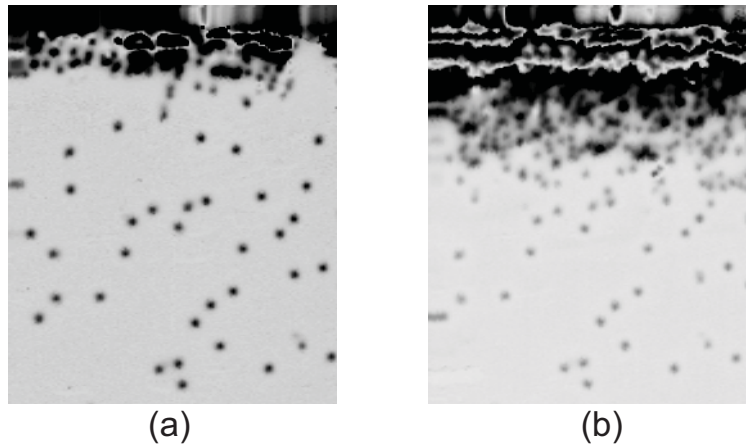


Figure 6.11: Flux penetration images near the edge of  $\text{Ba}(\text{Fe}_{0.958}\text{Ni}_{0.042})_2\text{As}_2$  sample. (a) and (b) were taken after increasing the magnetic field to 60 G and 120 G, then decreasing to 0 G, respectively. Both images were taken at  $T = 800$  mK and the sizes are  $70 \mu\text{m} \times 85 \mu\text{m}$ . The flux penetrates the sample  $14 \mu\text{m}$  and  $36 \mu\text{m}$  for (a) and (b), respectively.

From figure 6.11 one can see, the flux penetrates the sample very slowly. For  $H = 60$  G, the flux only

enters the sample  $14 \mu\text{m}$ , and for  $H = 120 \text{ G}$  only  $36 \mu\text{m}$ . In the lower critical field measurements, the active area of the Hall probe is  $10 \mu\text{m} \times 10 \mu\text{m}$ . Thus if the Hall probe is not on the edge of the sample, the results from the measurements will be overestimated. From figure 6.9 one also can see, the flux began to penetrate only from some parts of the sample. Thus even if the Hall probe is very close the edge of the sample, the results from the measurement still can be overestimated if the flux doesn't penetrate to the active area of the Hall probe at the beginning. We think this can explain why the penetration depths obtained from scanning nano-squid microscopy measurements are bigger than the results from lower critical field measurements.

### 6.3.3 Anti-vortices, weak pinning and partial vortices

As shown in figure 6.4, and also figure 6.12 and figure 6.13, one can see two different kinds of vortices, black and white. Usually, when a superconductor is cooled down to a temperature below  $T_c$  in magnetic field, the residual flux is bundled to vortices pinned in the superconductor, consequently all vortices should have the same chirality.

We frequently see vortices having an asymmetric shape as if they would have a tail. We think this is because there is some magnetic or non superconducting material on the sample surface or inside the sample. On the bottom of both figure 6.4 (a) and (b), some black-white spots are visible, and both their lateral size and amplitude are smaller than would be a vortex. We attribute this signal to the presence of a magnetic dipole, formed possibly by iron or nickel oxides left over from the synthesis process or oxidation of the sample surface. These magnetic materials disturb the magnetic field distribution of the vortices when they are close to the vortices. When the magnetic moments of these oxides are opposite to the applied magnetic field which is not strong enough to turn the magnetic moments over, opposite vortices can form under these oxides. These oxides may produce some variability to some local and surface sensitive measurements. The capacity to visualize them is very important.

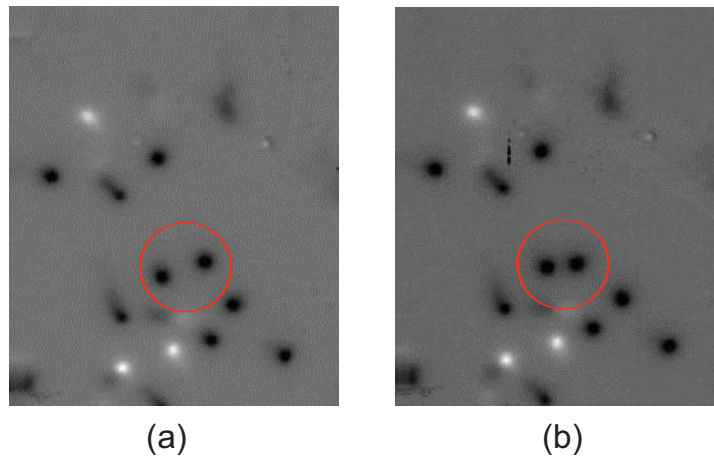


Figure 6.12: Two magnetic images from two consecutive scans at the same position of  $\text{Ba}(\text{Fe}_{0.926}\text{Ni}_{0.074})_2\text{As}_2$  single crystal at  $T = 700 \text{ mK}$  and  $H = -0.75 \text{ G}$ . Both images are  $70 \mu\text{m} \times 85 \mu\text{m}$  in size. Just after heating to  $1.7 \text{ K}$ , one vortex in (a) moved to another position, as indicated by the red ring.

Figure 6.12 shows two magnetic images from two consecutive scans at the same position of the  $\text{Ba}(\text{Fe}_{0.926}\text{Ni}_{0.074})_2\text{As}_2$  sample at  $T = 700 \text{ mK}$ . Just after heating to  $1.7 \text{ K}$ , one vortex moved to another position. We also observed this kind of phenomenon on other samples. For a strong pinning superconductor, the vortex cannot move at low temperatures, because thermal activation energy is much smaller than the pinning energy. Thus we think the pinning is very weak in some regions of the  $\text{Ba}(\text{Fe}_{1-x}\text{Ni}_x)_2\text{As}_2$  samples.

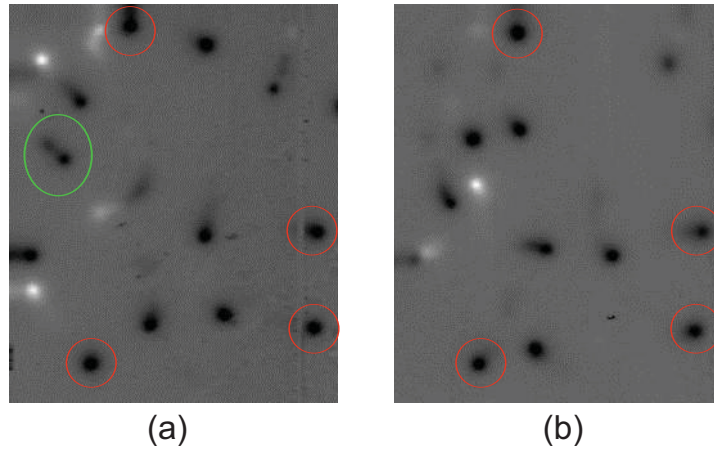


Figure 6.13: Two magnetic images at the same position of  $\text{Ba}(\text{Fe}_{0.926}\text{Ni}_{0.074})_2\text{As}_2$  single crystal at  $T = 700$  mK and  $H = -0.75$  G from two consecutive scans, but before (b) was taken, the sample was heated above  $T_c$  then cooled down again. Both of the sizes of the two images are  $70 \mu\text{m} \times 85 \mu\text{m}$ . One can see the positions of more than half of the vortices changed. The vortices sitting the same position are indicated by red rings. The vortex in the green ring seems to be separated to two parts.

We also used another way to check if the pinning is really weak in this family. For a strong pinning material, as the pinning energy is high compared to thermal energy, one expects that for different cooling down processes to the same magnetic field, the vortices will stay at the same positions. Figure 6.13 (a) and (b) are two magnetic images at the same position of the  $\text{Ba}(\text{Fe}_{0.926}\text{Ni}_{0.074})_2\text{As}_2$  sample at  $T = 700$  mK and  $H = -0.75$  G from two consecutive scans, but before (b) was taken, the sample was heated above  $T_c$  then cooled down again. The vortices sitting the same position are indicated by red rings. However, more than half of the vortices in the images changed their positions. Therefore, we think the pinning in the  $\text{Ba}(\text{Fe}_{1-x}\text{Ni}_x)_2\text{As}_2$  samples is not homogeneous, in some parts of the samples, the pinning is very weak. This inhomogeneity maybe come from the synthesis process or maybe it is one intrinsic property of this family, and this can explain why some STM measurements can see vortex lattice[145] and some cannot in the iron-based superconductors[140].

As indicated by the green ring in figure 6.13, one vortex seems to be separated into two parts. We observed this kind of vortex in all the  $\text{Ba}(\text{Fe}_{1-x}\text{Ni}_x)_2\text{As}_2$  samples we measured. It is similar to the pancake vortices observed in cuprates[216]. Because of the big anisotropy and weak interlayer coupling, the sheared pancake vortices can break into separate straight stacks of pancakes to create a kinked structure instead of tilting in cuprates[217]. Thus nearly isolated flux features with less than one flux quantum  $\Phi_0$  through the sample surface can be observed[218].

However, the anisotropy of  $\text{Ba}(\text{Fe}_{1-x}\text{Ni}_x)_2\text{As}_2$  is believed to be very small (of the order of 2), and the electronic structure is 3D not 2D. The pancake model seems not so suitable in this case. Specially from figure 6.14, we think here that the mechanism responsible for the splitting of the vortices it is much more complicated than the pancake model. Figure 6.14 (a) is a big image taken at  $T = 700$  mK and  $H = -0.75$  G. We chose the regions indicated by red rectangles to do fine scans, and the images taken at different temperatures are shown in figure 6.14(b). Some isolated vortices with one flux quantum  $\Phi_0$  in (a) separated to several "partial vortices" with each one  $< \Phi_0$ , which could move at temperature  $T < 1$  K. By integrating the images, we found that the flux of some "partial vortices" is close to  $0.5\Phi_0$ .

The difference between figure 6.14 (a) and (b) may be from a image effect from the different scan speed. If the vortices were moving slowly, when scanning quickly, we could see normal vortices, but when scanning slowly, it is possible to see some strange shape vortices. Thus we rescanned the region of (a) with the same speed. As shown in figure 6.14 (c), the shapes of vortices became very

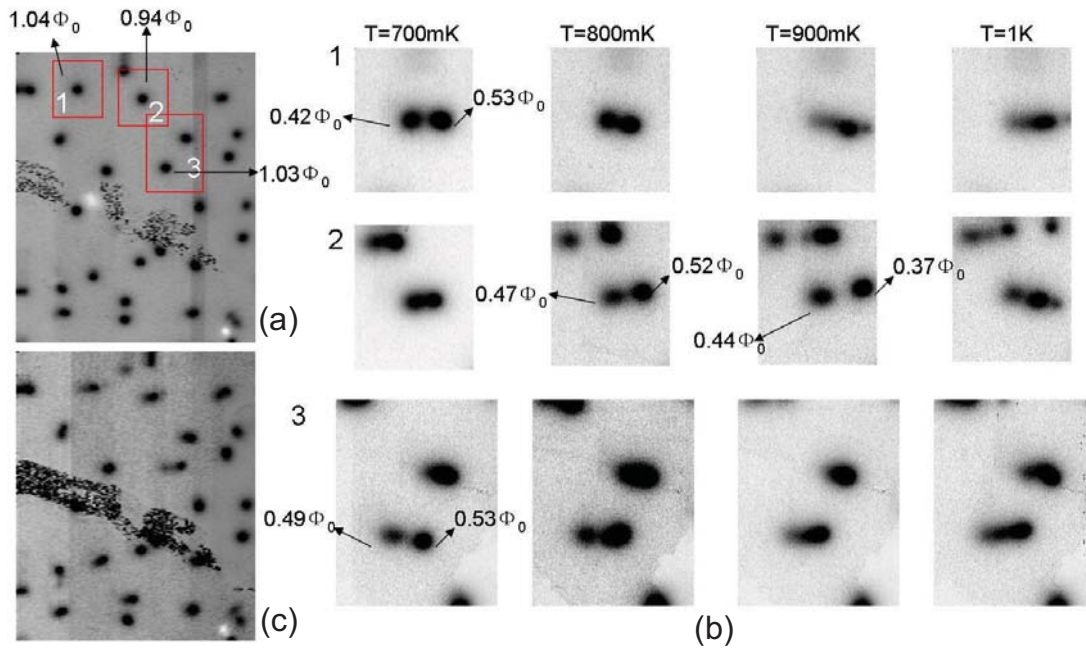


Figure 6.14: Measurements on  $\text{Ba}(\text{Fe}_{0.935}\text{Ni}_{0.065})_2\text{As}_2$  at  $H = -0.75$  G. (a) and (c) were taken at  $T = 700$  mK. Both of the images (a) and (c) are  $70 \mu\text{m} \times 85 \mu\text{m}$ . (b) are fine scans in the regions indicated by red rectangles in (a). Some isolated vortices with one flux quantum  $\Phi_0$  in (a) separated to several "partial vortices" with each one  $< \Phi_0$ , which could move at temperature  $T < 1\text{K}$ . The sizes of the images in (b) are  $17.5 \mu\text{m} \times 21.25 \mu\text{m}$  for 1 and 2, and  $23.8 \mu\text{m} \times 30.4 \mu\text{m}$  for 3. For more details see text.

different from the vortices in (a). This means that the "partial vortices" are not from the image effect from the slow movements of the isolated vortices. Some isolated vortices really separated to several "partial vortices".

Just like we did on the Rhenium film, in order to find out the reason for the movements of the "partial vortices", we took images on the sample with different SQUID/sample distance  $z$ . The images in figure 6.15 were taken in the region 2 of figure 6.14 (a). When  $z \geq 0.45 \mu\text{m}$ , all images are the same. When  $z = 0.35 \mu\text{m}$ , the "partial vortices" began to move and the image became different. Therefore, it is very similar to the Rhenium film: the pinning is very weak, vortices can be moved by the force between the SQUID loop and vortices. However, the movements of vortices are along the scanning direction in the Rhenium film, but it is a bit different in the  $\text{Ba}(\text{Fe}_{0.935}\text{Ni}_{0.065})_2\text{As}_2$  sample, and this is hard to understand.

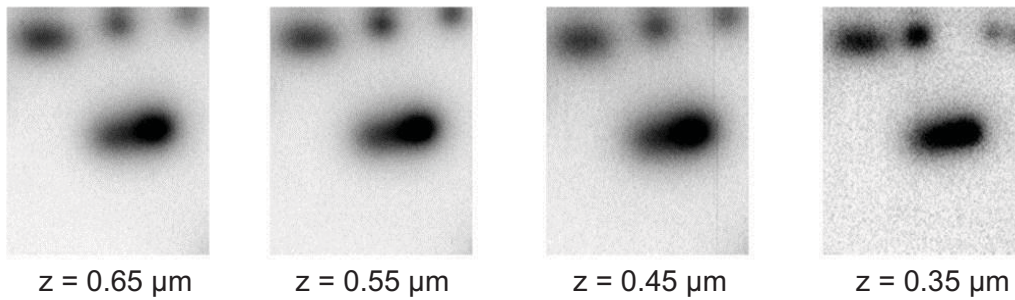


Figure 6.15: Scans in the region 2 of figure 6.14 (a) with different SQUID/sample distance  $z$  at  $T = 700$  mK and  $H = -0.75$  G. The size of the images is  $17.5 \mu\text{m} \times 21.25 \mu\text{m}$ . When  $z \geq 0.45 \mu\text{m}$ , all images are the same. When  $z = 0.35 \mu\text{m}$ , the image becomes different.

Even if the movement of "partial vortices" is due to the SQUID/vortex interaction, the reason for the separation of the isolated vortices to "partial vortices" is still elusive. Maybe it is some special properties of  $s\pm$  order parameter. More experiments are needed to clarify this issue.

### 6.3.4 $\lambda(T)$ measurements

From equation 6.1 we know, if the SQUID/sample distance  $z$  and the distance between the SQUID and the center of vortex  $r$  are known, from the magnetic field measured by the SQUID, we can calculate  $\lambda$ . Therefore, if we put the SQUID above the center of one vortex and keep the SQUID/sample distance as a constant, by measuring the magnetic field at different temperature, we can get the temperature dependence of  $\lambda$ . By this way, we can obtain  $\lambda(T)$  more simply and quickly with higher resolution than fitting  $\lambda$  from images at different temperature.

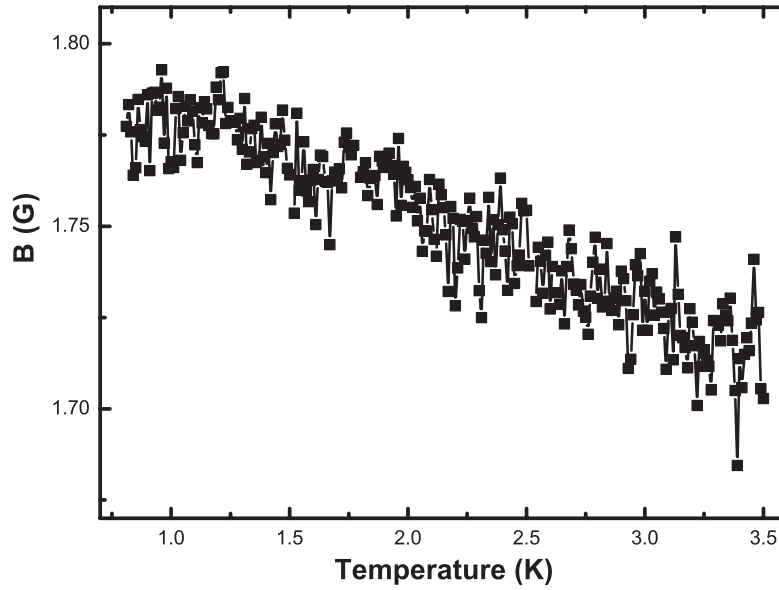


Figure 6.16: Temperature dependence of the magnetic field measured with SQUID  $0.54 \mu m$  above the center of one vortex in  $Ba(Fe_{0.958}Ni_{0.042})_2As_2$  sample.

From the fitting of  $\lambda$  from isolated vortex images at different temperature, we know the background of the vortex fitting also changing with temperature. Thus for the  $\lambda(T)$  measurements, we need to measure the magnetic field above the center of vortex and some part without any vortex to get the background, then subtract the background to get the magnetic field of the vortex. Figure 6.16 is the temperature dependence of the magnetic field measured with SQUID  $0.54 \mu m$  above the center of one vortex in  $Ba(Fe_{0.958}Ni_{0.042})_2As_2$  sample. The magnetic field decreases as temperature increasing.

However, the noise of the data is quite high, and because of the hysteresis of the scanners, the SQUID is not really above the center of the vortex, thus we cannot use these data to calculate  $\lambda(T)$ . Nevertheless, our measurement shows the possibility to do the  $\lambda(T)$  measurements with our instrument by improving the resolution of the SQUID and the measurement program.

## 6.4 Summary

In summary, we did lower critical field, tunnel diode oscillator, heat capacity and scanning nano-squid microscopy measurements on systematic doped  $Ba(Fe_{1-x}Ni_x)_2As_2$  single crystals. All the

measurements shows that  $\lambda(0)$  can be scaled with  $T_c$  by a power law on both sides of the superconducting dome, and the temperature dependence of the penetration depth is power exponential in all measured samples, indicating the presence of pair breaking effects in this system. Combining the results from tunnel diode oscillator and scanning nano-squid microscopy measurements, the clean two-gap model is excluded for this system. The results from the scanning nano-SQUID microscopy measurements is consistent with the proximity of a quantum critical point.

From the flux penetration measurements on  $\text{Ba}(\text{Fe}_{0.958}\text{Ni}_{0.042})_2\text{As}_2$  sample, we obtained  $H_{c1}$  directly, which is consistent with the value calculated with  $\lambda(0)$  from the vortex fitting. We also find that  $H_{c1}$  from the lower critical field measurements could be overestimated, yielding a small  $\lambda(0)$ , which can explain the  $\lambda(0)$  from the scanning nano-squid microscopy measurements are bigger than the results from the lower critical field measurements.

Some anti-vortices and vortices with tails were frequently observed on the  $\text{Ba}(\text{Fe}_{1-x}\text{Ni}_x)_2\text{As}_2$  samples, which maybe produced from some iron or nickel oxides from the synthesis process or the oxidation of the sample surface. Some vortices moved at very low temperature, which means the pinning is very weak in some regions of the  $\text{Ba}(\text{Fe}_{1-x}\text{Ni}_x)_2\text{As}_2$  samples. Some isolated vortices separated to "partial vortices", and the "partial vortices" also could move at low temperature. The movement of "partial vortices" could be due to the SQUID/vortex interaction, but the reason for the separation is still elusive and needs more experiments to clarify.

We tried to do  $\lambda(T)$  measurements. Because of the hysteresis of the scanners and the noise of the measurements, we could not obtain  $\lambda(T)$  yet. Nevertheless, by improving the resolution of the SQUID and the measurement program, it is possible to do the  $\lambda(T)$  measurements with our instruments.

# 7

## Summary

Though 100 years old, superconductivity is still one of the most active fields in condensed matter physics. The discovery of new superconductors attracts always great attention. Especially the high temperature superconductors such as the cuprate and iron-based superconductors put the superconductivity research in the forefront of condensed matter physics. The high temperature superconductivity is so mysterious and promising, that a lot of scientists devoted themselves to this subject. However, it is so elusive, that many questions remain open even more than twenty years after its discovery. The hope is that the research on the newly discovered iron-based superconductors may help to shed more light on this issue.

Hosono's group initiated the study of iron-based superconductors in 2006, and the subject came to the forefront in 2008 after the discovery of  $\text{LaFeAsO}_{1-x}\text{F}_x$  with  $T_c \simeq 26$  K. Since then, an enormous amount of research has been done on this new ever growing family, with  $T_c$  reaching temperatures as high as 55 K. Though the iron-based superconductor has a layer structure and a rather high critical temperature approaching those of the cuprates, both band calculation and experiments show that the iron-based superconductor is quite different from the cuprate. There are five sheets on the fermi surface of the iron-based superconductor, which is much more complicated than the cuprate, and the electronic structure is three dimensional rather than two dimensional. Calculation shows that electron-phonon coupling is not sufficient to explain superconductivity in the whole family of iron-based superconductors. Up to now,  $s\pm$ -wave, an extended  $s$ -wave pairing with opposite signs of the order parameters between the hole pockets and the electron pockets mediated by magnetic excitations, is a strong candidate for the gap symmetry in iron-based superconductors.

However, until now the experimental results on the iron-based superconductors don't give a consistent picture. For different compounds, different groups gave different results. Even for the same compound, different techniques gave different results. Maybe these inconsistencies stem from different sample qualities and geometries, or by the fact that different techniques get different information of the samples as the information obtained is often model dependent, and as the complicated electronic structures of the iron-based superconductors is not yet fully understood, different models may give rise to different interpretations. In this thesis we have mainly presented the work we have done on the Ba-122 iron-based superconductors, from sample synthesis to physical properties, gap structure and order parameter symmetry research by resistivity, Hall probe, point-contact spectroscopy, tunnel diode oscillator, heat capacity and scanning nano-squid microscopy measurements.

We synthesized some  $\text{Ba}_{1-x}\text{K}_x\text{Fe}_2\text{As}_2$  single crystals using FeAs as the self-flux. The characterization of the crystals with diffraction and energy dispersive analysis of x-ray, AC susceptibility and resistiv-

ity measurements showed their good quality. The temperature dependent resistivity measurements in magnetic fields up to 9 T showed that the  $\text{Ba}_{1-x}\text{K}_x\text{Fe}_2\text{As}_2$  system possesses a very high upper critical field and a very low superconducting anisotropy ratio of around 2 for all doping level samples. We also confirmed our finding of the anisotropy ratio by investigating the angle dependent resistivity in the  $\text{Ba}_{0.6}\text{K}_{0.4}\text{Fe}_2\text{As}_2$  single crystals, which yielded a similar values of the anisotropy ratio  $\Gamma$ . The resistivity measurements showed unconventional and 3D superconducting properties in the  $\text{Ba}_{1-x}\text{K}_x\text{Fe}_2\text{As}_2$  system, consistent with high magnetic field and thermodynamic measurements on different compounds of iron-based superconductors.

Both global and local magnetization measurements with VSM and Hall probe were employed to investigate the superconducting gap structure and order parameter of  $\text{SmFeAsO}_{0.9}\text{F}_{0.1}$  (F-SmFeAsO) polycrystal and  $\text{Ba}_{0.6}\text{K}_{0.4}\text{Fe}_2\text{As}_2$  single crystal. A simple isotropic *s*-wave type or a *d*-wave type of the order parameter were excluded for the F-SmFeAsO sample. A good agreement between the experimental data and the theory within the framework of a two *s*-wave gap or an anisotropic *s*-wave gap picture suggests that there are no nodes in the superconducting energy gap in F-SmFeAsO. The superfluid density of  $\text{Ba}_{0.6}\text{K}_{0.4}\text{Fe}_2\text{As}_2$  exhibits a pronounced kink at  $T \sim 15$  K, indicating a multi-gap nature in this compound. By using the two-*s*-wave-gap weak coupling BCS model to fit the data, we obtained a small gap of  $\Delta_a(0) \simeq 2.0 \pm 0.3$  meV and a large gap of  $\Delta_b(0) \simeq 8.9 \pm 0.4$  meV in  $\text{Ba}_{0.6}\text{K}_{0.4}\text{Fe}_2\text{As}_2$ .

With a "soft" point-contact technique, we fabricated highly transparent *c*-axis direction contacts to perform the Andreev reflection spectroscopy study on  $\text{Ba}_{0.6}\text{K}_{0.4}\text{Fe}_2\text{As}_2$  single crystals and a series of electron-doped  $\text{BaFe}_{2-x}\text{Ni}_x\text{As}_2$  single crystals over a wide doping range. For  $\text{Ba}_{0.6}\text{K}_{0.4}\text{Fe}_2\text{As}_2$ , a high Andreev reflection signal was obtained, but we could not discern a clear two-gap character in the results of our measurements. An extended *s*-wave with a gap function  $\Delta = \Delta_0 + \Delta_1 \cos(2\theta)$  can reproduce the experimental data well, yielding an anisotropic gap with  $\Delta_{max} = 7.4$  meV,  $\Delta_{min} = 2.8$  meV and  $\gamma = \Delta_{max}/\Delta_{min} = 2.7$ . The results from point-contact measurements on  $\text{Ba}_{0.6}\text{K}_{0.4}\text{Fe}_2\text{As}_2$  are different from the  $H_{c1}$  measurements. We think this is because the point-contact is along *c*-axis direction, so only a part of the Fermi surface is involved in this measurement. The measurements on a series of  $\text{BaFe}_{2-x}\text{Ni}_x\text{As}_2$  illustrated an evolution of the gap structure. The Andreev conductance spectra clearly show a full-gap state for underdoped crystals and a highly anisotropic, perhaps nodal-like gap state for overdoped crystals. Quantitative analysis of the spectral data of optimally-doped contacts using a generalized BTK formalism resolves two superconducting gaps in strong coupling limit. As a result from the analytical fitting, the small gap on the electron-like Fermi surface sheets shows a crossover from a nodeless in the underdoped side to a nodal feature in the overdoped region. This result provides evidence of the modulation of the gap amplitude on the Fermi surface with doping concentration, consistent with the calculation for the orbital dependent pair interaction mediated by the antiferromagnetic spin fluctuations.

We built a scanning nano-SQUID force microscope, which can take topographic and magnetic images simultaneously with a sub-micron resolution for the topographic images and a SQUID-size dependent spatial resolution for the magnetic images with an atomic force microscope based on the use of a tuning fork carrying the SQUID chip. Two cascaded PI controllers are used to regulate the tip/sample distance. The size of the SQUID is 0.6  $\mu\text{m}$  or 1.1  $\mu\text{m}$ , with a magnetic resolution about  $1.5 \times 10^{-4} \Phi_0 / \sqrt{\text{Hz}}$ . It can take image in a 4 mm  $\times$  4 mm region with a maximum scanning scale of 70.0  $\mu\text{m}$   $\times$  85.0  $\mu\text{m}$ . The work temperature region can be adjust from 160 mK to 9 K by different ways of thermal coupling between the sample and the various thermal baths. The scanning SQUID microscopy allows for obtaining an absolute value of the penetration depth of the magnetic field in superconductors. The measurements on a 80 nm epitaxially grown Rhenium film gave a penetration depth of about 103 nm extrapolated to  $T=0$ . The measurements also showed a very weak pinning force in the Rhenium film, indicating a high purity of the sample.

Lower critical field, tunnel diode oscillator, heat capacity and scanning nano-squid microscopy measurements were performed on the same systematically doped  $\text{Ba}(\text{Fe}_{1-x}\text{Ni}_x)_2\text{As}_2$  single crystals. The

---

$\lambda(0)$  from all the measurements can be scaled with  $T_c$  by a power law on both sides of the superconducting dome, and the temperature dependence of the penetration depth follows a unique power law for all measured samples, indicating the presence of pair breaking effects in this system. Combining the results from tunnel diode oscillator and scanning nano-squid microscopy measurements, the clean two-gap model is excluded for this system. The results of penetration depth from the scanning nano-SQUID microscopy measurements, which was verified by the flux penetration measurements, is consistent with a quantum critical behavior in dirty limit. From the scanning nano-SQUID microscopy measurements, we found that there some magnetic materials in the  $\text{Ba}(\text{Fe}_{1-x}\text{Ni}_x)_2\text{As}_2$  sample, and the pinning force is very different in different parts of the sample. These magnetic materials maybe stem from the synthesis process or the oxidation of the sample surface, and may produce some variability to some local and surface sensitive measurements.

After four years of intensive study, the mechanism behind the superconductivity of the iron-based superconductor is still disputed, but a lot of progress has been made. For example, compared with the cuprates, the electronic structures and magnetic properties of the iron-based superconductor are quite well understood. However, the determination the gap and pairing symmetry of the iron-based superconductor is still very difficult. Without phase sensitive measurements, the  $s\pm$ -wave superconducting energy gap is indistinguishable from the conventional  $s$ -wave superconducting energy gap unless nodal planes exist on the Fermi surface. So far, phase sensitive experiments are very rare for the iron-based superconductor. The scanning nano-SQUID microscopy measurements may provide some clues to this question. Determining the pairing symmetry of the iron-based superconductor will hopefully help determine the elusive mechanism of high temperature superconductivity.

# Bibliography

- [1] <http://www.magnet.fsu.edu/education>.
  - [2] H.K. Onnes. The Superconductivity of Mercury. *Leiden Comm.*, 120b, 1911.
  - [3] W. Meissner and R. Ochsenfeld. Ein neuer Effekt bei Eintritt der Supraleitfähigkeit. *Naturwissenschaften*, 21:787, 1933.
  - [4] D. Hykel. *Thèse de l'Université de Grenoble*, 2011.
  - [5] F. London and H. London. *Proc. Roy. Soc. Lond.*, A149:71, 1935.
  - [6] V.L. Ginzburg and L.D. Landau. *Zh. Eksperim. Teor. Fiz.*, 20:1064, 1950.
  - [7] A. A. Abrikosov. *Zh. Eksperim. Teor. Fiz.*, 32:1141, 1957.
  - [8] U. Essmann and H. Trübler. *Phys. Lett.*, 24A:526, 1967.
  - [9] H. F. Hess, R. B. Robinson, R. C. Dynes, J. M. Valles, and J. V. Waszczak. Scanning-Tunneling-Microscope Observation of the Abrikosov Flux Lattice and the Density of States near and inside a Fluxoid. *Phys. Rev. Lett.*, 62(2):214–216, Jan 1989.
  - [10] J. Bardeen, L. N. Cooper, and J.R. Schrieffer. Microscopic theory of superconductivity. *Phys. Rev.*, 106:162–164, 1957.
  - [11] J. Bardeen, L. N. Cooper, and J.R. Schrieffer. Theory of superconductivity. *Phys. Rev.*, 108:1175, 1957.
  - [12] P. L. Richards and M. Tinkham. Far-Infrared Energy Gap Measurements in Bulk Superconducting In, Sn, Hg, Ta, V, Pb, and Nb. *Phys. Rev.*, 119:575–590, Jul 1960.
  - [13] G. M. Eliashberg. Interactions between electrons and lattice vibrations in a superconductor. *Zh. Eksp. Teor. Fiz.*, 38:966, 1960.
  - [14] W. L. McMillan. Transition temperature of strong-coupled superconductors. *Phys. Rev.*, 167:331–344, 1968.
  - [15] Ruslan Prozorov and Russell W Giannetta. Magnetic penetration depth in unconventional superconductors. *Supercond. Sci. Technol.*, 19:R41–R67, 2006.
  - [16] F. Gross, B. S. Chandrasekhar, D. Einzel, K. Andres, P. J. Hirschfeld, H. R. Ott, J. Beuers, Z. Fisk, and J. L. Smith. Anomalous temperature dependence of the magnetic field penetration depth in superconducting UBe<sub>13</sub>. *Z. Phys. B*, 64:175–188, 1986. 10.1007/BF01303700.
  - [17] R. Khasanov, K. Conder, E. Pomjakushina, A. Amato, C. Baines, Z. Bukowski, J. Karpinski, S. Katrych, H.-H. Klauss, H. Luetkens, A. Shengelaya, and N. D. Zhigadlo. Evidence of nodeless superconductivity in FeSe<sub>0.85</sub> from a muon-spin-rotation study of the in-plane magnetic penetration depth. *Phys. Rev. B*, 78(22):220510, 2008.
  - [18] H. G. Luo and T. Xiang. Superfluid Response in Electron-Doped Cuprate Superconductors. *Phys. Rev. Lett.*, 94(2):027001, Jan 2005.
  - [19] B. D. Josephson. *Phys. Lett.*, 1:251, 1962.
  - [20] J. R. Gavaler. Superconductivity in Nb<sub>3</sub>Ge films above 22 K. *Appl. Phys. Lett.*, 23:480, 1973.
  - [21] J. G. Bednorz and K.A. Müller. Possible high T<sub>c</sub> superconductivity in the Ba-La-Cu-O system. *Z. Phys. B*, 64 (2):189, 1986.
-

- [22] M. K. Wu, J. R. Ashburn, C. J. Torng, P. H. Hor, R. L. Meng, L. Gao, Z. J. Huang, Y. Q. Wang, and C. W. Chu. Superconductivity at 93 K in a new mixed-phase Y-Ba-Cu-O compound system at ambient pressure. *Phys. Rev. Lett.*, 58(9):908–910, Mar 1987.
- [23] P. Dai, B. C. Chakoumakos, G. F. Sun, K. W. Wong, Y. Xin, and D. F. Lu. Synthesis and neutron powder diffraction study of the superconductor  $\text{HgBa}_2\text{Ca}_2\text{Cu}_3\text{O}_{8+\delta}$  by Tl substitution. *Physica C: Superconductivity*, 243:201, 1995.
- [24] L. Gao, Y. Y. Xue, F. Chen, Q. Xiong, R. L. Meng, D. Ramirez, C. W. Chu, J. H. Eggert, and H. K. Mao. Superconductivity up to 164 K in  $\text{HgBa}_2\text{Ca}_{m-1}\text{Cu}_m\text{O}_{2m+2+\delta}$  ( $m=1, 2, \text{ and } 3$ ) under quasihydrostatic pressures. *Phys. Rev. B*, 50(6):4260–4263, 1994.
- [25] [http://en.wikipedia.org/wiki/High-temperature\\_superconductivity](http://en.wikipedia.org/wiki/High-temperature_superconductivity).
- [26] A. A. Abrikosov and L. P. Gor'kov. Contribution to the theory of superconducting alloys with paramagnetic impurities. *Sov. Phys. JETP*, 12:1243, 1961.
- [27] Yoichi Kamihara, Hidenori Hiramatsu, Masahiro Hirano, Ryuto Kawamura, Hiroshi Yanagi, Toshio Kamiya, and Hideo Hosono. Iron-Based Layered Superconductor:  $\text{LaOFeP}$ . *J. Am. Chem. Soc.*, 128(31):10012–10013, 2006. PMID: 16881620.
- [28] Yoichi Kamihara, Takumi Watanabe, Masahiro Hirano, and Hideo Hosono. Iron-Based Layered Superconductor  $\text{La}[\text{O}_{1-x}\text{F}_x]\text{FeAs}$  ( $x = 0.05\text{-}0.12$ ) with  $T_c = 26$  K. *J. Am. Chem. Soc.*, 130(11):3296–3297, 2008.
- [29] Hiroki Takahashi, Kazumi Igawa, Kazunobu Arii, Yoichi Kamihara, Masahiro Hirano, and Hideo Hosono. Superconductivity at 43 K in an iron-based layered compound  $\text{LaO}_{1-x}\text{F}_x\text{FeAs}$ . *Nature*, 453(7193):376–378, May 2008.
- [30] X. H. Chen, T. Wu, G. Wu, R. H. Liu, H. Chen, and D. F. Fang. Superconductivity at 43 K in  $\text{SmFeAsO}_{1-x}\text{F}_x$ . *Nature*, 453:761, 2008.
- [31] Z. A. Ren, W. Lu, J. Yang, W. Yi, X. L. Shen, Z. C. Li, G. C. Che, X. L. Dong, L. L. Sun, F. Zhou, and Z. X. Zhao. Superconductivity at 55 K in iron-based F-doped layered quaternary compound  $\text{Sm}[\text{O}_{1-x}\text{F}_x]\text{FeAs}$ . *Chin. Phys. Lett.*, 25:2215, 2008.
- [32] Peng Cheng, Bing Shen, Gang Mu, Xiyu Zhu, Fei Han, Bin Zeng, and Hai-Hu Wen. High- $T_c$  superconductivity induced by doping rare-earth elements into  $\text{CaFeAsF}$ . *EPL*, 85(6):67003, 2009.
- [33] Johnpierre Paglione and Richard L. Greene. High-temperature superconductivity in iron-based materials. *Nature Physics*, 6(9):645–658, September 2010.
- [34] Jun Zhao, Q. Huang, Clarina de la Cruz, Shiliang Li, J. W. Lynn, Y. Chen, M. A. Green, G. F. Chen, G. Li, Z. Li, J. L. Luo, N. L. Wang, and Pengcheng Dai. Structural and magnetic phase diagram of  $\text{CeFeAsO}_{1-x}\text{F}_x$  and its relation to high-temperature superconductivity. *Nature Materials*, 7(12):953–959, December 2008.
- [35] H. Luetkens, H.-H. Klauss, M. Kraken, F. J. Litterst, T. Dellmann, R. Klingeler, C. Hess, R. Khasanov, A. Amato, C. Baines, M. Kosmala, O. J. Schumann, M. Braden, J. Hamann-Borrero, N. Leps, A. Kondrat, G. Behr, J. Werner, and B. Buchner. The electronic phase diagram of the  $\text{LaO}_{1-x}\text{F}_x\text{FeAs}$  superconductor. *Nature Materials*, 8(4):305–309, April 2009.
- [36] A. J. Drew, Ch. Niedermayer, P. J. Baker, F. L. Pratt, S. J. Blundell, T. Lancaster, R. H. Liu, G. Wu, X. H. Chen, I. Watanabe, V. K. Malik, A. Dubroka, M. Rossle, K. W. Kim, C. Baines, and C. Bernhard. Coexistence of static magnetism and superconductivity in  $\text{SmFeAsO}_{1-x}\text{F}_x$  as revealed by muon spin rotation. *Nature Materials*, 8(4):310–314, April 2009.
- [37] Jiun-Haw Chu, James G. Analytis, Chris Kucharczyk, and Ian R. Fisher. Determination of the phase diagram of the electron-doped superconductor  $\text{Ba}(\text{Fe}_{1-x}\text{Co}_x)_2\text{As}_2$ . *Phys. Rev. B*, 79(1):014506, Jan 2009.

- [38] Marianne Rotter, Michael Pangerl, Marcus Tegel, and Dirk Johrendt. Superconductivity and Crystal Structures of  $(\text{Ba}_{1-x}\text{K}_x)\text{Fe}_2\text{As}_2$  ( $x=0-1$ ). *Angew. Chem. Int. Ed.*, 47(41):7949–7952, 2008.
- [39] Shuai Jiang, Hui Xing, Guofang Xuan, Cao Wang, Zhi Ren, Chunmu Feng, Jianhui Dai, Zhu'an Xu, and Guanghan Cao. Superconductivity up to 30 K in the vicinity of the quantum critical point in  $\text{BaFe}_2(\text{As}_{1-x}\text{P}_x)_2$ . *J. Phys.: Condens. Matter*, 21(38):382203, 2009.
- [40] Chul-Ho Lee, Akira Iyo, Hiroshi Eisaki, Hijiri Kito, Maria Teresa Fernandez-Diaz, Toshimitsu Ito, Kunihiro Kihou, Hirofumi Matsuhata, Markus Braden, and Kazuyoshi Yamada. Effect of Structural Parameters on Superconductivity in Fluorine-Free  $\text{LnFeAsO}_{1-y}$  ( $\text{Ln} = \text{La}, \text{Nd}$ ). *J. Phys. Soc. Jpn.*, 77(8):083704, 2008.
- [41] D. J. Singh and M.-H. Du. Density Functional Study of  $\text{LaFeAsO}_{1-x}\text{F}_x$ : A Low Carrier Density Superconductor Near Itinerant Magnetism. *Phys. Rev. Lett.*, 100(23):237003, Jun 2008.
- [42] D.J. Singh. Electronic structure of Fe-based superconductors. *Physica C: Superconductivity*, 469(9-12):418 – 424, 2009. Superconductivity in Iron-Pnictides.
- [43] Kazuhiko Kuroki, Hidetomo Usui, Seiichiro Onari, Ryotaro Arita, and Hideo Aoki. Pnictogen height as a possible switch between high- $T_c$  nodeless and low- $T_c$  nodal pairings in the iron-based superconductors. *Phys. Rev. B*, 79(22):224511, Jun 2009.
- [44] C. C. Tsuei, J. R. Kirtley, C. C. Chi, Lock See Yu-Jahnes, A. Gupta, T. Shaw, J. Z. Sun, and M. B. Ketchen. Pairing Symmetry and Flux Quantization in a Tricrystal Superconducting Ring of  $\text{YBa}_2\text{Cu}_3\text{O}_{7-\delta}$ . *Phys. Rev. Lett.*, 73(4):593–596, Jul 1994.
- [45] D. J. Van Harlingen. Phase-sensitive tests of the symmetry of the pairing state in the high-temperature superconductors—Evidence for  $d_{x^2-y^2}$  symmetry. *Rev. Mod. Phys.*, 67:515–535, Apr 1995.
- [46] C. C. Tsuei and J. R. Kirtley. Pairing symmetry in cuprate superconductors. *Rev. Mod. Phys.*, 72:969–1016, Oct 2000.
- [47] H. Ding, P. Richard, K. Nakayama, K. Sugawara, T. Arakane, Y. Sekiba, A. Takayama, S. Souma, T. Sato, T. Takahashi, Z. Wang, X. Dai, Z. Fang, G. F. Chen, J. L. Luo, and N. L. Wang. Observation of Fermi-surface-dependent nodeless superconducting gaps in  $\text{Ba}_{0.6}\text{K}_{0.4}\text{Fe}_2\text{As}_2$ . *EPL*, 83(4):47001, 2008.
- [48] T. Y. Chen, Z. Tesanovic, R. H. Liu, X. H. Chen, and C. L. Chien. A BCS-like gap in the superconductor  $\text{SmFeAsO}_{0.85}\text{F}_{0.15}$ . *Nature*, 453:1224 – 1227, 2008.
- [49] I. I. Mazin, D. J. Singh, M. D. Johannes, and M. H. Du. Unconventional Superconductivity with a Sign Reversal in the Order Parameter of  $\text{LaFeAsO}_{1-x}\text{F}_x$ . *Phys. Rev. Lett.*, 101(5):057003, Jul 2008.
- [50] H.-J. Grafe, D. Paar, G. Lang, N. J. Curro, G. Behr, J. Werner, J. Hamann-Borrero, C. Hess, N. Leps, R. Klingeler, and B. B.chner.  $^{75}\text{As}$  NMR Studies of Superconducting  $\text{LaFeAsO}_{0.9}\text{F}_{0.1}$ . *Phys. Rev. Lett.*, 101(4):047003, Jul 2008.
- [51] K. Matano, Z. A. Ren, X. L. Dong, L. L. Sun, Z. X. Zhao, and Guo qing Zheng. Spin-singlet superconductivity with multiple gaps in  $\text{PrFeAsO}_{0.89}\text{F}_{0.11}$ . *EPL*, 83(5):57001, 2008.
- [52] Fanlong Ning, Kanagasingham Ahilan, Takashi Imai, Athena S. Sefat, Ronying Jin, Michael A. McGuire, Brian C. Sales, and David Mandrus.  $^{59}\text{Co}$  and  $^{75}\text{As}$  NMR Investigation of Electron-Doped High  $T_c$  Superconductor  $\text{BaFe}_{1.8}\text{Co}_{0.2}\text{As}_2$  ( $T_c = 22$  K). *J. Phys. Soc. Jpn*, 77(10):103705, 2008.
- [53] Clifford W. Hicks, Thomas M. Lippman, Martin E. Huber, Zhi-An Ren, Jie Yang, Zhong-Xian Zhao, and Kathryn A. Moler. Limits on the Superconducting Order Parameter in  $\text{NdFeAsO}_{1-x}\text{F}_y$  from Scanning SQUID Microscopy. *J. Phys. Soc. Jpn*, 78(1):013708, 2009.

- [54] C.-T. Chen, C. C. Tsuei, M. B. Ketchen, Z.-A. Ren, and Z. X. Zhao. Integer and half-integer flux-quantum transitions in a niobium-iron pnictide loop. *Nature Physics*, 6(4):260–264, April 2010.
- [55] Xiaohang Zhang, Yoon Seok Oh, Yong Liu, Liqin Yan, Kee Hoon Kim, Richard L. Greene, and Ichiro Takeuchi. Observation of the Josephson Effect in Pb/Ba<sub>1-x</sub>K<sub>x</sub>Fe<sub>2</sub>As<sub>2</sub> Single Crystal Junctions. *Phys. Rev. Lett.*, 102(14):147002, Apr 2009.
- [56] T. Hanaguri, S. Niitaka, K. Kuroki, and H. Takagi. Unconventional s-wave Superconductivity in Fe(Se,Te). *Science*, 328(5977):474–476, 2010.
- [57] Ni Ni. *Thesis of Iowa State University*, 2011.
- [58] Marianne Rotter, Marcus Tegel, Dirk Johrendt, Inga Schellenberg, Wilfried Hermes, and Rainer P ttgen. Spin-density-wave anomaly at 140 K in the ternary iron arsenide BaFe<sub>2</sub>As<sub>2</sub>. *Phys. Rev. B*, 78(2):020503, Jul 2008.
- [59] Marianne Rotter, Marcus Tegel, and Dirk Johrendt. Superconductivity at 38 K in the Iron Arsenide (Ba<sub>1-x</sub>K<sub>x</sub>)Fe<sub>2</sub>As<sub>2</sub>. *Phys. Rev. Lett.*, 101(10):107006, Sep 2008.
- [60] G. Wu, R. H. Liu, H. Chen, Y. J. Yan, T. Wu, Y. L. Xie, J. J. Ying, X. F. Wang, D. F. Fang, and X. H. Chen. Transport properties and superconductivity in Ba<sub>1-x</sub>M<sub>x</sub>Fe<sub>2</sub>As<sub>2</sub> (M=La and K) with double FeAs layers. *EPL*, 84(2):27010, 2008.
- [61] Gen-Fu Chen, Zheng Li, Gang Li, Wan-Zheng Hu, Jing Dong, Jun Zhou, Xiao-Dong Zhang, Ping Zheng, Nan-Lin Wang, and Jian-Lin Luo. Superconductivity in Hole-Doped (Sr<sub>1-x</sub>K<sub>x</sub>)Fe<sub>2</sub>As<sub>2</sub>. *Chin. Phys. Lett.*, 25(9):3403, 2008.
- [62] G. Wu, H. Chen, T. Wu, Y. L. Xie, Y. J. Yan, R. H. Liu, X. F. Wang, J. J. Ying, and X. H. Chen. Different resistivity response to spin-density wave and superconductivity at 20 K in Ca<sub>1-x</sub>Na<sub>x</sub>Fe<sub>2</sub>As<sub>2</sub>. *J. Phys.: Condens. Matter*, 20(42):422201, 2008.
- [63] Kalyan Sasmal, Bing Lv, Bernd Lorenz, Arnold M. Guloy, Feng Chen, Yu-Yi Xue, and Ching-Wu Chu. Superconducting Fe-Based Compounds (A<sub>1-x</sub>Sr<sub>x</sub>)Fe<sub>2</sub>As<sub>2</sub> with A = K and Cs with Transition Temperatures up to 37 K. *Phys. Rev. Lett.*, 101(10):107007, Sep 2008.
- [64] Milton S. Torikachvili, Sergey L. Bud'ko, Ni Ni, and Paul C. Canfield. Pressure Induced Superconductivity in CaFe<sub>2</sub>As<sub>2</sub>. *Phys. Rev. Lett.*, 101(5):057006, Jul 2008.
- [65] Tuson Park, Eunsung Park, Hanoh Lee, T. Klimczuk, E. D . Bauer, F. Ronning, and J. D. Thompson. Pressure-induced superconductivity in CaFe<sub>2</sub>As<sub>2</sub>. *J. Phys.: Condens. Matter*, 20(32):322204, 2008.
- [66] A. Leithe-Jasper, W. Schnelle, C. Geibel, and H. Rosner. Superconducting State in SrFe<sub>2-x</sub>Co<sub>x</sub>As<sub>2</sub> by Internal Doping of the Iron Arsenide Layers. *Phys. Rev. Lett.*, 101(20):207004, Nov 2008.
- [67] Athena S. Sefat, Rongying Jin, Michael A. McGuire, Brian C. Sales, David J. Singh, and David Mandrus. Superconductivity at 22 K in Co-Doped BaFe<sub>2</sub>As<sub>2</sub> Crystals. *Phys. Rev. Lett.*, 101(11):117004, Sep 2008.
- [68] Yanchao Chen, Xingye Lu, Meng Wang, Huiqian Luo, and Shiliang Li. Systematic growth of BaFe<sub>2-x</sub>Ni<sub>x</sub>As<sub>2</sub> large crystals. *Supercond. Sci. Technol.*, 24(6):065004, 2011.
- [69] S R Saha, T Drye, K Kirshenbaum, N P Butch, P Y Zavalij, and Johnpierre Paglione. Superconductivity at 23 K in Pt doped BaFe<sub>2</sub>As<sub>2</sub> single crystals. *Journal of Physics: Condensed Matter*, 22(7):072204, 2010.
- [70] H. L. Shi, H. X. Yang, H. F. Tian, J. B. Lu, Z. W. Wang, Y. B. Qin, Y. J. Song, and J. Q. Li. Structural properties and superconductivity of SrFe<sub>2</sub>As<sub>2-x</sub>P<sub>x</sub> (0.0 ≤ x ≤ 1.0) and CaFe<sub>2</sub>As<sub>2-y</sub>P<sub>y</sub> (0.0 ≤ y ≤ 0.3). *J. Phys.: Condens. Matter*, 22(12):125702, 2010.
- [71] Zhi Ren, Qian Tao, Shuai Jiang, Chunmu Feng, Cao Wang, Jianhui Dai, Guanghan Cao, and Zhu'an Xu. Superconductivity Induced by Phosphorus Doping and Its Coexistence with Ferromagnetism in EuFe<sub>2</sub>(As<sub>0.7</sub>P<sub>0.3</sub>)<sub>2</sub>. *Phys. Rev. Lett.*, 102(13):137002, Apr 2009.

- [72] N. Ni, S. L. Bud'ko, A. Kreyssig, S. Nandi, G. E. Rustan, A. I. Goldman, S. Gupta, J. D. Corbett, A. Kracher, and P. C. Canfield. Anisotropic thermodynamic and transport properties of single-crystalline  $\text{Ba}_{1-x}\text{K}_x\text{Fe}_2\text{As}_2$  ( $x = 0$  and  $0.45$ ). *Phys. Rev. B*, 78(1):014507, Jul 2008.
- [73] G. F. Chen, Z. Li, J. Dong, G. Li, W. Z. Hu, X. D. Zhang, X. H. Song, P. Zheng, N. L. Wang, and J. L. Luo. Transport and anisotropy in single-crystalline  $\text{SrFe}_2\text{As}_2$  and  $\text{A}_{0.6}\text{K}_{0.4}\text{Fe}_2\text{As}_2$  ( $A = \text{Sr}, \text{Ba}$ ) superconductors. *Phys. Rev. B*, 78(22):224512, Dec 2008.
- [74] F. Ronning, T. Klimczuk, E. D. Bauer, H. Volz, and J. D. Thompson. Synthesis and properties of  $\text{CaFe}_2\text{As}_2$  single crystals. *J. Phys.: Condens. Matter*, 20(32):322201, 2008.
- [75] J.-Q. Yan, A. Kreyssig, S. Nandi, N. Ni, S. L. Bud'ko, A. Kracher, R. J. McQueeney, R. W. McCallum, T. A. Lograsso, A. I. Goldman, and P. C. Canfield. Structural transition and anisotropic properties of single-crystalline  $\text{SrFe}_2\text{As}_2$ . *Phys. Rev. B*, 78(2):024516, Jul 2008.
- [76] Cheng Dong. PowderX: Windows-95-based program for powder X-ray diffraction data processing. *J. Appl. Cryst.*, 32(4):838, Aug 1999.
- [77] N. D. Zhigadlo, S. Katrych, Z. Bukowski, S. Weyeneth, R. Puzniak, and J. Karpinski. Single crystals of superconducting  $\text{SmFeAsO}_{1-x}\text{F}_y$  grown at high pressure. *J. Phys.: Condens. Matter*, 20(34):342202, 2008.
- [78] Clarina de la Cruz, Q. Huang, J. W. Lynn, Jiying Li, W. Ratcliff II, J. L. Zarestky, H. A. Mook, G. F. Chen, J. L. Luo, N. L. Wang, and Pengcheng Dai. Magnetic order close to superconductivity in the iron-based layered  $\text{LaO}_{1-x}\text{F}_x\text{FeAs}$  systems. *Nature*, 453(7197):899–902, June 2008.
- [79] H. Chen, Y. Ren, Y. Qiu, Wei Bao, R. H. Liu, G. Wu, T. Wu, Y. L. Xie, X. F. Wang, Q. Huang, and X. H. Chen. Coexistence of the spin-density wave and superconductivity in  $\text{Ba}_{1-x}\text{K}_x\text{Fe}_2\text{As}_2$ . *EPL*, 85(1):17006, 2009.
- [80] A. Dubroka, K. W. Kim, M. R. Ssle, V. K. Malik, A. J. Drew, R. H. Liu, G. Wu, X. H. Chen, and C. Bernhard. Superconducting Energy Gap and  $c$ -Axis Plasma Frequency of  $(\text{Nd},\text{Sm})\text{FeAsO}_{0.82}\text{F}_{0.18}$  Superconductors from Infrared Ellipsometry. *Phys. Rev. Lett.*, 101(9):097011, Aug 2008.
- [81] Ying Jia, Peng Cheng, Lei Fang, Huiqian Luo, Huan Yang, Cong Ren, Lei Shan, Changzhi Gu, and Hai-Hu Wen. Critical fields and anisotropy of  $\text{NdFeAsO}_{0.82}\text{F}_{0.18}$  single crystals. *Appl. Phys. Lett.*, 93(3):032503, 2008.
- [82] F. Hunte, J. Jaroszynski, A. Gurevich, D. C. Larbalestier, R. Jin, A. S. Sefat, M. A. McGuire, B. C. Sales, D. K. Christen, and D. Mandrus. Two-band superconductivity in  $\text{LaFeAsO}_{0.89}\text{F}_{0.11}$  at very high magnetic fields. *Nature*, 453(7197):903–905, June 2008.
- [83] Xiyu Zhu, Huan Yang, Lei Fang, Gang Mu, and Hai-Hu Wen. Upper critical field, Hall effect and magnetoresistance in the iron-based layered superconductor  $\text{LaFeAsO}_{0.9}\text{F}_{0.1-\delta}$ . *Supercond. Sci. Technol.*, 21(10):105001, 2008.
- [84] M. M. Altarawneh, K. Collar, C. H. Mielke, N. Ni, S. L. Bud'ko, and P. C. Canfield. Determination of anisotropic  $H_{c2}$  up to 60 T in  $\text{Ba}_{0.55}\text{K}_{0.45}\text{Fe}_2\text{As}_2$  single crystals. *Phys. Rev. B*, 78(22):220505, Dec 2008.
- [85] H. Q. Yuan, J. Singleton, F. F. Balakirev, S. A. Baily, G. F. Chen, J. L. Luo, and N. L. Wang. Nearly isotropic superconductivity in  $(\text{Ba},\text{K})\text{Fe}_2\text{As}_2$ . *Nature*, 457(7229):565–568, January 2009.
- [86] N. R. Werthamer, E. Helfand, and P. C. Hohenberg. Temperature and Purity Dependence of the Superconducting Critical Field,  $H_{c2}$ . III. Electron Spin and Spin-Orbit Effects. *Phys. Rev.*, 147(1):295–302, Jul 1966.
- [87] Cong Ren, Zhao-Sheng Wang, Hui-Qian Luo, Huan Yang, Lei Shan, and Hai-Hu Wen. Evidence for Two Energy Gaps in Superconducting  $\text{Ba}_{0.6}\text{K}_{0.4}\text{Fe}_2\text{As}_2$  Single Crystals and the Breakdown of the Uemura Plot. *Phys. Rev. Lett.*, 101(25):257006, Dec 2008.

- [88] A. M. Clogston. Upper Limit for the Critical Field in Hard Superconductors. *Phys. Rev. Lett.*, 9(6):266–267, Sep 1962.
- [89] G. Fuchs, S.-L. Drechsler, N. Kozlova, G. Behr, A. K hler, J. Werner, K. Nenkov, R. Klingeler, J. Hamann-Borrero, C. Hess, A. Kondrat, M. Grobosch, A. Narduzzo, M. Knupfer, J. Freudenberger, B. B chner, and L. Schultz. High-Field Pauli-Limiting Behavior and Strongly Enhanced Upper Critical Magnetic Fields near the Transition Temperature of an Arsenic-Deficient  $\text{LaO}_{0.9}\text{F}_{0.1}\text{FeAs}_{1-\delta}$  Superconductor. *Phys. Rev. Lett.*, 101(23):237003, Dec 2008.
- [90] D. J. Singh. Electronic structure and doping in  $\text{BaFe}_2\text{As}_2$  and  $\text{LiFeAs}$ : Density functional calculations. *Phys. Rev. B*, 78(9):094511, Sep 2008.
- [91] Ying Jia, Peng Cheng, Lei Fang, Huan Yang, Cong Ren, Lei Shan, Chang-Zhi Gu, and Hai-Hu Wen. Angular dependence of resistivity in the superconducting state of  $\text{NdFeAsO}_{0.82}\text{F}_{0.18}$  single crystals. *Supercond. Sci. Technol.*, 21(10):105018, 2008.
- [92] G. Blatter, V. B. Geshkenbein, and A. I. Larkin. From isotropic to anisotropic superconductors: A scaling approach. *Phys. Rev. Lett.*, 68(6):875–878, Feb 1992.
- [93] Q. Han, Y. Chen, and Z. D. Wang. A generic two-band model for unconventional superconductivity and spin-density-wave order in electron- and hole-doped iron-based superconductors. *EPL*, 82(3):37007, 2008.
- [94] V. Cvetkovic and Z. Tesanovic. Multiband magnetism and superconductivity in Fe-based compounds. *EPL*, 85(3):37002, 2009.
- [95] Edwin Hall. On a New Action of the Magnet on Electric Currents. *American Journal of Mathematics*, 2:287–92, 1879.
- [96] B. Khaykovich, E. Zeldov, D. Majer, T. W. Li, P. H. Kes, and M. Konczykowski. Vortex-Lattice Phase Transitions in  $\text{Bi}_2\text{Sr}_2\text{CaCu}_2\text{O}_8$  Crystals with Different Oxygen Stoichiometry. *Phys. Rev. Lett.*, 76:2555–2558, Apr 1996.
- [97] Gang Mu, Xi-Yu Zhu, Lei Fang, Lei Shan, Cong Ren, and Hai-Hu Wen. Nodal Gap in Fe-Based Layered Superconductor  $\text{LaO}_{0.9}\text{F}_{0.1-\delta}\text{FeAs}$  Probed by Specific Heat Measurements. *Chin. Phys. Lett.*, 25(6):2221, 2008.
- [98] H. Luetkens, H.-H. Klauss, R. Khasanov, A. Amato, R. Klingeler, I. Hellmann, N. Leps, A. Kondrat, C. Hess, A. K hler, G. Behr, J. Werner, and B. B chner. Field and Temperature Dependence of the Superfluid Density in  $\text{LaFeAsO}_{1-x}\text{F}_x$  Superconductors: A Muon Spin Relaxation Study. *Phys. Rev. Lett.*, 101(9):097009, Aug 2008.
- [99] J. P. Carlo, Y. J. Uemura, T. Goko, G. J. MacDougall, J. A. Rodriguez, W. Yu, G. M. Luke, Pengcheng Dai, N. Shannon, S. Miyasaka, S. Suzuki, S. Tajima, G. F. Chen, W. Z. Hu, J. L. Luo, and N. L. Wang. Static Magnetic Order and Superfluid Density of  $\text{RFeAs}(\text{O},\text{F})$  ( $\text{R}=\text{La},\text{Nd},\text{Ce}$ ) and  $\text{LaFePO}$  Studied by Muon Spin Relaxation: Unusual Similarities with the Behavior of Cuprate Superconductors. *Phys. Rev. Lett.*, 102(8):087001, Feb 2009.
- [100] K. Ahilan, F. L. Ning, T. Imai, A. S. Sefat, R. Jin, M. A. McGuire, B. C. Sales, and D. Mandrus.  $^{19}\text{F}$  NMR investigation of the iron pnictide superconductor  $\text{LaFeAsO}_{0.89}\text{F}_{0.11}$ . *Phys. Rev. B*, 78(10):100501, 2008.
- [101] Lei Shan, Yonglei Wang, Xiyu Zhu, Gang Mu, Lei Fang, Cong Ren, and Hai-Hu Wen. Point-contact spectroscopy of iron-based layered superconductor  $\text{LaO}_{0.9}\text{F}_{0.1-\delta}\text{FeAs}$ . *EPL*, 83(5):57004, 2008.
- [102] Yong-Lei Wang, Lei Shan, Lei Fang, Peng Cheng, Cong Ren, and Hai-Hu Wen. Multiple gaps in  $\text{SmFeAsO}_{0.9}\text{F}_{0.1}$  revealed by point-contact spectroscopy. *Supercond. Sci. Technol.*, 22(1):015018 (6pp), 2009.
- [103] L. Malone, J. D. Fletcher, A. Serafin, A. Carrington, N. D. Zhigadlo, Z. Bukowski, S. Katrych, and J. Karpinski. Magnetic penetration depth of single-crystalline  $\text{SmFeAsO}_{1-x}\text{F}_y$ . *Phys. Rev. B*, 79(14):140501, Apr 2009.

- [104] E. Zeldov, A. I. Larkin, V. B. Geshkenbein, M. Konczykowski, D. Majer, B. Khaykovich, V. M. Vinokur, and H. Shtrikman. Geometrical Barriers in High-Temperature Superconductors. *Phys. Rev. Lett.*, 73(10):1428–1431, Sep 1994.
- [105] Ruixing Liang, D. A. Bonn, W. N. Hardy, and David Broun. Lower Critical Field and Superfluid Density of Highly Underdoped  $\text{YBa}_2\text{Cu}_3\text{O}_{6+x}$  Single Crystals. *Phys. Rev. Lett.*, 94(11):117001, Mar 2005.
- [106] Ernst Helmut Brandt. Irreversible magnetization of pin-free type-II superconductors. *Phys. Rev. B*, 60(17):11939–11942, Nov 1999.
- [107] V.I. Fesenko, V.N. Gorbunov, and V.P. Smilga. Analytical properties of muon polarization spectra in type-II superconductors and experimental data interpretation for mono- and polycrystalline HTSCs. *Physica C: Superconductivity*, 176(4-6):551 – 558, 1991.
- [108] Rustem Khasanov, Hubertus Luetkens, Alex Amato, Hans-Henning Klauss, Zhi-An Ren, Jie Yang, Wei Lu, and Zhong-Xian Zhao. Muon spin rotation studies of  $\text{SmFeAsO}_{0.85}$  and  $\text{NdFeAsO}_{0.85}$  superconductors. *Phys. Rev. B*, 78(9):092506, 2008.
- [109] S. Weyeneth, R. Puzniak, U. Mosele, N. Zhigadlo, S. Katrych, Z. Bukowski, J. Karpinski, S. Kohout, J. Roos, and H. Keller. Anisotropy of Superconducting Single Crystal  $\text{SmFeAsO}_{0.8}\text{F}_{0.2}$  Studied by Torque Magnetometry. *J. Supercond. Nov. Magn.*, 22:325–329, 2009.
- [110] Takeshi Kondo, A. F. Santander-Syro, O. Copie, Chang Liu, M. E. Tillman, E. D. Mun, J. Schmalian, S. L. Bud'ko, M. A. Tanatar, P. C. Canfield, and A. Kaminski. Momentum Dependence of the Superconducting Gap in  $\text{NdFeAsO}_{0.9}\text{F}_{0.1}$  Single Crystals Measured by Angle Resolved Photoemission Spectroscopy. *Phys. Rev. Lett.*, 101(14):147003, 2008.
- [111] Huiqian Luo, Zhaosheng Wang, Huan Yang, Peng Cheng, Xiyu Zhu, and Hai-Hu Wen. Growth and characterization of  $\text{A}_{1-x}\text{K}_x\text{Fe}_2\text{As}_2$  ( $\text{A} = \text{Ba}, \text{Sr}$ ) single crystals with  $x = 0-0.4$ . *Supercond. Sci. Technol.*, 21(12):125014, 2008.
- [112] G. Li, W. Z. Hu, J. Dong, Z. Li, P. Zheng, G. F. Chen, J. L. Luo, and N. L. Wang. Probing the Superconducting Energy Gap from Infrared Spectroscopy on a  $\text{Ba}_{0.6}\text{K}_{0.4}\text{Fe}_2\text{As}_2$  Single Crystal with  $T_c = 37$  K. *Phys. Rev. Lett.*, 101(10):107004, Sep 2008.
- [113] F. Manzano, A. Carrington, N. E. Hussey, S. Lee, A. Yamamoto, and S. Tajima. Exponential Temperature Dependence of the Penetration Depth in Single Crystal  $\text{MgB}_2$ . *Phys. Rev. Lett.*, 88(4):047002, Jan 2002.
- [114] A. A. Golubov, A. Brinkman, O. V. Dolgov, J. Kortus, and O. Jepsen. Multiband model for penetration depth in  $\text{MgB}_2$ . *Phys. Rev. B*, 66(5):054524, Aug 2002.
- [115] Zhao Lin, Liu Hai-Yun, Zhang Wen-Tao, Meng Jian-Qiao, Jia Xiao-Wen, Liu Guo-Dong, Dong Xiao-Li, Chen Gen-Fu, Luo Jian-Lin, Wang Nan-Lin, Lu Wei, Wang Gui-Ling, Zhou Yong, Zhu Yong, Wang Xiao-Yang, Xu Zu-Yan, Chen Chuang-Tian, and Zhou Xing-Jiang. Multiple Nodeless Superconducting Gaps in  $(\text{Ba}_{0.6}\text{K}_{0.4})\text{Fe}_2\text{As}_2$  Superconductor from Angle-Resolved Photoemission Spectroscopy. *Chin. Phys. Lett.*, 25(12):4402, 2008.
- [116] Fa Wang, Hui Zhai, Ying Ran, Ashvin Vishwanath, and Dung-Hai Lee. Functional Renormalization-Group Study of the Pairing Symmetry and Pairing Mechanism of the FeAs-Based High-Temperature Superconductor. *Phys. Rev. Lett.*, 102(4):047005, Jan 2009.
- [117] Zhao-Sheng Wang, Hui-Qian Luo, Cong Ren, and Hai-Hu Wen. Upper critical field, anisotropy, and superconducting properties of  $\text{Ba}_{1-x}\text{K}_x\text{Fe}_2\text{As}_2$  single crystals. *Phys. Rev. B*, 78(14):140501, Oct 2008.
- [118] A. Carrington and F. Manzano. Magnetic penetration depth of  $\text{MgB}_2$ . *Physica C: Superconductivity*, 385(1-2):205 – 214, 2003.
- [119] R. Khasanov, D. V. Evtushinsky, A. Amato, H.-H. Klauss, H. Luetkens, Ch. Niedermayer, B. B chner, G. L. Sun, C. T. Lin, J. T. Park, D. S. Inosov, and V. Hinkov. Two-Gap Superconductivity in  $\text{Ba}_{1-x}\text{K}_x\text{Fe}_2\text{As}_2$ : A Complementary Study of the Magnetic Penetration Depth

- by Muon-Spin Rotation and Angle-Resolved Photoemission. *Phys. Rev. Lett.*, 102:187005, May 2009.
- [120] R. Khasanov, M. Bendele, A. Amato, K. Conder, H. Keller, H.-H. Klauss, H. Luetkens, and E. Pomjakushina. Evolution of Two-Gap Behavior of the Superconductor  $\text{FeSe}_{1-x}$ . *Phys. Rev. Lett.*, 104:087004, Feb 2010.
- [121] [http://en.wikipedia.org/wiki/Andreev\\_reflection](http://en.wikipedia.org/wiki/Andreev_reflection).
- [122] A. F. Andreev. Thermal conductivity of the intermediate state of superconductors. *Sov. Phys. JETP*, 19:1228, 1964.
- [123] G. E. Blonder, M. Tinkham, and T. M. Klapwijk. Transition from metallic to tunneling regimes in superconducting microconstrictions: Excess current, charge imbalance, and supercurrent conversion. *Phys. Rev. B*, 25:4515, 1982.
- [124] D. Daghero and R. S. Gonnelli. Probing multiband superconductivity by point-contact spectroscopy. *Supercond. Sci. Technol.*, 23(4):043001, 2010.
- [125] R. C. Dynes, V. Narayanamurti, and J. P. Garno. Direct Measurement of Quasiparticle-Lifetime Broadening in a Strong-Coupled Superconductor. *Phys. Rev. Lett.*, 41(21):1509–1512, Nov 1978.
- [126] A. Plecenik, M. Grajcar, Š. Beňačka, P. Seidel, and A. Pfuch. Finite-quasiparticle-lifetime effects in the differential conductance of  $\text{Bi}_2\text{Sr}_2\text{CaCu}_2\text{O}_y/\text{Au}$  junctions. *Phys. Rev. B*, 49(14):10016–10019, Apr 1994.
- [127] Satoshi Kashiwaya, Yukio Tanaka, Masao Koyanagi, and Koji Kajimura. Theory for tunneling spectroscopy of anisotropic superconductors. *Phys. Rev. B*, 53(5):2667–2676, Feb 1996.
- [128] Chia-Ren Hu. Midgap surface states as a novel signature for  $d_{xy}^2-x_b^2$ -wave superconductivity. *Phys. Rev. Lett.*, 72:1526–1529, Mar 1994.
- [129] I. K. Yanson. *Sov. Phys. JETP*, 39:506–513, 1974.
- [130] G. E. Blonder and M. Tinkham. Metallic to tunneling transition in Cu-Nb point contacts. *Phys. Rev. B*, 27(1):112–118, Jan 1983.
- [131] V. Baltz, A. D. Naylor, K. M. Seemann, W. Elder, S. Sheen, K. Westerholt, H. Zabel, G. Burnell, C. H. Marrows, and B. J. Hickey. Conductance features in point contact Andreev reflection spectra. *J. Phys.: Condens. Matter*, 21(9):095701, 2009.
- [132] Xiaohang Zhang, Yoon Seok Oh, Yong Liu, Liqin Yan, Shanta R. Saha, Nicholas P. Butch, Kevin Kirshenbaum, Kee Hoon Kim, Johnpierre Paglione, Richard L. Greene, and Ichiro Takeuchi. Evidence of a universal and isotropic  $2\Delta/k_B T_C$  ratio in 122-type iron pnictide superconductors over a wide doping range. *Phys. Rev. B*, 82(2):020515, Jul 2010.
- [133] P. Szabó, Z. Pribulová, G. Pristáš, S. L. Bud'ko, P. C. Canfield, and P. Samuely. Evidence for two-gap superconductivity in  $\text{Ba}_{0.55}\text{K}_{0.45}\text{Fe}_2\text{As}_2$  from directional point-contact Andreev-reflection spectroscopy. *Phys. Rev. B*, 79(1):012503, Jan 2009.
- [134] L. Shan, H. J. Tao, H. Gao, Z. Z. Li, Z. A. Ren, G. C. Che, and H. H. Wen. *s*-wave pairing in  $\text{MgCNi}_3$  revealed by point contact tunneling. *Phys. Rev. B*, 68:144510, Oct 2003.
- [135] Xin Lu, W. K. Park, H. Q. Yuan, G. F. Chen, G. L. Luo, N. L. Wang, A. S. Sefat, M. A. McGuire, R. Jin, B. C. Sales, D. Mandrus, J. Gillett, Suchitra E. Sebastian, and L. H. Greene. Point-contact spectroscopic studies on normal and superconducting  $\text{AFe}_2\text{As}_2$ -type iron pnictide single crystals. *Supercond. Sci. Technol.*, 23(5):054009, 2010.
- [136] D. Daghero, M. Tortello, R. S. Gonnelli, V. A. Stepanov, N. D. Zhigadlo, and J. Karpinski. Evidence for two-gap nodeless superconductivity in  $\text{SmFeAsO}_{1-x}\text{F}_x$  from point-contact Andreev-reflection spectroscopy. *Phys. Rev. B*, 80:060502, Aug 2009.
- [137] J. R. Kirtley. Inelastic transport through normal-metal–superconductor interfaces. *Phys. Rev. B*, 47:11379–11383, May 1993.

- [138] K. Hasselbach, J. R. Kirtley, and J. Flouquet. Symmetry of the gap in superconducting URu<sub>2</sub>Si<sub>2</sub>. *Phys. Rev. B*, 47:509–512, Jan 1993.
- [139] P. Samuely, Z. Pribulová, P. Szabó, G. Pristáš, S.L. Bud’ko, and P.C. Canfield. Point contact Andreev reflection spectroscopy of superconducting energy gaps in 122-type family of iron pnictides. *Physica C: Superconductivity*, 469(9-12):507 – 511, 2009. Superconductivity in Iron-Pnictides.
- [140] Yi Yin, M. Zech, T. L. Williams, X. F. Wang, G. Wu, X. H. Chen, and J. E. Hoffman. Scanning Tunneling Spectroscopy and Vortex Imaging in the Iron Pnictide Superconductor BaFe<sub>1.8</sub>Co<sub>0.2</sub>As<sub>2</sub>. *Phys. Rev. Lett.*, 102(9):097002, Mar 2009.
- [141] F. Masee, Y. Huang, R. Huisman, S. de Jong, J. B. Goedkoop, and M. S. Golden. Nanoscale superconducting-gap variations and lack of phase separation in optimally doped BaFe<sub>1.86</sub>Co<sub>0.14</sub>As<sub>2</sub>. *Phys. Rev. B*, 79(22):220517, Jun 2009.
- [142] GuangTao Wang, Yumin Qian, Gang Xu, Xi Dai, and Zhong Fang. Gutzwiller Density Functional Studies of FeAs-Based Superconductors: Structure Optimization and Evidence for a Three-Dimensional Fermi Surface. *Phys. Rev. Lett.*, 104(4):047002, Jan 2010.
- [143] M. Tortello, D. Daghero, G. A. Ummarino, V. A. Stepanov, J. Jiang, J. D. Weiss, E. E. Hellstrom, and R. S. Gonnelli. Multigap Superconductivity and Strong Electron-Boson Coupling in Fe-Based Superconductors: A Point-Contact Andreev-Reflection Study of Ba(Fe<sub>1-x</sub>Co<sub>x</sub>)<sub>2</sub>As<sub>2</sub> Single Crystals. *Phys. Rev. Lett.*, 105:237002, Dec 2010.
- [144] A. B. Vorontsov and I. Vekhter. Nodes versus Minima in the Energy Gap of Iron Pnictide Superconductors from Field-Induced Anisotropy. *Phys. Rev. Lett.*, 105:187004, Oct 2010.
- [145] Lei Shan, Yong-Lei Wang, Bing Shen, Bin Zeng, Yan Huang, Ang Li, Da Wang, Huan Yang, Cong Ren, Qiang-Hua Wang, Shuheng H. Pan, and Hai-Hu Wen. Observation of ordered vortices with Andreev bound states in Ba<sub>0.6</sub>K<sub>0.4</sub>Fe<sub>2</sub>As<sub>2</sub>. *Nature Physics*, 7(4):325–331, April 2011.
- [146] Bin Zeng, Gang Mu, HuiQian Luo, and HaiHu Wen. Low temperature specific heat in BaFe<sub>1.9</sub>Ni<sub>0.1</sub>As<sub>2</sub> single crystals. *Sci China Phys Mech Astron*, 53:1221–1224, 2010. 10.1007/s11433-010-4032-z.
- [147] Yukio Tanaka and Satoshi Kashiwaya. Theory of Tunneling Spectroscopy of *d*-Wave Superconductors. *Phys. Rev. Lett.*, 74:3451–3454, Apr 1995.
- [148] E. Schachinger and J. P. Carbotte. Microwave conductivity in the ferropnictides with specific application to Ba<sub>1-x</sub>K<sub>x</sub>Fe<sub>2</sub>As<sub>2</sub>. *Phys. Rev. B*, 80:174526, Nov 2009.
- [149] D. Wu, N. Barišić, M. Dressel, G. H. Cao, Z. A. Xu, J. P. Carbotte, and E. Schachinger. Nodes in the order parameter of superconducting iron pnictides investigated by infrared spectroscopy. *Phys. Rev. B*, 82:184527, Nov 2010.
- [150] A. V. Chubukov, M. G. Vavilov, and A. B. Vorontsov. Momentum dependence and nodes of the superconducting gap in the iron pnictides. *Phys. Rev. B*, 80:140515, Oct 2009.
- [151] I. I. Mazin, T. P. Devereaux, J. G. Analytis, Jiun-Haw Chu, I. R. Fisher, B. Muschler, and R. Hackl. Pinpointing gap minima in Ba(Fe<sub>0.94</sub>Co<sub>0.06</sub>)<sub>2</sub>As<sub>2</sub> via band-structure calculations and electronic Raman scattering. *Phys. Rev. B*, 82:180502, Nov 2010.
- [152] K. Terashima, Y. Sekiba, J. H. Bowen, K. Nakayama, T. Kawahara, T. Sato, P. Richard, Y.-M. Xu, L. J. Li, G. H. Cao, Z.-A. Xu, H. Ding, and T. Takahashi. Fermi surface nesting induced strong pairing in iron-based superconductors. *Proc. Natl. Acad. Sci.*, 106(18):7330–7333, 2009.
- [153] J.-Ph. Reid, M. A. Tanatar, X. G. Luo, H. Shakeripour, N. Doiron-Leyraud, N. Ni, S. L. Bud’ko, P. C. Canfield, R. Prozorov, and Louis Taillefer. Nodes in the gap structure of the iron arsenide superconductor Ba(Fe<sub>1-x</sub>Co<sub>x</sub>)<sub>2</sub>As<sub>2</sub> from *c*-axis heat transport measurements. *Phys. Rev. B*, 82:064501, Aug 2010.

- [154] M. A. Tanatar, J.-Ph. Reid, H. Shakeripour, X. G. Luo, N. Doiron-Leyraud, N. Ni, S. L. Bud'ko, P. C. Canfield, R. Prozorov, and Louis Taillefer. Doping Dependence of Heat Transport in the Iron-Arsenide Superconductor  $\text{Ba}(\text{Fe}_{1-x}\text{Co}_x)_2\text{As}_2$ : From Isotropic to a Strongly  $k$ -Dependent Gap Structure. *Phys. Rev. Lett.*, 104:067002, Feb 2010.
- [155] V. G. Kogan, C. Martin, and R. Prozorov. Superfluid density and specific heat within a self-consistent scheme for a two-band superconductor. *Phys. Rev. B*, 80:014507, Jul 2009.
- [156] Hyoung Joon Choi, David Roundy, Hong Sun, Marvin L. Cohen, and Steven G. Louie. The origin of the anomalous superconducting properties of  $\text{MgB}_2$ . *Nature*, 418(6899):758–760, August 2002.
- [157] G. A. Ummarino, M. Tortello, D. Daghero, and R. S. Gonnelli. Three-band  $s \pm$  Eliashberg theory and the superconducting gaps of iron pnictides. *Phys. Rev. B*, 80:172503, Nov 2009.
- [158] L. Benfatto, E. Cappelluti, and C. Castellani. Spectroscopic and thermodynamic properties in a four-band model for pnictides. *Phys. Rev. B*, 80:214522, Dec 2009.
- [159] Miaoyin Wang, Huiqian Luo, Jun Zhao, Chenglin Zhang, Meng Wang, Karol Marty, Songxue Chi, Jeffrey W. Lynn, Astrid Schneidewind, Shiliang Li, and Pengcheng Dai. Electron-doping evolution of the low-energy spin excitations in the iron arsenide superconductor  $\text{BaFe}_{2-x}\text{Ni}_x\text{As}_2$ . *Phys. Rev. B*, 81:174524, May 2010.
- [160] Guy Deutscher. Andreev–Saint-James reflections: A probe of cuprate superconductors. *Rev. Mod. Phys.*, 77:109–135, Mar 2005.
- [161] A. A. Golubov, A. Brinkman, Yukio Tanaka, I. I. Mazin, and O. V. Dolgov. Andreev Spectra and Subgap Bound States in Multiband Superconductors. *Phys. Rev. Lett.*, 103:077003, Aug 2009.
- [162] Athena S. Sefat, Michael A. McGuire, Rongying Jin, Brian C. Sales, David Mandrus, Filip Ronning, E. D. Bauer, and Yuriy Mozharivskyj. Structure and anisotropic properties of  $\text{BaFe}_{2-x}\text{Ni}_x\text{As}_2$  ( $x = 0, 1, \text{ and } 2$ ) single crystals. *Phys. Rev. B*, 79:094508, Mar 2009.
- [163] M. A. Tanatar, N. Ni, C. Martin, R. T. Gordon, H. Kim, V. G. Kogan, G. D. Samolyuk, S. L. Bud'ko, P. C. Canfield, and R. Prozorov. Anisotropy of the iron pnictide superconductor  $\text{Ba}(\text{Fe}_{1-x}\text{Co}_x)_2\text{As}_2$  ( $x = 0.074$ ,  $T_c = 23$  K). *Phys. Rev. B*, 79:094507, Mar 2009.
- [164] Lei Fang, Huiqian Luo, Peng Cheng, Zhaosheng Wang, Ying Jia, Gang Mu, Bing Shen, I. I. Mazin, Lei Shan, Cong Ren, and Hai-Hu Wen. Roles of multiband effects and electron-hole asymmetry in the superconductivity and normal-state properties of  $\text{Ba}(\text{Fe}_{1-x}\text{Co}_x)_2\text{As}_2$ . *Phys. Rev. B*, 80:140508, Oct 2009.
- [165] F. Rullier-Albenque, D. Colson, A. Forget, and H. Alloul. Hall Effect and Resistivity Study of the Magnetic Transition, Carrier Content, and Fermi-Liquid Behavior in  $\text{Ba}(\text{Fe}_{1-x}\text{Co}_x)_2\text{As}_2$ . *Phys. Rev. Lett.*, 103:057001, Jul 2009.
- [166] S. Maiti, M. M. Korshunov, T. A. Maier, P. J. Hirschfeld, and A. V. Chubukov. Evolution of symmetry and structure of the gap in iron-based superconductors with doping and interactions. *Phys. Rev. B*, 84:224505, Dec 2011.
- [167] Walid Malaeb, Teppei Yoshida, Atsushi Fujimori, Masato Kubota, Kanta Ono, Kunihiro Kihou, Parasharam M. Shirage, Hijiri Kito, Akira Iyo, Hiroshi Eisaki, Yasuyuki Nakajima, Tsuyoshi Tamegai, and Ryotaro Arita. Three-Dimensional Electronic Structure of Superconducting Iron Pnictides Observed by Angle-Resolved Photoemission Spectroscopy. *Journal of the Physical Society of Japan*, 78(12):123706, 2009.
- [168] Gang Mu, Jun Tang, Yoichi Tanabe, Jingtao Xu, Satoshi Heguri, and Katsumi Tanigaki. Evidence for line nodes in the energy gap of the overdoped  $\text{Ba}(\text{Fe}_{1-x}\text{Co}_x)_2\text{As}_2$  from low-temperature specific heat measurements. *Phys. Rev. B*, 84:054505, Aug 2011.
- [169] Simon J. BENDING. Local magnetic probes of superconductors. *Advances in Physics*, 48(4):449–535, 1999.

- [170] J. R. Kirtley. Fundamental studies of superconductors using scanning magnetic imaging. *Reports on Progress in Physics*, 73(12):126501, 2010.
- [171] H. J. H. Smilde, Ariando, D. H. A. Blank, H. Hilgenkamp, and H. Rogalla.  $\pi$ -SQUIDs based on Josephson contacts between high- $T_c$  and low- $T_c$  superconductors. *Phys. Rev. B*, 70:024519, Jul 2004.
- [172] K Hasselbach, C Veauvy, and D Mailly. Microsquid magnetometry and magnetic imaging. *Physica C: Superconductivity*, 332(1-4):140 – 147, 2000.
- [173] Nanonis GmbH. Piezoelectric Quartz Tuning Forks for Scanning Probe Microscopy. <http://www.specs-zurich.com>.
- [174] P. G. N. U. Ch. Fischer, and K. Dransfeld. Scanning near-field acoustic microscopy. *Applied Physics B: Lasers and Optics*, 48:89–92, 1989. 10.1007/BF00694423.
- [175] Khaled Karrai and Robert D. Grober. Piezoelectric tip-sample distance control for near field optical microscopes. *Appl. Phys. Lett.*, 66(14):1842–1844, 1995.
- [176] Walid A. Atia and Christopher C. Davis. A phase-locked shear-force microscope for distance regulation in near-field optical microscopy. *Appl. Phys. Lett.*, 70(4):405–407, 1997.
- [177] A. G. T. Ruiter, J. A. Veerman, K. O. van der Werf, and N. F. van Hulst. Dynamic behavior of tuning fork shear-force feedback. *Appl. Phys. Lett.*, 71(1):28–30, 1997.
- [178] J.-P. Ndobu-Epoy, E. Lesniewska, and J.-P. Guicquero. Shear force microscopy with a nanoscale resolution. *Ultramicroscopy*, 103(3):229 – 236, 2005.
- [179] Jeffrey Siegel, Jeff Witt, Naia Venturi, and Stuart Field. Compact large-range cryogenic scanner. *Rev. Sci. Instrum.*, 66(3):2520–2523, 1995.
- [180] Brian Willard Gardner. *Thesis of Stanford University*, 2004.
- [181] Per G. Björnsson. *Thesis of Stanford University*, 2005.
- [182] S. H. Pan. *Piezo-electric motor*. International Bureau, World Intellectual Property Organization, 1993.
- [183] Alexander Ako Khajetoorians. *Thesis of the University of Texas at Austin*, 2008.
- [184] N. Moussy, H. Courtois, and B. Pannetier. A very low temperature scanning tunneling microscope for the local spectroscopy of mesoscopic structures. *Rev. Sci. Instrum.*, 72(1):128–131, 2001.
- [185] J. Pearl. Structure of superconductive vortices near a metal-air interface. *Journal of Applied Physics*, 37(11):4139, 1966.
- [186] John R. Clem. Simple model for the vortex core in a type ii superconductor. *Journal of Low Temperature Physics*, 18:427–434, 1975. 10.1007/BF00116134.
- [187] V. G. Kogan, A. Yu. Simonov, and M. Ledvij. Magnetic field of vortices crossing a superconductor surface. *Phys. Rev. B*, 48:392–397, Jul 1993.
- [188] Gilson Carneiro and Ernst Helmut Brandt. Vortex lines in films: Fields and interactions. *Phys. Rev. B*, 61:6370–6376, Mar 2000.
- [189] J. R. Kirtley, C. C. Tsuei, K. A. Moler, V. G. Kogan, J. R. Clem, and A. J. Turberfield. Variable sample temperature scanning superconducting quantum interference device microscope. *Appl. Phys. Lett.*, 74(26):4011–4013, 1999.
- [190] A. M. Chang, H. D. Hallen, L. Harriott, H. F. Hess, H. L. Kao, J. Kwo, R. E. Miller, R. Wolfe, J. van der Ziel, and T. Y. Chang. Scanning hall probe microscopy. *Appl. Phys. Lett.*, 61(16):1974–1976, 1992.
- [191] V. G. Kogan. Meissner response of anisotropic superconductors. *Phys. Rev. B*, 68:104511, Sep 2003.

- [192] R.P. Huebener. *Magnetic Flux Structure in Superconductors*. Springer-Verlag, 1979.
- [193] Kazuhiko Kuroki, Seiichiro Onari, Ryotaro Arita, Hidetomo Usui, Yukio Tanaka, Hiroshi Kon-tani, and Hideo Aoki. Unconventional Pairing Originating from the Disconnected Fermi Sur-faces of Superconducting  $\text{LaFeAsO}_{1-x}\text{F}_x$ . *Phys. Rev. Lett.*, 101:087004, Aug 2008.
- [194] S. Graser, A. F. Kemper, T. A. Maier, H.-P. Cheng, P. J. Hirschfeld, and D. J. Scalapino. Spin fluctuations and superconductivity in a three-dimensional tight-binding model for  $\text{BaFe}_2\text{As}_2$ . *Phys. Rev. B*, 81:214503, Jun 2010.
- [195] T. A. Maier, S. Graser, D. J. Scalapino, and P. J. Hirschfeld. Origin of gap anisotropy in spin fluctuation models of the iron pnictides. *Phys. Rev. B*, 79:224510, Jun 2009.
- [196] J. D. Fletcher, A. Serafin, L. Malone, J. G. Analytis, J.-H. Chu, A. S. Erickson, I. R. Fisher, and A. Carrington. Evidence for a Nodal-Line Superconducting State in  $\text{LaFePO}$ . *Phys. Rev. Lett.*, 102:147001, Apr 2009.
- [197] Clifford W. Hicks, Thomas M. Lippman, Martin E. Huber, James G. Analytis, Jiun-Haw Chu, Ann S. Erickson, Ian R. Fisher, and Kathryn A. Moler. Evidence for a Nodal Energy Gap in the Iron-Pnictide Superconductor  $\text{LaFePO}$  from Penetration Depth Measurements by Scanning SQUID Susceptometry. *Phys. Rev. Lett.*, 103:127003, Sep 2009.
- [198] J. K. Dong, S. Y. Zhou, T. Y. Guan, H. Zhang, Y. F. Dai, X. Qiu, X. F. Wang, Y. He, X. H. Chen, and S. Y. Li. Quantum Criticality and Nodal Superconductivity in the FeAs-Based Superconductor  $\text{KFe}_2\text{As}_2$ . *Phys. Rev. Lett.*, 104:087005, Feb 2010.
- [199] K. Hashimoto, A. Serafin, S. Tonegawa, R. Katsumata, R. Okazaki, T. Saito, H. Fukazawa, Y. Kohori, K. Kihou, C. H. Lee, A. Iyo, H. Eisaki, H. Ikeda, Y. Matsuda, A. Carrington, and T. Shibauchi. Evidence for superconducting gap nodes in the zone-centered hole bands of  $\text{KFe}_2\text{As}_2$  from magnetic penetration-depth measurements. *Phys. Rev. B*, 82:014526, Jul 2010.
- [200] K. Hashimoto, M. Yamashita, S. Kasahara, Y. Senshu, N. Nakata, S. Tonegawa, K. Ikada, A. Serafin, A. Carrington, T. Terashima, H. Ikeda, T. Shibauchi, and Y. Matsuda. Line nodes in the energy gap of superconducting  $\text{BaFe}_2(\text{As}_{1-x}\text{P}_x)_2$  single crystals as seen via penetration depth and thermal conductivity. *Phys. Rev. B*, 81:220501, Jun 2010.
- [201] Frédéric Hardy, Peter Adelman, Thomas Wolf, Hilbert v. L. hneysen, and Christoph Meingast. Large Anisotropic Uniaxial Pressure Dependencies of  $T_c$  in Single Crystalline  $\text{Ba}(\text{Fe}_{0.92}\text{Co}_{0.08})_2\text{As}_2$ . *Phys. Rev. Lett.*, 102:187004, May 2009.
- [202] R. Prozorov, M. A. Tanatar, N. Ni, A. Kreyssig, S. Nandi, S. L. Bud'ko, A. I. Goldman, and P. C. Canfield. Intrinsic pinning on structural domains in underdoped single crystals of  $\text{Ba}(\text{Fe}_{1-x}\text{Co}_x)_2\text{As}_2$ . *Phys. Rev. B*, 80:174517, Nov 2009.
- [203] C. Martin, H. Kim, R. T. Gordon, N. Ni, V. G. Kogan, S. L. Bud'ko, P. C. Canfield, M. A. Tanatar, and R. Prozorov. Evidence from anisotropic penetration depth for a three-dimensional nodal superconducting gap in single-crystalline  $\text{Ba}(\text{Fe}_{1-x}\text{Ni}_x)_2\text{As}_2$ . *Phys. Rev. B*, 81:060505, Feb 2010.
- [204] K. Gofryk, A. B. Vorontsov, I. Vekhter, A. S. Sefat, T. Imai, E. D. Bauer, J. D. Thompson, and F. Ronning. Effect of annealing on the specific heat of  $\text{Ba}(\text{Fe}_{1-x}\text{Co}_x)_2\text{As}_2$ . *Phys. Rev. B*, 83:064513, Feb 2011.
- [205] Hideto Fukazawa, Takehiro Yamazaki, Kenji Kondo, Yoh Kohori, Nao Takeshita, Parasharam M. Shirage, Kunihiro Kihou, Kiichi Miyazawa, Hijiri Kito, Hiroshi Eisaki, and Akira Iyo.  $^{75}\text{As}$  NMR Study of Hole-Doped Superconductor  $\text{Ba}_{1-x}\text{K}_x\text{Fe}_2\text{As}_2$  ( $T_c \simeq 38$  K). *J. Phys. Soc. Jpn.*, 78(3):033704, 2009.
- [206] B. Muschler, W. Prestel, R. Hackl, T. P. Devereaux, J. G. Analytis, Jiun-Haw Chu, and I. R. Fisher. Band- and momentum-dependent electron dynamics in superconducting  $\text{Ba}(\text{Fe}_{1-x}\text{Co}_x)_2\text{As}_2$  as seen via electronic Raman scattering. *Phys. Rev. B*, 80:180510, Nov 2009.

- [207] R. T. Gordon, H. Kim, N. Salovich, R. W. Giannetta, R. M. Fernandes, V. G. Kogan, T. Prozorov, S. L. Bud'ko, P. C. Canfield, M. A. Tanatar, and R. Prozorov. Doping evolution of the absolute value of the London penetration depth and superfluid density in single crystals of  $\text{Ba}(\text{Fe}_{1-x}\text{Co}_x)_2\text{As}_2$ . *Phys. Rev. B*, 82:054507, Aug 2010.
- [208] T. Klein, D. Braithwaite, A. Demuer, W. Knafo, G. Lapertot, C. Marcenat, P. Rodiere, I. Sheikin, P. Strobel, A. Sulpice, and P. Toulemonde. Thermodynamic phase diagram of  $\text{FeSe}_{0.5}\text{Te}_{0.5}$  single crystals in fields up to 28 tesla. *Phys. Rev. B*, 82:184506, Nov 2010.
- [209] R. T. Gordon, H. Kim, M. A. Tanatar, R. Prozorov, and V. G. Kogan. London penetration depth and strong pair breaking in iron-based superconductors. *Phys. Rev. B*, 81:180501, May 2010.
- [210] John R. Clem, R. P. Huebener, and D. E. Gallus. Gibbs free-energy barrier against irreversible magnetic flux entry into a superconductor. *J. Low Temp. Phys.*, 12:449–477, 1973. 10.1007/BF00654950.
- [211] Angela Kopp and Sudip Chakravarty. Criticality in correlated quantum matter. *Nature Physics*, 1(1):53–56, October 2005.
- [212] M. Franz and A. P. Iyengar. Superfluid Density of Strongly Underdoped Cuprate Superconductors from a Four-Dimensional XY Model. *Phys. Rev. Lett.*, 96:047007, Feb 2006.
- [213] Iulian Hetel, Thomas R. Lemberger, and Mohit Randeria. Quantum critical behaviour in the superfluid density of strongly underdoped ultrathin copper oxide films. *Nature Physics*, 3(10):700–702, October 2007.
- [214] R. Ramazashvili and P. Coleman. Superconducting quantum critical point. *Phys. Rev. Lett.*, 79:3752–3754, Nov 1997.
- [215] R. Ramazashvili. Anomalous behavior at a superconducting quantum critical point. *Phys. Rev. B*, 56:5518–5520, Sep 1997.
- [216] Lan Luan, Ophir M. Auslaender, Douglas A. Bonn, Ruixing Liang, Walter N. Hardy, and Kathryn A. Moler. Magnetic force microscopy study of interlayer kinks in individual vortices in the underdoped cuprate superconductor  $\text{YBa}_2\text{Cu}_3\text{O}_{6+x}$ . *Phys. Rev. B*, 79:214530, Jun 2009.
- [217] M. Benkraouda and John R. Clem. Instability of a tilted vortex line in magnetically coupled layered superconductors. *Phys. Rev. B*, 53:438–442, Jan 1996.
- [218] J. W. Guikema, Hendrik Bluhm, D. A. Bonn, Ruixing Liang, W. N. Hardy, and K. A. Moler. Two-dimensional vortex behavior in highly underdoped  $\text{YBa}_2\text{Cu}_3\text{O}_{6+x}$  observed by scanning Hall probe microscopy. *Phys. Rev. B*, 77:104515, Mar 2008.